Direct normal irradiance forecasting by artificial intelligence and predictive control of a solar reactor

Youssef Karout

École doctorale « Énergie et Énvironnement » (ED 305)

Prévision de l'éclairement normal direct par intelligence artificielle et commande prédictive d'un réacteur solaire

Thèse présentée pour l'obtention du grade de
Docteur de l'Université de Perpignan Via Domitia
Spécialité : Sciences de l'ingénieur

par

Youssef Karout

Soutenue le 24 octobre 2022, devant le jury composé de :

Rapporteurs :	Ted Soubdhan	Professeur, Université des Antilles
	Laurent Linguet	Professeur, Université de Guyane
Examinateurs :	Gilles Flamant	Directeur de recherche, PROMES-CNRS
	Didier Dumur	Professeur, CentraleSupélec
	Gilles Notton	Professeur, Université de Corse Pasquale Paoli
	Sylvain Rodat	Chargé de recherche, PROMES-CNRS
Encadrants :	Stéphane Grieu	Professeur, Université de Perpignan Via Domitia
	Stéphane Thil	Maître de conférences, Université de Perpignan Via Domitia
	Julien Eynard	Maître de conférences, Université de Perpignan Via Domitia
Invité :	Emmanuel Guillot	Ingénieur de recherche, PROMES-CNRS

Laboratoire « Procédés, Matériaux et Énergie Solaire »
PROMES-CNRS (UPR 8521)

Contents

List of Figures

List of Tables

Nomenclature

Abbreviations	Meaning
ANN	Artificial neural network
CF	Cloud fraction
CNN	Convolutional neural network
CSP	Concentrated solar power
EIA	Energy Information Administration
HDR	High dynamic range
k-NN	k-nearest neighbors
LDR	Low dynamic range
LSTM	Long short-term memory
MLP	Multilayer Perceptron
MPC	Model-based predictive control
RNN	Recurrent neural network
ROI	Region of interest
PID	Proportional integral derivative
TSI	Total Sky Imager

Variables	Meaning	Unit
DHI	Diffuse horizontal irradiance	$[\mathrm{W\,m^{-2}}]$
DNI	Direct normal irradiance	$[\mathrm{W\,m^{-2}}]$
$\mathrm{DNI_{CS}}$	Clear-sky direct normal irradiance	$[\mathrm{W\,m^{-2}}]$
GHI	Global horizontal irradiance	$[\mathrm{W\,m^{-2}}]$
I_0	Extraterrestrial solar irradiance	$[\mathrm{W\,m^{-2}}]$
$\mathrm{T_{LI}}$	Linke turbidity coefficient	–
SZA	Sun zenith angle	[rad]
H	Forecast horizon	[min]
P	Prediction horizon of the MPC controller	[min]
T_s	Data sampling time	[s]
SF	Skill factor	[%]
RDI	Ramp detection index	[%]
RM	Ramp magnitude	$[\mathrm{W\,m^{-2}}]$
nRMSE	Normalized root mean squared error	–
RGB	Red, green, and blue channels	–
RBR	Red-to-blue ratio	–
NRBR	Normalized red-to-blue ratio	–
I	Object intensity	–
(f_x, f_y)	Focal lengths	–
(c_x, c_y)	Center of distortion's coordinate	[pixel]
(k_1, k_2, k_3, k_4)	Distortion coefficients	[pixel]
$\mathrm{ROI}_H^{\mathrm{RGB}}$	RGB image of the ROI for forecast horizon H	–

(I_x, I_y, I_t)	Spatial and temporal gradients	–
(ϕ, l)	Polar coordinates of the ROI	[(rad, pixel)]
(c_x, c_y)	Distortion center coordinates	–
σ_d	Dominant cloud direction	[°]
σ_v	Dominant cloud velocity	[pixel/30s]
ATV	Average temperature variation	[K]
T	Reactor's temperature	[K]
h_i	Enthalpy of reactants and products	[kJ]
f_i^{in}	Reactants flow rate	$[\mathrm{kg\,s^{-1}}]$
f_i^{out}	Products flow rate	$[\mathrm{kg\,s^{-1}}]$
n_{rea}, n_{prod}	Number of reactants and products	–
D	Defocusing factor	$D \in [0, 1]$
$Q_{reaction}$	Power gained from the chem. reaction	[W]
Q_{Sun}	Power obtained from the Sun	[W]
$Q_{radiationloss}$	Power lost by radiation	[W]
$Q_{conductionloss}$	Power lost by conduction	[W]
m	Mass of the reactor walls	[kg]
$C_{p,w}$	Specific heat of the reactor walls	$[\mathrm{J\,kg^{-1}\,K^{-1}}]$
C	Concentration factor	3000
$\eta_{optical}$	Optical efficiency	0.6
$A_{aperture}$	Aperture's area	$3.15\,\mathrm{m^2}$ (0 if DNI $< 150\,\mathrm{W\,m^{-2}}$)
σ	Stefan–Boltzmann constant	$5.67 \times 10^{-8}\,\mathrm{W\,m^{-2}\,K^{-4}}$
T_{amb}	Ambient temperature	$298\,\mathrm{K}$
R	Conduction thermal resistance	$2.25 \times 10^{-1}\,\mathrm{K\,W^{-1}}$
S_p	Temperature setpoint	[K]
$\mathcal{M}$	Discretized reactor model	–

N.B. Cette thèse a été rédigée en anglais pour qu'elle soit accessible à un large public. Néanmoins, le lecteur francophone trouvera ci-après un résumé étendu rédigé en français récapitulant les principales contributions de ces travaux.

N.B. This thesis is written in English to make it more accessible to a wider audience. That being said, the interested reader will find hereinafter an extended summary in French of the main scientific contributions that this work makes.

Résumé en français

A Introduction

En raison de l'activité humaine au cours des dernières décennies, la planète est confrontée à des menaces existentielles qui exigent des actions rapides avant qu'il ne soit trop tard. Étant donné que l'augmentation de la demande en énergie induit une augmentation de la production d'énergie ainsi que des émissions de gaz à effet de serre, les gouvernements recherchent de nouvelles sources d'énergie respectueuses de l'environnement et fiables qui peuvent accompagner l'augmentation de la demande tout en réduisant l'impact anthropique sur la planète. Au cours des dernières années, de nombreux projets de recherche ont vu le jour avec pour objectif d'évaluer ces options énergétiques alternatives et de proposer des solutions intelligentes et durables. Par exemple, le gouvernement français a décidé d'une feuille de route et de règlementations, telles que la Stratégie Nationale Bas-Carbone (SNBC) [1] et le Plan Énergétique Pluriannuel (PPE) [2], afin d'influer sur le profil carbone du pays.

Au niveau européen, plusieurs projets ont pour ambition de concrétiser la vision verte de l'UE. L'un de ces projets est SFERA (Solar Facilities for the European Research Area) III [3] qui vise à fournir aux industriels œuvrant dans le domaine du solaire à concentration (ou solaire thermodynamique) des solutions techniques adaptées. Ce projet est structuré en groupes de tâches (WP), parmi lesquels les WP8 et WP10. Le WP10, auquel la première partie des travaux présentés dans ce manuscrit (Part I – DNI intra-hour forecasting destined to CSP infrastructure users) contribue, vise à :

- améliorer les instruments de mesure et les bancs d'essais de laboratoire utilisés pour la caractérisation de prototypes ;
- étudier et résoudre les problèmes liés à l'intermittence et à la variabilité de la ressource solaire lors d'essais réalisés au sein des infrastructures de recherche et évaluer de nouveaux systèmes ou des paramètres spécifiques ; la première partie des travaux de thèse contribuent à atteindre cet objectif ;
- améliorer la qualité de service pour la caractérisation optique des concentrateurs à focalisation linéaire ou ponctuelle.

Le WP8, auquel la deuxième partie des travaux présentés dans ce manuscrit (Part II – Model-based predictive control of a solar reactor dedicated to syngas production) contribue, vise à :

- évaluer les différentes technologies solaires à concentration pour la production de carburant solaire ;
- développer des outils de diagnostic destinés aux systèmes de production de carburant solaire utilisant l'énergie solaire concentrée ;
- développer des algorithmes pour le contrôle dynamique et l'optimisation du fonctionnement de chaque sous-système et de l'ensemble du système intégré de production de carburant solaire ;

- développer des outils pour l'évaluation des performances et de la fiabilité des matériaux, des composants et des sous-systèmes impliqués dans la production de carburant solaire.

La première partie des travaux de thèse présentés dans ce manuscrit est structurée par trois chapitres :

- le premier chapitre présente le contexte scientifique du projet SFERA III, tout en détaillant les défis scientifiques et techniques auxquels sont confrontées les technologies solaires à concentration. L'intérêt d'une prévision de la ressource solaire est argumenté. Enfin, un aperçu des modèles de prévision les plus courants (pour différentes données d'entrée et différents horizons de prévision) est donné au lecteur. Les questions de recherche abordées sont posées, les modèles de prévision développés sont argumentés. Les prévisions infra-horaire de l'éclairement normal direct (ou DNI, pour *direct normal irradiance*) seront transmises aux utilisateurs des infrastructures solaires à concentration qui pourront, ainsi, mieux planifier leurs expérimentations. Les horizons de prévision considérés sont 5, 10 et 15 minutes.

- le deuxième chapitre détaille le développement de deux modèles statitiques pour la prévision infra-horaire du DNI : un modèle LSTM (pour *long short-term memory*) et un modèle CNN-LSTM (pour *convolution neural network-long short-term memory*). L'implémentation de ces modèles, qui ne tirent profit que d'observations passées du DNI et qui fournissent des performances de référence, est discutée. Une étude comparative est réalisée afin de déterminer le paramétrage optimal des réseaux de neurones utilisées. Sur la base des performances obtenues, une conclusion est tirée.

- le troisième chapitre traite du développement d'un modèle hybride pour la prévision infra-horaire du DNI. Ce modèle est fondé sur l'analyse d'images du ciel et la prévision de séries temporelles. Le DNI par ciel clair est prédit à partir de mesures du DNI fournies par un pyrhéliomètre par un modèle empirique combiné à une persistance du trouble atmosphérique. Des caractéristiques utiles à la prévision du DNI sont extraites d'images du ciel à plage dynamique élevée (ou HDR, pour *high dynamic range*) générées par une caméra à grand angle de champ. Ces images sont traitées afin de corriger la distorsion que produit l'objectif grand angle. Un modèle k-NN (pour k-nearest neighbors ou, en français, méthode des k plus proches voisins) – une étude comparative est réalisée pour justifier le développement d'un outil de segmentation – permet la détection des nuages dont le mouvement est estimé à l'aide de l'algorithme de flot optique de Farnebäck. La région d'intérêt (ROI) est localisée sur la base du mouvement estimé des nuages à l'aide de la méthode de regroupement k-means et la fraction de nuages dans cette région ($\mathrm{CF}_{\mathrm{ROI}_H}$) est calculée. Le DNI est prédit, quelle que soit la situation du ciel, à l'aide d'un modèle fondé sur l'apprentissage automatique. Dans ce chapitre et pour chaque étape de l'algorithme de prévision, un état de l'art est présenté et la solution proposée est argumentée. Enfin, les résultats obtenus sont présentés et comparés aux résultats que produisent les modèles de référence mentionnés ci-avant. L'amélioration apportée par la prise en compte des images du ciel est mise en évidence. Les résultats obtenus mettent en évidence la pertinence d'associer modèles de connaissance et modèles guidés par les données et permettent d'évaluer l'apport d'images du ciel dans le processus de prévision du DNI. Ce chapitre marque la fin de la première partie des travaux.

La deuxième partie des travaux de thèse présentés dans ce manuscrit est structurée par deux chapitres : le premier traite de la modélisation d'un réacteur solaire pour la production de gaz de synthèse, le deuxième de la commande prédictive de ce réacteur. Le modèle développé par PROMES-CNRS et le CEA-LITEN [4, 5] est présenté et simulé afin de mettre en évidence la dynamique du réacteur. Ce dernier est conçu pour être chauffé à la fois par l'apport en énergie

solaire concentrée (chauffage allothermique) et la combustion in-situ (chauffage autothermique) [6, 5], permettant une conversion continue de la biomasse. Pendant les périodes ensoleillées, seule la réaction endothermique de gazéification se produit. Cependant, lorsque le DNI est inférieur à un certain seuil, l'injection d'oxygène est nécessaire afin de contrôler la température du réacteur. Le contrôleur MPC (pour *model-based predictive control*) développé est comparé à un contrôleur PID (proportionnel-intégral-dérivé) adaptatif. L'objectif est ici d'assurer la stabilité du réacteur en maintenant sa température à sa valeur nominale. Les contrôleurs manipulent deux entrées : le débit d'injection d'oxygène, qui est responsable de l'augmentation de la température du réacteur en cas de besoin, et le facteur de défocalisation pour limiter la puissance solaire reçue par le réacteur. Deux stratégies prédictives sont proposées et mises en œuvre. Différentes prévisions du DNI sont utilisées : des prévisions parfaites (définissant les performances optimales), des prévisions fournies par un modèle de persistance intelligent (définissant les performances de référence) et des prévisions fournies par un modèle basé sur des images du ciel à plage dynamique élevée (mettant en évidence l'amélioration des performances du contrôleur MPC que ce type de prévisions permet). Une étude comparative est réalisée afin de conclure sur les différents contrôleurs proposés.

B L'éclairement solaire et sa prévision

Dans cette section, l'éclairement solaire et ses composantes sont définis afin d'envisager un modèle adapté à la prévision infra-horaire du DNI. La section commence par un bref aperçu des principes fondamentaux du rayonnement électromagnétique permettant de comprendre l'origine des différentes composantes de l'éclairement solaire. Ensuite, ces composantes et leurs instruments de mesure associés sont passés en revue. La deuxième partie de cette section présente un état de l'art des modèles de prévision des différentes composantes de l'éclairement solaire.

B.1 Principes fondamentaux

L'éclairement solaire est défini comme la puissance par unité de surface associée au rayonnement électromagnétique émis par le Soleil. L'éclairement solaire reçu au sol dépend de la position du Soleil, de l'éclairement solaire extra-atmosphérique, des conditions atmosphériques et des caractéristiques du site considéré.

- L'éclairement solaire extra-atmosphérique est défini comme l'éclairement atteignant avec une incidence normale le sommet de l'atmosphère terrestre. La distance Terre-Soleil n'étant pas constante, cet éclairement ne l'est pas non plus. Or, d'après le principe de conservation de l'énergie, on peut écrire :

$$I_0 = \left(\frac{D_0}{D_{UA}}\right)^2 \cdot I_{UA} \tag{1}$$

  où I_0 est l'éclairement solaire extra-atmosphérique à la distance Terre-Soleil D_0 et D_{UA} est la distance moyenne entre la Terre et le Soleil ($D_{UA} = 1\text{UA} \approx 15 \times 10^7\,\text{km}$). I_{UA} est l'éclairement solaire extra-atmosphérique incident à la distance moyenne Terre-Soleil, également appelé constante solaire.

- l'interaction du rayonnement électromagnétique émis par le Soleil avec l'atmosphère terrestre atténue l'éclairement reçu au sol ; ce rayonnement est en partie absorbé et dispersé par les différents gaz présents dans l'atmosphère. Ces gaz ont des facteurs d'absorption et de transmission qui dépendent de la longueur d'onde. Ce phénomène explique une partie de la variabilité de l'éclairement solaire, la composition de l'atmosphère étant variable dans le temps et dans l'espace. L'éclairement normal direct (DNI), qui est l'éclairement

direct reçu sur un plan normal au Soleil (voir Section 2.1.3.1), peut être modélisé comme suit par la loi de Beer-Lambert :

$$\mathrm{DNI} = I_0 \exp\left(-m\tau\right) \tag{2}$$

où I_0 est l'éclairement solaire extra-atmosphérique, m est la masse d'air optique relative et τ est la profondeur optique de l'atmosphère.

Les nuages affectent l'éclairement solaire reçu au sol. Selon leur altitude, leur épaisseur optique et leur composition, les nuages ont des formes et des propriétés différentes, ce qui signifie qu'ils peuvent avoir différents effets d'atténuation. L'influence des nuages sur l'éclairement solaire reçu au sol est difficile à décrire de manière quantitative mais il ne dépend pas de la longueur d'onde de l'onde incidente, l'Équation (2) peut alors se réécrire comme suit :

$$\begin{aligned} \mathrm{DNI} &= I_0 \exp\left(-m(\tau_{cs} + \tau_{cloud})\right) && (3)\\ &= \exp\left(-m\tau_{cloud}\right) \cdot I_0 \exp\left(-m\tau_{cs}\right) && (4)\\ &= k_c \cdot \mathrm{DNI}_{cs} && (5) \end{aligned}$$

où k_c est l'indice ciel clair et DNI_{cs} est l'éclairement normal direct par ciel clair, qui est une fonction du coefficient τ_{cs}. Le coefficient τ_{cs} rend compte des phénomènes d'absorption et de diffusion évoqués ci-avant. L'indice k_c témoigne de la présence de nuages occultant le Soleil. Cet indice varie entre 0 et 1 ; $k_c = 0$ signifie qu'un nuage épais occulte le Soleil tandis que $k_c = 1$ signifie qu'aucun nuage n'occulte le Soleil (dans ce cas, la situation est dite « ciel clair »). Enfin, les cas intermédiaires correspondent à des nuages fins occultant le Soleil.

La Figure 1, illustrant l'Équation (3), est à la base de la plupart des modèles de prévision du DNI basés sur des images du ciel. Ces modèles dissocient le DNI en une composante déterministe, l'éclairement normal direct par ciel clair I_{cs}, et une composante stochastique, l'indice ciel clair k_c, traduisant l'influence des nuages occultant le Soleil sur l'éclairement. Ces modèles sont présentés dans la Section 2.2.4.

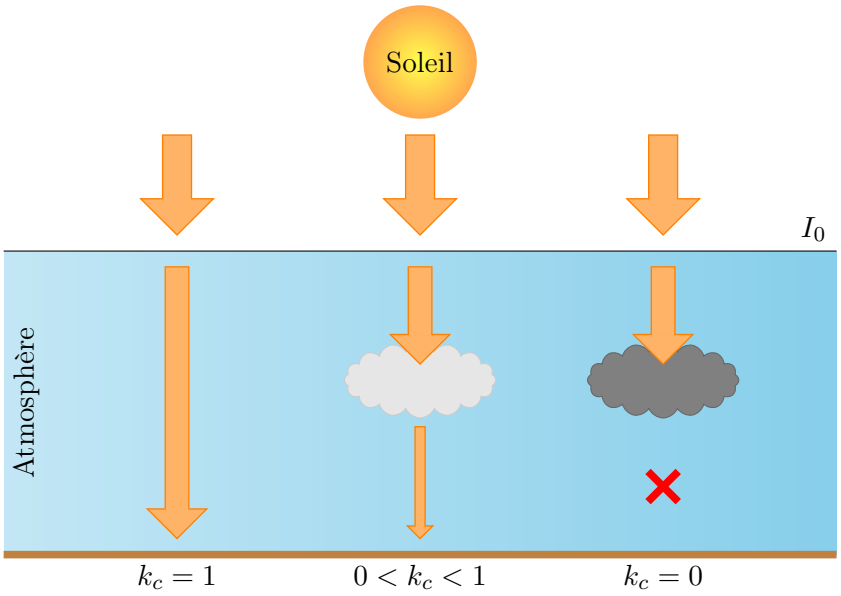

FIGURE 1 : L'indice ciel clair.

B.2 Les composantes de l'éclairement solaire

Les trois composantes de l'éclairement solaire sont définies ci-après.

- L'éclairement normal direct (DNI), qui est défini comme l'éclairement direct reçu sur un plan normal au Soleil [7], fait référence aux photons qui n'ont pas interagi avec l'atmosphère lors de leur trajet vers l'observateur. Il peut être formulé par [8] :

$$\mathrm{DNI}_{Sun} = 2\pi \int_0^{\xi_{Sun}} L(\xi)\sin(\xi)\, d\xi \tag{6}$$

  où ξ est l'angle du disque solaire ($\xi_{Sun} = 0.2666^o \pm 1.7\%$) et L est la luminance émanant du disque solaire mesurée en $\mathrm{W\,m^{-2}\,sr^{-1}}$.

  Divers instruments peuvent être utilisés pour mesurer le DNI ; ces instruments diffèrent par leur précision, leur coût et leurs fonctionnalités. L'instrument le plus utilisé est le pyrhéliomètre (Figure 2.4). Une thermopile [9] permet de mesurer l'éclairement direct. Le pyrhéliomètre devant être aligné avec le Soleil, un suiveur solaire est donc nécessaire. La précision de la mesure dépend fortement de l'étalonnage de l'instrument et de son entretien [10]. Si le pyrhéliomètre est correctement calibré et régulièrement entretenu, cette incertitude est de l'ordre de 2 %. L'instrument coûte environ 2500 € et le suiveur solaire coûte environ 10 000 €.

  Dans ce travail, le DNI est mesuré par un pyrhéliomètre (Kipp & Zonen CH1) et enregistré par un module industriel d'acquisition de données ModBus basse tension et haute précision (Gantner A4). Le suivi de la course du Soleil est réalisé en boucle ouverte par un suiveur solaire à deux axes (Kipp & Zonen 2 GD). En plus du nettoyage périodique des instruments, un contrôle qualité des mesures est assuré grâce à la mesure simultanée du DHI (Section 2.1.3.2) et du GHI (Section 2.1.3.3) par des pyranomètres équipés d'unités de ventilation (Kipp & Zonen CMP21). La base de données disponible est complète, sans données manquantes ou corrompues (des informations sur la base de données utilisée sont disponibles dans la Section 3.3.1). Des alternatives moins coûteuses existent, telles que le pyranomètre à bande rotative (RSI) (Figure 2.5). Cet instrument est équipé d'une photodiode montée horizontalement pour mesurer l'éclairement global. Une bande rotative occulte périodiquement la photodiode pour mesurer l'éclairement diffus, c'est-à-dire l'éclairement global privé de sa composante directe. À partir des éclairements global et diffus mesurés et de la position estimée du Soleil, le DNI peut être calculé. Cet instrument peut fournir des mesures des trois composantes de l'éclairement solaire, contrairement au pyrhéliomètre. Il ne nécessite pas de suiveur solaire à deux axes, ce qui en réduit la complexité tout en améliorant sa robustesse. De plus, des études ont montré qu'un RSI est nettement moins sensible à l'encrassement qu'un pyrhéliomètre. Il convient par ailleurs de mentionner qu'un RSI est moins cher qu'un pyrhéliomètre, pour un coût d'environ 7000 €. Par contre, un calibrage spectral précis de la photodiode est nécessaire. Cet étalonnage est complexe, d'où une incertitude plus élevée que celle d'un pyrhéliomètre : typiquement proche de 5 %.

- L'éclairement diffus horizontal (ou DHI, pour diffuse horiziontal irradiance) est défini comme l'éclairement qui n'est pas reçu directement du Soleil. Autrement dit, il s'agit de l'éclairement reçu sur un plan horizontal après interaction du rayonnement électromagnétique émis par le Soleil avec l'atmosphère ou l'environnement (diffusion dans l'atmosphère, réflexions simples ou multiples avec les nuages, l'atmosphère, le sol, ou les objets présents dans l'environnement). Le DHI est généralement mesuré avec un pyranomètre (équipé d'une boule d'ombrage masquant le Soleil). Une thermopile convertit le flux solaire en flux thermique puis en signal électrique. L'incertitude d'un pyranomètre correctement calibré est d'environ 3,2 % [11].

- L'éclairement global horizontal (ou GHI, pour global horizontal irradiance) est défini comme la somme des éclairements direct et diffus reçus au sol sur un plan horizontal. Le

GHI est donc une fonction du DNI et du DHI :

$$\mathrm{GHI} = \mathrm{DNI} \cdot \cos(\mathrm{SZA}) + \mathrm{DHI} \tag{7}$$

où SZA est l'angle entre le Soleil et le zénith. Le GHI peut être mesuré par un pyranomètre monté horizontalement ou une caméra à grand angle de champ [12].

B.3 Introduction à la prévision de l'éclairement solaire

La prévision de l'éclairement solaire est au cœur des activités de recherche et de développement visant à lever les verrous scientifiques et techniques qui pénalisent le déploiement des technologies solaires à concentration. Comme nous l'avons vu précédemment, la prévision de l'éclairement solaire peut contribuer au développement de stratégies prédictives de gestion et de maintenance ainsi qu'à l'optimisation de la durée et de la planification des expérimentations solaires pour les utilisateurs des infrastructures. Les prévisions de l'éclairement solaire sont caractérisées par leur résolution spatio-temporelle, certaines approches étant par conséquent, du fait de l'objectif poursuivi, plus appropriées que d'autres. Le travail présenté dans ce manuscrit traite de la prévision du DNI pour un horizon de temps H tel que $H = h \cdot T_s$, avec $T_s = 30\,\mathrm{s}$, allant jusqu'à 30 min. Cette section présente différents modèles de persistance du DNI puis une revue des modèles ciel clair est réalisée. Enfin, un état de l'art des modèles de prévision est présenté. Cependant, pour cette étude, des modèles de prévision du GHI sont également mentionnés car une majorité des travaux qu'il est possible de trouver dans la littérature lui sont consacrés.

B.3.1 Modèles d'éclairement par ciel clair

Les modèles d'éclairement par ciel clair permettent d'estimer l'éclairement au niveau du sol dans des conditions dites ciel clair, c'est-à-dire en l'absence de nuages occultant le Soleil. Le DNI par ciel clair varie en fonction de l'angle entre le Soleil et le zénith, de l'altitude du site considéré et de divers paramètres atmosphériques. Il existe un vaste choix de modèles ciel clair dans la littérature [13]. Le DNI par ciel clair peut être calculé à l'aide de modèles radiatifs ou empiriques. Les modèles radiatifs sont généralement dérivés de la loi de Beer-Lambert (Équation (2)). Bien que ces modèles puissent être plus précis que les modèles empiriques, ils nécessitent des données qui ne sont pas toujours disponibles. C'est pourquoi la communauté scientifique s'est tournée vers le développement de modèles empiriques et a cherché à en améliorer la précision. Le modèle de prévision du DNI par ciel clair proposé par Nou et al. [14], basé sur l'Équation (2.16), est utilisé dans ce travail. Ainsi, la prévision du DNI par ciel clair à l'instant $k+h$ est donnée par :

$$\widehat{\mathrm{DNI}}_{\mathrm{CS}}(k+h) = bI_0 \exp\left(-0.09\widehat{m}(k+h)(\widehat{\mathrm{T}}_{\mathrm{LI}}(k+h) - 1)\right) \tag{8}$$

où :

- b est calculé comme suit :

$$b = 0.664 + 0.163 \exp\left(\frac{alt}{8000}\right) \tag{9}$$

  avec alt l'altitude du site considéré ;

- Le trouble de Linke est prédit par une simple persistance : $\widehat{\mathrm{T}}_{\mathrm{LI}}(k+h) = \mathrm{T}_{\mathrm{LI}}(k)$, puisque sa variabilité journalière est relativement faible ; l'estimation de sa valeur à l'instant k est réalisée en utilisant des mesures du DNI, comme proposé par Nou et al. [14].

- $\widehat{m}(k+h)$ est la masse d'air optique relative prédite.

B.3.2 Modèles de prévision

Les principales approches de prévision de l'éclairement solaire sont les modèles statistiques, les modèles basés sur des images du ciel et les modèles numériques de prévision météorologique ou modèles NWP (pour *numerical weather prediction*) [15]. Chaque approche est caractérisée par une gamme d'horizons spatio-temporels, comme le montre la Figure 2. En outre, le choix du type de modèle dépend de l'objectif poursuivi. Les modèles statistiques peuvent fournir des prévisions à haute résolution temporelle, pour des horizons longs, mais sont pénalisés par de faibles capacités spatiales. D'autre part, les modèles NWP, qui nécessitent la résolution d'équations météorologiques, ont une capacité spatio-temporelle importante et fournissent des prévisions pour des horizons longs mais dépendent fortement de l'état initial des variables considérées (ce qui nécessite des mesures précises par des capteurs spécifiques judicieusement positionnés). Par ailleurs, ils exigent d'importantes ressources informatiques pour de faibles résolutions. Enfin, les modèles basés sur des images du ciel sont des modèles à haute résolution spatio-temporelle, pour des besoins en ressources calculatoires moindres que ceux des modèles NWP.

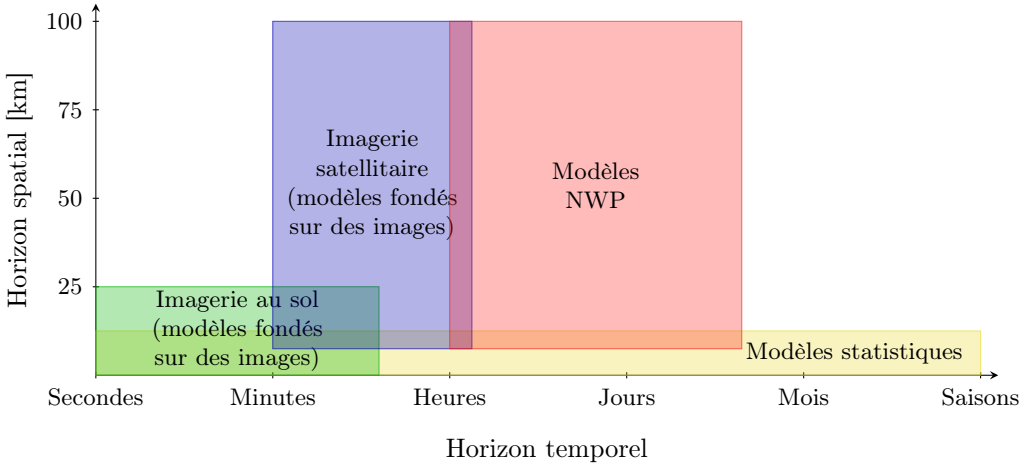

FIGURE 2 : Approches pour la prévision de la ressource solaire, selon l'horizon spatio-temporel (adapté de [16]).

Dans la suite de cette section, un état de l'art des approches statistiques et des approches fondées sur l'imagerie au sol pour la prévision intra-horaire de la ressource solaire est réalisé. Bien que les travaux présentés dans ce manuscrit traitent de la prévision du DNI, le domaine est élargi à la ressource solaire, puisqu'un grand nombre de travaux est consacré au GHI. Il convient de mentionner que la prévision du DNI est considérée comme plus compliquée que la prévision du GHI en raison de la grande variabilité du DNI : le DNI peut varier entre sa valeur par ciel clair (la valeur du DNI lorsqu'aucun nuage n'occulte le Soleil) et zéro en quelques secondes seulement, contrairement au GHI, en raison de sa composante diffuse. De plus, le solaire à concentration est beaucoup plus affecté par les brusques variations de la ressource solaire (appelées « rampes ») que le solaire photovoltaïque, ce qui rend la prédiction de ces événements cruciale. L'étude des approches dédiées à la prévision du GHI est intéressante car certaines de ces approches peuvent être similaires à celles utilisées pour la prévision du DNI.

Les travaux issus de la littérature peuvent être classifiés en fonction des données d'entrée utilisées (de plus amples détails sur les différentes références citées ci-après peuvent être trouvés dans le Tableau 2.1).

- Des mesures d'éclairement (et éventuellement d'autres variables). Même si certaines approches classiques de prévision de séries temporelles sont utilisées, la plupart des travaux récents traitent du développement de modèles statistiques fondés sur les outils

de l'apprentissage automatique [17, 18, 19, 20]. Ces modèles peuvent prédire la ressource solaire pour des horizons allant de quelques minutes à plusieurs jours. Cependant, comme ils sont uniquement basés sur des observations passées, ces modèles ne parviennent généralement pas à prédire avec précision les rampes.

- Des images du ciel (fournies par une caméra à grand angle de champ) et des mesures d'éclairement (et éventuellement d'autres variables). Pour ces modèles, l'horizon de prévision est fortement réduit, culminant généralement à 30 min : en effet, les informations contenues dans les images du ciel deviennent limitées à mesure que l'on se rapproche du bord de l'image. Cependant, l'utilisation des images du ciel permet d'anticiper l'influence des perturbations atmosphériques sur la ressource solaire, ce qui contribue à une meilleure prédiction des rampes. Les algorithmes de prévision de la ressource solaire comptent généralement trois étapes principales : tout d'abord, les images sont acquises et traitées afin de détecter les nuages ; ensuite, le mouvement des nuages est estimé ; enfin, sur la base de ces informations et, éventuellement, d'autres mesures, des caractéristiques sont extraites des images afin de réaliser la prévision. En particulier, cette dernière étape peut impliquer l'utilisation d'un modèle ciel clair [21, 22, 23, 24, 25]. En effet, comme mentionné ci-avant, le DNI peut être scindé en une composante déterministe, le DNI par ciel clair ($\mathrm{DNI_{CS}}$), et une composante stochastique, l'indice ciel clair (k_c). Enfin, le mouvement estimé des nuages peut également être utilisé afin de générer une image artificielle à l'horizon de prévision considéré [26].

  Il va sans dire qu'il existe des modèles qui ne suivent pas exactement les mêmes étapes. On peut trouver des solutions sans détection des nuages ni estimation de leur mouvement, reposant uniquement sur la capacité des outils utilisés à apprendre de caractéristiques extraites d'images du ciel ou de mesures d'éclairement : par exemple, une approche du type « plus proche voisin »[27] ou des modèles fondés sur des réseaux de neurones artificiels [28]. Par ailleurs, l'utilisation de la totalité de l'image peut ne pas conduire aux meilleurs résultats : même si la détection des nuages et, surtout, l'estimation de leur mouvement sont difficiles à réaliser avec précision, ces étapes peuvent fournir des informations essentielles car elles permettent de déterminer des régions au sein de l'image – appelées régions d'intérêt – qui interagiront avec le Soleil à l'horizon de prévision considéré.

C Prévision infra-horaire du DNI

C.1 Modèles neuronaux

Les réseaux de neurones artificiels sont des outils de l'apprentissage automatique, généralement structurés en couches : une couche d'entrée, une ou plusieurs couches cachées et une couche de sortie. Ces couches contiennent des unités (ou neurones) qui sont connectés à d'autres unités, imitant l'interaction entre les neurones biologiques. Chaque neurone, défini par ses poids synaptiques et son biais, est optimisé pour minimiser l'erreur entre la sortie du réseau (la prédiction) et la cible, sur la base d'une fonction de perte qu'il convient de minimiser. Ce processus d'optimisation est itératif et réalisé à partir d'un jeu d'observations composées d'entrées et de sorties cibles. Il est connu sous le nom d'apprentissage supervisé. Différentes architectures neuronales existent, telles que les réseaux de neurones à propagation avant (ou Perceptrons multicouches), les réseaux de neurones récurrents, les réseaux de neurones convolutifs, etc. Au cours de cette thèse, les modèles développés sont fondés sur des réseaux de neurones récurrents.

Un réseau de neurones récurrent (RNN) est un réseau dont les neurones ont une mémoire. Cette mémoire permet au réseau de d'appréhender les comportements dynamiques. Ce type

de réseau est utilisé lorsque la sortie est influencée par des entrées passées (des observations), pour :

- l'analyse et la prévision de séries temporelles, comme indiqué dans la Section 2.2.4 de ce manuscrit, ou la détection d'anomalies [29, 30]. Ces réseaux ont démontré de très bonnes aptitudes dès lors qu'il s'agit d'appréhender les caractéristiques temporelles de ces séries ;

- le traitement naturel du langage ; ces réseaux sont utilisés, par exemple, pour la traduction automatique [31] ou l'analyse des sentiments [32], des tâches pour lesquelles ils ont prouvé leur efficacité dans le traitement et la manipulation de textes.

Du fait de la popularité des réseaux RNN pour la prévision de séries temporelles, deux de ces réseaux sont optimisés et mis en œuvre pour la prévision du DNI. Tout comme pour le modèle de persistance intelligent, ces modèles statistiques servent de modèles de référence afin d'évaluer les performances du modèle fondé sur des images du ciel présenté dans le Chapitre 4 de ce manuscrit. Ces modèles sont :

- un réseau LSTM (long short-term memory) profond (Section 3.2.1) ;

- un réseau LSTM profond précédé d'une couche convolutive (Section 3.2.2) utilisée comme couche de prétraitement favorisant l'apprentissage des couches LSTM.

Ces deux modèles considèrent en entrée des observations passées du DNI (le nombre d'observations considérées définit le support de prévision ; la taille de ce support doit être optimisée). La base de données utilisée est composée de 34 jours, chacun de ces jours comptant 1200 observations (des images du ciel et des mesures du DNI) de 7h00 à 17h00, collectées au laboratoire PROMES-CNRS à Odeillo (France) où la variabilité du DNI est élevée. Ces 40 jours (issus de différentes saisons) ont été sélectionnés parmi les 373 jours disponibles et correspondent à des situations mixtes. Cette base de données a ensuite été scindée en deux sous-ensembles : le premier destiné à l'apprentissage et à la validation (22 jours, ce qui représente 26400 observations), le deuxième pour le test des modèles (12 jours, ce qui représente 14400 observations). Les réseaux LSTM et CNN-LSTM sont entraînés et validés à l'aide d'une technique dite de validation croisée : le premier sous-ensemble est divisé de manière aléatoire mais égale en cinq groupes d'exemples ; pour chaque groupe, 70 % des données sont utilisées pour l'entrainement et 30 % pour la validation. L'algorithme Adam, une méthode d'optimisation efficace d'un point de vue calculatoire fondée sur une descente de gradient stochastique à taux d'apprentissage adaptatif [33], est utilisé. Pour éviter le sur-apprentissage, une régularisation par *dropout* est effectuée pour chacune des couches du réseau avec un taux fixé à 50 % [34]. L'erreur quadratique moyenne est choisie comme fonction de perte. Enfin, 20 itérations sont réalisées pour chaque groupe afin de garantir la convergence de l'algorithme au cours de l'apprentissage.

Les réseaux RNN dont la topologie et le support de prévision ont été optimisés (voir Section 3.3.3.1 et Section 3.3.3.2) sont ensuite évalués grâce aux données de test (des situations mixtes) et leurs performances sont comparées en calculant l'erreur quadratique moyenne normalisée (nRMSE), le *skill factor* (SF) et l'indice de détection de rampe (RDI). Une analyse globale est réalisée. Les résultats présentés par la Figure 3 montrent que le modèle CNN-LSTM surpasse légèrement le modèle LSTM (pour tous les horizons de prévision), obtenant un nRMSE inférieur et un SF supérieur grâce à sa couche convolutive. On peut observer que le nRMSE obtenu par les deux modèles augmente à mesure que l'horizon de prévision augmente, ce qui s'explique par la forte variabilité du DNI. Cela signifie qu'à mesure que l'horizon de prévision augmente, il devient de plus en plus difficile de prévoir le DNI, comme en témoignent des valeurs du nRMSE plus élevées. Ceci explique aussi l'augmentation du SF. À mesure que l'horizon de prévision augmente, la probabilité que le DNI soit stable entre l'instant présent

et l'horizon de prévision diminue et les performances du modèle de persistance se dégradent considérablement, permettant aux modèles RNN développés d'obtenir un SF plus élevé.

En raison du manque d'information concernant la situation du ciel (présence de nuages ; position, épaisseur et mouvement des nuages), les deux modèles RNN n'ont pas réussi à prévoir les rampes. Les faibles valeurs de RDI obtenues montrent que ces approches statistiques ne sont pas adaptées à la détection de rampes et, pour améliorer cet aspect, d'autres données, comme des images du ciel, devraient être considérées.

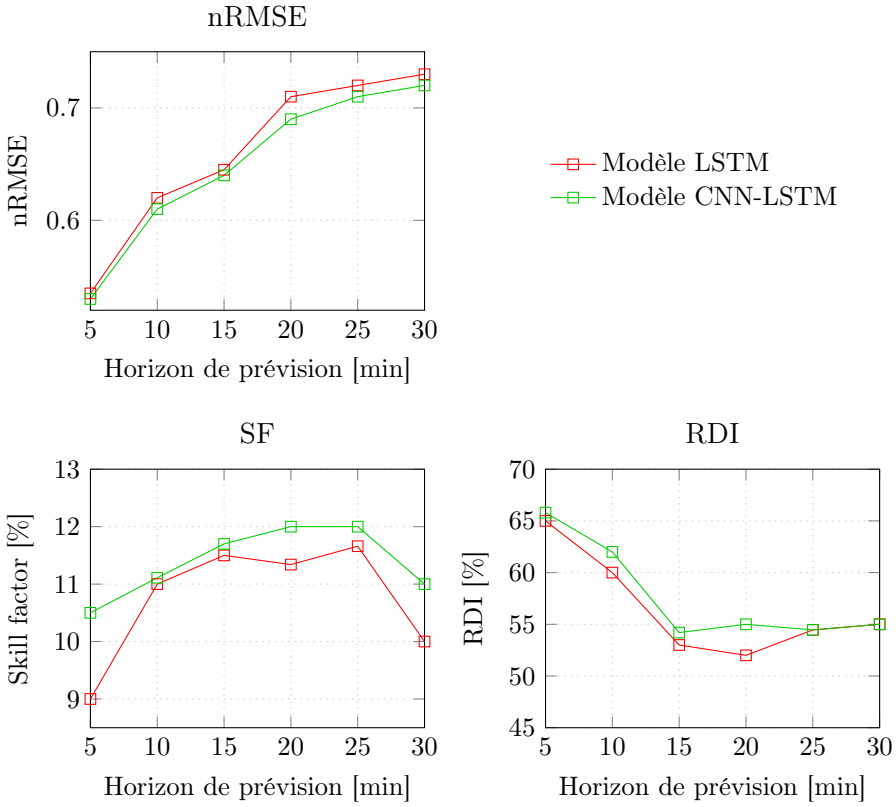

FIGURE 3 : Comparaison des modèles LSTM et CNN-LSTM grâce au jeu de données de test.

C.2 Modèle hybride

Comme indiqué dans la section précédente, alors que les modèles statistiques peuvent fournir des prévisions acceptables du DNI (en termes de SF et de nRMSE), pour de longs horizons de prévision, leur capacité à prédire des rampes est médiocre. Cela est dû aux entrées des modèles, qui n'ont pas de lien direct avec le mouvement des nuages (la principale cause d'une brusque variation du DNI). Ce résultat justifie la prise en considération d'images du ciel pour la prévision du DNI : si l'interaction des nuages avec le Soleil est à l'origine de rampes, alors il est crucial d'utiliser des images du ciel pour analyser le comportement des nuages et anticiper cette interaction.

Ainsi, le modèle hybride proposé tire profit d'images du ciel pour la détection des nuages et l'estimation de leur mouvement, ce qui permet de localiser une région d'intérêt (ROI). Cette région d'intérêt est censée interagir avec le Soleil à l'horizon de prévision considéré. Après la localisation de cette région sur l'image, des caractéristiques en sont extraites et utilisées comme entrées d'un modèle de prévision du DNI. Dans cette section, les différents composantes du modèle, illustré par la Figure 4, sont expliquées. La section commence par une brève description de la caméra à grand angle de champ utilisée et de la base de données considérée dans cette étude. Le modèle ciel clair est ensuite implémenté pour différentes

conditions atmosphériques afin d'étudier sa robustesse. Les algorithmes proposés pour la détection des nuages sont détaillés puis une étude comparative est réalisée afin de décider d'une approche de segmentation précise, robuste et rapide. Après avoir détecté les nuages, leur mouvement doit être estimé. L'algorithme d'estimation du mouvement des nuages est implémenté dans des conditions contrôlées pour déterminer sa précision et sa robustesse. Ensuite, l'algorithme de localisation de la région d'intérêt est présenté. Enfin, la méthode d'extraction des caractéristiques est détaillée, conduisant au modèle de prévision du DNI proposé. Les performances du modèle sont étudiées pour diverses situations du ciel afin, d'une part, d'évaluer sa capacité à détecter des rampes et sa robustesse et, d'autre part, de mettre en évidence les bénéfices que procure la prise en considération d'images du ciel pour la prévision infra-horaire du DNI.

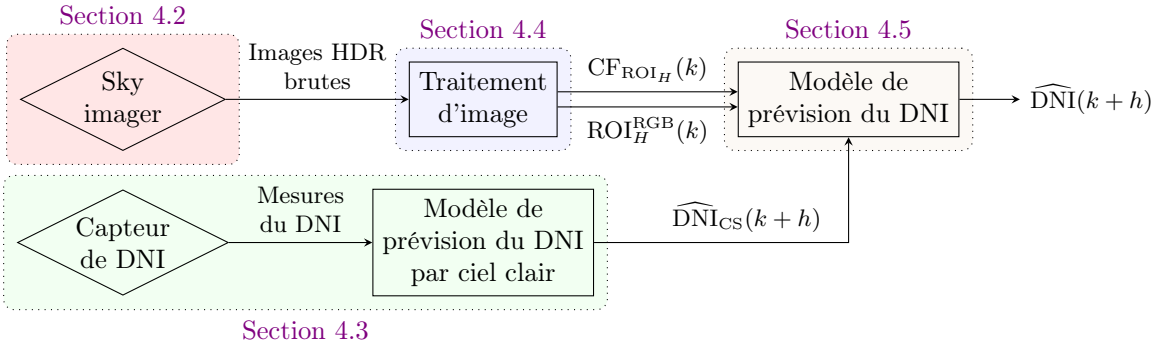

FIGURE 4 : Architecture du modèle hybride proposé, avec cinq principales étapes : l'acquisistion d'images à plage dynamique élevée (HDR), le modèle de prévision du DNI par ciel clair, le traitement d'image et le modèle de prévision du DNI ($\mathrm{ROI}_H^{\mathrm{RGB}}$ est l'image RVB de la région d'intérêt (ROI), $\mathrm{CF}_{\mathrm{ROI}_H}$ est la fraction de nuage dans la région d'intérêt).

C.2.1 Caméra à grand angle de champ

La caméra à grand angle de champ utilisée dans ce travail a été développée, avec l'aide du laboratoire PROMES-CNRS, par la société PROMECA (voir Figure 4.3a). Il s'agit d'un système d'imagerie numérique automatique, fonctionnant en continu, conçu pour l'acquisition d'images du ciel avec un champ de vision de 180° (voir Figure 4.3b). La caméra à grand angle de champ fournit une analyse à la volée de la situation du ciel pendant la journée. Les principales caractéristiques matérielles/logicielles sont les suivantes : un capteur CMOS couleur d'une résolution de 1,5 MP, un ordinateur embarqué permettant l'implémentation de solutions logicielles de pointe et une sous-couche logicielle pour, d'une part, la génération d'une image à plage dynamique élevée (HDR) permettant une mesure de l'éclairement et, d'autre part, l'autocalibration géométrique de l'instrument. L'image HDR, obtenue en fusionnant une séquence d'images du ciel à basse dynamique prises à différents temps de pause, est essentielle pour une détection efficace des nuages, en particulier dans la région circumsolaire (où les pixels ont tendance à être saturés), ce qui primordial pour la prévision précise du DNI. L'algorithme d'autocalibration géométrique de l'instrument est basé sur une comparaison entre la position théorique du Soleil et sa position sur l'image.

La caméra à grand angle de champ enregistre une image toutes les 30 secondes. Comme mentionné ci-avant, la base de données utilisée dans cette étude est composée d'images du ciel collectées à Odeillo (373 jours), sans données manquantes. La classification des données révèle 128 journées ciel clair (34,4 %), 49 journées couvertes (13,1 %) et 196 journées caractérisées par des situations mixtes (52,5 %). Les profils du DNI sont classifiés, comme indiqué au Chapitre 3, selon les situations définies ci-après.

- La situation est dite ciel clair si le DNI mesuré est inférieur de moins de 10 % de sa valeur par ciel clair pendant 90 % de la journée.
- La situation est dite ciel couvert si le DNI mesuré est inférieur à 60 % de sa valeur par ciel clair pendant 90 % de la journée et si la variation moyenne du DNI est inférieure à 20 $\mathrm{W\,m^{-2}}$.
- La situation est dite mixte pour les autres cas de figure ; ces journées peuvent donc être partiellement ciel clair ou partiellement couvertes.

Il convient de mentionner que les situations mixtes sont jugées plus importantes que les autres situations : les situations ciel clair et ciel couvert sont moins difficiles à appréhender et sont moins fréquentes à Odeillo ; par ailleurs, les modèles à la pointe de l'état de l'art ont du mal à appréhender les situations mixtes en raison de leur grande complexité. C'est pourquoi, dans cette étude, l'accent est mis sur ce type de situation. Ainsi, le modèle hybride proposé est entrainé, validé et testé à l'aide de profils du DNI correspondant à des situations mixtes. Enfin, le modèle hybride est également testé avec des profils du DNI correspondant à des situations ciel clair et ciel couvert afin d'évaluer sa capacité à prédire le DNI pour des profils moins complexes. Les caractéristiques de la caméra à grand angle de champ, du site considéré (Odeillo) et de la base de données sont regroupées dans le Tableau 4.1.

C.2.2 Modèle ciel clair

Le modèle ciel clair présenté dans la Section B.3.1 du manuscrit a été implémenté pour différentes conditions atmosphériques, comme le montre la Figure 5. Grâce à sa nature adaptative, le modèle fournit des estimations précises pour différentes conditions atmosphériques : le graphique de gauche présente une atmosphère peu chargée en aérosols et des valeurs du DNI élevées, le graphique de droite présente une atmosphère chargée en aérosols et des valeurs du DNI faibles.

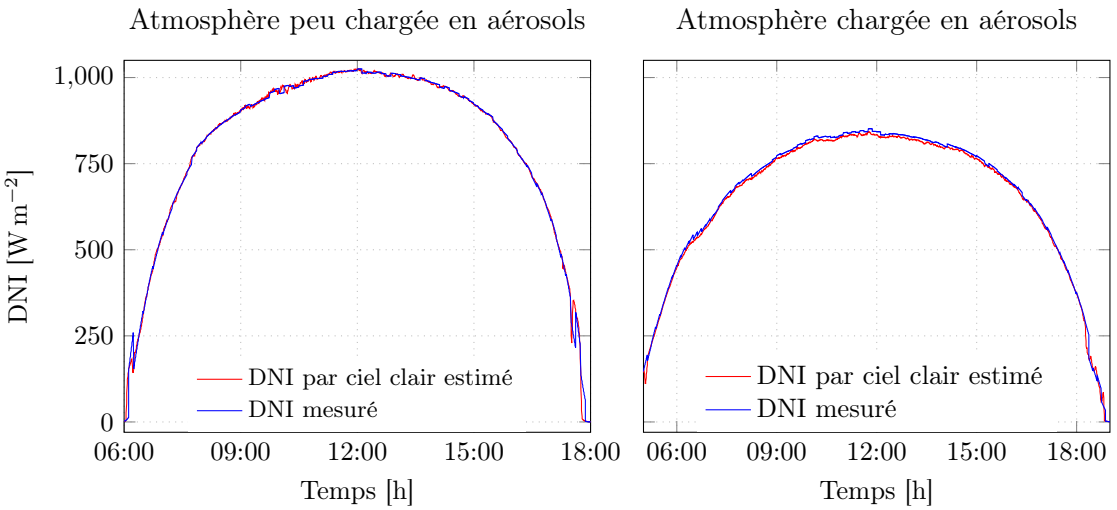

FIGURE 5 : Implémentation du modèle donnant le DNI par ciel clair pour différentes conditions atmosphériques.

C.2.3 Traitement d'image

L'étape de traitement d'image est cruciale dans le processus de prévision du DNI car, comme mentionné précédemment, la situation du ciel doit être analysée avec précision afin d'obtenir des prévisions précises. Le traitement d'image est utilisé pour extraire des informations utiles

à la prévision du DNI. La Figure 6 résume l'ensemble des étapes de traitement menant à l'extraction de caractéristiques des images du ciel :

- les images HDR sont traitées afin de corriger la distorsion causée par l'objectif hypergone (Section 4.4.1) ;
- les nuages sont détectés à l'aide d'un modèle fondé sur l'apprentissage automatique (Section 4.4.3) ;
- le mouvement des nuages est ensuite estimé à l'aide de l'algorithme de flot optique de Farnebäck (Section 4.4.4) ;
- la région d'intérêt (ROI) est alors localisée sur la base du mouvement estimé des nuages à l'aide de la méthode de regroupement k-means (Section 4.4.5) ;
- enfin, la fraction de nuages dans la région d'intérêt est calculée ($\mathrm{CF}_{\mathrm{ROI}_H}$) et transmise au modèle de prévision du DNI dont les entrées sont par ailleurs l'image RVB de la région d'intérêt ($\mathrm{ROI}_H^{\mathrm{RGB}}$) et le DNI par ciel clair prédit (Section 4.4.6).

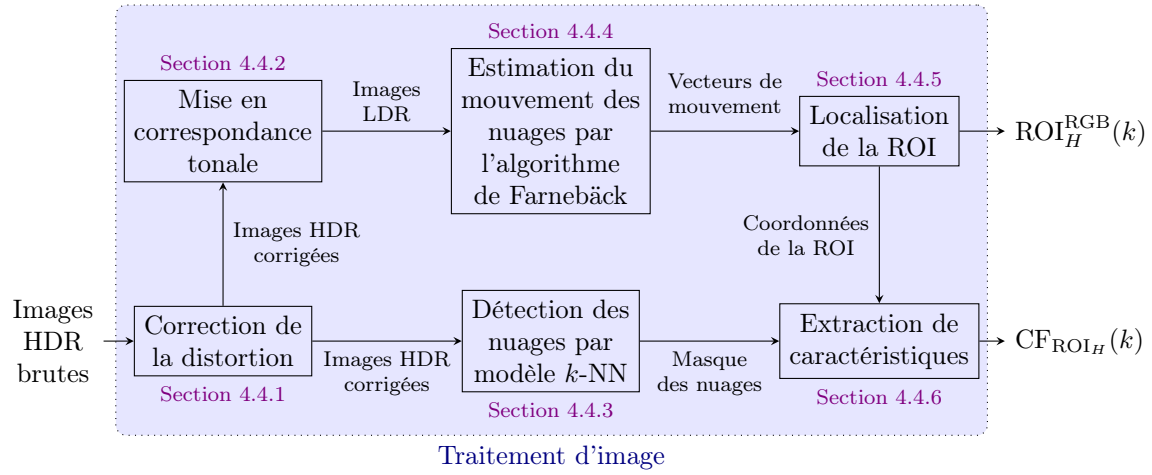

FIGURE 6 : Étapes du traitement d'image pour l'extraction de caractéristiques. Les principales étapes sont : la correction de la distorsion des images HDR, la détection des nuages, l'estimation de leur mouvement, la localisation de la région d'intérêt (ROI) et le calcul de la fraction de nuages dans cette région ($\mathrm{CF}_{\mathrm{ROI}_H}$).

Les différentes étapes de cet algorithme sont détaillées ci-après.

C.2.3.1 Correction de la distorsion et mise en correspondance tonale La première étape est la correction de la distorsion de l'image. Le processus de correction associe un point d'un environnement 3D à une image 2D à l'aide des paramètres extrinsèques et intrinsèques de la caméra, obtenus lors de son autocalibration géométrique. Les points de l'environnement sont transformés en coordonnées caméra en utilisant les paramètres extrinsèques (entraînant une rotation et une translation). Les coordonnées de la caméra sont ensuite « mappées »dans le plan de l'image à l'aide des paramètres intrinsèques (longueur focale, centre de distorsion et coefficients de distorsion radiale). Pour plus d'informations sur ce processus, le lecteur est renvoyé à [35, 36].

L'algorithme de mise en correspondance tonale (ou *tone-mapping*) est présenté ; l'importance d'implémenter un algorithme robuste est soulignée. Différentes solutions pour la mise en correspondance tonale sont passées en revue afin de choisir une méthode adaptée. La mise en correspondance tonale consiste en la conversion d'une image HDR en une image LDR, qui

sera l'entrée de l'algorithme de flot optique utilisé. Il convient de mentionner que ce bloc est crucial dans l'étape de traitement d'image car il joue un rôle clé dans la bonne estimation du mouvement des nuages. Plusieurs algorithmes de mise en correspondance tonale existent [37], tels que :

- la méthode de Drago [38] : une mise en correspondance tonale logarithmique adaptative pour l'affichage de scènes à contraste élevé ;
- la méthode de Durand [39] : cette approche préserve les détails en compressant le contraste de l'image ;
- la méthode de Mantiuk [40] : cet algorithme reconstruit l'image à partir de nouvelles valeurs de contraste calculées à l'aide de gradients pour tous les niveaux de la pyramide gaussienne ; il transforme les valeurs de contraste en réponse de teinte, saturation et valeur (HSV) et met à l'échelle la réponse ;
- la méthode de Reinhard [41] : il s'agit d'un opérateur global de mise en correspondance tonale qui modélise le système visuel humain. La fonction de mise en correspondance tonale est paramétrée par des paramètres d'adaptation, calculés à l'aide de l'adaptation à la lumière et aux couleurs.

Le fabricant de la caméra à grand angle de champ (la société PROMECA) recommande d'utiliser la méthode de Reinhard en raison de sa nature adaptative et de sa capacité à tenir compte des changements d'intensité. Cette méthode est robuste aux images très lumineuses lorsque le Soleil est apparent et aux images sombres lorsque le Soleil est complètement occulté. Comme mentionné ci-avant, la fonction de mise en correspondance tonale doit être paramétrée avec précision afin d'obtenir la meilleure qualité d'image et de préserver les détails et, par conséquent, que le mouvement des nuages puisse être correctement estimé. Ces paramètres sont :

- la valeur de correction gamma ;
- le facteur d'intensité ;
- le facteur d'adaptation à la lumière.

C.2.3.2 Détection des nuages Les prévisions du DNI sont fortement influencées par le mouvement des nuages. C'est pourquoi un algorithme de segmentation est nécessaire afin d'identifier précisément les pixels de l'image correspondant à des nuages. Deux types d'approches sont possibles : les approches à seuils et les approches fondées sur l'apprentissage automatique. Les approches à seuils sont performantes dans des cas simples, pour lesquels l'intensité des nuages est uniforme, mais lorsqu'il s'agit d'identifier différents types de nuages (des cirrostratus, cirrocumulus, cirrus, altostratus, etc.), les approches à seuils doivent faire face au problème de sur- ou de sous-identification selon le seuil choisi et la tolérance aux détails. De plus, ces approches perdent en précision sur les contours de l'image (à noter que ces approches sont généralement appliquées à des images prises par un appareil photo ayant un objectif grand angle ; les contours de l'image contiennent des informations importantes). Les approches fondées sur l'apprentissage automatique peuvent surmonter ce problème grâce à la phase d'apprentissage. Enfin, l'effet de réverbération du soleil affecte ces approches de façon significative. Ainsi, l'objectif est de surmonter au mieux ce problème, de préserver autant d'informations que possible et de développer un modèle sans paramètres prédéfinis pouvant traiter les images à plage dynamique élevée. Pour obtenir les performances souhaitées, deux approches tirant profit de l'apprentissage supervisé sont développées et détaillées. La première approche est un modèle fondé sur un réseau de neurones multicouche (modèle ANN), la deuxième est un modèle k-NN entrainé à partir de caractéristiques.

Il convient de mentionner que le ratio rouge sur bleu et le ratio rouge sur bleu normalisé sont ici associés car l'utilisation de plusieurs combinaisons des canaux rouge et bleu de l'image autorise de meilleures performances [42]. Comme le montre la Figure 4.11, ces caractéristiques améliorent le contraste visuel entre le ciel et les nuages, ce qui aide à identifier les pixels correspondant aux nuages et les pixels correspondant au ciel. L'écart-type local pour un voisinage spécifié est considéré car il contribue à l'apprentissage des motifs qui décrivent la relation d'un pixel de l'image avec son voisinage [43]. Il informe le réseau des variations d'intensité qui peuvent indiquer le bord d'un nuage ou des variations de l'épaisseur des nuages. Ainsi, avec l'aide des autres caractéristiques, le réseau peut classifier plus facilement. Le Laplacien du Gaussien fournit des informations binaires concernant le bord des nuages. Enfin, l'échelle de gris aide à identifier les nuages selon l'intensité des pixels. Ces caractéristiques peuvent être visualisées sur la Figure 4.11. Sur la base de cette analyse, ces caractéristiques sont utilisées comme entrées d'un réseau de neurones afin qu'il puisse apprendre des motifs en lien avec le bord des nuages, l'intensité des pixels et la relation entre un pixel de l'image et son voisinage. La performance des modèles est évaluée en calculant l'erreur quadratique moyenne (RMSE) ; notons que que les masques de vérification de terrain sont étiquetés manuellement. Trois tests sont réalisés afin d'évaluer les algorithmes de segmentation développés.

(a) Image test 1.

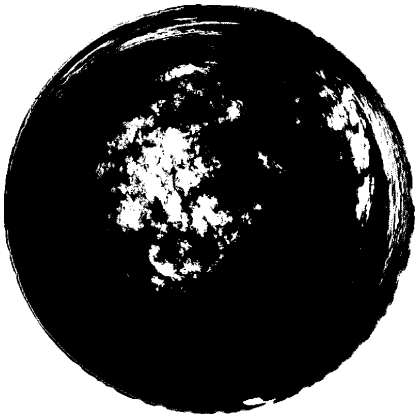

(b) Vérification de terrain pour l'image test 1.

(c) Image test 2.

(d) Vérification de terrain pour l'image test 2.

FIGURE 7 : Images test.

- Le premier test a pour objectif, d'une part, d'évaluer la robustesse de ces algorithmes à

l'effet de réverbération du soleil (une image complète avec Soleil apparent est utilisée pour le test ; le ciel est dégagé, quelques nuages épars sont présents sur l'image) et, d'autre part, d'évaluer leurs performances dans les zones de l'image où les algorithmes à seuils sont habituellement les plus performants (une partie d'une image nuageuse est utilisée pour le test) (Figure 7). Les résultats obtenus sont présentés dans le Tableau 4.2.

- Le deuxième test vise à déterminer le temps d'exécution moyen des différents algorithmes considérés. 20 images de test sont ici utilisées (Tableau 4.3).
- Le troisième test, réalisé à partir de cinq images issues de la base de données de test (Tableau 4.4), a pour objectif de démontrer (visuellement) que les algorithmes développés sont capables de surmonter les problèmes posés par l'effet de réverbération du soleil, la présence sur l'image de nuages fins et de nuages épais et l'anisotropie du ciel clair.

Tableau 2 : RMSE (premier test).

Méthode	Otsu	MCE	Hou et Lu	k-NN	Modèle ANN
Cas 1	0,55	0,47	0,26	0,21	0,15
Cas 2	0,13	0,11	0,27	0,13	0,10

Les résultats présentés dans le Tableau 2 témoignent des performances des approches proposées. Les modèles ANN et k-NN surpassent les approches issues de la littérature dans les deux cas (premier test), ce qui prouve que ces modèles sont, d'une part, robustes à l'effet de réverbération du soleil et, d'autre part, suffisamment précis localement. La haute précision du modèle ANN est obtenue au prix d'un temps d'exécution long (deuxième test), comme indiqué dans le Tableau 3, tandis que les autres modèles présentent un temps d'exécution similaire. Le troisième test réalisé démontre le bien-fondé d'une approche fondée sur l'apprentissage automatique. Les résultats obtenus sont détaillés dans le Tableau 4.4.

Tableau 3 : Temps d'exécution moyen pour les 20 images test sélectionnées (deuxième test).

Méthode	Otsu	MCE	Huo et Lu	k-NN	Modèle ANN
Temps (sec)	0,22	0,55	0,74	0,43	52,63

C.2.3.3 Estimation du mouvement des nuages Dans cette section, l'algorithme utilisé pour l'estimation du mouvement des nuages est présenté. Dans un premier temps, les principales approches issues de la littérature sont discutées. Dans un deuxième temps, l'algorithme est implémenté selon différents scénarios afin d'en évaluer la robustesse.

Dans la littérature, plusieurs approches ont été mises en œuvre afin d'estimer le mouvement des nuages. La méthode de corrélation croisée (CCM), proposée dans [44], est appliquée à deux images du ciel successives pour calculer les vecteurs de mouvement, qui sont filtrés grâce à un filtre à moyenne mobile sur 5 minutes [25]. Des techniques de suivi des nuages peuvent également être utilisées : le masque des nuages est distribué sur une grille angulaire/radiale et le mouvement général des nuages est estimé à l'aide de la méthode de corrélation croisée entre chaque cellule de la grille [23]. La vélocimétrie par image de particules (PIV) [45] a également été utilisée pour déterminer le mouvement des nuages [22]. Cette estimation peut être améliorée en appliquant un regroupement k-means aux vecteurs de mouvement calculés [24] afin d'estimer le mouvement dominant des nuages. Enfin, des algorithmes de flot optique peuvent être utilisés. Le modèle proposé dans [21] utilise un algorithme de flot optique dense qui fournit une estimation du mouvement pour chaque pixel de l'image [46]. Dans [47], le

mouvement des nuages est estimé grâce à l'algorithme de flot optique de Farnebäck, démontrant une estimation du mouvement robuste et précise. Une estimation précise du mouvement des nuages [21, 47] est obtenue grâce aux deux principales hypothèses sur lesquelles les algorithmes de flot optique sont fondés : la persistance de l'intensité des pixels et le déplacement identique de pixels adjacents. Dans la plupart des cas, le mouvement des nuages vérifie ces hypothèses (une étude de robustesse est réalisée dans la Section 4.4.4.2 pour s'assurer de la validité de cette approche). De plus, l'algorithme de flot optique est adapté à l'estimation de mouvements ayant de petites amplitudes : ce type de mouvement est celui des nuages. Pour cette raison, un algorithme de flot optique est utilisé dans ce travail afin d'estimer le mouvement des nuages.

Les algorithmes de flot optique les plus populaires sont les algorithmes de flot optique creux et dense [48]. Les algorithmes de flot optique creux calculent le vecteur de mouvement d'un ensemble prédéfini de pixels, nécessitant ainsi une étape de pré-traitement afin de déterminer les objets à suivre alors que les algorithmes de flot optique dense estiment le mouvement de chaque pixel. Il est possible d'utiliser l'algorithme de Lucas-Kanade [49], l'algorithme de Farnebäck [50, 51], entre autres algorithmes. Dans ce travail, l'algorithme de Farnebäck, qui a fait ses preuves [21, 47], est utilisé pour calculer les vecteurs de mouvement. L'idée principale de cet algorithme est d'approximer les voisins d'un pixel spécifique au sein de la première image par une équation quadratique. La solution détaillée de l'Équation (4.21) mal posée peut être trouvée dans [51]. Enfin, il convient de noter que chaque vecteur de mouvement est exprimé en coordonnées polaires afin de faciliter l'estimation de la direction et de l'amplitude dominantes, comme détaillé ci-après.

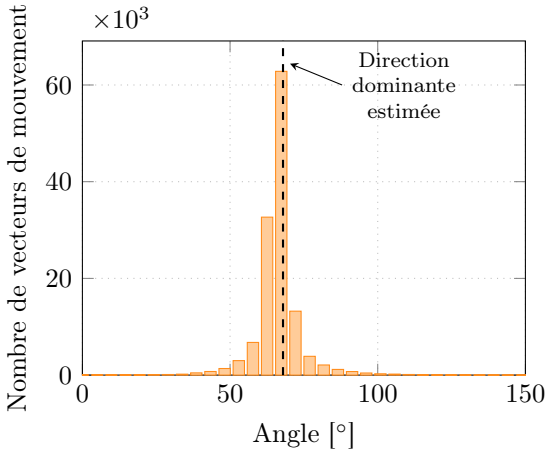

(a) Distribution de la direction des vecteurs de mouvement ; la direction dominante du mouvement des nuages est déterminée par la méthode de regroupement k-means.

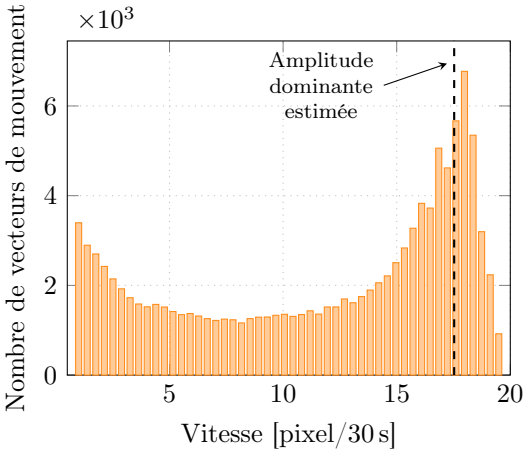

(b) Distribution de l'amplitude des vecteurs de mouvement dans la direction dominante précédemment calculée ; l'amplitude dominante des vecteurs de mouvement selon la direction dominante est déterminée par la méthode de regroupement k-means.

FIGURE 8 : Histogrammes de la distribution (a) de la direction des vecteurs de mouvement et (b) de l'amplitude des vecteurs de mouvement dans la direction dominante (les résultats sont basés sur les images présentées par la Figure 4.17).

C.2.3.4 Localisation de la région d'intérêt et calcul de la fraction de nuages

L'algorithme hybride proposé considère une région d'intérêt (ROI) déterminée à l'aide d'une estimation de la direction et de l'amplitude dominantes de la couverture nuageuse. Les valeurs de direction et d'amplitude dominantes estimées sont déterminées à l'aide de l'algorithme de regroupement k-means [52], qui est utilisé dans [22, 23, 24]. Un regroupement k-means à

deux classes est appliqué à la direction de tous les vecteurs de mouvement non nuls ; le centre dominant est alors sélectionné comme direction dominante des nuages. Enfin, l'amplitude dominante des vecteurs de mouvement est le centre d'un regroupement k-means (à une classe) de tous les vecteurs de mouvement dans la direction dominante $\pm 5°$. Cette approche a été appliquée à l'exemple présenté par la Figure 4.18 : la Figure 8a présente la distribution de la direction des vecteurs de mouvement et la direction dominante estimée ; la Figure 8b présente la distribution de l'amplitude des vecteurs de mouvement dans la direction dominante précédemment calculée et l'amplitude dominante estimée.

La région d'intérêt localisée avec précision, la valeur moyenne de son masque des nuages à l'instant k, appelée fraction de nuages dans la ROI ($\mathrm{CF}_{\mathrm{ROI}_H}(k)$), est calculée. La fraction de nuages dans la ROI (à l'instant k) influence fortement la valeur du DNI à l'instant $k+h$ et, par conséquent, est une information pertinente dans l'optique du développement d'un modèle de prévision du DNI par apprentissage.

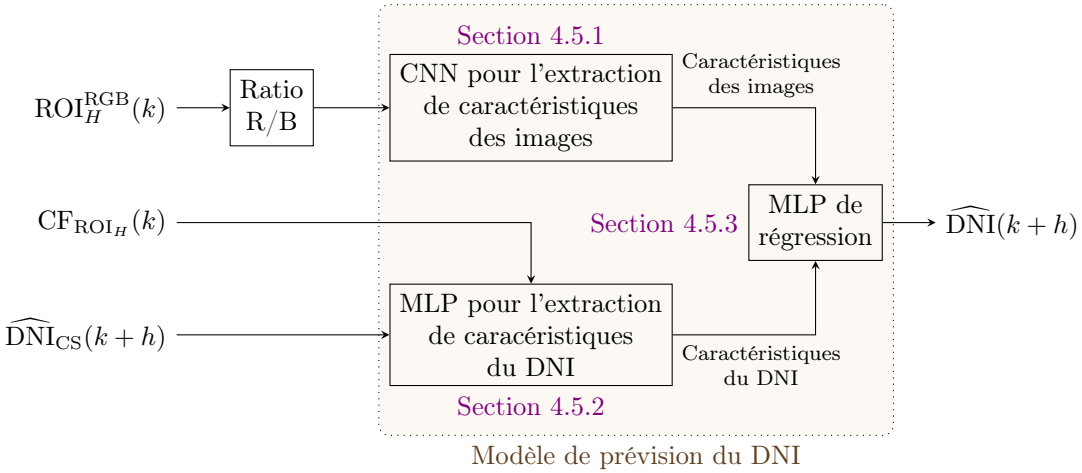

FIGURE 9 : Modèle de prévision du DNI ($\widehat{\mathrm{DNI}}$) dont les entrées sont l'image RVB de la région d'intéret ($\mathrm{ROI}_H^{\mathrm{RGB}}$), la fraction de nuage dans la région d'intérêt ($\mathrm{CF}_{\mathrm{ROI}_H}$) et le DNI par ciel clair prédit ($\widehat{\mathrm{DNI}}_{\mathrm{CS}}$). Trois réseaux de neurones sont utilisés : un réseau CNN pour l'extraction de caractéristiques des images à partir du ratio rouge-sur-bleu (R/B) de l'image RVB de la région d'intéret ($\mathrm{ROI}_H^{\mathrm{RGB}}$), un réseau MLP pour l'extraction de caractéristiques du DNI à partir de $\mathrm{CF}_{\mathrm{ROI}_H}$ et $\widehat{\mathrm{DNI}}_{\mathrm{CS}}$ et un réseau MLP qui prédit le DNI à partir de ces caractéristiques.

C.2.4 Modèle de prévision du DNI

Le modèle de prévision du DNI est composé de trois blocs (voir Figure 9) détaillés ci-après. Le premier bloc, responsable de l'extraction de caractéristiques des images, est un réseau de neurones à convolution (CNN). Le deuxième bloc est un Perceptron multicouche (MLP) dont les entrées sont la fraction de nuage ($\mathrm{CF}_{\mathrm{ROI}_H}$) et le DNI par ciel clair prédit. Les sorties des réseaux CNN et MLP sont ensuite transmises à un autre réseau MLP chargé de résoudre un problème de régression et, à partir des caractéristiques susmentionnées, de prévoir le DNI à l'horizon H (tel que $H = h \cdot T_s$, avec $T_s = 30\,\mathrm{s}$). Ce modèle de prévision est entraîné et validé à l'aide de la technique de validation croisée. La base de données – des images du ciel et des mesures du DNI (40 jours) – utilisée est la même que celle qui a permis le développement, le test et la validation des modèles LSTM et CNN-LSTM. L'entrainement des réseaux est réalisé grâce à l'algorithme Adam ; une régularisation par *dropout* est effectuée pour chacune des couches des réseaux (le taux est fixé à 50 %) afin de limiter les risques de sur-apprentissage. L'erreur quadratique moyenne est choisie comme fonction de perte. Les réseaux sont entraînés à l'aide de la version assistée par GPU de TensorFlow - Keras sur une machine avec 32 Gbit de

RAM, un processeur Intel Xeon E-2146G @3,50 GHz et un GPU Nvidia Quadro P620 18 Gbit.

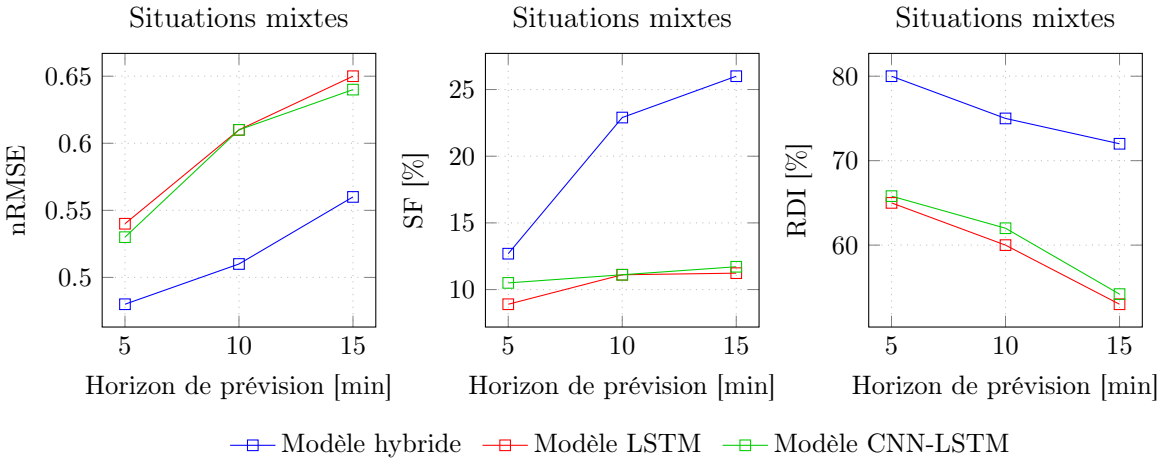

FIGURE 10 : Comparaison des modèles LSTM, CNN-LSTM et hybride pour les situations mixtes du jeu de données de test. Gauche : erreur quadratique moyenne normalisée (nRMSE). Centre : skill factor (SF). Droite : indice de détection de rampe (RDI).

Les performances du modèle hybride, du modèle LSTM et du modèle CNN-LSTM (voir Section 3.3.3 du manuscrit) sont tout d'abord comparées, pour les situations mixtes, grâce aux données de test. Les résultats sont présentés par la Figure 10 : le modèle hybride obtient, pour chaque horizon de prévision, le nRMSE le plus faible et le SF et le RDI les plus élevés. Cette performance supérieure s'explique par la prise en considération d'images du ciel, ce qui permet une meilleure détection des rampes et des prévisions du DNI plus précises que celles obtenues grâce aux modèles basés uniquement sur des mesures DNI. Le modèle CNN-LSTM surpasse de peu le modèle LSTM, obtenant un nRMSE plus faible et un SF plus élevé grâce à sa couche convolutive. Comme on peut le voir, le modèle hybride produit le RDI le plus élevé pour tous les horizons de prévision. Les modèles LSTM et CNN-LSTM, qui sont basés uniquement sur des mesures du DNI, ne prévoient pas les rampes aussi bien que le modèle hybride, justifiant de fait la prise en considération d'images du ciel au cours du processus de prévision : estimer le mouvement des nuages est en effet essentiel afin de mieux anticiper les brusques variations du DNI. Le modèle hybride, le modèle LSTM et le modèle CNN-LSTM sont maintenant comparés grâce à 6 journées à faible variabilité provenant de la base de données de test (3 journées ciel clair et 3 journées couvertes issues de différentes saisons, soit 7200 observations). Le modèle de persistance intelligent obtient généralement des valeurs de nRMSE très faibles dans de tels cas. Comme on peut le voir sur la Figure 11, le modèle hybride surpasse le modèle de persistance intelligent pour tous les horizons de prévision, avec un SF compris entre 6 % et 9 %. Les faibles valeurs de nRMSE et le SF positif obtenus par le modèle hybride confirment qu'il est capable de distinguer les situations ciel clair et les situations ciel couvert. De plus, le modèle est capable de compenser les variations saisonnières de la valeur maximale du DNI par ciel clair grâce au modèle ciel clair adaptatif utilisé. Cependant, pour de telles situations, marquées par une faible variabilité, les résultats obtenus par les modèles LSTM et CNN-LSTM sont nettement moins bons que ceux obtenus par le modèle de persistance intelligent. Contrairement au modèle hybride, ces modèles ne sont pas capables de gérer correctement ces situations qui ne sont pas décrites par les exemples appris lors de la phase d'entraînement : bien que le nRMSE soit faible (environ 0,16 %), le modèle de persistance intelligent est si performant qu'ils obtiennent un SF négatif (environ -120% pour $H = 5\,\text{min}$, -50% pour $H = 10\,\text{min}$ et -25% pour $H = 15\,\text{min}$). Cela démontre les bénéfices que l'on retire des images du ciel : même s'il a été entrainé avec les mêmes mesures du DNI, le modèle hybride est capable de généraliser à ces situations.

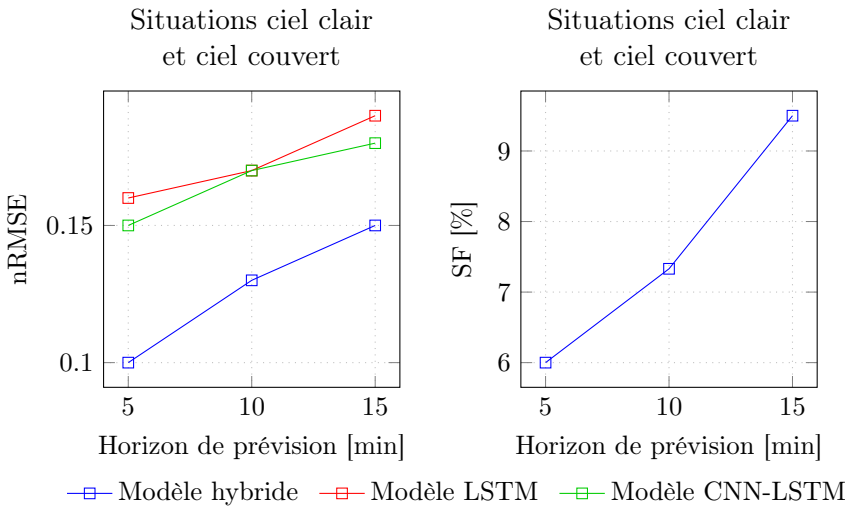

FIGURE 11 : Comparaison des modèles LSTM, CNN-LSTM et hybride pour les situations ciel clair et ciel couvert du jeu de données de test. Gauche : erreur quadratique moyenne normalisée (nRMSE). Droite : SF. Pour les modèles LSTM et CNN-LSTM, les valeurs du SF ne sont pas présentées car elles sont trop faibles (environ $-120\,\%$ pour $H = 5\,\text{min}$, $-50\,\%$ pour $H = 10\,\text{min}$ et $-25\,\%$ pour $H = 15\,\text{min}$).

En résumé, les résultats obtenus montrent que les modèles développés sont capables de surpasser le modèle de persistance intelligent en cas de situation mixte : le SF obtenu par le modèle hybride varie entre 12 % et 26 % à mesure que l'horizon de prévision augmente (de 5 min à 15 min), alors que les modèles LSTM et CNN-LSTM obtiennent un SF d'environ 10 % pour tous les horizons. Ce résultat démontre par ailleurs que le modèle hybride surpasse systématiquement ces deux modèles. L'indice de détection de rampe (RDI) montre que les modèles développés sont capables de prédire les brusques variations du DNI : le modèle hybride est capable de prévoir 72 % à 80 % des rampes observées alors que les modèles LSTM et CNN-LSTM sont moins efficaces mais détectent malgré tout entre 53 % et 66 % de ces rampes. Cette différence s'explique bien évidemment par la nature des modèles LSTM et CNN-LSTM qui s'appuient uniquement sur des observations passées du DNI pour fournir des prévisions, sans tenir compte de la situation du ciel : une détection efficace des nuages et une estimation précise de leur mouvement permettent une meilleure prévisions des rampes et des prévisions du DNI plus précises. Pour les situations ciel clair et ciel couvert, le modèle de persistance intelligent obtient de très bons résultats, les résultats obtenus par les modèles LSTM et CNN-LSTM étant nettement moins bons. Cependant, le modèle hybride parvient toujours à surpasser le modèle de persistance intelligent, avec un SF compris entre 6 % et 9 % selon l'horizon. Grâce à la prise en considération d'images du ciel, le modèle hybride gère avec succès toutes les situations : ciel clair, ciel couvert et mixtes. Pour ce qui est de la complexité des modèles, il est intéressant de noter que, même si le modèle hybride est plus complexe que les autres modèles, prend plus de temps et demande plus de ressources de calcul, il lui faut moins de 7 % du pas d'échantillonnage (30 s) pour fournir une prévision. Dans le cadre du projet européen H2020 SFERA III, le modèle hybride proposé a été implémenté in situ et fournit des prévisions du DNI en temps réel aux utilisateurs des infrastructures CSP, ce qui leur permet de mieux planifier leurs expérimentations.

D Contrôle prédictif d'un réacteur solaire

Cette section traite de la modélisation et du contrôle dynamique d'un réacteur solaire thermochimique dédié à la gazéification à haute température de la biomasse (voir Figure 12). Les

gazogènes solaires sont étudiés expérimentalement depuis le début des années 1980, les travaux menés par [53] et [54] traitant notamment des technologies à lit fixe et à lit fluidisé. L'intérêt pour la thermochimie solaire s'est accru du fait du changement climatique [55], en particulier depuis le milieu des années 2000, ce qui a conduit à des recherches ayant permis des innovations majeures en matière de conception, comme examiné dans [56]. Des travaux plus récents ont été menés sur les lits fluidisés à double boucle afin de séparer les zones où se déroulent les procédés d'oxydation et de réduction en cas de fonctionnement basé sur un cycle thermodynamique [57] ou pour séparer les zones où se déroulent les procédés de gazéification et de combustion en cas de fonctionnement hybride solaire-autothermique [58]. Un gazogène solaire à lit jaillissant a été conçu par [6] et son fonctionnement hybride solaire-autothermique a été étudié successivement par [5] et [59]. D'autres travaux expérimentaux récents ont démontré la faisabilité d'une telle opération hybride [60, 61] mais la question du contrôle dynamique du système reste posée.

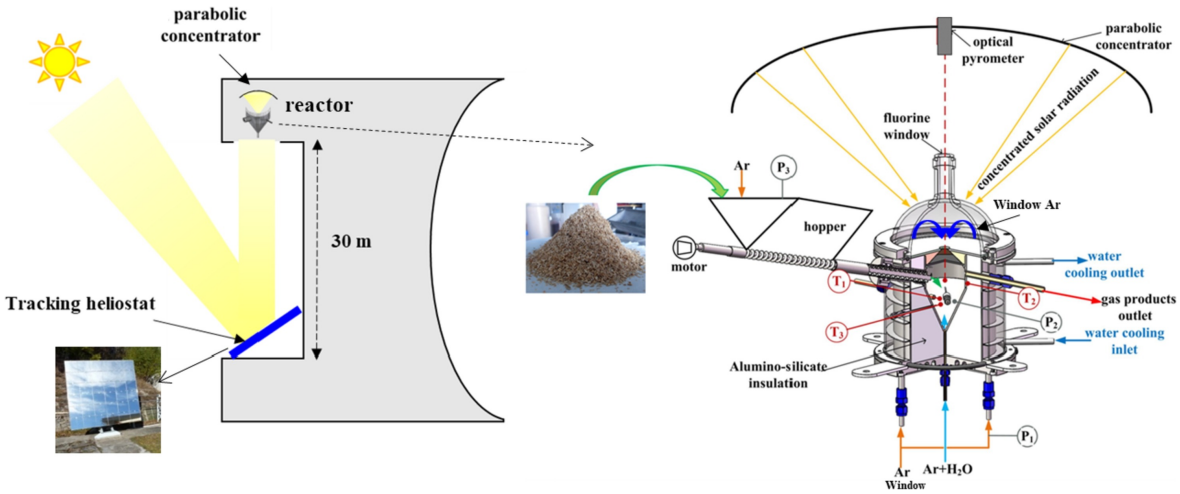

FIGURE 12 : Design du réacteur solaire [5].

Le travail présenté dans ce manuscrit vise à concilier stratégie de contrôle d'un gazogène hybride solaire-autothermique et implémentation efficace d'un algorithme MPC (pour *model-based predictive control*). L'objectif est de maintenir le réacteur à sa température nominale, malgré un DNI variable, tout en minimisant l'injection d'oxygène au cours du fonctionnement. Le modèle de gazogène solaire à lit jaillissant proposé dans [4] est considéré dans ces travaux, impliquant des bilans thermiques globaux et un modèle chimique à l'équilibre thermodynamique. Pour la première fois, il est tiré profit de prévisions de l'éclairement normal direct pour un meilleur lissage des perturbations au cours de la journée, tirant ainsi pleinement profit de la stratégie prédictive. Le contrôleur MPC agit sur le débit d'oxygène et le facteur de défocalisation des miroirs afin de maintenir la température du réacteur à sa valeur nominale, assurant de fait sa stabilité. Ce contrôleur est comparé à un contrôleur PID adaptatif, ce qui permet d'évaluer l'apport de la stratégie prédictive. De plus, le contrôleur MPC est implémenté avec différentes prévisions : des prévisions parfaites, des prévisions fournies par un modèle de persistance et des prévisions fournies par un modèle basé sur des images du ciel. Une étude est menée afin d'évaluer l'effet des erreurs de prévision sur les performances du contrôleur MPC.

D.1 Modélisation du réacteur

Le modèle développé s'inspire des travaux de [4], qui a calculé la production annuelle d'un gazogène solaire à biomasse pour évaluer l'hybridation allotherme-autotherme. Le gazogène est conçu pour être chauffé à la fois par l'énergie solaire concentrée (chauffage allothermique) et la combustion in situ (chauffage autothermique) [6, 5], permettant une conversion continue de la biomasse 24h/24. Pour un débit de biomasse maintenu constant à $1{,}465\,\mathrm{t\,h^{-1}}$, les paramètres

du réacteur sont réglés de sorte que la température nominale de 1473 K (1199,85 °C) soit atteinte pour un DNI égal à 800 W m^{-2}, ce qui correspond à environ 80 % du DNI maximum observé au cours d'une année. A l'équilibre thermodynamique, les réactions chimiques se déroulant dans le réacteur solaire sont les suivantes (voir Figure 13) :

- Lorsque le DNI est supérieur à 800 W m^{-2}, seule la réaction endothermique de gazéification se produit, comme décrit par l'équation suivante :

$$\mathrm{CH_{1.66}O_{0.69}} + 0.31\,\mathrm{H_2O} \longrightarrow \mathrm{CO} + 1.14\,\mathrm{H_2} \tag{10}$$

  avec un changement d'enthalpie $\Delta H_r^o = 143\,\mathrm{kJ\,mol^{-1}}$ (réaction endothermique). Un débit de H_2O avec un rapport molaire vapeur sur biomasse 1,22 fois supérieur au rapport stœchiométrique est injecté pour garantir la conversion totale de la biomasse.

- Lorsque le DNI est inférieur à 800 W m^{-2}, l'injection d'oxygène est nécessaire afin de maintenir la température du réacteur à son niveau d'équilibre. L'impact de l'injection d'oxygène peut, en première approximation, être décrit par l'oxycombustion du bois :

$$\mathrm{CH_{1.66}O_{0.69}} + 1.07\,\mathrm{O_2} \longrightarrow \mathrm{CO_2} + 0.83\,\mathrm{H_2} \tag{11}$$

  avec un changement d'enthalpie $\Delta H_r^o = -452\,\mathrm{kJ\,mol^{-1}}$ (réaction exothermique).

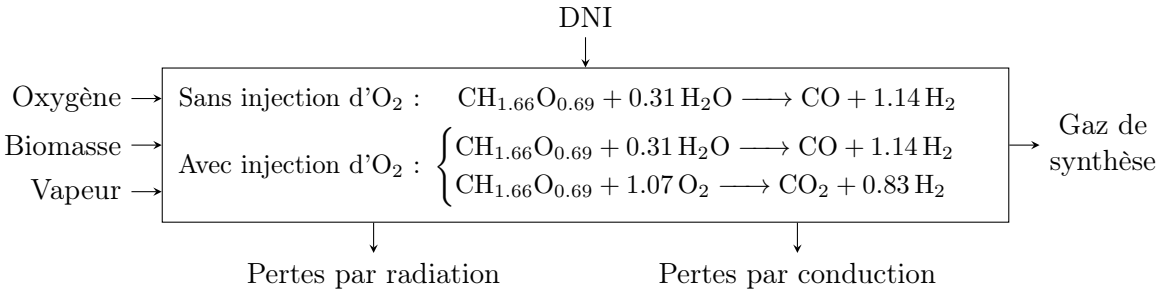

FIGURE 13 : Réacteur solaire pour la production de gaz de synthèse.

Le modèle de réacteur discrétisé ($t = k \cdot \Delta t$, avec $\Delta t = 30\,\mathrm{s}$) est formulé comme suit, avec D le facteur de défocalisation et f_{oxygen}^{in} le débit d'oxygène :

$$T(k+1) = \mathcal{M}(D(k), f_{oxygen}^{in}(k), T(k)) \tag{12}$$

Dans la suite de ce manuscrit, le débit de biomasse $f_{biomass}^{in}$ et le débit de vapeur f_{steam}^{in} sont fixés à leurs valeurs nominales de conception.

D.2 Stratégies de contrôle

Un contrôleur de référence est d'abord développé pour maintenir la température à l'intérieur du réacteur à sa valeur nominale (1473 K). Ce contrôleur fournit des performances de référence auxquelles le contrôleur MPC (deux stratégies prédictives sont proposées) peut être comparé. Les variables de contrôle sont présentées ci-après.

- Le débit d'oxygène (f_{oxygen}^{in}) : en cas de DNI insuffisant (DNI $\leqslant 800\,\mathrm{W\,m^{-2}}$), de l'oxygène peut être injecté pour augmenter la température du réacteur par combustion de la biomasse.

- Le facteur de défocalisation (D) : en cas de DNI en excès (DNI $> 800\,\mathrm{W\,m^{-2}}$), les miroirs peuvent être défocalisés pour compenser le surplus d'éclairement.

Ce contrôleur de référence associe deux contrôleurs (voir Figure 6.1) : le débit d'oxygène est régulé par un contrôleur PID adaptatif, comme détaillé dans la Section 6.1.1.1 du manuscrit, alors que le facteur de défocalisation est déterminé par un contrôleur fondé sur des règles, comme détaillé dans la Section 6.1.1.2. La stratégie MPC est formulée comme suit : à chaque instant, un problème d'optimisation est résolu afin de déterminer les commandes $\boldsymbol{D} \in \mathbb{R}^n$ et $\boldsymbol{f}^{in}_{oxygen} \in \mathbb{R}^n$ [62], pour une fonction objectif donnée, des contraintes et des limites. Une variante est proposée. La stratégie MPC 1 permet la résolution du problème d'optimisation suivant :

$$\begin{aligned}(D^\star, f^{in\,\star}_{oxygen}) = \operatorname{argmin} \; & \sum_{i=1}^{n} \big(S_p - T(k+i)\big)^2 \\ & \text{avec} \;\; T(k+1) = \mathcal{M}\big(T(k), D(k), f^{in}_{oxygen}(k)\big) \\ & \text{sujet à} \;\; 0 \leqslant D(k+i) \leqslant 1 \text{ et } 0 \leqslant f^{in}_{oxygen}(k+i) \leqslant 2\end{aligned} \tag{13}$$

L'objectif est ici de minimiser l'écart quadratique entre la température de consigne et la température simulée sur l'horizon de prédiction considéré, sans contraintes sur la consommation d'oxygène ou sur l'utilisation de l'énergie solaire. La stratégie MPC 2 permet la résolution du problème d'optimisation suivant :

$$\begin{aligned}(D^\star, f^{in\,\star}_{oxygen}) = \operatorname{argmin} \; & \sum_{i=1}^{n} \alpha\big(S_p - T(k+i)\big)^2 + \beta\big(f^{in}_{oxygen}(k+i)\big)^2 - \gamma\big(D(k+i)\big)^2 \\ & \text{avec} \;\; T(k+1) = \mathcal{M}\big(T(k), D(k), f^{in}_{oxygen}(k)\big) \\ & \text{sujet à} \;\; 0 \leqslant D(k+i) \leqslant 1 \text{ et } 0 \leqslant f^{in}_{oxygen}(k+i) \leqslant 2\end{aligned} \tag{14}$$

L'objectif est ici de trouver un compromis entre le respect de la température de consigne, la minimisation de la consommation d'oxygène et la maximisation de l'utilisation de l'énergie solaire. Ce compromis est déterminé par les pondérations α, β et γ. Bien évidemment, des prévisions du DNI sont nécessaires à la mise en œuvre de la stratégie prédictive. Selon l'horizon de prévision, plusieurs approches peuvent être envisagées : des modèles fondés sur l'apprentissage automatique développés grâce à un jeu de données (des observations passées du DNI) permettant l'apprentissage de motifs ayant trait aux variations du DNI ou des modèles fondés sur des images du ciel, traitées pour en extraire des informations en lien avec la situation du ciel qui influence le DNI. Comme présenté dans la Section 6.2.1, l'horizon de prédiction optimal est inférieur à 5 minutes et, pour un horizon aussi court, les modèles de persistance commettent des erreurs très faibles. Cependant, ces modèles ne sont pas capables de prédire les rampes, qui ont une influence significative, comme indiqué par la Figure 5.6. Ainsi, l'objectif est de disposer d'un modèle de prévision du DNI capable d'en appréhender les brusques variations. De fait, les modèles purement statistiques ne sont pas adaptés. Par ailleurs, cet objectif justifie la prise en considération d'images du ciel. Par conséquent, pour la mise en œuvre de la stratégie prédictive proposée, une hybridation entre approche statistique et approche fondée sur des images du ciel, tirant profit des avantages de ces deux approches, est considérée pour la prévision à très court terme du DNI.

Afin d'évaluer l'influence des prévisions sur les performances des stratégies MPC proposées, des prévisions parfaites et des prévisions fournies par un modèle de persistance intelligent sont également considérées.

D.3 Résultats

Les contrôleurs PID et MPC développés sont testés sur une semaine (les nuits ne sont pas incluses) ; leurs performances sont évaluées à partir de l'erreur quadratique moyenne (RMSE), de la quantité d'oxygène utilisée au cours de la simulation réalisée (m_{O_2}) et de la variation

moyenne de température (ATV) à l'intérieur du réacteur (sauf pour DNI $< 150\,\mathrm{W\,m^{-2}}$ puisque, dans ce cas, le réacteur est fermé et qu'il n'y a pas de perte de puissance ; la température peut donc être facilement maintenue en injectant $0{,}88\,\mathrm{t\,h^{-1}}$ d'oxygène). Les deux stratégies MPC proposées ont leurs points forts et leurs points faibles, comme indiqué dans le Tableau 4. Avec des prévisions parfaites, la stratégie MPC 2 est la stratégie à privilégier car l'augmentation de l'erreur quadratique moyenne est minime au regard de la quantité d'oxygène économisée (environ 28 %). Cependant, avec des prévisions obtenues grâce à une persistance intelligente ou au modèle basé sur des images du ciel, la stratégie MPC 1 réduit l'erreur quadratique moyenne et la variation moyenne de température à l'intérieur du réacteur. L'erreur RMSE est réduite de 16 % avec la stratégie MPC 1 et des prévisions obtenues grâce au modèle basé sur des images du ciel. Par contre, la stratégie MPC 2 est à privilégier si l'objectif principal est de minimiser l'injection d'oxygène : avec des prévisions obtenues grâce au modèle basé sur des images du ciel, cette stratégie permet d'économiser environ 10 % d'oxygène.

Tableau 4 : Comparaison des stratégies de contrôle. Pour la stratégie MPC 1, quel que soit le modèle de prévision considéré, l'horizon de prévision optimal est 2 min. Pour la stratégie MPC 2, les horizons de prévision optimaux sont 1 min (prévisions parfaites), 2 min (persistance intelligente) et 2 min (prévisions basées sur des images).

Strategie	Critère de performance	Prévisions parfaites	Prévisions basées sur des images	Persistance intelligente
Stratégie MPC 1	RMSE [K]	$\ll$0,01	1,34	1,45
	m_{O_2} [kg]	41 920,00	36 365,80	38 509,00
	ATV [K]	$\ll$0,01	1,32	1,32
Stratégie MPC 2	RMSE [K]	0,07	1,60	1,71
	m_{O_2} [kg]	31 968,33	32 091,00	32 076,00
	ATV [K]	0,03	1,54	1,54
Stratégie de référence	RMSE [K]		4,88	
	m_{O_2} [kg]		31 933,00	
	ATV [K]		2,27	

$Q_{reaction}$ est calculé à l'aide de la boîte à outils Cantera pour une température et un flux de réactifs (biomasse, vapeur et oxygène) donnés. Le temps d'optimisation est long, ce qui est dû à l'utilisation de cette boîte à outils : calculer $Q_{reaction}$ prend en moyenne 0,05 s à chaque pas de temps. Un calcul plus rapide est nécessaire. C'est pourquoi il est proposé de remplacer la boite à outils Cantera par une fonction dont les arguments sont la température actuelle du réacteur et le débit d'oxygène et qui calcule $Q_{reaction}$. Les débits de biomasse et de vapeur sont fixés à leurs valeurs nominales. La robustesse du contrôleur MPC à la simplification du modèle est évaluée. Après analyse de l'influence de la température du réacteur et du débit d'oxygène sur $Q_{reaction}$, on constate que :

- pour une température de réacteur donnée, $Q_{reaction}$ est une fonction quasi linéaire du débit d'oxygène ($0\,\mathrm{t\,h^{-1}} \leqslant f^{in}_{oxygen} \leqslant 1{,}8\,\mathrm{t\,h^{-1}}$) ;
- pour un débit d'oxygène donné, $Q_{reaction}$ est une fonction linéaire de la température du réacteur ($1453\,\mathrm{K} \leqslant T \leqslant 1493\,\mathrm{K}$).

Le voisinage choisi se situe autour de la performance nominale ($1453\,\mathrm{K} \leqslant T \leqslant 1493\,\mathrm{K}$), tout en respectant la contrainte de débit d'oxygène ($0\,\mathrm{t\,h^{-1}} \leqslant f^{in}_{oxygen} \leqslant 1{,}8\,\mathrm{t\,h^{-1}}$). Ainsi, la solution proposée est de remplacer la boîte à outils Cantera par une fonction d'interpolation 2D. Les arguments utilisés pour calculer $Q_{reaction}$ sont les points d'un maillage déterminé par

les deux vecteurs d'entrée discrétisés : le débit d'oxygène f_{oxygen}^{in}, avec un pas de discrétisation égal à 0,05, et la température du réacteur T, avec un pas de discrétisation identique (0,05). Il convient de noter que la fonction d'interpolation 2D n'a besoin que de quelques millisecondes pour fournir une estimation. Le contrôleur MPC (utilisant le modèle simplifié du réacteur), pour un horizon de prédiction optimal, est comparé au contrôleur de référence. Le Tableau 5 met en lumière que, même lorsque le modèle simplifié du réacteur est utilisé, le contrôleur MPC parvient toujours à surpasser le contrôleur de référence : les valeurs de RMSE et ATV sont plus faibles, au prix d'une augmentation de la consommation d'oxygène d'environ 0,1 % pour la stratégie MPC 1 et de moins de 0,01 % pour la stratégie MPC 2.

Tableau 5 : Comparaison des stratégies de contrôle avec utilisation du modèle simplifié. Pour la stratégie MPC 1, les horizons de prévision optimaux sont 1 min (prévisions parfaites), 2 min (persistance intelligente) et 2 min (prévisions basées sur des images). Pour la stratégie MPC 2, les horizons de prévision optimaux sont 1 min (prévisions parfaites), 1,5 min (persistance intelligente) et 2 min (prévisions basées sur des images).

Stratégie	Critère de performance	Prévisions parfaites	Prévisions basées sur des images	Persistance intelligente
Stratégie MPC 1	RMSE [K]	0,01	1,47	1,55
	m_{O_2} [kg]	36 767,00	36 052,00	36 222,00
	ATV [K]	0,01	1,42	1,41
Stratégie MPC 2	RMSE [K]	0,10	1,62	1,73
	m_{O_2} [kg]	31 961,00	32 126,00	32 152,00
	ATV [K]	0,05	1,47	1,49
Stratégie de référence	RMSE [K]		4,88	
	m_{O_2} [kg]		31 933,00	
	ATV [K]		2,27	

E Conclusion

Les répercussions néfastes de l'activité humaine sur l'environnement, dues en partie à l'utilisation à grande échelle des énergies fossiles, deviennent indéniables. Ainsi, un consensus émerge quant à l'urgence de développer des solutions durables, tirant profit des énergies renouvelables, en particulier pour répondre à la demande croissante en électricité. L'une de ces solutions est l'énergie solaire concentrée pour la production d'électricité ou d'hydrogène. Toutefois, le déploiement des systèmes CSP (pour *concentrated solar power*) est pénalisé par de nombreux verrous scientifiques et techniques. Les travaux présentés dans ce manuscrit ont été réalisés dans le cadre du projet SFERA III qui a pour ambition de lever certains de ces verrous. Deux groupes de tâches sont concernés : le WP10, qui aborde les problèmes liés à l'intermittence et à la variabilité de la ressource solaire et qui a permis le développement d'un modèle pour la prévision infra-horaire de l'éclairement normal direct (ou DNI, pour *direct normal irradiance*) à partir d'images du ciel à plage dynamique élevée et de mesures du DNI ; le WP8, qui traite de la production de carburant solaire et qui a permis le développement d'un contrôleur prédictif, tirant profit de prévisions du DNI, pour garantir la stabilité d'un réacteur solaire destiné à la production de gaz de synthèse, tout en préservant ses performances.

F Références

[1] *National low-carbon strategy for climate*. https ://www.gouvernement.fr/en/adoption-of-the-national-low-carbon-strategy-for-climate. 2015.

[2] *Multiannual energy plan*. https ://www.ecologie.gouv.fr/programmations-pluriannuelles-lenergie-ppe. 2017.

[3] *European project SFERA III*. https ://sfera3.sollab.eu/.

[4] H. Boujjat, G. M. Y. Junior, S. Rodat et S. Abanades. "Dynamic simulation and control of solar biomass gasification for hydrogen-rich syngas production during allothermal and hybrid solar/autothermal operation". In : *International Journal of Hydrogen Energy* 45.48 (sept. 2020), p. 25827-25837. doi : 10.1016/j.ijhydene.2020.01.072.

[5] H. Boujjat, S. Rodat, S. Chuayboon et S. Abanades. "Experimental and numerical study of a directly irradiated hybrid solar/combustion spouted bed reactor for continuous steam gasification of biomass". In : *Energy* 189 (déc. 2019), p. 116118. doi : 10.1016/j.energy.2019.116118.

[6] Q. Bellouard, S. Abanades et S. Rodat. "Biomass Gasification in an Innovative Spouted-Bed Solar Reactor : Experimental Proof of Concept and Parametric Study". In : *Energy Fuels* 31.10 (sept. 2017), p. 10933-10945. doi : 10.1021/acs.energyfuels.7b01839.

[7] P. Blanc, B. Espinar, N. Geuder, C. Gueymard, R. Meyer, R. Pitz-Paal, B. Reinhardt, D. Renné, M. Sengupta, L. Wald et S. Wilbert. "Direct normal irradiance related definitions and applications : The circumsolar issue". In : *Solar Energy* 110 (déc. 2014), p. 561-577. doi : 10.1016/j.solener.2014.10.001.

[8] P. Blanc, B. Espinar, N. Geuder, C. Gueymard, R. Meyer, R. Pitz-Paal, B. Reinhardt, D. Renné, M. Sengupta, L. Wald et S. Wilbert. "Direct normal irradiance related definitions and applications : The circumsolar issue". In : *Solar Energy* 110 (déc. 2014), p. 561-577. doi : 10.1016/j.solener.2014.10.001.

[9] Kipp et Zonen. *CH1 Pyrheliometer*. 2001.

[10] N. Geuder et V. Quaschning. "Soiling of irradiation sensors and methods for soiling correction". In : *Solar Energy* 80.11 (nov. 2006), p. 1402-1409. doi : 10.1016/j.solener.2006.06.001.

[11] N. Geuder, R. Affolter, B. Kraas et S. Wilbert. "Long-term Behavior, Accuracy and Drift of LI-200 Pyranometers as Radiation Sensors in Rotating Shadowband Irradiometers (RSI)". In : *Energy Procedia* 49 (2014), p. 2330-2339. doi : 10.1016/j.egypro.2014.03.247.

[12] R. Chauvin, J. Nou, S. Thil et S. Grieu. "System for measuring components of solar radiation". WO2019053232. 2019.

[13] F. Antonanzas-Torres, R. Urraca, J. Polo, O. Perpiñán-Lamigueiro et R. Escobar. "Clear sky solar irradiance models : A review of seventy models". In : *Renewable and Sustainable Energy Reviews* 107 (juin 2019), p. 374-387. doi : 10.1016/j.rser.2019.02.032.

[14] J. Nou, R. Chauvin, S. Thil et S. Grieu. "A new approach to the real-time assessment of the clear-sky direct normal irradiance". In : *Applied Mathematical Modelling* 40.15 (août 2016), p. 7245-7264. issn : 0307-904X. doi : https://doi.org/10.1016/j.apm.2016.03.022.

[15] E. W. Law, A. A. Prasad, M. Kay et R. A. Taylor. "Direct normal irradiance forecasting and its application to concentrated solar thermal output forecasting–A review". In : *Solar Energy* 108 (2014), p. 287-307. DOI : 10.1016/j.solener.2014.07.008.

[16] L. Ramírez et J. M. Vindel. "Forecasting and nowcasting of DNI for concentrating solar thermal systems". In : *Advances in Concentrating Solar Thermal Research and Technology*. Sous la dir. de M. J. Blanco et L. R. Santigosa. Woodhead Publishing, 2017.

[17] L. Martín, L. F. Zarzalejo, J. Polo, A. Navarro, R. Marchante et M. Cony. "Prediction of global solar irradiance based on time series analysis : Application to solar thermal power plants energy production planning". In : *Solar Energy* 84.10 (2010), p. 1772-1781.

[18] S. Mishra et P. Palanisamy. "Multi-time-horizon solar forecasting using recurrent neural network". In : *2018 IEEE Energy Conversion Congress and Exposition (ECCE)*. IEEE. 2018, p. 18-24. DOI : 10.1109/ECCE.2018.8558187.

[19] S. Malakar, S. Goswami, B. Ganguli, A. Chakrabarti, S. S. Roy, K. Boopathi et A. G. Rangaraj. "Designing a long short-term network for short-term forecasting of global horizontal irradiance". In : *SN Applied Sciences* 3.477 (mars 2021). DOI : 10.1007/s42452-021-04421-x.

[20] B. Brahma et R. Wadhvani. "Solar Irradiance Forecasting Based on Deep Learning Methodologies and Multi-Site Data". In : *Symmetry* 12.11 (nov. 2020), p. 1830. ISSN : 2073-8994. DOI : 10.3390/sym12111830.

[21] J. Du, Q. Min, P. Zhang, J. Guo, J. Yang et B. Yin. "Short-Term Solar Irradiance Forecasts Using Sky Images and Radiative Transfer Model". In : *Energies* 11.5 (mai 2018), p. 1107. ISSN : 1996-1073. DOI : 10.3390/en11051107.

[22] Y. Chu, H. T. C. Pedro et C. F. M. Coimbra. "Hybrid intra-hour DNI forecasts with sky image processing enhanced by stochastic learning". In : *Solar Energy* 98 (déc. 2013), p. 592-603. ISSN : 0038-092X. DOI : 10.1016/j.solener.2013.10.020.

[23] S. Quesada-Ruiz, Y. Chu, J. Tovar-Pescador, H. T. C. Pedro et C. F. M. Coimbra. "Cloud-tracking methodology for intra-hour DNI forecasting". In : *Solar Energy* 102 (avr. 2014), p. 267-275. DOI : 10.1016/j.solener.2014.01.030.

[24] R. Marquez et C. F. M. Coimbra. "Intra-hour DNI forecasting based on cloud tracking image analysis". In : *Solar Energy* 91 (mai 2013), p. 327-336. DOI : 10.1016/j.solener.2012.09.018.

[25] M. Caldas et R. Alonso-Suárez. "Very short-term solar irradiance forecast using all-sky imaging and real-time irradiance measurements". In : *Renewable Energy* 143 (déc. 2019), p. 1643-1658. DOI : 10.1016/j.renene.2019.05.069.

[26] A. Moncada, W. Richardson et R. Vega-Avila. "Deep Learning to Forecast Solar Irradiance Using a Six-Month UTSA SkyImager Dataset". In : *Energies* 11.8 (juill. 2018), p. 1988. DOI : 10.3390/en11081988.

[27] H. T. C. Pedro et C. F. M. Coimbra. "Nearest-neighbor methodology for prediction of intra-hour global horizontal and direct normal irradiances". In : *Renewable Energy* 80 (août 2015), p. 770-782. ISSN : 0960-1481. DOI : 10.1016/j.renene.2015.02.061.

[28] J. O. Kamadinata, T. L. Ken et T. Suwa. "Sky image-based solar irradiance prediction methodologies using artificial neural networks". In : *Renewable Energy* 134 (2019), p. 837-845. ISSN : 0960-1481.

[29] A. Nanduri et L. Sherry. "Anomaly detection in aircraft data using Recurrent Neural Networks (RNN)". In : *Integrated Communications Navigation and Surveillance (ICNS)*. IEEE, avr. 2016. doi : 10.1109/icnsurv.2016.7486356.

[30] H. Nguyen, K. Tran, S. Thomassey et M. Hamad. "Forecasting and Anomaly Detection approaches using LSTM and LSTM Autoencoder techniques with the applications in supply chain management". In : *International Journal of Information Management* 57 (avr. 2021), p. 102282. doi : 10.1016/j.ijinfomgt.2020.102282.

[31] D. Debajit, E. D. Preetha, M. Dhruv et J. Anukriti. "Neural Machine Translation using Recurrent Neural Network". In : *International Journal of Engineering and Advanced Technology* 9.4 (avr. 2020), p. 1395-1400. doi : 10.35940/ijeat.d7637.049420.

[32] K. Lilis et S. Arif. "Sentiment Analysis using Recurrent Neural Network". In : *Journal of Physics : Conference Series* 1471.1 (fév. 2020), p. 012018. doi : 10.1088/1742-6596/1471/1/012018.

[33] D. P. Kingma et J. Ba. "Adam : A Method for Stochastic Optimization". In : *3rd International Conference on Learning Representations, ICLR 2015*. San Diego, CA, USA, mai 2015.

[34] N. Srivastava, G. Hinton, A. Krizhevsky et R. Sutskever Ilyaand Salakhutdinov. "Dropout : A Simple Way to Prevent Neural Networks from Overfitting". In : *Journal of Machine Learning Research* 15 (juin 2014), p. 1929-1958.

[35] D. Scaramuzza, A. Martinelli et R. Siegwart. "A Toolbox for Easily Calibrating Omnidirectional Cameras". In : *2006 IEEE/RSJ International Conference on Intelligent Robots and Systems*. Oct. 2006, p. 5695-5701.

[36] R. Chauvin, J. Nou, S. Thil et S. Grieu. "Modelling the clear-sky intensity distribution using a sky imager". In : *Solar Energy* 119 (2015), p. 1-17.

[37] G. Bradski. "The OpenCV Library". In : *Dr. Dobb's Journal of Software Tools* (2000).

[38] F. Drago, K. Myszkowski, T. Annen et N. Chiba. "Adaptive Logarithmic Mapping For Displaying High Contrast Scenes". In : *Computer Graphics Forum* 22.3 (sept. 2003), p. 419-426. doi : 10.1111/1467-8659.00689.

[39] F. Durand et J. Dorsey. "Fast bilateral filtering for the display of high-dynamic-range images". In : *ACM Transactions on Graphics* 21.3 (juill. 2002), p. 257-266. doi : 10.1145/566654.566574.

[40] R. Mantiuk, K. Myszkowski et H.-P. Seidel. "A perceptual framework for contrast processing of high dynamic range images". In : *ACM Transactions on Applied Perception* 3.3 (juill. 2006), p. 286-308. doi : 10.1145/1166087.1166095.

[41] E. Reinhard et K. Devlin. "Dynamic Range Reduction Inspired by Photoreceptor Physiology". In : *IEEE Transactions on Visualization and Computer Graphics* 11.01 (jan. 2005), p. 13-24. doi : 10.1109/tvcg.2005.9.

[42] S. Dev, Y. H. Lee et S. Winkler. "Color-based segmentation of sky/cloud images from ground-based cameras". In : *IEEE Journal of Selected Topics in Applied Earth Observations and Remote Sensing* 10.1 (jan. 2017), p. 231-242. doi : 10.1109/JSTARS.2016.2558474.

[43] Z. Peng, D. Yu, D. Huang, J. Heiser et P. Kalb. "A hybrid approach to estimate the complex motions of clouds in sky images". In : *Solar Energy* 138 (nov. 2016), p. 10-25. issn : 0038-092X. doi : 10.1016/j.solener.2016.09.002.

[44] T. M. Hamill et T. Nehrkorn. "A Short-Term Cloud Forecast Scheme Using Cross Correlations". In : *Weather and Forecasting* 8.4 (déc. 1993), p. 401-411. doi : 10.1175/1520-0434(1993)008<0401:ASTCFS>2.0.CO;2.

[45] N. Mori et K.-A. Chang. *Introduction to MPIV*. http ://www.oceanwave.jp/softwares/mpiv. 2003.

[46] D. Sun, S. Roth et M. J. Black. "A Quantitative Analysis of Current Practices in Optical Flow Estimation and the Principles Behind Them". In : *International Journal of Computer Vision* 106.2 (sept. 2014), p. 115-137. ISSN : 0920-5691. DOI : 10.1007/s11263-013-0644-x.

[47] S. R. West, D. Rowe, S. Sayeef et A. Berry. "Short-term irradiance forecasting using skycams : Motivation and development". In : *Solar Energy* 110 (déc. 2014), p. 188-207. DOI : 10.1016/j.solener.2014.08.038.

[48] J. Wulff et M. J. Black. "Efficient sparse-to-dense optical flow estimation using a learned basis and layers". In : *2015 IEEE Conference on Computer Vision and Pattern Recognition (CVPR)*. IEEE, juin 2015. DOI : 10.1109/cvpr.2015.7298607.

[49] J.-Y. Bouguet. "Pyramidal implementation of the Lucas Kanade feature tracker Description of the algorithm". In : *Intel Corporation, Microprocessor Research Labs* (1999).

[50] G. Farnebäck. "Polynomial Expansion for Orientation and Motion Estimation". Dissertation No 790, ISBN 91-7373-475-6. Thèse de doct. SE-581 83 Linköping, Sweden : Linköping University, Sweden, 2002.

[51] G. Farnebäck. "Two-Frame Motion Estimation Based on Polynomial Expansion". In : *Image Analysis*. Sous la dir. de J. Bigun et T. Gustavsson. Berlin, Heidelberg : Springer Berlin Heidelberg, 2003, p. 363-370. ISBN : 978-3-540-45103-7.

[52] X. Jin et J. Han. "K-Means Clustering". In : *Encyclopedia of Machine Learning and Data Mining*. Springer US, 2017, p. 695-697. DOI : 10.1007/978-1-4899-7687-1_431.

[53] D. Gregg, R. Taylor, J. Campbell, J. Taylor et A. Cotton. "Solar gasification of coal, activated carbon, coke and coal and biomass mixtures". In : *Solar Energy* 25.4 (1980), p. 353-364. DOI : 10.1016/0038-092x(80)90347-3.

[54] R. Taylor, R. Berjoan et J. Coutures. "Solar gasification of carbonaceous materials". In : *Solar Energy* 30.6 (1983), p. 513-525. DOI : 10.1016/0038-092x(83)90063-4.

[55] D. Yadav et R. Banerjee. "A review of solar thermochemical processes". In : *Renewable and Sustainable Energy Reviews* 54 (fév. 2016), p. 497-532. DOI : 10.1016/j.rser.2015.10.026.

[56] M. Puig-Arnavat, E. Tora, J. Bruno et A. Coronas. "State of the art on reactor designs for solar gasification of carbonaceous feedstock". In : *Solar Energy* 97 (nov. 2013), p. 67-84. DOI : 10.1016/j.solener.2013.08.001.

[57] M. Milanese, G. Colangelo, F. Iacobazzi et A. de Risi. "Modeling of double-loop fluidized bed solar reactor for efficient thermochemical fuel production". In : *Solar Energy Materials and Solar Cells* 160 (fév. 2017), p. 174-181. DOI : 10.1016/j.solmat.2016.10.028.

[58] A. Gómez-Barea, M. Suárez-Almeida et A. Ghoniem. "Analysis of fluidized bed gasification of biomass assisted by solar-heated particles". In : *Biomass Conversion and Biorefinery* 11.1 (sept. 2020), p. 143-158. DOI : 10.1007/s13399-020-00865-0.

[59] A. Curcio, S. Rodat, V. Vuillerme et S. Abanades. "Experimental assessment of woody biomass gasification in a hybridized solar powered reactor featuring direct and indirect heating modes". In : *International Journal of Hydrogen Energy* 46.75 (oct. 2021), p. 37192-37207. DOI : 10.1016/j.ijhydene.2021.09.008.

[60] A. P. Muroyama, I. Guscetti, G. L. Schieber, S. Haussener et P. G. Loutzenhiser. “Design and demonstration of a prototype 1.5 kWth hybrid solar/autothermal steam gasifier”. In : *Fuel* 211 (jan. 2018), p. 331-340. doi : 10.1016/j.fuel.2017.09.059.

[61] B. J. Hathaway et J. H. Davidson. “Autothermal hybridization and controlled production of hydrogen-rich syngas in a molten salt solar gasifier”. In : *International Journal of Hydrogen Energy* 46.29 (avr. 2021), p. 15257-15267. doi : 10.1016/j.ijhydene.2021.02.048.

[62] C. E. García, D. M. Prett et M. Morari. “Model predictive control : Theory and practice—A survey”. In : *Automatica* 25.3 (mai 1989), p. 335-348. doi : 10.1016/0005-1098(89)90002-2.

Chapter 1

General introduction

In this chapter, after a discussion on the rise of renewable energies, a detailed presentation of concentrating solar power systems, their functionalities, and their perspectives is given. The scientific path and the industrial motivations behind this work are then given. There are two main objectives pursued during this thesis, that belong to two work packages of the H2020 project SFERA III, which is briefly presented in the sequel.

- The development of a solar resource forecasting model that can anticipate strong DNI variations for complex sky situations, to help the solar infrastructure users to plan their experiments, and optimize their on-Sun experimentation time. It should be mentioned that these forecasts can also help operators optimize the real-time management of concentrated solar power systems to reduce maintenance costs, thus contributing to the overall effort to improve the competitiveness of this technology.

- The development of an advanced predictive controller of a solar reactor, designed to produce syngas from biomass, in order to ensure its stability while preserving performance.

1.1 The rise of renewable energies

The rise of renewable energies has been fast and massive in scale. In this section, we shed light on the current climate status and the evolution of energy consumption versus the exhaustion of fossil fuels. The current common forms of renewable energies are presented. Then, the H2020 project SFERA III is discussed, while highlighting the contribution of this thesis in the corresponding work packages.

1.1.1 Climate change

It is undeniable that mankind is currently facing existential threats caused by global warming and climate change. Disastrous effects such as extreme weather conditions [1, 2], extinction of certain species, accelerating ice melting [3], and rising water levels [4] are already triggered by global warming. Faced with this environmental context, the Intergovernmental Panel on Climate Change (IPCC) was established in 1988 to provide detailed assessments of the state of scientific, technical and socio-economic knowledge related to the causes and potential repercussions of global warming. It also identifies strategies for mitigating global warming and the possibilities of adapting to the expected changes. In its report of 2014 [5], the IPCC sheds light on the impact of climatic events caused by climate change. In France, several research teams are working on these topics, involving hundreds of scientists, some of whom are contributing to the IPCC's reports. The global warming is mainly due to the concentration of greenhouse gases (GHG) in the atmosphere. According to the IPCC, GHG emissions increased sharply between 1970 and 2010, with a significant increase towards the end of this period.

Despite the growing number of policies implemented to limit these emissions, global GHG emissions did not cease to rise [6]. Carbon dioxide (CO_2) alone accounts for nearly 70% of GHG emissions. Its concentration does not cease to increase, risking irreversible climate changes [7]. CO_2 emissions, attributable to the use of fossil fuels, contributed to 78% of global GHG emissions between 1970 and 2010. Despite the decline in 2020 due to Covid-19, CO_2 emissions due to energy production remained at 31.5 Gt, which contributed to CO_2 reaching its highest ever average annual concentration (50% higher than in the beginning of the industrial revolution era [8]). In addition, emissions are expected to increase due to an anticipated augmentation in coal and natural gas usage caused by the rapidly increasing coal-fired generation in Asia and the increase in natural gas demand.

1.1.2 Evolution of energy consumption

In view of the above, it is clear that global warming and the energy market are linked. The improvement in living conditions, caused by the advancement of science and technology, is translated by a worldwide increase in energy consumption, which increased from 3699.3 mega tonnes of oil equivalent (Mtoe) in 1965 to 13 724.2 Mtoe in 2018, with an annual growth rate of 6% according to British Petroleum (BP) [9]. In its 2021 report on global energy consumption [10], the U.S. Energy Information Administration (EIA) forecasts a 50% increase in global energy consumption between 2020 and 2050. This increase in global energy demand is attributable to population and economic growth. Indeed, most of this growth comes from developing countries, with strong economic growth, particularly in Africa and Asia. Developed countries continue to consume an enormous amount of energy. For example, China is the largest consumer of electricity in the world. Furthermore, the EIA estimates a constant and unprecedented increase in power generation between 2020 and 2050 which will also grow strongly with the increase in population and progress in all sectors around the world. Based on the current energy consumption/demand, the depletion of fossil energy resources, and current environmental concerns, it is necessary to seek other eco-friendly energy sources.

1.1.3 Depletion of fossil fuels

Ever since the industrial revolution, fossil fuels have been the backbone of the world's energy supply. Oil, for instance, provided 32.9% of the world's total primary energy supply in 2016 [11]. In Europe, 41% of the overall energy net generation in 2017 was fossil-fuel based [12]. The composition of net power generation sources differs from one European country to another (see Table 1.1). The share of fossil-fuel based generation, though decreasing in half of the presented countries, still represents a significant share in many of them. Table 1.1 also shows an increase in the share of solar and wind energy in net generation across the board. Even with the introduction of alternative energy sources, many sectors remain dependent on liquid fuels, such as the transportation fleet whose energy is over 90% oil-based [13]. The fossil fuel industry therefore continues to develop more effective drilling techniques. As a result, studies show that giant heavily-exploited oil fields are being depleted [14, 15]. The replenishment of these fields is not a viable option at all, as the rate of creation of fossil fuels is far slower than its rate of extraction. The International Energy Agency (IEA) has declared in 2010 that the peak of conventional oil production occurred in 2006 [16]. From here onwards, more energy and money are needed to extract fossil fuel as fields are becoming fewer and less accessible. On this account, renewable energy sources are becoming increasingly attractive, as they offer the prospect of clean and sustainable power generation.

1.1.4 International law and renewable energy growth

Faced with the depletion of fossil energy resources, global warming, and environmental degradation, organizations and governments are increasingly seeking to adapt their strategies,

Table 1.1: Energy net generation in European countries in 2017 and its evolution between 2014 and 2017 [12].

	Energy net generation [%]				
	Nuclear	Fossil fuels	Hydraulic	Solar	Wind
Italy	–	61.6 (+1.7)	13.7 (−8.0)	9.1 (+0.4)	6.4 (+1.2)
Portugal	–	57.9 (+21.7)	13.5 (−19.5)	1.6 (+0.4)	22.0 (−2.2)
U.K.	21.0 (+5.5)	53.6 (+4.8)	2.4 (−0.3)	3.3 (+3.3)	14.1 (+4.4)
Germany	12.1 (−4.6)	52.4 (−3.4)	4.3 (−0.1)	5.9 (+0.4)	17.3 (+7.2)
Spain	21.4 (+0.8)	45.2 (+8.0)	7.9 (−8.0)	5.3 (+0.4)	18.4 (−0.7)
Belgium	50.6 (−3.2)	29.8 (−3.3)	1.7 (−0.4)	3.7	7.8 (+1.2)
Finland	33.6 (−1.0)	19.0 (−6.3)	22.8 (+2.6)	–	7.5 (+5.8)
France	71.9 (−4.9)	10.3 (+5.2)	10.2 (−2.4)	1.7 (+0.6)	4.6 (+1.5)
Sweden	39.8 (−1.3)	1.7 (−0.4)	40.4 (−2.5)	–	10.9 (+3.3)
Switzerland	32.5 (−5.2)	1.4 (−1.6)	61.0 (+4.6)	1.7 (+1.7)	0.2
Mean value	28.3	33.3	17.8	3.2	10.9

modes of energy production and consumption in order to be more eco-friendly. Renewable energy, also referred to as "green energy" or "clean energy", is becoming a major influential component in governments around the world due to its low environmental impact and its status as an unlimited resource on the human time scale. There are several types of renewable energies such as: solar energy, wind energy, hydro energy, biomass, and geothermal energy [17]. Their exploitation generates few pollutants, compared to fossil fuels, which makes these energies a key element in the fight against global warming. In addition, governments have issued numerous rules and regulations to face global warming, for example the European Union (EU) has envisaged the 2030 climate and energy framework, which plans on: reducing greenhouse gas emissions by 30% compared to the 1990 level; improving energy efficiency by 32.5%; and increasing the portion of the EU clean energy supply by 32% [18]. The French government has adopted a climate-energy law aiming to: reduce greenhouse gas emissions by 40% compared to the 1990 level; close the last coil-fired power plants by 2022; reduce 50% of the energy consumption by 2050 with respect to the 2012 level; reduce 40% of fossil fuel-based energy consumption by 2030 compared to the 2012 level; and achieve 33% of renewable energy contribution in the total energy mix. Beside this law, the French government issued several strategies to ensure the success of the discussed law such as the national low-carbon strategy (SNBC) [19] and the multi-annual energy plan (PPE) [20]. On the global level, 1260 climate-change laws were in effect worldwide [21]. Thanks to these initiatives, the share of renewable energies in the world's final energy production is expected to increase to 30% by 2022, as confirmed by the IEA [22]. In 2020, according to the IEA, 90% of the newly installed power capacity will be provided by renewable energies, particularly wind, solar and hydro [23]. It should be mentioned that the adapted strategies aim to resolve health issues since, besides the fact that large-scale use of renewable energies contributes to the mitigation of environmental problems, it also reduces the health consequences of air pollution and global warming. The mitigation of health damages can, in some cases, compensate for the costs of a climate policy. For example, a study in the United States showed that the economic health benefits of renewable energy use are about 60% higher than wind energy subsidies [24].

1.2 Concentrated solar power

Development of sophisticated and efficient techniques for renewable energy is a major concern nowadays. Among the various renewable energy technologies, concentrated solar power (CSP) systems convert solar radiation into energy by producing heat and then converting it into

electricity by using steam turbines or Stirling engines, for example. In this section, the concept behind CSP is presented, then different types of CSP technologies are discussed, while highlighting the technical difficulties and challenges to overcome.

1.2.1 CSP principles

From a technological point of view, a concentrating solar power system converts the thermal energy of solar radiation into electricity. With the help of mirrors, the Sun rays are concentrated on a receiver where a heat transfer fluid circulates [25]. This process heats up the fluid that feeds a steam turbine to generate electricity. A simplified diagram showcasing the operation of a CSP plant, with the four most known technologies, is shown in Figure 1.1. CSP has several advantages such as: the possibility to couple these systems with other energy sources, such as photovoltaic sources, to increase their efficiency and meet the electricity demand; the CSP plants can also be coupled with thermal storage systems to meet the grid's needs outside Sunny hours, please note that these storage systems can be optimally managed if intra-hour DNI forecasts are provided; and finally these systems are based on conventional equipment and thermodynamic cycle (Rankine cycle [26]) that has already been widely tested and approved.

1.2.2 Concentrated solar power technologies

The four main CSP technologies are described in the following section, while highlighting their advantages, disadvantages, and the technical challenges that they face.

1.2.2.1 Parabolic trough (PT) and linear Fresnel reflectors (LFR)

These technologies are based on linear solar concentration, where Sun light is concentrated onto a point in a line [28]. PT systems are currently the most widespread systems, with almost 85% of the CSP capacity installed [29]. As a consequence, these technologies benefit from more experience than other types of CSP technologies. Most of these technologies are inspired by the first commercial CSP power plant in the world [30]. The concept of the parabolic trough can be explained as: long mirrors are aligned as shown in Figure 1.1, rotating around a single axis in the length direction. This axis is usually oriented in the North/South direction to allow the mirrors to follow the Sun's path throughout the day. The heat transfer fluid moves in a tube located in the focal line of the concentrator, to receive the concentrated solar flux. The main tube design can be optimized by reducing the convection losses, for example with a glass isolation. In general, the fluid used for this technology is synthetic oil heated to 390 °C. Heat is then transferred, through a heat transfer block, to a conventional steam cycle to power a turbine. Although this technology is very common, it has its disadvantages, such as a small range of temperatures for the heat transfer fluid as well as the current impossibility of using a more efficient or less expensive fluid on a large scale. On the other hand, LFR is still in an early stage of industrial deployment [29]. This technology is similar to the parabolic trough, where the solar field consists of a series of flat (or slightly curved) parallel mirrors rotating on a single axis (see Figure 1.2) [31].

The difference between this technology and PT is that the mirrors redirect the solar irradiance on a fixed linear receiver, placed a few meters above the ground. This receiver contains the tube (or tubes) where the heat transfer fluid circulates. This fluid allows pressurized steam production. The cost of this technology can be reduced by using simple geometry mirrors, for example, the integration of a secondary mirror installed above the receiver can increase the concentration factor significantly. Comparing this technology to PT, the solar field and receivers cost 44% less [33] (for 100 MW plant). This fact can be of great importance in the commercializing phase. However, the LFR technology has its disadvantages as well: its optical efficiency is less than that's of PT [34], which penalizes its performance,

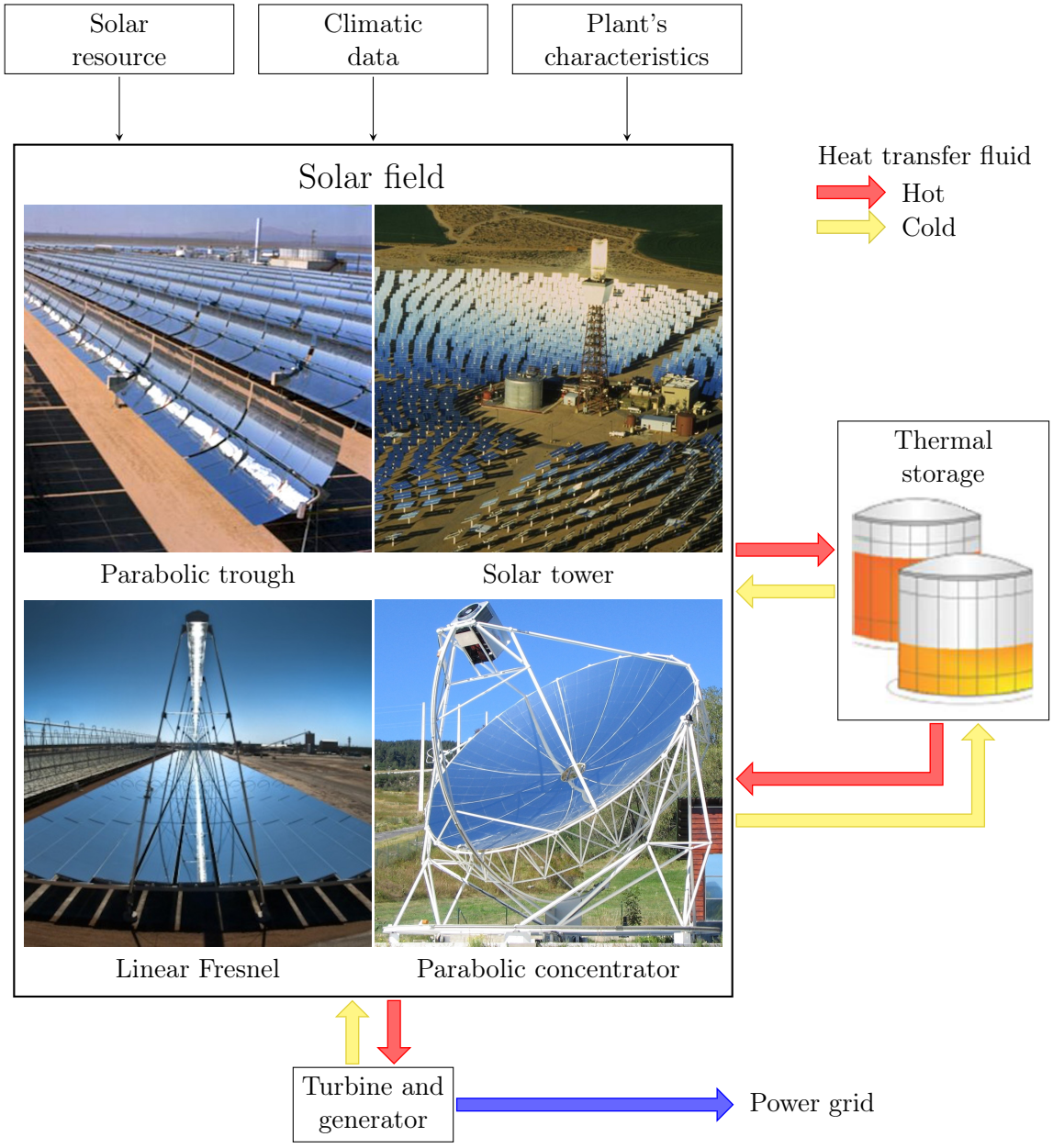

Figure 1.1: CSP technologies (adapted from [27]).

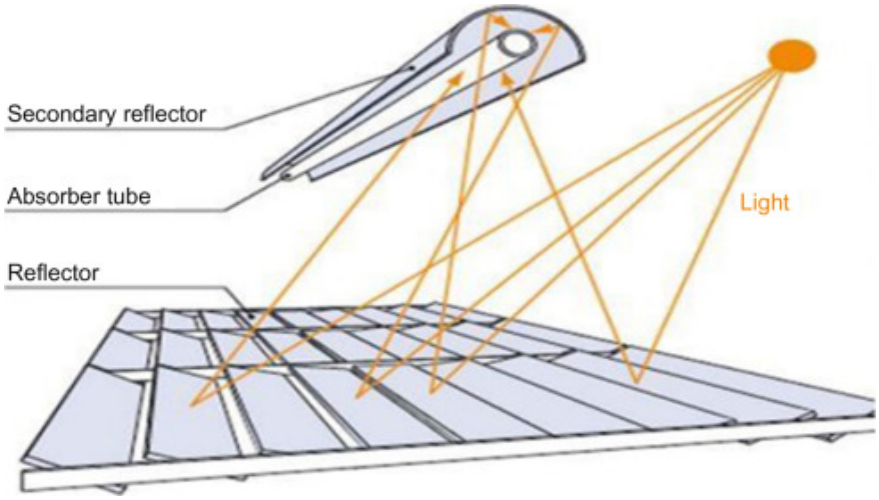

Figure 1.2: Linear Fresnel reflector design [32].

especially for low solar heights [30]. With that said, researchers are working on solutions for the optical efficiency [35]. It appears that this technology becomes interesting for low capacities (typically from a few hundred kW to a few tens of MW) or to be associated with other industrial processes requiring heat.

Several power plants featuring parabolic collectors are constructed such as: the 64 MW plant built in Boulder city, Nevada, USA; a hybrid plant combing parabolic collectors (25 MW) and a gas turbine plant (130 MW) built in Hassi Rmel, southern Algeria. On the other hand, several plants with LFR technology can be found: the eLLO plant, France, can generate up to 9 MW power output with its 23,800 collectors (Figure 1.3); the plant constructed in Bakersfield, California, USA, can generate up to 5 MW of electricity. A thorough comparative study is carried out in [36] to highlight the differences between the two designs.

Figure 1.3: eLLO 9 MW linear Fresnel CSP plant (Llo, France).

1.2.2.2 Solar tower

The solar field consists of many heliostats which concentrate the solar irradiance at the top of a tower on which the receiver is installed [37, 38]. It is the second most common type of CSP system [29]. These mirrors can be installed on uneven ground thanks to the

numerous design solutions and possibilities for this technology. This design permits the mirrors to track the Sun on two axes, unlike PT for example, thus reaching higher concentration factors and temperatures (typically between 300 °C and 2000 °C [39]). Since the efficiency of a solar concentrator increases with temperature until it reaches a maximum that depends on its concentration factor [40], the solar tower technology therefore inherently offers a higher theoretical efficiency than PT, for an equivalent solar surface. In addition, this technology is more robust to seasonal variations such as Sun height variations, compared to LFR for example. It should be mentioned that, the high temperature range and the compactness of the receiver allow the utilization of superheated steam or molten salts as a heat transfer fluid. The superheated steam saves an exchanger between the solar field circuit and the turbine circuit, while the molten salt saves an exchanger between the solar field circuit and the storage circuit. Multiple solar towers exist such as: the 10 MW PS10 plant (Spain) consisting of 624 heliostats or the 392 MW Ivanpah plant (United States) with 173,500 heliostats. It cost 2200 M$ and occupies an area of 2.6 km^2. The heat transfer fluid is superheated water to over 560 °C.

Figure 1.4: Solar tower technology.

1.2.2.3 Dish–Stirling systems and parabolic concentrators

Parabolic concentrators are still demonstration projects. For this type of configuration the solar field is made up of a multitude of parabolas following the path of the Sun on two axes. Each parabola constitutes a small power station. This specificity makes the parabolic concentrators a modular technology by nature that can be installed on uneven terrain, same as the solar tower. Due to its configuration, this system also allows the highest concentration factor of the four technologies presented, i.e., higher theoretical yields [41]. The records for conversion efficiency, close to 32%, are obtained with this type of concentrator. The receiver can be replaced by a Stirling engine (external combustion engine) which has the particularity of not requiring a cooling circuit. It consists of a parabolic reflector that concentrates Sunlight in the fixed receiver that transfers the energy to the Stirling engine working fluid, a cavity zone, and a second re-concentration zone [42]. The Stirling engine directly converts solar energy

into mechanical energy and then into electricity. An example of this system is PROMES's 10 kW Dish-Stirling system (see Figure 1.5) studied in [43]. Since this system is not suitable for thermal storage, it is in direct competition with PV or wind power plants, which are much cheaper today. As mentioned before, this technology is facing various technical difficulties especially on large-scale deployment, which is explained by its lack of maturity.

Figure 1.5: PROMES's 10 kW Dish-Stirling system (Odeillo, France).

1.2.3 CSP for hydrogen production

As shown in Section 1.2.1, the CSP systems can generate electric power by converting the thermal energy of solar irradiance into electricity, but this is not the full potential of these systems. They can also produce "green hydrogen". This topic is a research target [44, 45]. There exists three main techniques to generate hydrogen using CSP systems:

- it can be through photo-conversion process [46]. An example of this method is the thermo-chemical two-step water splitting process using redox systems, where the concentrated power needed is delivered by a solar tower system [44], this technique necessitates high temperatures (up to 2000 °C [47]) to drive series of chemical reactions that produce hydrogen;

- electric power generated by CSP systems can be used to produce hydrogen by electrolysis [48]. An example of this method is the techno-economic study carried out on a hybrid solar gas power-electrolysis system [49]. This system uses a fuel unit and parabolic trough system to generate steam that is fed to a turbine. The power generated is used in an electrolysis unit, that converts water to oxygen and hydrogen gas;

- solar irradiance is converted to heat which is used to drive the hydrogen production processes, such as biomass gasification, electrolysis, electrolysis at high temperature, or thermo-chemical cycle [49]. An example of this methodology can be the PROMES's solar reactor prototype presented in Figure 1.6. It produces hydrogen by burning biomass,

where the parabolic mirror on the top concentrates solar irradiance to generate the heat required to drive the chemical gasification reaction [50]. This system is studied in details in the second part of this thesis, where a model is developed to control this solar reactor with the help of solar irradiance forecasts.

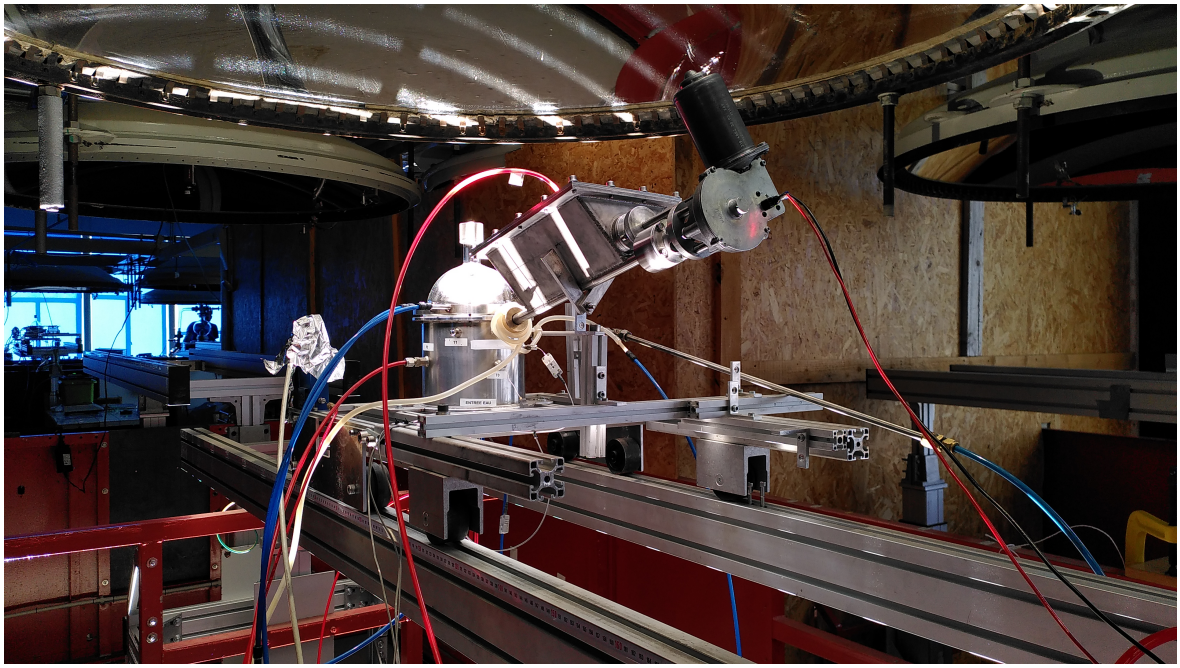

Figure 1.6: PROMES's solar reactor prototype (Odeillo, France).

1.2.4 The current state of CSP

In this section, the current and expected CSP share in the energy mix is presented and discussed, while highlighting the perspectives and potentials of this technology.

1.2.4.1 CSP contribution to the energy mix

The share of renewables in global power production increased from 26% in 2019 to 28% in 2020 [51]. The increase in renewables came mainly at the cost of coal and gas, though those two sources still represent close to 60% of global power supply. PV share of power generation increased from 135.1 GW in 2014 to more than 288.9 GW [52]. This growth has been driven by a massive reduction in PV panel production costs, particularly related to China's entry to the market. This craze for the PV sector, on the other hand, has been detrimental to the development of the CSP sector, which has experienced a slower-than-expected growth in recent years, where CSP's share of power generation has grown in the last decade as shown in Figure 1.7. This growth has been concentrated in Spain and the United States. Market prices, which have been slow to diminish, seem to be finally falling. New technologies have reached commercial maturity and new concepts have emerged. Thermal storage in molten salts is routinely used in trough configurations and has been demonstrated in solar towers.

On the global scale, Figure 1.8 shows the distribution of CSP power share by country: it shows that Spain (2304 MW) and the United States of America (1740 MW) lead the CSP campaign with the highest operational power plant installed. However, it should be mentioned that other countries are constructing CSP plants to join the two leading countries such as China and countries in the Middle East and North Africa region (MENA).

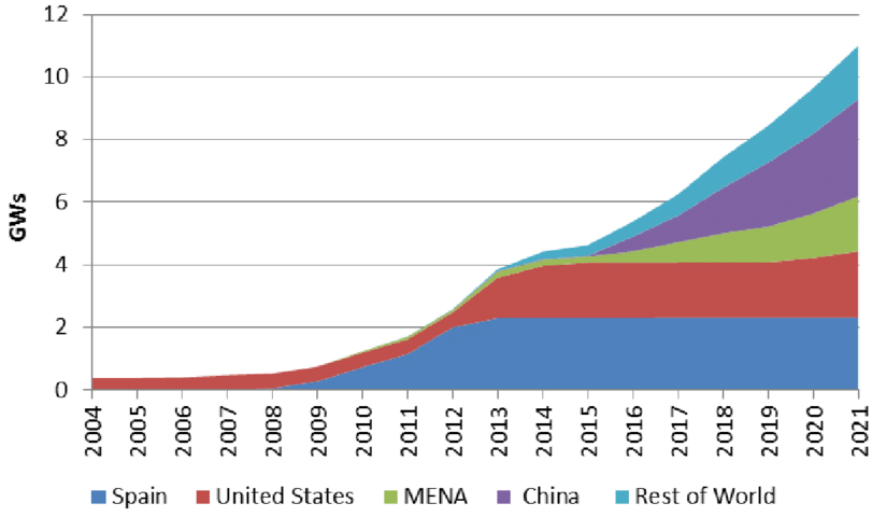

Figure 1.7: Actual and projected global cumulative growth of CSP capacity [53].

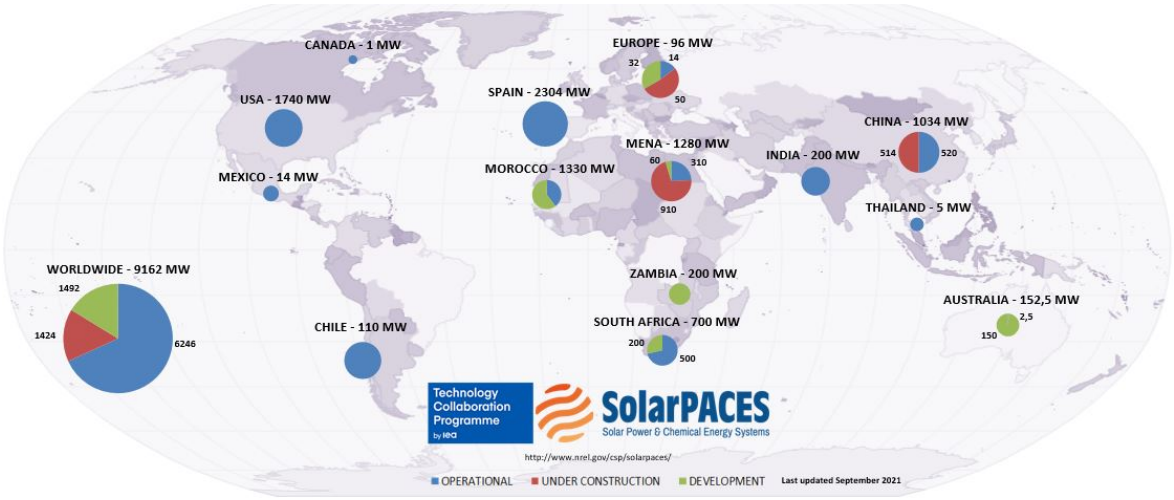

Figure 1.8: Distribution of CSP projects worldwide (source SolarPACES).

The share of CSP technology is expected to continue to rise, as it will play a key role in the future, thanks to the integration of thermal storage systems: its share of global electricity is envisioned to reach 13–15% in 2050 [54]. The hybridization between CSP and PV plants is considered the most efficient, pertinent, and reliable combination. It can meet the energy demand despite its variability throughout seasons or days. The integration of thermal storage provided whole new perspective and future for this technology. In addition, the integration of DNI forecasts can drastically optimize the management of production and storage phases.

1.2.4.2 Challenges and difficulties

CSP plants present some technical challenges, such as:

- cost and maintenance: CSP is expensive with a cost ranging from 3000 €kW^{-1} to 4000 €kW^{-1} [55];
- limited equivalent operating hours: about 3000 h versus 7500 h for fossil fuel power plants;
- the necessity of water for cooling and cleaning;
- some technologies such as linear Fresnel reflector have limited operational temperatures, causing a decrease in their efficiency.

To solve these problems, several solutions have been implemented, such as the hybridization of these plants with another energy source (oil, gas, coal, and biomass). This so-called hybrid operation increases the power availability and decreases its economic cost. The storage problem is solved by introducing thermal energy storage (TES) combined with larger collector fields. Solar heat collected during daytime can be stored in the TES systems and used later. It can be based on synthetic oil or molten salt [56], known as the sensible heat approach, where thermal energy is stored by the change of salt's or oil's temperature and reserving the hot fluid in specific containers [57] to be used later when needed. This solution reduces maintenance costs of the power block and can ensure production continuity. It should be mentioned that this method is the most common and reliable TES system [58] because of its low cost and the ability to discharge in controlled conditions. Regarding the cost, the levelized cost of energy (LCOE) is expected to decrease drastically thanks to the research and development these technologies are receiving (see Figure 1.9).

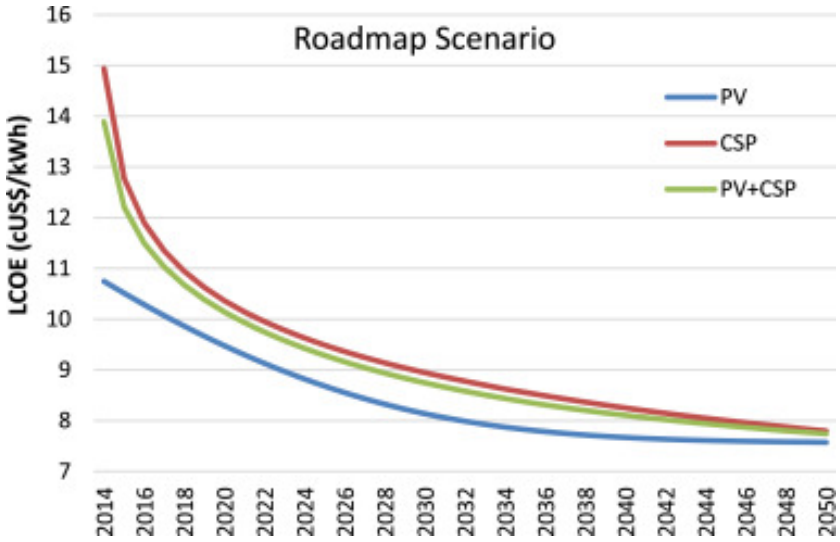

Figure 1.9: LCOE projection for a hybrid PV-CSP plant in the Atacama Desert [59].

1.3 The importance of solar irradiance forecasting

Deployment of CSP technologies is penalized by various scientific and technical bottlenecks, such as the efficient control of CSP systems [27]. The H2020 project SFERA III (Solar Facilities for the European Research Area) [60] aims to tackle some of these bottlenecks, in order to achieve better competitiveness of CSP systems. One way to optimize their management is to use model-based predictive control, which necessitates prediction of variables of interest, DNI in particular. Accurate DNI forecasts are of great importance, especially during cloudy days, where DNI varies a lot [61, 62]. They can contribute to the reduction of fluctuations and uncertainties of CSP plants' output due to solar irradiance intermittency and variability [63]. More specifically, the integration of DNI forecasts allows to:

- optimize the turbine start-up and shutdown sequences: turbines are started up progressively in order to maximize their life span. This gradual increase in power makes it possible to minimize the thermal stresses on the turbine components. However, this operating mode is not adapted to the intermittent nature of the solar resource. Thus integrating a DNI forecast model could help the operators to take better decisions regarding these sequences;

- ensure the optimal plants' maintenance: due to the hostile environment of the CSP plants (deserts for example), the intermittence of the solar resource, and the resulting thermal shocks, require certain equipment to operate in extreme conditions. In addition, the turbine is subject to daily start-ups and shutdowns, which accelerates its aging. These different factors influence the lifetime of the power plant. Accelerated fatigue tests are also carried out in order to improve the characterization of equipment over time. At this level, DNI measurements and forecasts can help users to: know with higher confidence the testing environment thus optimizing the experiments for the forecast horizon; and plan better the maintenance schedule so that the plant can function optimally, with minimized splurged solar power.

- optimize the control strategies: CSP plants require dynamic controllers based on forecasts to optimize the performance over a given forecast horizon, especially when the system dynamic is important. The optimal strategy should manage the heat transfer fluid to maximize the exploitation of available DNI while considering the system's inertia, and optimize the coordination between the solar field, the thermal storage system, and the turbine. Based on DNI forecasts, the controller should find the optimal solution for a required performance, in particular the optimal charging and discharging of thermal energy.

In this context, one of H2020 project SFERA III (Solar Facilities for the European Research Area) [60] objectives is to optimize the on-Sun experimentation time for CSP infrastructure users. To this end, intrahour DNI forecasts are needed (up to 15 minutes), with an accurate prediction of ramp events, allowing to anticipate strong DNI variations.

1.4 Horizon 2020 project SFERA III

SFERA III is a Horizon 2020 (H2020) project funded under the Research Infrastructure Program. It is a collaboration of 15 partners from 9 EU countries. The project duration is five years, starting from January 2019 and ending by December 2023, and it received a 9130 M€ grant over 5 years.

This project is the continuation of previous projects (SFERA I and SFERA II), and it aims to reinforce the sustainability of the activities of the European advanced concentrating solar power research infrastructures. It addresses scientific challenges and integrated research

activities in the field of concentrating solar power to provide the R&D community a new level of high-quality services.

The activities are divided into 13 different work packages (WPs) categorized into three main sections (see Figure 1.10):

- networking activities to improve the cooperation between the research infrastructures, the scientific community, industries and other stakeholders;
- transnational access activities aiming at providing access to all European researchers from both academia and industry to singular scientific and technological solar research infrastructures;
- joint research activities whose aim is to improve the infrastructure's integrated services.

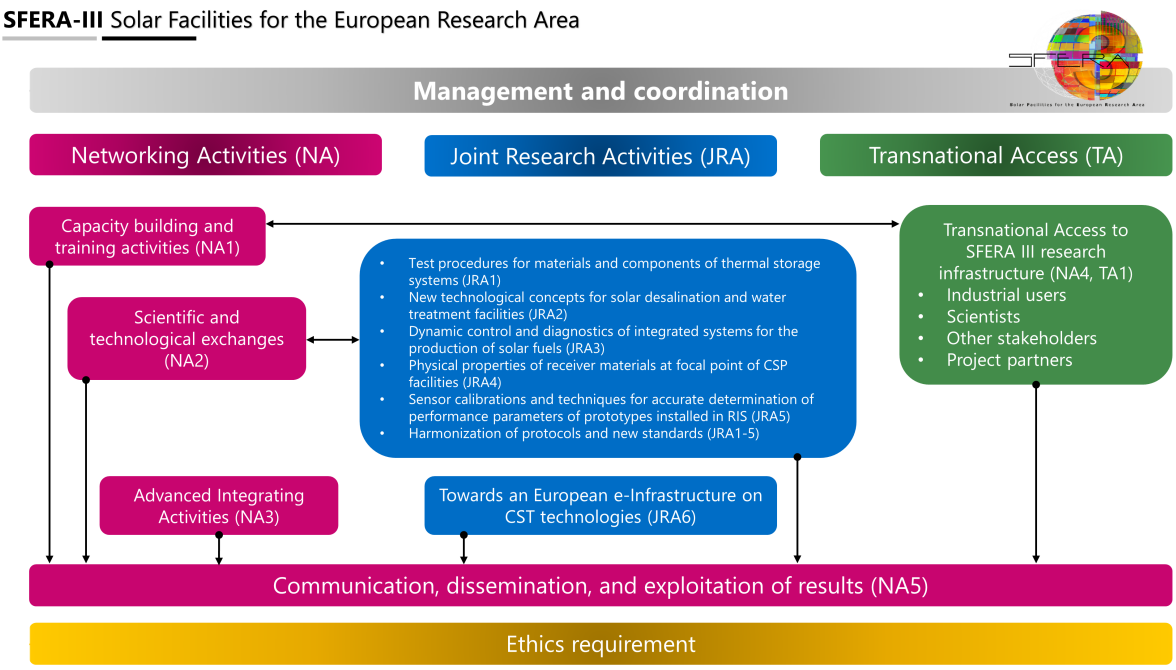

Figure 1.10: SFERA III activities [60].

The French National Center for Scientific Research (CNRS) is a founding member of the EU-SOLARIS ESFRI project, and has been deeply involved in numerous European projects on CSP for decades, particularly in previous infrastructure and coordination projects such as SOLFACE, SFERA, SFERA II and STAGE-STE. The CNRS posses some of the world finest facilities such as high concentration solar furnaces and parabolic trough and solar tower plants [64]. Concerning this project, the CNRS is involved in most of the WPs, however the work done in this thesis is distributed over WP8 and WP10. The first part of the thesis belongs to the WP10, which aims to:

- improve sensors and laboratory test benches during prototypes characterization;
- study and solve problems related to solar irradiance intermittence and variability during solar tests in research infrastructures and during evaluation of new developed systems or specific parameters, this is the objective of the first part of the thesis;
- increase the quality of services for optical characterization of line- and point-focussing concentrators.

In particular, the first part of this thesis targets the problems related to solar irradiance intermittence and variability by providing a DNI forecasting model based on DNI observations and sky images from a ground-based camera (sky imager).This model is supposed to handle complex sky situations, where solar irradiance variations are important. The second part of this thesis lays under the WP8 which aims to:

- develop high-performance diagnostic and dynamic control tools for solar thermochemical fuel production system using concentrated solar energy;
- benchmarking the various technologies available for solar fuel production via CST technologies;
- developing techniques for testing of components, subsystems, and materials performance and reliability;
- developing dedicated software and algorithms for dynamic control and optimized operation of each subsystem and of the entire integrated fuel production system.

In particular, the second part of this thesis proposes a dynamic controller, based on DNI forecasts, to maintain the performance and stability of a solar reactor, designed to produce hydrogen gas.

1.5 Dissemination

The work presented in this manuscript has led to the following peer-reviewed publications and conference papers:

- Conference paper #1. Karout et al. (2020). Cloud/sky segmentation from ground camera based on supervised machine learning approach. In: 33rd International Conference on efficiency, cost, optimization, Simulation and Environmental Impact of Energy Systems (ECOS 2020), Osaka, Japan.
- Conference paper #2. Karout et al. (2022). Intrahour direct normal irradiance forecasting based on sky image processing and time-series analysis. In: 28th SolarPaces Conference, Albuquerque, USA.
- Conference paper #3. Karout et al. (2022). Model-based predictive control of a solar reactor dedicated to syngas production. In: 28th SolarPaces Conference, Albuquerque, USA.
- Conference paper #4. Karout et al. (2023). Model-based predictive control of a solar reactor dedicated to syngas production. In: 22nd IFAC World Congress, Yokohama, Japan.
- Publication #1. Karout et al. (2023). Hybrid intrahour DNI forecast model based on DNI measurements and sky-imaging data. In: Solar Energy 249 pp. 541-548.
- Publication #2. Karout et al. (2023). Model-based predictive control of a solar thermochemical reactor dedicated to the high-temperature steam-gasification of biomass. In: Clean Technologies, *accepted for publication.*

Part I

DNI intra-hour forecasting destined to CSP infrastructure users

Chapter 2

Introduction

In this chapter, the behavior of solar irradiance is explained in order to propose a suitable forecast model. It starts with a brief overview of the electromagnetic radiation fundamentals to understand the origin of the different components of solar irradiance. Then, based on this understanding, these components and their corresponding measuring instruments are reviewed. The second part of this chapter presents the state-of-art forecasting models.

2.1 Introduction to solar resource

In this section, a brief introduction to electromagnetic radiation fundamentals is presented to help understanding the main components of solar irradiance. The measuring instruments for every component are detailed as well.

2.1.1 Electromagnetic radiation fundamentals

An electromagnetic wave is composed of an electric field and a magnetic field that oscillate perpendicular to each other and to the axis of propagation of the wave, as shown in Figure 2.1 [65]. The wavelength λ, defined by the distance between two maxima of the sinusoid, is related to the period T_w by Equation (2.1), where c is the speed of propagation of the wave:

$$c = \frac{\lambda}{T_w} \tag{2.1}$$

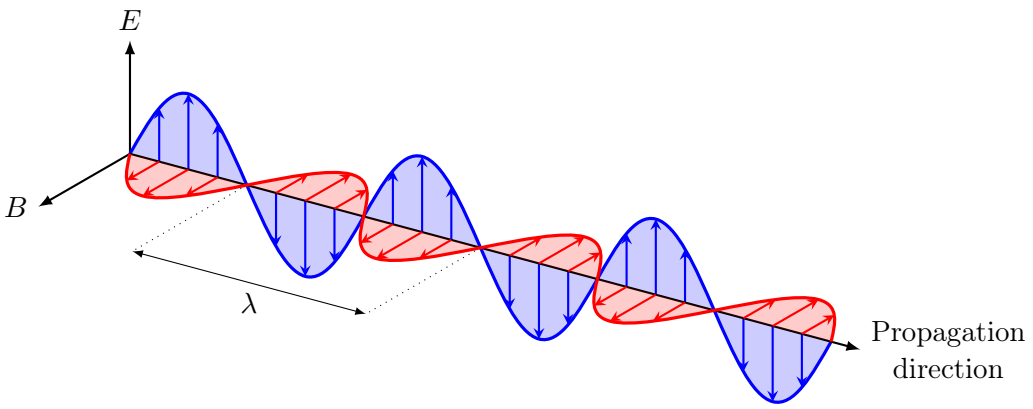

Figure 2.1: Propagation of the electric (E) and magnetic (B) fields [65].

However, it should be mentioned that an electromagnetic wave, characterized by the wavelength λ, has different behaviors once it encounters the atmosphere. A part of the wave

will be reflected, another will be absorbed, and the rest will be diffused. These phenomena are characterized by the following parameters:

- the absorption factor β_λ, defined by the ratio of the absorbed to the incident irradiance;
- the reflection factor δ_λ, defined by the ratio of the reflected to the incident irradiance;
- the transmittance factor τ_λ, defined by the ratio of the diffused to the incident irradiance.

2.1.2 The solar resource

Solar irradiance refers to all electromagnetic waves emitted by the Sun. It should be mentioned that there is a difference between the irradiance outside the atmosphere and that at ground level. The latter depends on the extraterrestrial solar irradiance, the characteristics of the studied site, and the atmospheric conditions that vary in time and space. In this section, the major factors that affect solar irradiance are studied.

2.1.2.1 Extraterrestrial solar irradiance

The extraterrestrial solar irradiance is the irradiance arriving at normal incidence on the outer layer of the atmosphere. Since the distance Earth-Sun is not constant, this irradiance is not constant either. However, according to the principle of conservation of energy, we can write:

$$I_0 = \left(\frac{D_0}{D_{UA}}\right)^2 \cdot I_{UA} \tag{2.2}$$

where I_0 is the extraterrestrial solar irradiance at the Earth-Sun distance D_0, D_{UA} is the mean distance between the Earth and the Sun ($D_{UA} = 1\text{UA} \approx 15 \times 10^7\,\text{km}$), and I_{UA} is the extraterrestrial solar irradiance incident at the average Earth-Sun distance, also called solar constant.

The estimation of the solar constant has been the subject of many satellite missions, because of its importance in the development of climate models [66, 67]. Several measurements can thus be found in the literature [68, 69]. However, a re-evaluation of the solar constant using a database covering 42 years was recently carried out and allowed to obtain $I_{UA} = 1361.1\,\text{W}\,\text{m}^{-2}$ [70]. For the calculation of the $\frac{D_0}{D_{UA}}$ ratio, the SG2 algorithm (for Solar Geometry 2), which is accurate and fast, has been chosen [71].

2.1.2.2 Interaction with the atmosphere

The atmosphere attenuates the solar irradiance received from the Sun; part of this irradiance is absorbed by the gases in the atmosphere. These gases have factors of absorption and transmission that depend on the wavelength. This phenomenon explains part of the solar irradiance variability (the atmospheric composition is variable in time and space). The direct normal irradiance (DNI), which is the direct irradiance received on a plane normal to the Sun (see Section 2.1.3.1), can be modeled by the Beer-Lambert law as follows:

$$\text{DNI} = I_0 \exp\left(-m\tau\right) \tag{2.3}$$

where I_0 is the extraterrestrial solar irradiance, m is the optical air mass, and τ is the optical depth of the atmosphere.

2.1.2.2.1 Relative optical air mass As shown in Figure 2.2, the relative optical air mass m is the ratio of the distance traveled by the light through the atmosphere and the distance that this beam would travel through a standard atmosphere, at sea level and with the Sun at zenith ($m = 1$). The position of the Sun is therefore necessary to calculate the relative optical air mass. Several formulations of m exist in the literature [72], designed to account for the effects of the curvature of the Earth, the sites' altitude, and the variable densities of the atmosphere on the average path of solar irradiance. In this thesis, the formula of the relative optical air mass m is chosen to be:

$$m = \frac{1}{\cos(\mathrm{SZA}) + a_1 (a_2 - \mathrm{SZA})^{-a_3}} \tag{2.4}$$

where SZA is the Sun zenith angle. This air mass estimation provides accurate results for all zenith angles (maximum absolute error of 6.90×10^{-2} and maximum relative error 0.18%) [72], with the coefficients $a_1 = 0.50572$, $a_2 = 96.079951$, and $a_3 = 1.63643$ proposed by Kasten and Young [73].

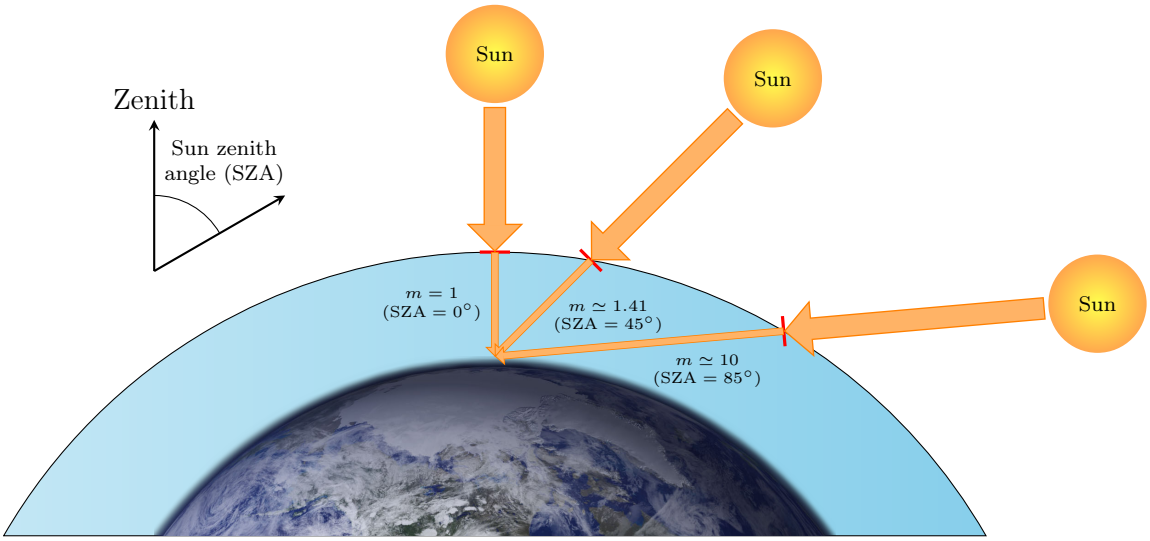

Figure 2.2: Optical air mass as a function of the Sun zenith angle.

2.1.2.2.2 Optical depth As explained in Equation (2.3), the optical depth also attenuates the extraterrestrial solar irradiance. A part of irradiance is absorbed or diffused as it traverses the atmosphere. Four constituents are mainly responsible for the absorption phenomenon: ozone, oxygen, carbon dioxide and water vapor. However, for the diffusion part, two types can be observed.

- Rayleigh diffusion: it occurs when the size of the particles is much smaller than the incident wavelength. This is the case for gas molecules (O_2, N_2, CO_2) and small particles of dust. This diffusion is more remarkable when the wavelength is short and at high altitudes, where the atmosphere contains less aerosols or water vapor.
- Mie diffusion: it occurs when the size of the particles is comparable to the wavelength of the incident radiation. This is the case for water vapor and aerosols (dust, smoke, pollen). This means that Mie diffusion occurs more often at low altitudes, where aerosols are concentrated.

In addition, clouds affect solar irradiance. Depending on their altitude, optical thickness, and composition, they have various forms and properties, which means that clouds can have

different attenuation effects. The impact of clouds on the solar irradiance received at ground level is difficult to describe in a quantitative way, but it does not depend on the wavelength of the incident wave, then Equation (2.3) can be re-written as follows:

$$\begin{aligned} \mathrm{DNI} &= I_0 \exp\left(-m(\tau_{\mathrm{CS}} + \tau_{cloud})\right) && (2.5)\\ &= \exp\left(-m\tau_{cloud}\right) \cdot I_0 \exp\left(-m\tau_{\mathrm{CS}}\right) && (2.6)\\ &= k_c \cdot \mathrm{DNI}_{\mathrm{CS}} && (2.7) \end{aligned}$$

where k_c is the clear-sky index and $\mathrm{DNI}_{\mathrm{CS}}$ is the clear-sky direct normal irradiance, which is a function of the coefficient τ_{CS}.

The coefficient τ_{CS} takes into account the absorption and diffusion phenomena without Sun-blocking clouds, while the coefficient k_c accounts for the influence of Sun-blocking clouds. As illustrated in Figure 2.3, this coefficient varies between 0 and 1: $k_c = 0$ means that a thick cloud occults the Sun, while $k_c = 1$ means that there is no clouds blocking the Sun (resulting in the so-called clear-sky situations); of course, the intermediate cases appear when thin clouds block the Sun.

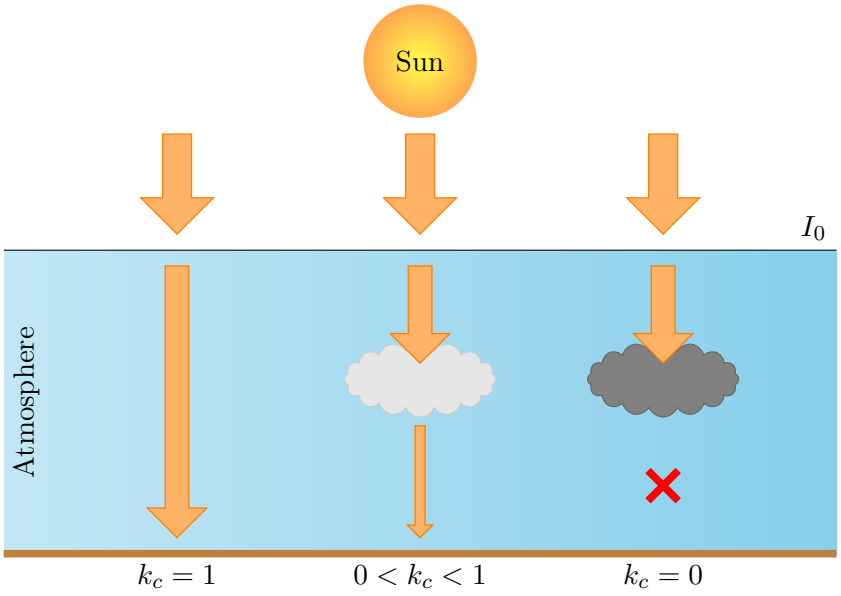

Figure 2.3: Clear-sky index presentation.

Equation (2.7) forms the base of many image-based solar irradiance forecast models: they exploit the division of DNI into a deterministic part, the clear-sky irradiance I_{CS}, and a stochastic part, the clear-sky index k_c. These models are presented in Section 2.2.4.

2.1.3 Solar irradiance components and measuring instruments

As seen in the previous sections, solar irradiance interacts with the atmosphere in various ways. The three resulting components are discussed in this section.

2.1.3.1 Direct normal irradiance

Direct normal irradiance (DNI), which is the direct irradiance received on a plane normal to the Sun [74], refers to photons that did not interact with the atmosphere on their way to the observer; thus DNI can be represented as [75]:

$$\mathrm{DNI}_{Sun} = 2\pi \int_0^{\xi_{Sun}} L(\xi) sin(\xi)\, d\xi \qquad (2.8)$$

where ξ is the solar disk angle ($\xi_{Sun} = 0.2666° \pm 1.7\%$) and L is the solar radiance measured in $\mathrm{W\,m^{-2}\,sr^{-1}}$.

As mentioned before, DNI is the most important component of solar irradiance for CSP systems. Furthermore, CSP systems' concentrators benefit also from the circumsolar region's irradiance [76, 77]. This sensitivity varies depending on the technology used [78] and the Sun's position. So, in order to unify the DNI measurements, the instruments measure DNI with an angle fixed by the world meteorological organization (WMO), $\xi_{\mathrm{WMO}} = 2.5°$, which is approximately 10 times more than ξ_{Sun} [79].

Various instruments can be found to measure DNI; they differ in accuracy, cost, and functionality. The most used instrument is the pyrheliometer (Figure 2.4), which is presented in the form of a tube whose dimensions define the opening angle. At the bottom, a thermopile is placed [80] in order to measure the direct solar irradiance. Since the pyrheliometer must be aligned with the Sun, a solar tracker is therefore necessary. Concerning the measurement's accuracy, it depends strongly on the instrument calibration and the maintenance [81, 82]. For a correctly calibrated and regularly maintained pyrheliometer, this uncertainty is around 2%. The device costs around 2500 € and the Sun tracker costs around 10 000 €.

Figure 2.4: Pyrheliometer installed on a solar tracker at the PROMES laboratory (Odeillo, France).

For this work, DNI is measured with a pyrheliometer (Kipp & Zonen CH1) and recorded by a low-voltage high-precision industrial ModBus data acquisition module (Gantner A4). Sun tracking is made by a 2-axis robot (Kipp & Zonen 2 GD) in open loop. In addition to periodic cleaning of the instruments, quality checks of the measurements are assured thanks to the simultaneous measurement of diffuse horizontal irradiance (see Section 2.1.3.2) and global horizontal irradiance (see Section 2.1.3.3) with pyranometers (Kipp & Zonen CMP21) equipped with ventilation units (see Figure 2.4). The available database is complete, without missing data (more information on the database used can be found in Section 3.3.1).

Less expensive alternatives can be found, such as the rotating shadowband irradiometer (RSI) (Figure 2.5). This instrument is equipped with a horizontally mounted photodiode

to measure the global horizontal irradiance. A rotating shadowband covers the photodiode periodically, to measure the diffuse horizontal irradiance, i.e. the global irradiance deprived of its direct component. From the measured global and diffuse irradiances, and the estimated Sun position, DNI can then be calculated. This instrument can provide measurements of the three solar irradiance components, unlike the pyrheliometer. This device does not require a 2-axis Sun tracker, which reduces the complexity of the system while improving its robustness. In addition, studies have shown that the RSI is significantly less susceptible to fouling than the pyrheliometer. It should be mentioned that the RSI is less expensive than the pyrheliometer, costing around 7000 €. On the other hand, a precise spectral calibration of the photodiode is necessary. This calibration is complex, resulting in a higher uncertainty than a pyrheliometer: typically close to 5%.

Figure 2.5: The RSI installed at the PROMES laboratory (Perpignan, France).

2.1.3.2 Diffuse horizontal irradiance

Diffuse horizontal irradiance (DHI) represents the irradiance that is not received directly from the Sun. In other words, it is the irradiance received by all other possible paths on a horizontal plane (scattering of the atmosphere, simple or multiple reflections with clouds, the atmosphere, the ground, or objects in the environment). DHI is usually measured with an irradiometer (equipped with a shading ball masking the Sun). It uses a thermopile to convert the solar flux into thermal flux and then into an electrical signal. The uncertainty for a properly calibrated irradiometer is about 3.2% [83].

2.1.3.3 Global horizontal irradiance

Global horizontal irradiance represents the total amount of shortwave irradiance received on a plane horizontal to the ground. GHI is a function of DNI and DHI:

$$\mathrm{GHI} = \mathrm{DNI} \cdot \cos(\mathrm{SZA}) + \mathrm{DHI} \tag{2.9}$$

where SZA is the Sun zenith angle.

GHI is usually measured by an irradiometer mounted horizontally, but other instruments are possible, like a sky imager [84].

2.2 Solar irradiance forecasting models

Solar irradiance forecasting is an important asset in the research and development of CSP systems. As seen before, it can help to develop predictive management and maintenance strategies, optimize the on-Sun time of the infrastructure users, and plan wisely the research experiments. Solar irradiance forecasts are characterized by their spatio-temporal resolution, especially since, depending on these time characteristics, some approaches are more appropriate than others. The temporal horizon of the forecast is the time between the current moment and the moment at which the forecast is desired. The temporal resolution corresponds to the sampling period of the forecast. On the other hand, the spatial horizon is related to the area over which the forecast is obtained. The spatial resolution corresponds to the spatial sampling of the forecast. The work done in this PhD thesis deals with spatially-localized DNI forecasting, with a temporal horizon H up to 30 min and a resolution of 30 s ($H = h \cdot T_s$, with T_s the data sampling time).

This section presents the classical DNI persistence models, followed by a review of clear-sky DNI models. Finally, a state-of-art of forecasting models is given[1].

2.2.1 Persistence models

This section presents the basic forecasting models: the classical persistence and the smart persistence models. They are considered in many works as the reference models, and can provide good results, depending on the forecast horizon and the DNI's variability.

2.2.1.1 Classical persistence model

This model is based on the simple supposition that DNI is not going to change between time k and time $k + h$:

$$\widehat{\mathrm{DNI}}(k+h) = \mathrm{DNI}(k) \tag{2.10}$$

where $\widehat{\mathrm{DNI}}$ is the forecast DNI value.

Of course, this model's performance degrades as the forecast horizon increases and when DNI presents high variability.

2.2.1.2 Smart persistence model

The smart persistence model is based on the supposition that the clear-sky index k_c is constant over the forecast horizon, between time k and time $k + h$. Using Equation (2.7), this index can be calculated as follows:

$$\mathrm{DNI}(k) = k_c(k) \cdot \mathrm{DNI}_{\mathrm{CS}}(k) \Longleftrightarrow k_c(k) = \frac{\mathrm{DNI}(k)}{\mathrm{DNI}_{\mathrm{CS}}(k)} \tag{2.11}$$

where $\mathrm{DNI}_{\mathrm{CS}}$ is the clear-sky DNI.

Now, DNI is forecast using a persistence on the clear-sky index k_c:

$$\widehat{\mathrm{DNI}}(k+h) = k_c(k) \cdot \widehat{\mathrm{DNI}}_{\mathrm{CS}}(k+h) = \frac{\mathrm{DNI}(k)}{\mathrm{DNI}_{\mathrm{CS}}(k)} \cdot \widehat{\mathrm{DNI}}_{\mathrm{CS}}(k+h) \tag{2.12}$$

The smart persistence model thus needs clear-sky DNI forecasts, which are provided by a clear-sky DNI model.

[1] Note that the scope is broadened to include both GHI and DNI forecasting models, since a large percentage of existing works is dedicated to GHI.

2.2.2 Clear-sky DNI models

Clear-sky DNI models allow to estimate DNI under clear-sky situations, i.e., in the absence of Sun-blocking clouds. The clear-sky DNI varies according to the angle between the Sun and the zenith (Sun zenith angle), the altitude of the site, and various atmospheric parameters. There is a vast choice of clear-sky models in the literature [85]. Clear-sky DNI can be calculated using either radiative or empirical models. Radiative models are usually derived from the Beer-Lambert law (Equation (2.3)). Although these models may be more accurate than empirical ones, they require inputs that might not be available. That is why the scientific community has focused on the development of accurate empirical models.

A practical approach is a model based on the polynomial of the cosine of the Sun zenith angle [86]:

$$\mathrm{DNI}_{\mathrm{CS}}(k) = \sum_{n=0}^{N} a_n \cos(\mathrm{SZA})^n \tag{2.13}$$

where SZA is the Sun zenith angle, and the coefficients a_n are calculated using the least-squares method.

Clear-sky DNI can also be modeled based on measurements, as presented in [87]:

$$\mathrm{DNI}_{\mathrm{CS}}(k) = I_0 0.7^{0.678m(k)} \tag{2.14}$$

where I_0 is the extraterrestrial solar irradiance, and m is the relative optical air mass.

This model can be improved by introducing the optical atmospheric turbidity coefficient, as follows:

$$\mathrm{DNI}_{\mathrm{CS}}(k) = I_0 \exp\left(-0.8662 m(k) \cdot \delta \cdot \mathrm{T}_{\mathrm{LI}}(k)\right) \tag{2.15}$$

where δ is the optical thickness of a clean and dry atmosphere (water- and aerosol-free), and T_{LI} is the Linke turbidity coefficient.

Eliminating the optical thickness δ from equation Equation (2.15), the clear-sky DNI can be expressed as follows [66]:

$$\mathrm{DNI}_{\mathrm{CS}}(k) = b I_0 \exp\left(-0.09 m(k)(\mathrm{T}_{\mathrm{LI}}(k) - 1)\right) \tag{2.16}$$

where b is a function of the considered site's altitude.

The clear-sky DNI model developed in [88], based on Equation (2.16), is utilised in this work. This decision is driven by the accurate estimations provided by the model as shown in Section 4.3. The clear-sky DNI forecast at time $k+h$ is given by:

$$\widehat{\mathrm{DNI}}_{\mathrm{CS}}(k+h) = b I_0 \exp\left(-0.09 \widehat{m}(k+h)(\widehat{\mathrm{T}}_{\mathrm{LI}}(k+h) - 1)\right) \tag{2.17}$$

where:

- b is calculated as follows:

$$b = 0.664 + 0.163 \exp\left(\frac{alt}{8000}\right) \tag{2.18}$$

  with alt the site's altitude;

- the forecast of the the Linke turbidity coefficient is given by a simple persistence: $\widehat{\mathrm{T}}_{\mathrm{LI}}(k+h) = \mathrm{T}_{\mathrm{LI}}(k)$, since its variation throughout the day is relatively small; the estimation of its value at time k is achieved using DNI measurements, as proposed by Nou et al. [88].

- $\widehat{m}(k+h)$ is the relative optical air mass forecast based on Equation (2.4).

2.2.3 Solar irradiance forecast models

The main approaches to forecast solar irradiance are statistical models, image-based models, and numerical weather prediction (NWP) models [63]. Each approach is characterised by a range of spatio-temporal horizons, as shown in Figure 2.6. In addition, the choice of the strategy is based on the purpose of the forecast. Statistical models can provide forecasts with high temporal resolutions and for long forecast horizons, but they are limited by low spatial capabilities. On the other hand, the NWP models, that solve weather equations to forecast irradiance, are characterised by very high spatio-temporal capability and are capable of handling long forecast horizons, but are highly dependent on the initial state of the variables used in the equations (which in turn requires accurate measurements with specific sensors that must be distributed wisely) and demand important computational resources for low forecast resolutions. Finally, image-based models provide high spatio-temporal resolution with less computational requirements[2] compared to the NWP models.

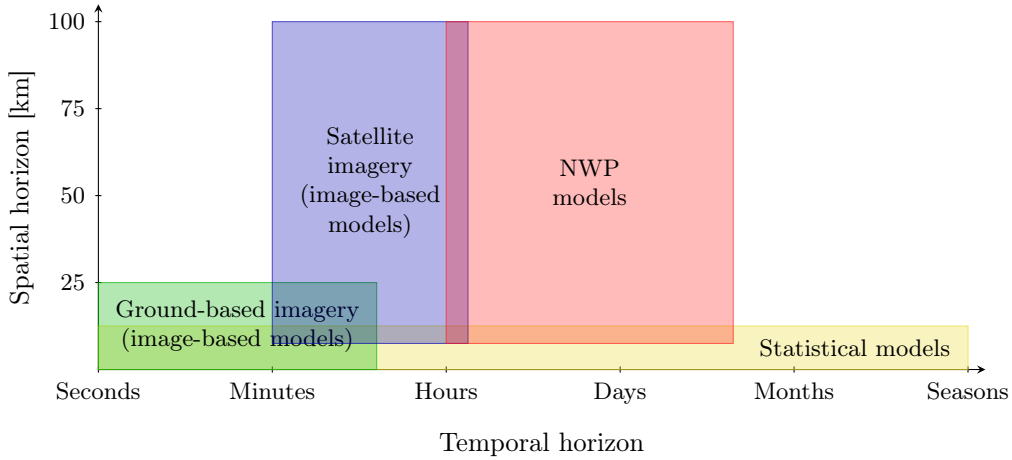

Figure 2.6: Approaches for solar resource forecasting, depending on spatio-temporal horizon (adapted from [89]).

As this work discusses DNI forecasting for forecast horizons less than 30 minutes, the focus will be on statistical and ground-based sky imagery models. A hybrid forecast model is developed, that can harness the advantages of both approaches. This model is compared to the smart persistence model and two machine-learning-based models using only past DNI observations as input.

2.2.4 Related work

In this section, a review of statistical and ground-based sky imagery approaches for intrahour solar resource forecasting is made. Even though we are interested in DNI forecasting, the scope is broadened here to include GHI, since a large percentage of existing works is dedicated to GHI. It should be mentioned that DNI forecasting is considered more complicated due to DNI's high variability: DNI can vary between its clear-sky value (the DNI value when no cloud is blocking the Sun) and zero in a matter of seconds, contrary to global irradiance, due to its diffuse component. Also, CSP technologies are much more affected by ramp events than photovoltaics, for example, making the accurate prediction of these events crucial. Nonetheless, studying approaches dedicated to GHI is interesting, since parts of the forecasting procedure can be similar.

[2]The complexity of image-based models depends on the code optimization and the type of algorithms implemented in the image processing steps.

Existing works can be divided according to the input data used (more details on the various references cited below can be found in Table 2.1).

- Solar resource measurements (and possibly other variables). Even if some classical time series approaches are employed, most of the recent works are statistical models based on machine learning tools [90, 91, 92, 93]. These models can predict the solar resource for horizons ranging from a few minutes to several days. However, as they are purely based on past observations, these models usually fail at accurately predicting ramp events (sudden variations).

- Ground-based sky images and solar resource measurements (and possibly other variables). For these models, the forecast horizon is greatly reduced, generally culminating at 30 min: indeed, the information contained in sky images becomes limited as we approach their frame bounds. However, using sky images allows to predict how the atmospheric disturbances will affect the solar resource, which in turn can lead to accurate prediction of ramp events. The solar resource forecast generally consists of three major steps: first, images are acquired and processed in order to detect clouds (the state-of-the-art study justifying the proposed segmentation model is presented in Section 4.4.3); second, cloud motion is estimated (the state-of-the-art study supporting the chosen clouds motion estimation algorithm is conducted in Section 4.4.4); finally, based on that knowledge and possibly other measurements, features are extracted in order to perform the forecast. In particular, that last step can involve using a clear-sky model (discussed in Section 2.2.2) [94, 95, 86, 96, 97]. Indeed, direct normal irradiance can be divided into the clear-sky DNI ($\mathrm{DNI_{CS}}$) and the clear-sky index (k_c), as shown in Equation (2.7). The clear-sky DNI can be viewed as a deterministic component that can be removed to focus on the stochastic part of DNI, the clear-sky index k_c. Finally, the estimated cloud motion can also be used to generate an artificial image that would have been obtained at the considered forecast horizon [98].

  Needless to say, there exists models that do not follow the same steps exactly. Solutions with no flow estimation nor clouds identification, relying solely on their ability to learn from features extracted from measured solar resource and sky images can be found: for example, a nearest-neighbour approach [99] and models based on neural networks [100]. However, using the whole sky image may not lead to the best results: even if cloud detection and especially cloud motion estimation are hard to perform accurately, it can provide pivotal information, as it allows to determine regions of interest in sky images that will interact with the Sun after the considered forecast horizon.

In this work, high dynamic range (HDR) images provided by a sky imager [101] are fed to a machine-learning-based model, which is used to accurately detect the clouds without losing critical information near the Sun. Then, the dominant cloud motion is estimated with an optical flow algorithm and clustering. An adaptive approach is then used to determine a region of interest (ROI), that may contain Sun-blocking clouds after the considered forecast horizon. All these informations are then fed to a complex artificial neural network model. The developed approach is designed to be able to forecast DNI ramps and to be robust to different kinds of clouds. The proposed model is specifically designed to handle complex sky situations with high DNI variability, but it can also handle less-complicated situations (clear-sky and overcast situations). These topics are some of the difficulties that most models struggle with. This model is compared to the smart persistence model as well as two recurrent neural networks that use past DNI observations only. The first model is based on long short-term memory layers, and the second is based on the combination of long short-term memory layers and convolutional layers.

Table 2.1: Statistical and ground-based sky imagery approaches to intrahour forecasting of global horizontal irradiance (GHI) or direct normal irradiance (DNI).

Ref.	Input variables	Output variables	Forecast horizons	Forecasting method	Clear-sky model?
[90]	GHI	GHI	Up to 72 h	A dense neural network that takes the clear-sky index and the difference between GHI and the clear-sky GHI as input.	Yes
[91]	GHI	GHI	Up to 4 h	A recurrent neural network that takes past DNI observations as input and performs multi-horizon forecasts.	No
[92]	GHI	GHI	Up to 2.5 h	A long short-term memory (LSTM) neural network that takes past DNI observations as input and performs GHI forecasts for a specific horizon.	No
[93]	GHI	GHI	Up to 10 days	Recurrent neural networks (LSTM, bi-directional LSTM, gated recurrent unit, convolutional neural network) that take past DNI observations as input and perform GHI forecasts for a specific horizon.	No
[94]	GHI, sky image	GHI	1 min to 10 min	Estimated cloud motion is used to predict an image corresponding to the clouds' position after the forecast horizon; GHI is forecast based on the predicted image.	Yes
[95]	DNI, sky image	DNI	5 min and 10 min	The cloud fraction is calculated based on cloud motion; DNI is forecast using a neural network (based on the variability of DNI) that combines the clear-sky DNI value and the cloud fraction.	Yes
[86]	Sky image, Sun zenith angle	DNI	1 min to 20 min	The cloud fraction is calculated based on the clouds' tracking algorithm; DNI is forecast using Equation (2.7).	Yes
[96]	DNI, sky image	DNI	3 min to 15 min	The cloud fraction is calculated based on cloud motion; DNI is forecast using Equation (2.7).	Yes
[97]	GHI, sky image	GHI	1 min to 10 min	The cloud fraction is calculated based on cloud motion, and then averaged with the clear-sky ratio of the last 5 min; GHI is forecast using Equation (2.7).	Yes
[98]	GHI, sky image	GHI	15 min	Recreate an image corresponding to the forecast clouds' position after 15 min; that new image and GHI measurements are inputs of an artificial neural network that performs the forecasts.	No
[99]	GHI or DNI, sky image	GHI and DNI	5 min to 30 min	k-nearest-neighbour model with different features manually extracted from the sky image, DNI, or GHI.	No
[100]	GHI, sky image	GHI	1 min to 5 min	An artificial neural network that takes features extracted from the sky image (from the region near the sun only) with the lagged GHI values as input and performs multi-horizon forecasts.	No

2.2.5 Performance metrics and hardware description

1. The root mean squared error (RMSE) is calculated as follows:

$$\mathrm{RMSE} = \sqrt{\frac{1}{n_{obs}} \sum_{k=1}^{n_{obs}} \left(\mathrm{DNI}(k) - \widehat{\mathrm{DNI}}(k)\right)^2} \tag{2.19}$$

where n_{obs} is the number of observations, DNI is the measured DNI and $\widehat{\mathrm{DNI}}$ is the predicted DNI.

2. The normalized root mean squared error (nRMSE) is calculated as follows:

$$\mathrm{nRMSE} = \frac{\sqrt{\frac{1}{n_{obs}} \sum_{k=1}^{n_{obs}} \left(\mathrm{DNI}(k) - \widehat{\mathrm{DNI}}(k)\right)^2}}{\frac{1}{n_{obs}} \sum_{k=1}^{n_{obs}} \mathrm{DNI}(k)} \tag{2.20}$$

where n_{obs} is the number of observations, DNI is the measured DNI and $\widehat{\mathrm{DNI}}$ is the forecast DNI.

3. The skill factor (SF) is employed to evaluate the models' performance versus the smart persistence model; it is defined as:

$$\mathrm{SF} = 100 \cdot \left(1 - \frac{\mathrm{nRMSE_M}}{\mathrm{nRMSE_{PE}}}\right) \tag{2.21}$$

where $\mathrm{nRMSE_M}$ and $\mathrm{nRMSE_{PE}}$ are the nRMSE of the proposed model and the persistence model, respectively.

A positive skill factor means that the proposed model outperforms the persistence model.

4. The mean average error (MAE) is calculated as follows:

$$\mathrm{MAE} = \frac{1}{n_{obs}} \sum_{k=1}^{n_{obs}} \left(\mathrm{DNI}(k) - \widehat{\mathrm{DNI}}(k)\right) \tag{2.22}$$

where n_{obs} is the number of observations, DNI is the measured DNI and $\widehat{\mathrm{DNI}}$ is the predicted DNI.

5. Finally, a metric called the ramp detection index (RDI) is used [102]. It is designed to evaluate the ability of the model to predict ramps, which have an important impact on CSP plants: predicting them can thus be helpful in the control process. First, the ramp magnitude (RM) is calculated as:

$$\mathrm{RM}(k) = \frac{|\mathrm{DNI}(k) - \mathrm{DNI}(k+h)|}{\widehat{\mathrm{DNI}}_{\mathrm{CS}}(k)} \tag{2.23}$$

where $\widehat{\mathrm{DNI}}_{\mathrm{CS}}$ is the estimated clear-sky DNI.

Usually, high-magnitude ramps are defined by $\mathrm{RM}(k) > 0.5$ and moderate ramps by $0.3 < \mathrm{RM}(k) < 0.5$. A ramp detection (also called a '*hit*') is achieved if both the following conditions are satisfied:

$$\mathrm{RM}(k) > 0.15 \tag{2.24}$$

$$\mathrm{sign}(\mathrm{DNI}(k) - \widehat{\mathrm{DNI}}(k+h)) = \mathrm{sign}(\mathrm{DNI}(k) - \mathrm{DNI}(k+h)) \tag{2.25}$$

where $\widehat{\text{DNI}}$ and DNI are the forecast and measured DNI, respectively. The chosen RM value represents ramps with high occurrence probability, thus increasing the challenge of scoring high RDI by increasing the number of considered ramps in the RDI calculation. The ramp is not detected (a '*miss*') if Equation (2.24) is met while Equation (2.25) is not. Finally, the RDI is calculated as:

$$\text{RDI} = \frac{N_{hit}}{N_{hit} + N_{miss}} \tag{2.26}$$

where N_{hit} and N_{miss} are the numbers of hits and misses, respectively.

All the developments made during this work have been conducted with a computer with 32 GB of rapid access memory (RAM), with an Intel Xeon E-2146G @3.50 GHz as the central processing unit (CPU) and a Nvidia Quadro P620 18 GB as the graphical processing unit (GPU).

Chapter 3

Recurrent neural network models

3.1 Introduction to recurrent neural networks

Artificial neural networks, or neural networks, are a subset of machine learning. They are composed of an input layer, one or more hidden layers, and an output layer. These layers contain nodes (or neurons) which are connected to other nodes, mimicking the interaction between biological neurons. Each node, defined by its weights and bias, is optimized to minimize the error between the network output (the prediction) and the target, based on a certain loss function. This optimization process is done by processing a set of observations containing different inputs and target outputs over multiple epochs. This approach is known as supervised learning. Various architectures can be found, such as the multi-layer perceptron neural networks [103], the convolutional neural networks [104], the recurrent neural networks [105], etc. In this chapter, the developed models are two recurrent neural networks.

Recurrent neural networks (RNN) refer to a class of artificial neural networks where a memory-state is added to the neurons. This memory-state allows the network to exhibit a temporal dynamic behavior, thus allowing to process input sequences of variable lengths. This kind of network is employed when the output is related to past inputs, such as:

- time series analysis, these models can forecast time series, as shown in Section 2.2.4, or detect anomalies in time series [106, 107]. They showed excellent understanding of the temporal aspect of time series;
- natural language processing, they are used for machine translation [108] and sentiment analysis [109], where they proved their effectiveness in treating and handling text.

Several types of RNN can be found, such as:

- one to one: similar to a classical neural network with one input and one output;
- one to many: takes one input that propagates in the RNN cells to provide multiple outputs. It can be used for music generation, for example [110];
- many to one: takes multiple inputs and provides only one output, it is used for sentiment classification [111] or time series forecasting;
- many to many: takes multiple inputs and outputs, it is used for time series forecasting or machine translation [112]. It should be mentioned that the output's dimension can be different from the input's dimension.

Multiple RNN variants can also be found, such as the bi-directional RNN, where the information in the network flows in different directions. For example, a sentence like "I love my thesis" is processed simultaneously in the forward sense ("I", "love", "my", and "thesis") and

in the backward sense ("thesis", "my", "love", and "I"). This allows the network to use inputs from the past and future simultaneously. This variant is generally used for natural language processing applications. Another popular variant is the long short-term memory (LSTM) neural network which is used to overcome the exploding or vanishing gradient problems (see Section 3.2.1). It should be mentioned that these networks are computationally complex; to improve this aspect, a graphics processing unit (GPU) can be used to train and run the network, drastically reducing the computational time [113].

3.2 Presentation of the proposed models

Based on RNN networks' great success in the forecasting of time series, two of these networks are optimized and implemented for DNI forecasting. As the smart persistence model, these statistical models will serve as reference models to be compared with the image-based model presented in Chapter 4. These models are:

- a deep LSTM network (Section 3.2.1) with several layers containing LSTM units;
- a deep LSTM network preceded by a convolutional layer (Section 3.2.2), used as a pre-processing layer to help the LSTM layers learn better.

Both these models take past DNI observations as input (the number of past observations has to be optimized).

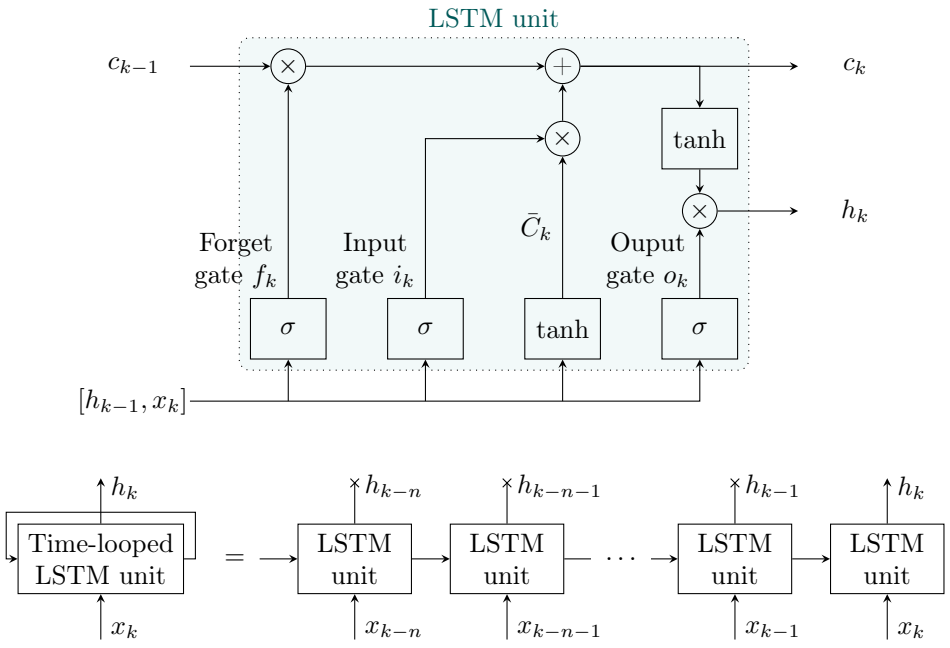

Figure 3.1: Above: a LSTM unit defined by its three main gates (forget, input, and output gates); $\bar{C}_k$ is the current candidate state, h_k is the current hidden state, and x_k is the current state. Below: an unfolded time-looped LSTM unit.

3.2.1 LSTM model

The first proposed model is based on a LSTM network. It consists of multiple layers of LSTM units (see Figure 3.1), followed by a fully connected layers combining the output of the LSTM layers, in order to perform the forecast (see Figure 3.2). The LSTM units are used to face both the common exploding-gradient and vanishing-gradient problems [114], and can be divided

into three main parts: the 'forget gate' f_k, responsible for the portion of data to be ignored; the 'input gate' i_k, which updates the status of the unit based on the current state x_k and the previous hidden state h_{k-1}; finally, the 'output gate' o_k, which determines the current hidden state h_k, that is used for the computation of the unit's status for the next time step.

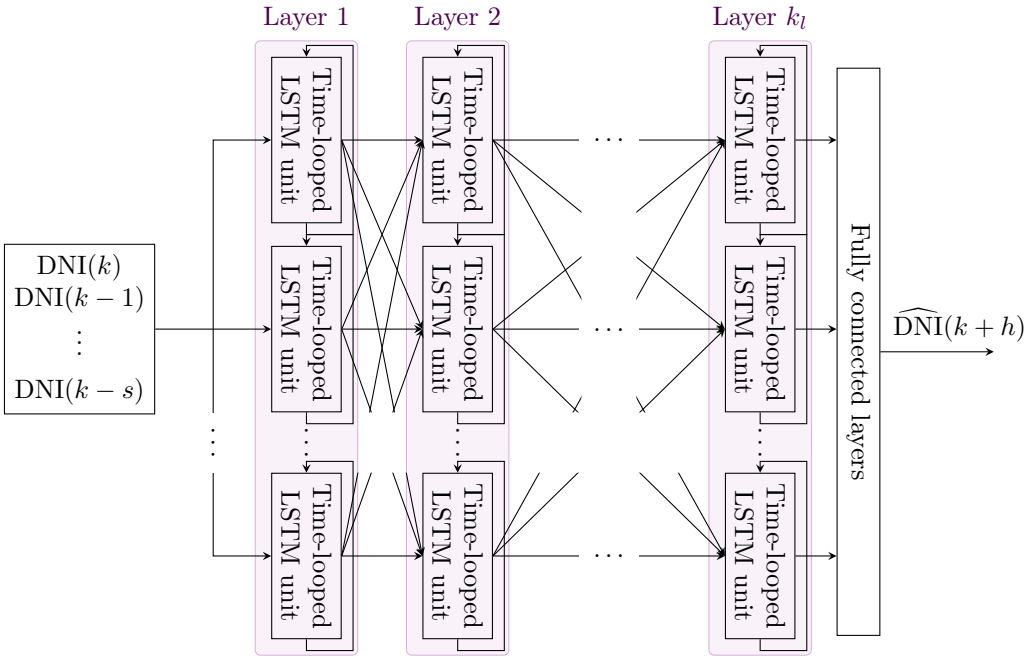

Figure 3.2: LSTM model structure with k_l LSTM layers followed by fully connected layers, taking past DNI observations as time-support, and providing a DNI forecast at time $k+h$.

At time k, a LSTM unit is characterized by:

$$f_k = \sigma(W_f \cdot [h_{k-1}, x_k] + b_f) \tag{3.1}$$
$$i_k = \sigma(W_i \cdot [h_{k-1}, x_k] + b_i) \tag{3.2}$$
$$o_k = \sigma(W_o \cdot [h_{k-1}, x_k] + b_o) \tag{3.3}$$
$$\bar{C}_k = \tanh(W_c \cdot [h_{k-1}, x_k] + b_c) \tag{3.4}$$
$$C_k = i_k \bar{C}_k + f_k C_{k-1} \tag{3.5}$$
$$h_k = o_k \cdot \tanh(C_k) \tag{3.6}$$

where σ is the sigmoid activation function, W_f, W_i, W_o, and W_c are the weight matrices, b_f, b_i, b_o, and b_c are the bias vectors, and $\bar{C}_k$ represents the current candidate state, calculated from the previous hidden state and the current input.

The proposed LSTM model takes a vector of past DNI observations (of predefined dimension n) as input, called time-support, and predicts DNI at time $k+h$, with $H = h \cdot T_s$. The neural network is thus characterized by:

- the number of LSTM layers and the number of units per LSTM layer;
- the number of fully connected layers and the number of units per fully connected layer;
- the dimension of the time-support (the number of past observations in the input vector);
- the activation function of the units in the fully connected layers.

It should be mentioned that output of a neuron in the fully connected layers can be written as

follows:

$$y(x, w) = f\left(\sum_{i=1}^{d} w_i x_i + b\right) \tag{3.7}$$

where f is the activation function, w and x are the vectors of the weights and inputs from the d neurons of the previous layer, and b is the bias. These parameters are estimated during the training phase. How these characteristics are obtained is detailed in Section 3.3.3.

3.2.2 CNN-LSTM model

The second proposed model is a CNN-LSTM network consisting of a convolutional layer, serving as a preprocessing step in order to extract features to facilitate DNI forecasting [115], LSTM layers and fully connected layers (see Figure 3.3). The model predicts DNI at time $k+h$, with $H = h \cdot T_s$. The convolutional layer performs a dot product of the convolution kernel: as this kernel slides along the input matrix, the convolution operation generates a feature map, which becomes the input of the next layer. Thus, this layer is characterized by the number and dimension of the filters. The LSTM and fully connected layers are characterized as described in Section 3.2.1. This type of network is used when there is a spatial structure in the input, as in an image, or when there is a temporal structure in the input, such as a sequence of images (video) or values (time series). It can also be used when the output possesses a temporal structure, such as in multi-horizon time series forecast models.

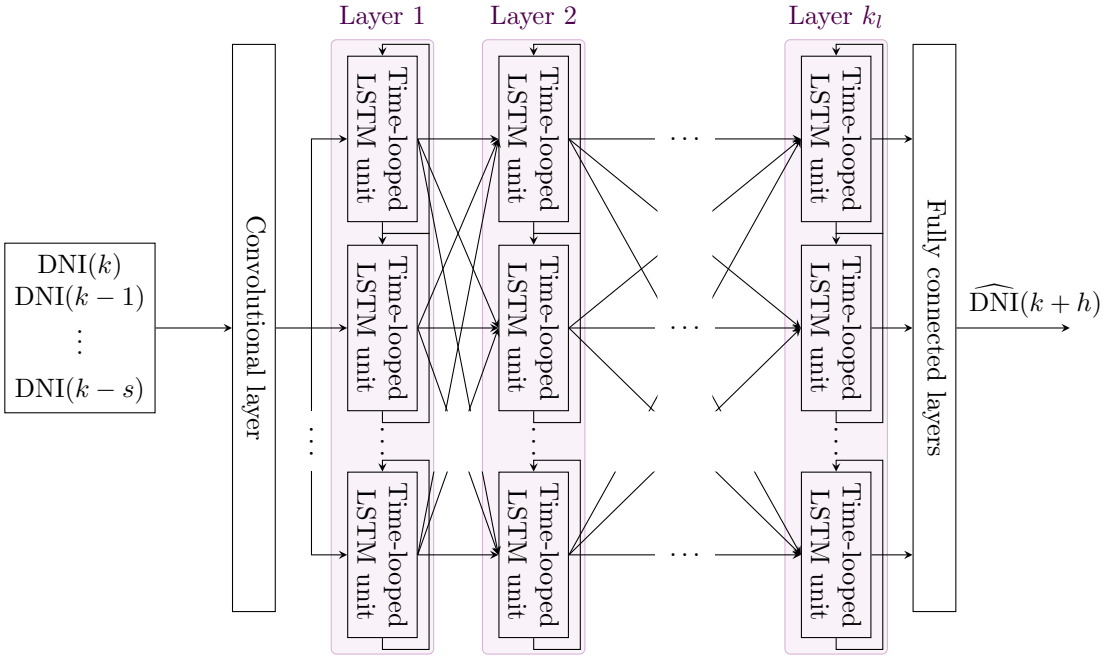

Figure 3.3: CNN-LSTM model structure, taking past DNI observations as time-support, and providing a DNI forecast at time $k+h$. The network consists of a convolutional layer, k_l LSTM layers, and fully connected layers.

3.3 RNN models implementation

3.3.1 Database presentation

The database consists of DNI measurements obtained with a pyrheliometer at the PROMES-CNRS laboratory in Odeillo (see Figure 2.4), where DNI variability is high. The measurements

cover 373 days, from 7:00 AM to 5:00 PM, with a sampling time T_s of 30 seconds[1], resulting in 1200 observations for each day. DNI is measured with a pyrheliometer (Kipp & Zonen CH1), recorded by a low-voltage high-precision industrial ModBus data acquisition module (Gantner A4). Sun tracking is made by a 2-axis robot (Kipp & Zonen 2 GD) in open loop. In addition to periodic cleaning of the instruments, quality checks of the measurements are assured thanks to the simultaneous measurement of DHI and GHI with pyranometers (Kipp & Zonen CMP21) equipped with ventilation units. The available database is complete, without missing data.

To gain some insight into the 373 days of the database, DNI profiles are classified using the following criteria:

- clear-sky situation: if the measured DNI is within 10% of the corresponding clear-sky DNI value for 90% of the day;
- overcast situation: if the measured DNI is less than 60% of its clear-sky value for 90% of the day, and if the mean DNI variation is less than 20 $\mathrm{W\,m^{-2}}$;
- mixed situation: otherwise; please note that these days can thus be partially clear-sky or partially overcast.

The results of this classification reveals 128 clear-sky days (34.4%), 49 overcast days (13.1%) and 196 days with mixed situations (52.5%). Examples of these three DNI profiles are given in Figure 3.4.

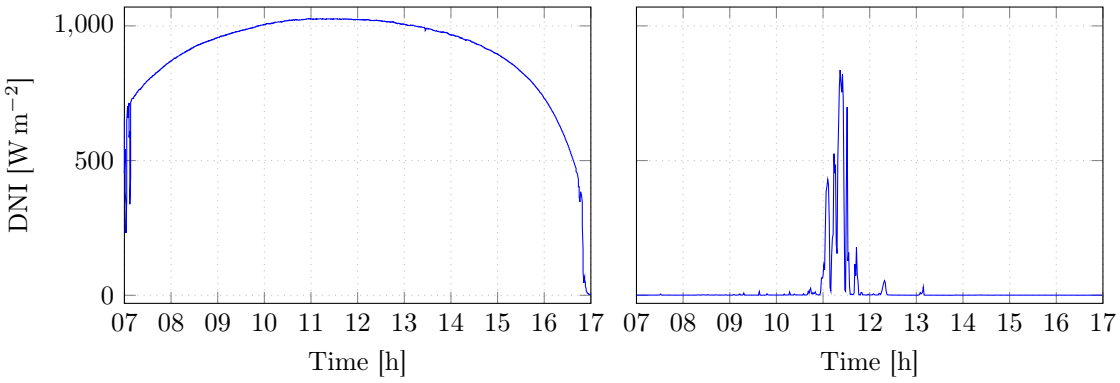

(a) Clear-sky situation. (b) Overcast situation.

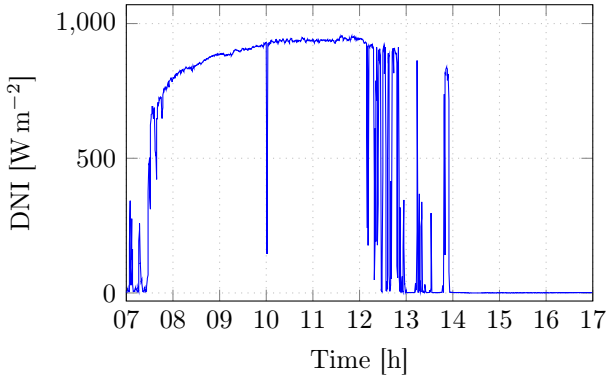

(c) Mixed situation.

Figure 3.4: Example of a clear-sky situation, an overcast situation, and a mixed situation, observed at the PROMES laboratory (Odeillo, France).

[1]The DNI sampling time is set to 30 s because the sky imager used for the development of the hybrid model registers an image every 30 s (see Section 4.2).

From a forecasting point of view, the mixed situations are the most interesting, as they are not only more frequent, but also possess a higher DNI variability than the other two situations, which increases the complexity of forecasting. To assess the DNI variability during these mixed situations, ΔDNI and the mean ($\mu_{\Delta\text{DNI}}$) and standard ($\sigma_{\Delta\text{DNI}}$) deviation of DNI variations are introduced:

$$\Delta\text{DNI}(k) = |\text{DNI}(k) - \text{DNI}(k+h)| \tag{3.8}$$

$$\mu_{\Delta\text{DNI}} = \frac{1}{n_{obs}} \sum_{k=1}^{n_{obs}} \Delta\text{DNI}(k) \tag{3.9}$$

$$\sigma_{\Delta\text{DNI}} = \sqrt{\frac{1}{n_{obs}} \sum_{k=1}^{n_{obs}} (\Delta\text{DNI}(k) - \mu_{\Delta\text{DNI}})^2} \tag{3.10}$$

where n_{obs} is the number of DNI observations.

In addition, the normalized ramp count (nRC), equal the number of DNI variations greater than 100 W m^{-2} over the total number of DNI observations, is computed. The result of the calculation of these values for the 196 days in the mixed situation dataset is given in Table 3.1 for each forecast horizon H.

Table 3.1: Variability analysis for the 196 days in the mixed situation dataset. $\mu_{\Delta\text{DNI}}$ and $\sigma_{\Delta\text{DNI}}$ are the mean and standard deviation of DNI variations, respectively, and nRC is the normalized ramp count.

Metric	Forecast horizon H [min]					
	5	10	15	20	25	30
$\mu_{\Delta\text{DNI}}$ [W m^{-2}]	92.5	117.7	133	147	158	170
$\sigma_{\Delta\text{DNI}}$ [W m^{-2}]	177.47	203.96	217.39	228.32	236.51	245.21
nRC	0.23	0.28	0.31	0.33	0.35	0.37

Table 3.2: Variability analysis for the 34 mixed situations in the training and validation dataset, and in the test dataset. $\mu_{\Delta\text{DNI}}$ and $\sigma_{\Delta\text{DNI}}$ are the mean and standard deviation of DNI variations, respectively, and nRC is the normalized ramp count.

Dataset	Metric	Forecast horizon H [min]					
		5	10	15	20	25	30
Training and validation	$\mu_{\Delta\text{DNI}}$ [W m^{-2}]	86.00	116.41	135.28	150.47	162.98	174.13
	$\sigma_{\Delta\text{DNI}}$ [W m^{-2}]	179.72	215.79	234.63	247.26	257.04	265.83
	nRC	0.20	0.24	0.27	0.30	0.31	0.33
Test	$\mu_{\Delta\text{DNI}}$ [W m^{-2}]	101.30	132.84	154.48	170.73	179.62	187.63
	$\sigma_{\Delta\text{DNI}}$ [W m^{-2}]	189.86	221.44	239.07	250.90	255.58	260.82
	nRC	0.25	0.32	0.35	0.38	0.40	0.41

The high mean and standard deviation of DNI variations obtained shows the high variability of the mixed situations appearing in Odeillo, especially for long forecast horizons. These characteristics explain why state-of-the-art models usually struggle with these complex situations, and why persistence models fail to provide acceptable results. Based on this analysis, the training and validation databases used to develop the RNN models and the hybrid model (developed in Chapter 4) are taken from the mixed situation profiles: 22 days

(representing 26400 observations) from different seasons have been selected. The test dataset, however, contains 18 days (representing 21600 observations), with 12 mixed situations, 3 overcast situations, and 3 clear-sky situations. To make sure that the mixed situations in those datasets still have the same DNI variability, the previous variability analysis has been performed on these 34 days; the results are found in Table 3.2.

Both the LSTM and the CNN-LSTM networks are trained and validated using a cross-validation technique: the training dataset is randomly but equally divided into five groups of samples called folds; in each fold 70% of data is used for training and 30% for validation. Adaptive moments (Adam), a computationally-efficient stochastic gradient descent optimization method based on an adaptive estimation of the momentum [116], is used. To prevent overfitting, dropout regularization is performed for each layer in the network with a rate of 50% [117]. The loss function is chosen to be the mean squared error over the mean average error. Finally, the models are trained using 20 epochs for each fold where convergence is assured. The networks are trained with the computer described in Section 2.2.5, using TensorFlow - Keras (graphical processing unit-aided version).

3.3.2 Performance metrics

Three performance metrics are used here to evaluate the models:

1. the normalized root mean squared error (nRMSE);
2. the skill factor (SF);
3. the ramp detection index (RDI).

The reader is referred to Section 2.2.5 for a detailed description of these metrics.

3.3.3 RNN models optimization and evaluation

As mentioned before, the LSTM and the CNN-LSTM models use past DNI observations as input. As a consequence, the dimension of the time-support vector has to be optimized for each forecast horizon. The networks' optimal topology has also to be found. In order to determine it, various networks with different numbers of layers and units have been trained for each time-support with the help of an optimization framework [118]. Similar results have been obtained for time-supports up to 8 min, after what a deterioration has been observed. For clarity's sake, the results for time-supports up to 4.5 min only are given in the sequel.

3.3.3.1 LSTM model

The optimized LSTM networks' topology, for each forecast horizon and each time-support, are given in Table 3.3. SF and nRMSE values for mixed situations are presented in Figure 3.5. These values should be both analyzed to compare different models and different datasets. It should be noted that since nRMSE level depends deeply on the DNI variability of the studied dataset, then scoring lower nRMSE values does not always imply superior performance, that's why the SF metric is introduced. In addition, SF provides a clear comparison with the smart persistence model. Based on the lower nRMSE and the higher SF score on the test dataset (see Figure 3.5), it can be seen that the optimal dimension of the time-support depends on the forecast horizon H:

- for $H = 5$ min, the best time-support is 3.5 min (i.e., $s = 7$);
- for $H = 10$ min, the best time-support is 2.5 min (i.e., $s = 5$);
- for $H = 15$ min, the best time-support is 2.5 min (i.e., $s = 5$);

Table 3.3: Optimal LSTM networks' topology for each forecast horizon H and each time-support.

H [min]	Time-support [min]	Number of units					
		LSTM layers					Fully connected layer
		1st	2nd	3rd	4th	5th	
5	1.5	166	108	166	∅	∅	1
	2.0	52	72	146	232	240	1
	2.5	29	54	∅	∅	∅	1
	3.0	230	180	∅	∅	∅	1
	3.5	116	10	246	208	∅	1
	4.0	24	42	∅	∅	∅	1
	4.5	54	204	54	179	∅	1
10	1.5	194	216	156	54	144	1
	2.0	116	242	∅	∅	∅	1
	2.5	104	54	4	154	∅	1
	3.0	32	134	136	∅	∅	1
	3.5	156	28	132	∅	∅	1
	4.0	24	42	∅	∅	∅	1
	4.5	54	154	79	229	∅	1
15	1.5	232	32	186	218	14	1
	2.0	102	4	28	6	250	1
	2.5	136	40	90	24	∅	1
	3.0	14	90	73	122	∅	1
	3.5	136	40	90	24	∅	1
	4.0	104	29	104	229	∅	1
	4.5	104	254	∅	∅	∅	1
20	1.5	129	104	54	∅	∅	1
	2.0	29	104	254	∅	∅	1
	2.5	104	29	129	170	∅	1
	3.0	104	79	154	254	∅	1
	3.5	54	4	∅	∅	∅	1
	4.0	179	154	129	179	∅	1
	4.5	104	204	79	229	∅	1
25	1.5	129	79	154	4	254	1
	2.0	154	54	∅	∅	∅	1
	2.5	54	154	∅	∅	∅	1
	3.0	54	154	79	229	∅	1
	3.5	129	54	104	104	∅	1
	4.0	54	4	∅	∅	∅	1
	4.5	54	204	54	179	∅	1
30	1.5	129	204	179	∅	∅	1
	2.0	79	229	204	∅	∅	1
	2.5	29	229	154	254	∅	1
	3.0	179	154	4	154	129	1
	3.5	129	204	104	∅	∅	1
	4.0	29	104	254	∅	∅	1
	4.5	154	54	∅	∅	∅	1

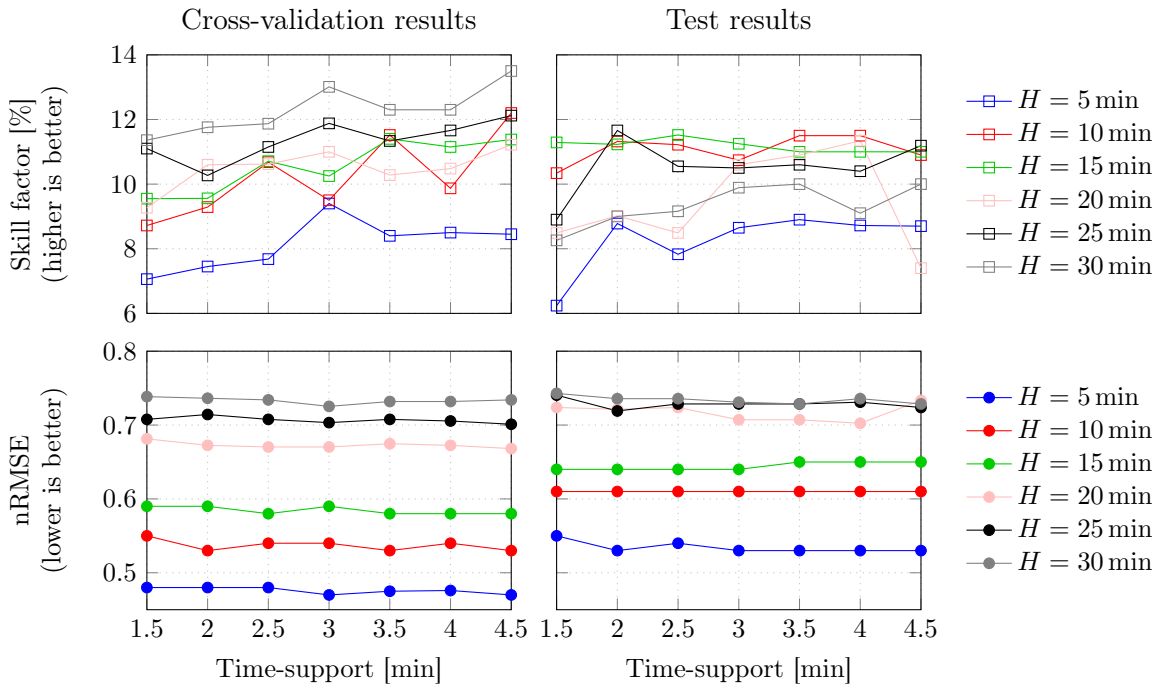

Figure 3.5: LSTM model results: nRMSE and SF values as a function of the time-support.

- for $H = 20\,\text{min}$, the best time-support is $4\,\text{min}$ (i.e., $s = 8$);
- for $H = 25\,\text{min}$, the best time-support is $2\,\text{min}$ (i.e., $s = 4$);
- for $H = 30\,\text{min}$, the best time-support is $3.5\,\text{min}$ (i.e., $s = 7$).

When taking the best LSTM model per forecast horizon, the SF ranges between 10% and 11.7%. It should be noted that a slight increase in SF is observed as the horizon increases, which is caused by the degrading performance of the persistence model for long horizons (except for $H = 30\,\text{min}$, where the LSTM model's performance degrades as well).

3.3.3.2 CNN-LSTM model

The best CNN-LSTM networks' topology obtained after optimization, for each forecast horizon and each time-support, is given in Table 3.4. SF and nRMSE values for mixed situations are presented in Figure 3.6. Based on the lower nRMSE and the higher SF score on the test dataset (see Figure 3.6), it can be seen that the optimal dimension of the time-support depends on the forecast horizon H:

- for $H = 5\,\text{min}$, the best time-support is $2.5\,\text{min}$ (i.e., $s = 5$);
- for $H = 10\,\text{min}$, the best time-support is $3.5\,\text{min}$ (i.e., $s = 7$);
- for $H = 15\,\text{min}$, the best time-support is $3\,\text{min}$ (i.e., $s = 6$);
- for $H = 20\,\text{min}$, the best time-support is $3.5\,\text{min}$ (i.e., $s = 7$);
- for $H = 25\,\text{min}$, the best time-support is $4\,\text{min}$ (i.e., $s = 8$);
- for $H = 30\,\text{min}$, the best time-support is $2.5\,\text{min}$ (i.e., $s = 5$).

When taking the best CNN-LSTM model per forecast horizon, the SF ranges between 10% and 12%.

Table 3.4: Optimal CNN-LSTM networks' topology for each forecast horizon H and each time-support.

H [min]	Time-support [min]	Number of units							
		CNN layer	LSTM layers				Fully connected layers		
			1st	2nd	3rd	4th	1st	2nd	3rd
5	1.5	175	8	16	16	∅	50	25	10
	2.0	50	48	96	96	32	10	∅	∅
	2.5	75	104	129	54	∅	50	25	∅
	3.0	126	204	104	229	∅	50	25	∅
	3.5	76	154	29	79	254	50	25	∅
	4.0	126	154	204	∅	∅	50	25	∅
	4.5	76	154	104	179	∅	5	20	∅
10	1.5	176	204	254	29	∅	50	25	∅
	2.0	150	8	32	32	32	25	10	∅
	2.5	176	129	29	104	∅	50	25	∅
	3.0	76	229	79	104	∅	50	25	∅
	3.5	151	54	54	104	∅	50	25	∅
	4.0	151	79	79	∅	∅	50	25	∅
	4.5	101	29	179	79	229	20	5	∅
15	1.5	76	154	104	254	∅	50	25	∅
	2.0	126	179	129	20	229	50	25	∅
	2.5	126	229	204	179	229	50	25	∅
	3.0	26	204	54	104	79	50	25	∅
	3.5	126	254	154	154	∅	50	25	∅
	4.0	151	54	129	254	∅	50	25	∅
	4.5	126	79	104	∅	∅	20	5	∅
20	1.5	51	54	179	54	∅	5	5	5
	2.0	76	54	4	279	∅	20	20	5
	2.5	176	204	104	104	∅	5	20	∅
	3.0	51	229	229	∅	∅	5	5	∅
	3.5	26	204	104	204	∅	5	20	∅
	4.0	176	204	104	204	∅	5	20	∅
	4.5	104	204	79	229	∅	1	∅	∅
25	1.5	51	229	299	∅	∅	5	5	∅
	2.0	51	204	254	∅	∅	5	20	5
	2.5	101	54	4	154	∅	20	20	∅
	3.0	51	4	54	129	79	5	5	5
	3.5	126	179	179	79	204	20	20	∅
	4.0	176	104	254	∅	∅	20	20	20
	4.5	54	204	54	179	∅	1	∅	∅
30	1.5	101	29	179	229	54	20	5	∅
	2.0	126	54	204	54	∅	20	20	5
	2.5	126	54	129	254	54	5	5	∅
	3.0	51	229	299	∅	∅	5	5	∅
	3.5	176	104	254	∅	∅	20	20	20
	4.0	26	79	204	4	29	5	5	∅
	4.5	76	129	179	29	∅	20	20	20

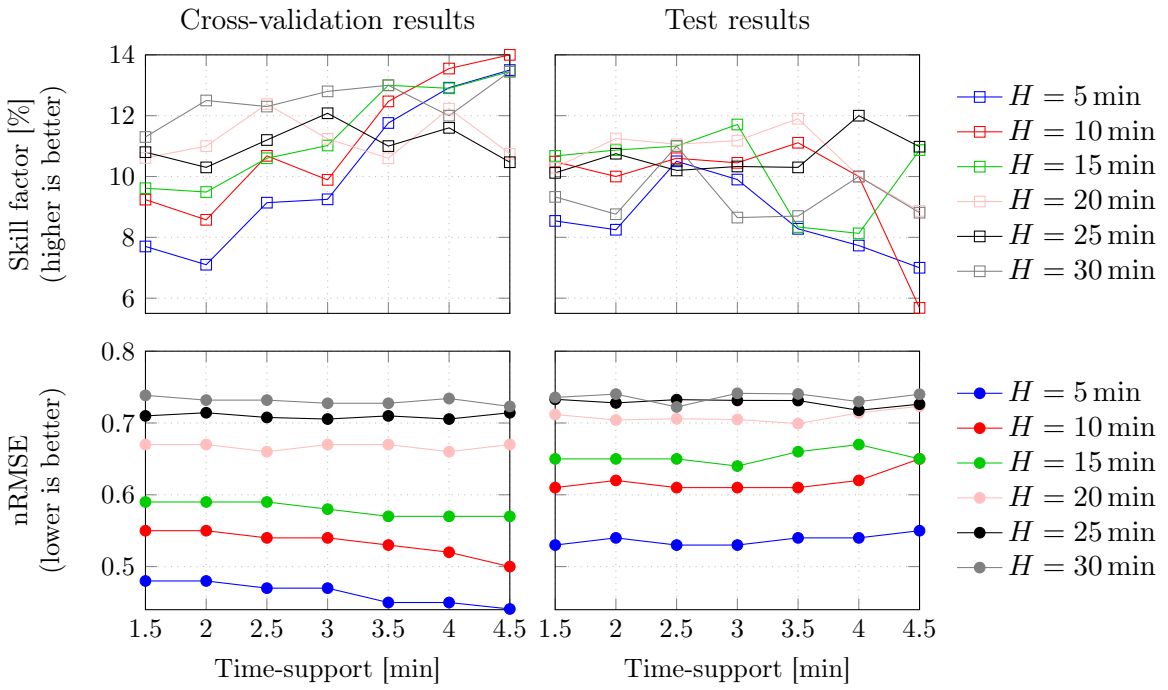

Figure 3.6: CNN-LSTM model results: nRMSE and SF values as a function of the time-support.

3.3.4 Comparative study

In this section, the RNNs with optimized topologies and time-supports obtained in Sections 3.3.3.1 and 3.3.3.2 are evaluated on the test dataset (mixed situations), and their performance is compared. An overall analytical analysis is given, followed by two case studies with different DNI profiles.

3.3.4.1 Analytical study

The results, that can be found in Figure 3.7, show that the CNN-LSTM model slightly outperforms the LSTM model for each forecast horizon, scoring lower nRMSE and higher SF thanks to its additional convolutional layer. It can be observed that the nRMSE scored by both models increases as the forecast horizon increases, since it becomes harder to forecast DNI. An increase in SF is also observed because, as the forecast horizon increases, the probability that DNI does not change over the forecast horizon becomes lower; the performance of the persistence model thus degrades drastically, allowing the RNN models to score a higher SF.

Both RNN models failed to forecast DNI ramps due to the lack of information concerning the sky situation (clouds' position, thickness, and motion). These low RDI values show that these statistical approaches are not adapted to ramp detection. To ameliorate this aspect, other inputs should be integrated, such as sky images.

3.3.4.2 Case studies

In this section, to gain more insight on their performance, the LSTM and the CNN-LSTM models are used to perform 15 min forecasts on two mixed situations: one day with a high variability, and one day with a low variability.

3.3.4.2.1 Low-variability case A low-variability case is presented in Figure 3.8: most of the day features a clear-sky situation, with thin clouds in the morning and in the evening.

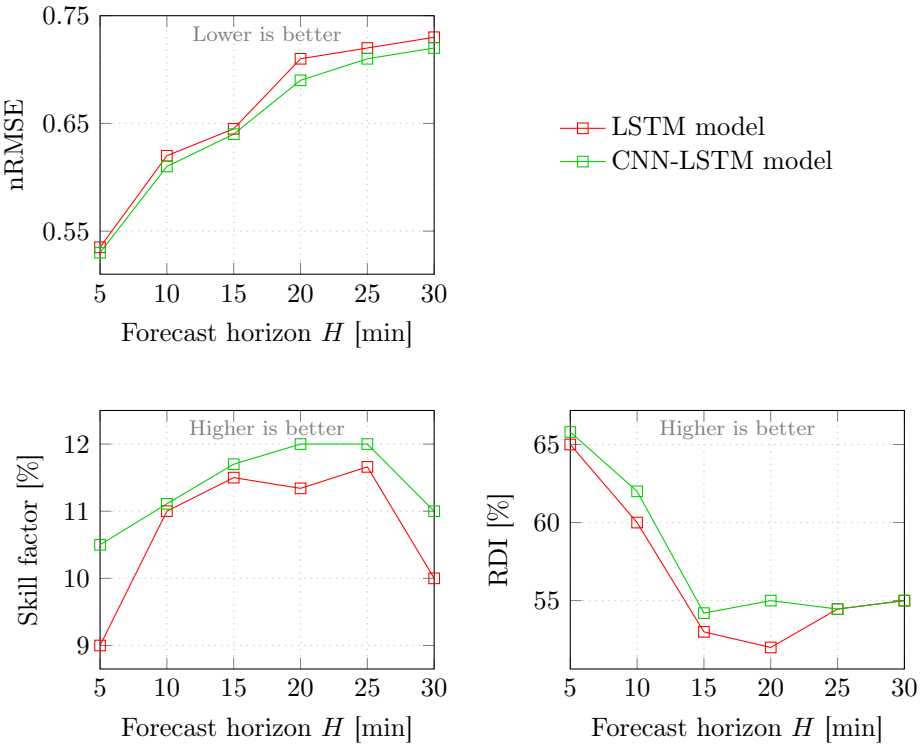

Figure 3.7: Comparison of LSTM and CNN-LSTM models on the test dataset.

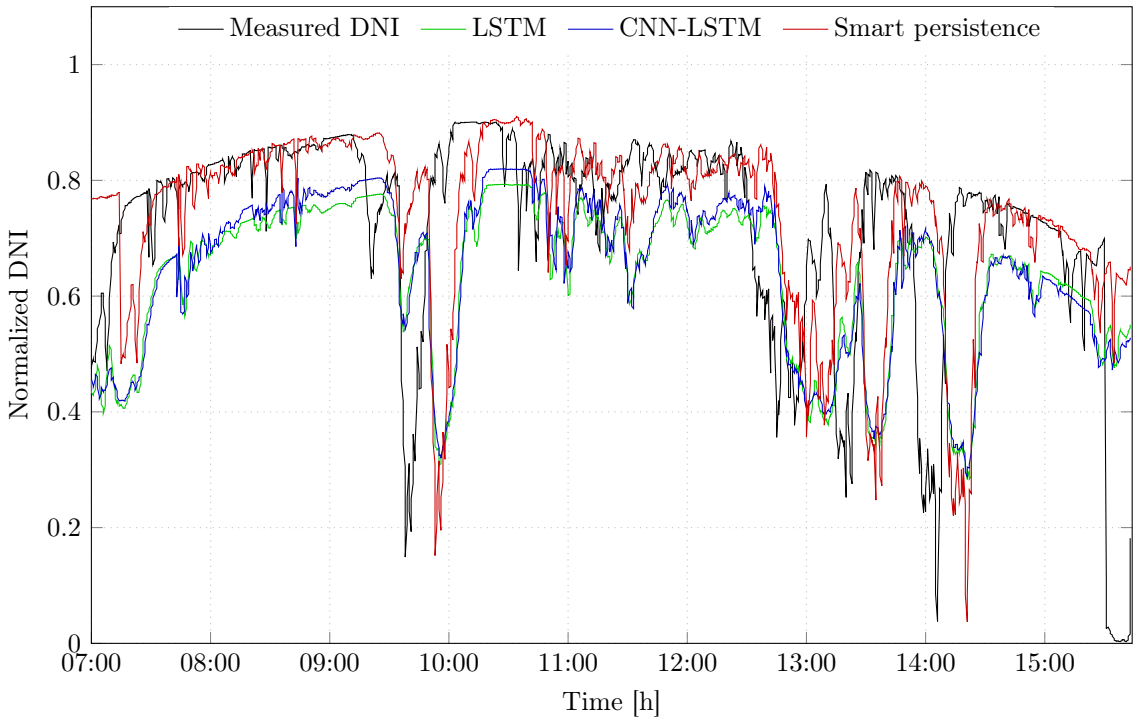

Figure 3.8: Low-variability DNI forecast at $H = 15\,\text{min}$ ($\text{nRMSE}_{\text{PE}} = 0.3$, $\text{nRMSE}_{\text{LSTM}} = 0.29$, $\text{nRMSE}_{\text{CNN-LSTM}} = 0.28$).

Although the smart persistence model typically provides great results on such cases (here $\text{nRMSE}_{\text{PE}} = 0.3$), both RNN models were able to outperform it ($\text{nRMSE}_{\text{LSTM}} = 0.29$, $\text{nRMSE}_{\text{CNN-LSTM}} = 0.28$). The RNN models were able to follow the overall shape of DNI and provided acceptable forecasts. It can be noticed that:

- there is an amplitude offset between measurements and forecasts (see the clear-sky period, for example). While this could be improved by adding simple rules to the models, in order to compensate the obvious errors made during clear-sky and overcast situations, it would not improve ability to detect ramps;
- although the performances of both RNNs are similar, the CNN-LSTM model slightly outperforms the LSTM model;
- the performances of the RNN models are very similar to the performance of the smart persistence model, which is explained by the nature of the provided input and the required task. DNI variability, which is determined by atmospheric variations, is not easily predictable by models based solely on past DNI observations. Thus, throughout the learning phase, the networks learned that the best way to deal with this problem is to provide forecasts similar to the persistence model with some corrections, resulting in a positive SF.

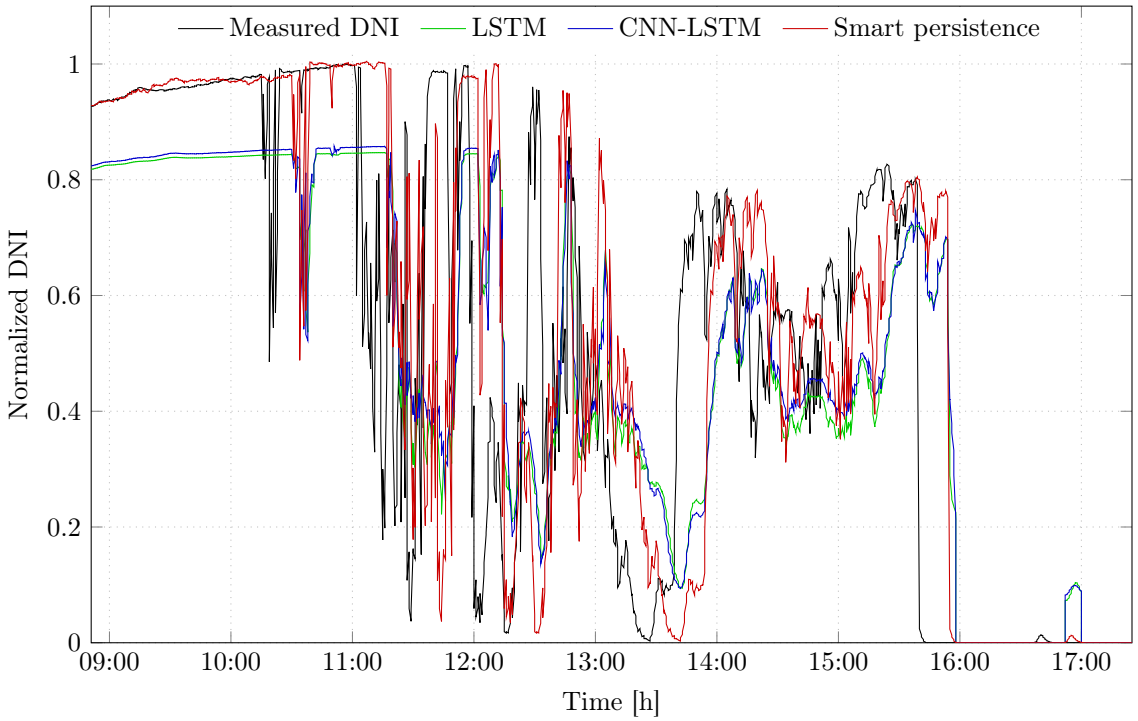

Figure 3.9: High-variability DNI forecast at $H = 15\,\text{min}$ ($\text{RMSE}_p = 0.56$, $\text{RMSE}_{\text{LSTM}} = 0.52$, $\text{RMSE}_{\text{CNN-LSTM}} = 0.5$).

This analysis indicates that although results seem acceptable when looking at global indicators (positive SF and nRMSE lower than that of the smart persistence), but this is not the targeted performance. The goal is to follow the DNI trend and forecast important DNI variations that these observation-based models are missing. The execution time of both models, using the computer described in Section 3.3, is approximately 0.2 s.

3.3.4.2.2 High-variability case A high-variability case is presented in Figure 3.9. After a few hours of clear-sky (until 10:00), high-frequency sudden variations can be observed. This case is challenging due to these fast, and sometimes hard-to-predict, DNI variations.

The smart persistence model performs very poorly, scoring $\text{nRMSE}_{\text{PE}} = 0.56$, while the RNN models give $\text{nRMSE}_{\text{CNN-LSTM}} = 0.5$ and $\text{nRMSE}_{\text{LSTM}} = 0.52$. The RNN models, however, again fail to predict most of the ramps. This performance proves that statistical models can outperform the smart persistence model for high-variability DNI profiles, but in terms of ramp detection, they miss most of the important ramps. The execution time of both models, using the computer described in Section 3.3, is approximately 0.2 s.

3.4 Conclusion

In this chapter, two statistical models are developed. These two models, a LSTM model and a CNN-LSTM model, are based on RNN networks that take past DNI observations as input to forecast DNI up to 30 minutes. The networks' architectures are optimized for each time-support and each horizon. The models are evaluated on a test dataset of DNI with mixed situations, that is not involved in the learning phase. The results show that RNNs are able to forecast DNI, scoring a positive SF (up to 12.5% for the CNN-LSTM model and 11.66% for the LSTM model). However, these statistical models have poor ramp detection capabilities for such complex mixed situations, where DNI variations are important and frequent. This is explained by their nature as pure statistical models, with no input concerning the clouds' motion and interaction with the Sun (which is the main cause for a DNI ramp). The low RDI values scored by both RNN models prove that these models can not be trusted for ramp detection. In the next chapter, the integration of HDR sky images in the forecasting process is studied to quantify the amelioration this approach can present, and to investigate the capability of this proposed model to handle situations with high DNI variations.

Chapter 4

Hybrid intrahour DNI forecast model based on DNI measurements and sky-imaging data

4.1 Introduction

As shown in the previous chapter, while statistical models can provide admissible DNI forecasts (in terms of SF and nRMSE) for long forecast horizons, their ramp prediction capability is mediocre. This is caused by type of the input provided to the models, which is not directly linked to the clouds' motion (the main cause of a DNI ramp). This analysis justifies the benefits behind integrating sky images in the forecasting model: if clouds' interaction with the Sun is the cause of ramps, then it is crucial to use sky images to analyze the clouds' behavior, so that these interactions can be forecasted. Such a phenomenon is illustrated in Figure 4.1, where the measured DNI is plotted along with three images taken with a sky imager. As can be seen on the plot, a sudden drop of DNI appears at 7h37. The first image is taken 5 min before this ramp; some thin clouds block the Sun and the measured DNI is equal to $725\,\mathrm{W\,m^{-2}}$ (almost the clear-sky value). The second image is taken 3 min before the ramp; looking sequentially at the two sky images, an observer could easily see that thick clouds are approaching the Sun. Finally, 3 min later, thick clouds block the Sun, resulting in a negative DNI ramp (from the clear-sky DNI value to $23\,\mathrm{W\,m^{-2}}$). This ramp could never be predicted by a statistical model solely based on past DNI observations.

The example presented in Figure 4.1 describes the basics of the model presented in this chapter. It uses sky images to detect clouds and determine their motion, which permits to localize a region of interest (ROI). This ROI is supposed to interact with the Sun at the considered forecast horizon. After its localization, some features are extracted from the ROI and fed to a forecast model to provide DNI forecasts. Throughout this chapter, the different components of the model, given in Figure 4.2, are explained and examined. First, the camera and the database used in this study are described. The chosen clear-sky model is then implemented under different atmospheric conditions to study its robustness. Cloud detection algorithms are detailed, and then a comparative study is carried out to choose an accurate, robust, and fast segmentation model. After detecting the clouds, their motion has to be estimated. The motion estimation algorithm is implemented under controlled conditions to determine its accuracy and robustness. Then, the ROI localization algorithm is presented and implemented under different sky conditions. Finally, the features extraction technique is presented, leading to the proposed forecast model. The model performance is studied under various sky conditions to examine its ramp detection capabilities, prove its robustness, and highlight the benefits of integrating sky images.

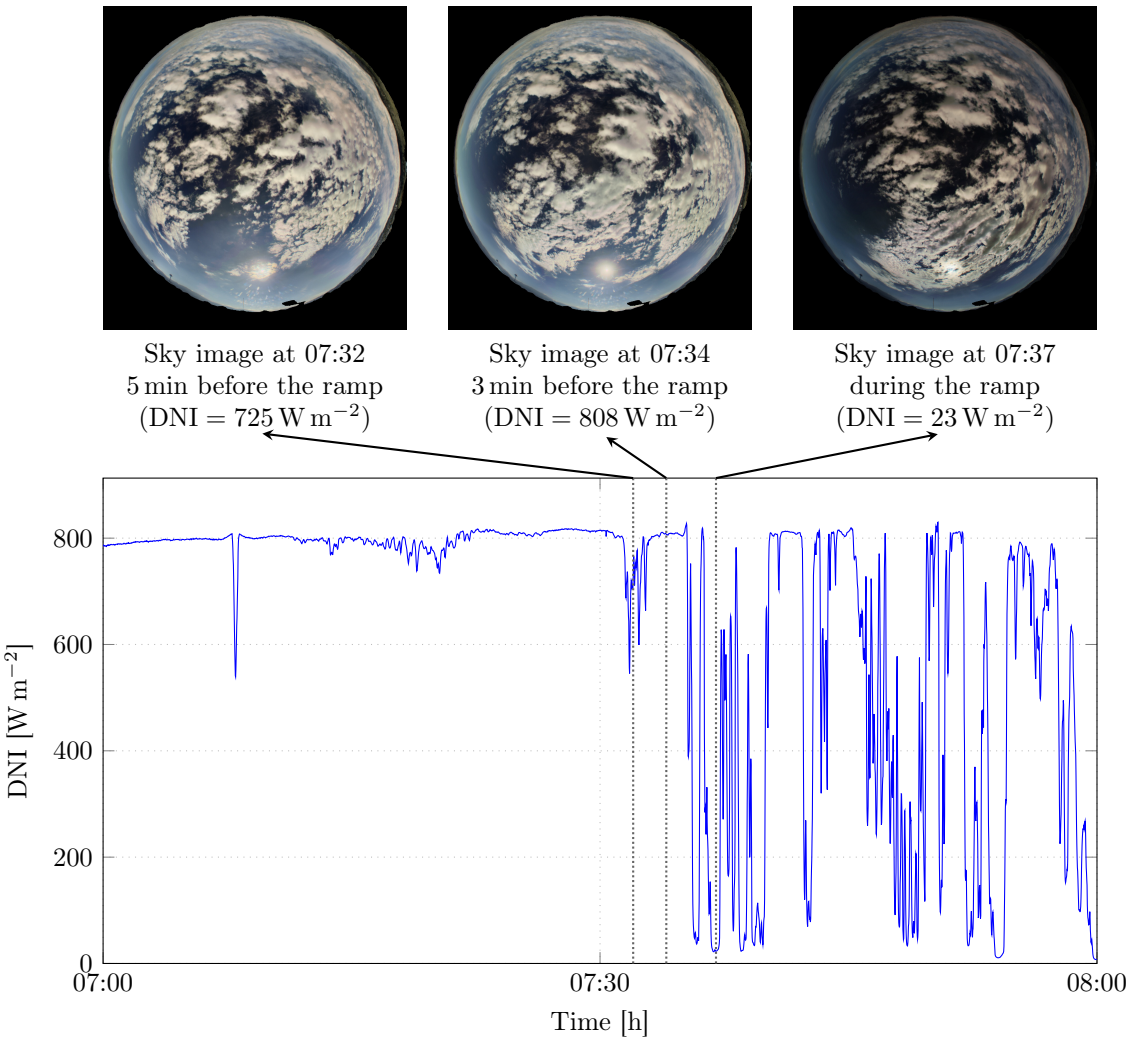

Figure 4.1: DNI ramp caused by Sun blocking clouds.

4.2 Sky images and DNI measurements database

The sky imager used in this work has been developed by PROMECA (see Figure 4.3a), with the help of PROMES-CNRS. It consists of an automatic, continuously operating, digital imaging system designed to capture sky images with a 180° field of view thanks to a fisheye lens (see Figure 4.3b). The sky imager provides on-the-fly analysis of sky conditions during daytime hours. Main hardware/software features are: high-end color CMOS (complementary metal oxide semiconductor) 1.5MP sensor, embedded computer enabling edge computing solutions, high dynamic range imaging enabling irradiance measurement and geometrical self-calibration. HDR imaging, obtained by merging a sequence of low dynamic range sky images, is key for the efficient detection of clouds, in particular in the circumsolar area (where the pixel values tend to be saturated), resulting in accurate DNI forecasting. The geometrical self-calibration algorithm is based on a comparison between the theoretical position of the Sun and its position on the image. The sky imager registers a 1.5MP HDR image every 30 seconds.

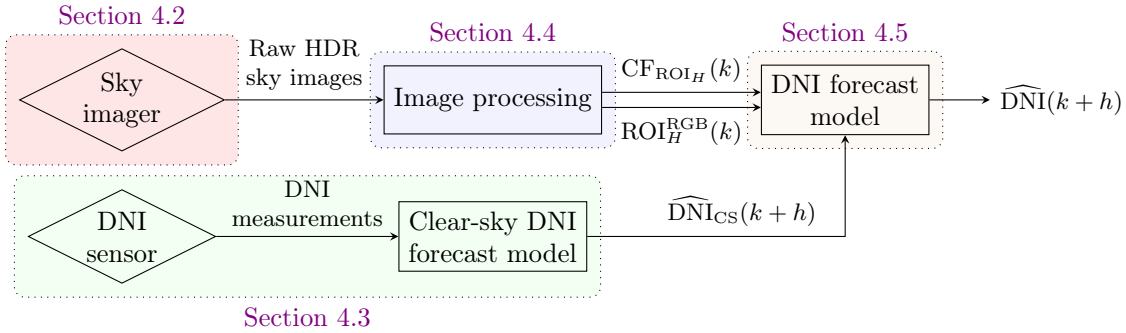

Figure 4.2: Global architecture of the proposed hybrid model, showing four main steps: high dynamic range (HDR) images acquisition, clear-sky direct normal irradiance (DNI) model, image processing, and DNI forecast model. $\mathrm{ROI}_H^{\mathrm{RGB}}$ is a RGB image of the region of interest (ROI), and $\mathrm{CF}_{\mathrm{ROI}_H}$ is the cloud fraction in the ROI.

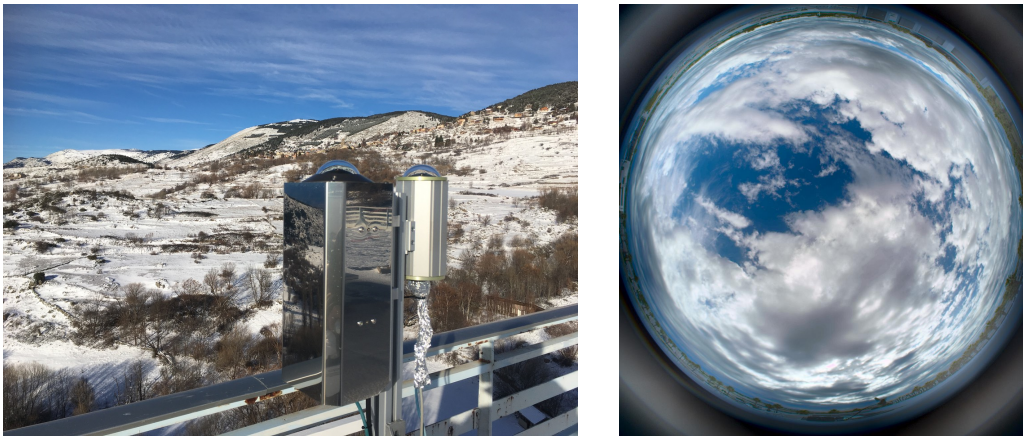

(a) Sky imager used (on the left).

(b) High dynamic range sky image.

Figure 4.3: (a) Sky imager installed at the PROMES-CNRS laboratory in Odeillo. (b) A HDR sky image, without the distortion correction.

The DNI database is the same than the one used for the RNN models, described in Section 3.3.1, and the image database consists of the corresponding sky images. The whole database (images and DNI) thus consists of 373 days, without missing data. The data classification reveals 128 clear-sky days (34.4%), 49 overcast days (13.1%) and 196 days with

mixed situations (52.5%). It should be mentioned that mixed situations are deemed more important than other situations: they are more complicated to handle and more frequent in Odeillo. That's why in this work, the focus is shifted toward mixed situations. The characteristics of the sky imager, the site, and the image database can be found in Table 4.1.

Table 4.1: Sky imager, study site and database specifications.

	Characteristic	Type/value
Sky imager	Camera sensor	CMOS
	Camera manufacturer	PROMECA
	Resolution	1300 × 1216
	Temperature range	0 °C to 50 °C
	Temperature regulation	Yes
	Field of view	180° (fisheye)
Site	Longitude	2.03 E
	Latitude	42.50 N
	Elevation	1603 m
Image database	Image format	Network Common Data Form (NetCDF)
	Interface Type	Ethernet
	Acquisition frequency	2 images/min
	File size	Around 2 Mbit
	Database size	373 days

4.3 Clear-sky DNI model

As mentioned in Section 2.2.2, the clear-sky DNI model developed in [88] is utilised in the proposed hybrid model. The clear-sky DNI forecast at time $k+h$ is given by:

$$\widehat{\mathrm{DNI}}_{\mathrm{CS}}(k+h) = bI_0 \exp\left(-0.09\widehat{m}(k+h)(\widehat{\mathrm{T}}_{\mathrm{LI}}(k+h)-1)\right) \tag{4.1}$$

where:

- I_0 is the extraterrestrial solar irradiance;
- b is calculated as follows:

$$b = 0.664 + 0.163 \exp\left(\frac{alt}{8000}\right) \tag{4.2}$$

  with alt the site's altitude;

- the forecast of the relative optical air mass m is given by:

$$\widehat{m}(k+h) = \frac{1}{\cos\left(\mathrm{SZA}(k+h)\right) + 0.50572\left(96.07995 - \mathrm{SZA}(k+h)\right)^{-1.6364}} \tag{4.3}$$

  with SZA the Sun zenith angle;

- the forecast of the the Linke turbidity coefficient is given by a simple persistence: $\widehat{\mathrm{T}}_{\mathrm{LI}}(k+h) = \mathrm{T}_{\mathrm{LI}}(k)$, since its variations throughout the day are relatively small; the estimation of its value at time k is achieved using DNI measurements, as proposed by Nou et al. [88].

The clear-sky DNI model was implemented under different atmospheric conditions, as shown in Figure 4.4. Thanks to its adaptive nature, the model provides accurate estimations for different atmospheric conditions: the left graph presents a clean atmosphere with high DNI values, the right graph presents a dusty atmosphere with low DNI values.

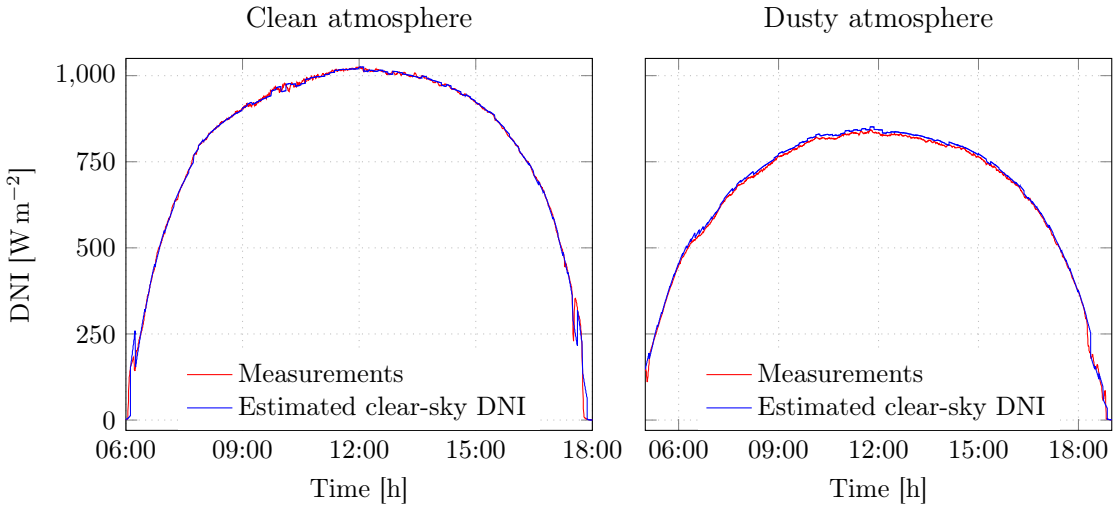

Figure 4.4: Comparison between the estimated clear-sky DNI and DNI measurements for two clear-sky days with different atmospheric conditions.

4.4 Image processing

This step is crucial in the DNI forecasting process, since, as seen before, the sky conditions should be accurately analyzed to provide accurate forecasts. Image processing is used to extract information relevant to DNI forecasts. Figure 4.5 summarizes all the image processing steps leading to the extraction of features from the sky images. Each step is detailed separately in the following sections of this chapter:

- the HDR images are treated to correct the fisheye lens distortion (Section 4.4.1);
- A LDR image is generated from the HDR image to be used in the cloud estimation block (Section 4.4.2);
- clouds are detected using the developed machine-learning-based model (Section 4.4.3);
- clouds motion are then estimated using the Farnebäck optical flow algorithm (Section 4.4.4);
- the ROI is then located based on the dominant motion, estimated using the k-means clustering method (Section 4.4.5);
- finally, the cloud fraction in the ROI is calculated ($\mathrm{CF}_{\mathrm{ROI}_H}$) and fed to the DNI forecast model that takes the RGB image of the ROI ($\mathrm{ROI}_H^{\mathrm{RGB}}$) as input as well (Section 4.4.6).

4.4.1 Distortion correction

Due to the camera's fisheye lens, the image is distorted. The distortion correction process relates a 3D world point on to a 2D image using the camera extrinsic and intrinsic parameters, obtained during the camera's geometrical self-calibration. World points are transformed into

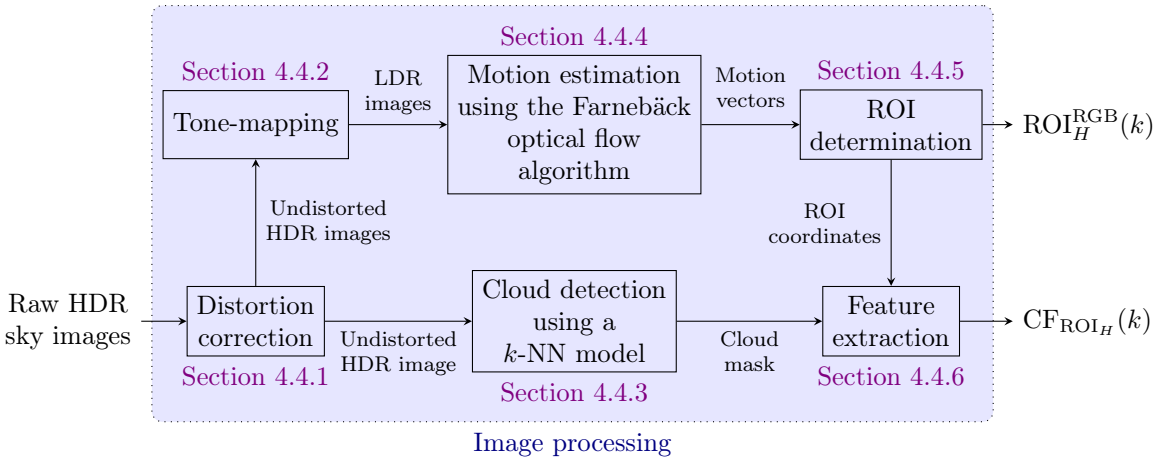

Figure 4.5: Image processing steps leading to the features' calculation. It starts with the distortion correction of the HDR image, followed by motion estimation and cloud detection. Based on that, the region of interest (ROI) is located and the cloud fraction in the ROI is calculated ($\mathrm{CF}_{\mathrm{ROI}_H}$).

camera coordinates using the extrinsic parameters (leading to a rotation and a translation). The camera coordinates are then mapped into the image plane using the intrinsic parameters (focal length, distortion center, and radial distortion coefficients). For more information about this process, the reader is referred to [119, 120]. The extrinsic parameters are applied as follows:

$$X_c = M_R \cdot X + M_T \tag{4.4}$$

where M_R and M_T are the rotation and translation matrices related to the position of the camera, respectively. X_c and X are the pixel coordinates in the camera frame and the world frame, respectively. Now, in order to present the pixels in the image frame, the intrinsic parameters should be applied as follows:

$$u = f_x(x' + \alpha y') + c_x \tag{4.5}$$

$$v = f_y y' + c_y \tag{4.6}$$

where (f_x,f_y) are the focal lengths, (c_x,c_y) are the center of distortion coordinates, and (x',y') are the distorted pixel coordinates in the camera frame calculated as follows:

$$x' = a(\theta_d / r) \tag{4.7}$$

$$y' = b(\theta_d / r) \tag{4.8}$$

where:

$$a = x_c / z \tag{4.9}$$

$$b = y_c / z \tag{4.10}$$

$$r^2 = a^2 + b^2 \tag{4.11}$$

$$\theta = atan(r) \tag{4.12}$$

$$\theta_d = \theta(1 + d_1\theta^2 + d_2\theta^4 + d_3\theta^6 + d_4\theta^8) \tag{4.13}$$

Here, d_1, d_2, d_3, and d_4 are the distortion coefficients calculated during the calibration phase, and (x_c, y_c) are the pixel coordinates in the camera frame. An example of distortion correction is shown in Figure 4.6.

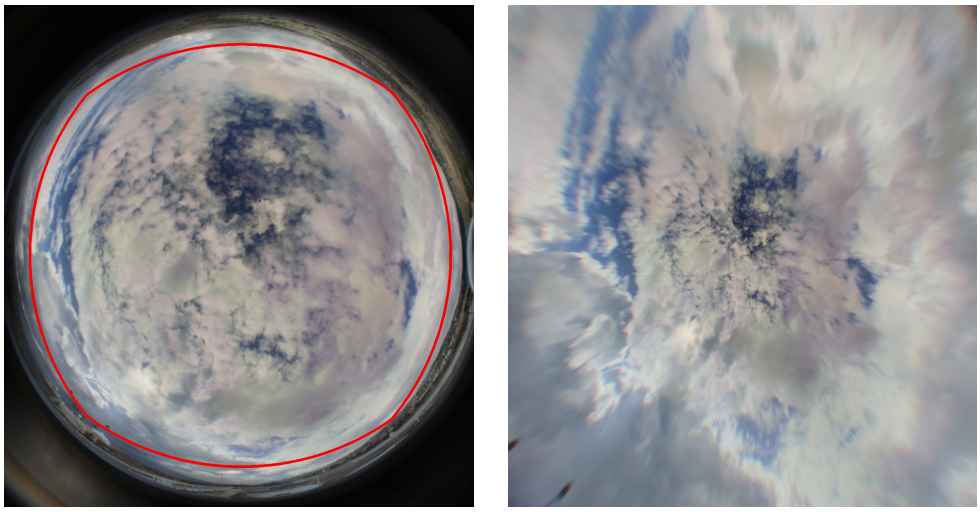

(a) Distorted image, with the boundaries of the undistorted image in red.

(b) Image after distortion correction.

Figure 4.6: Example of distortion correction, based on the camera's intrinsic and extrinsic coefficients.

4.4.2 Tone-mapping

In this section, the tone-mapping algorithm is presented while highlighting the importance of implementing a robust algorithm. Different tone-mapping solutions are reviewed to choose a suitable method. Tone-mapping is the process of converting an HDR image to a LDR image, which will be the input to the optical flow algorithm[1]. It should be mentioned that this step is crucial, since it plays a key role in cloud motion estimation performance, as showed in this analysis. Many tone-mapping algorithms exist [121], such as:

- the Drago method [122]: an adaptive logarithmic mapping for displaying high contrast scenes;
- the Durand method [123]: this approach preserves details by compressing the image's contrast;
- the Mantiuk method [124]: this algorithm reconstructs the image from new contrast values calculated using gradients on all levels of gaussian pyramid, it transforms contrast values to hue, saturation, and value (HSV) response and scales the response;
- the Reinhard method [125]: this is a global tone-mapping operator that models human visual system. The mapping function is parameterized by adaptation parameters, computed using light and color adaptation.

The sky imager's manufacturer (PROMECA) recommends using Reinhard method, because of its adaptive nature and its ability to account for intensity change. This method is robust against very bright images when the Sun is apparent, and against dark images when the Sun is completely blocked.

As said before, the mapping function should be accurately parameterized to provide the best image quality and details, so that the clouds' motion can be correctly estimated. These parameters are:

- the intensity factor (IF): it varies the pixels' intensity;

[1]The optical flow implementation using OpenCV library requires LDR input images.

- the gamma correction (GC): it is used to control the overall contrast and brightness of an image, generally on images that are either bleached out or too dark [126];
- the light adaptation factor (LAF): it compensates for the light intensity variations (variations caused by clouds blocking the Sun for example) [127].

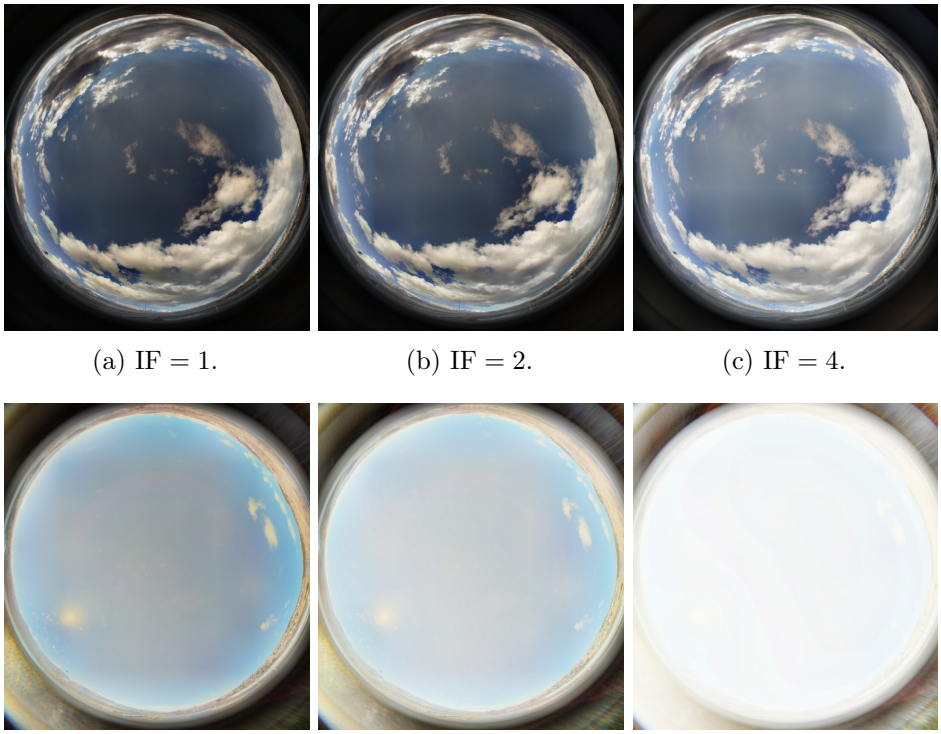

(a) IF = 1. (b) IF = 2. (c) IF = 4.

(d) IF = 1. (e) IF = 2. (f) IF = 4.

Figure 4.7: Influence of the intensity factor IF.

The influence of these parameters is highlighted by Figures 4.7 to 4.9.

- An increase in the intensity factor will result in a brighter image as shown in Figures 4.7a to 4.7f. However, when the Sun is apparent, the image becomes excessively bright, resulting in the failure of the cloud motion estimation (no apparent details).
- An increase in the gamma correction will result in a brighter and clearer image as shown in Figures 4.8a to 4.8f; even when the Sun is apparent, the image's details are preserved.
- In Figures 4.9a to 4.9f, it can be observed that an increase in the intensity adaptation factor will result in a clearer image; even when the Sun is apparent, the image's details are preserved.

From these tests, the tone-mapping algorithm parameters are fixed as follows: the intensity factor is equal to 1; the gamma correction is equal to 0.8; and the intensity adaptation factor is equal to 0.8.

4.4.3 Cloud detection

As shown before, DNI forecasts are strongly influenced by cloud motion. That's why a segmentation algorithm is required to identify cloud pixels with high accuracy. First, a review of the state-of-the-art clouds segmentation solutions is presented. Based on this review, two machine-learning-based methods are proposed and a comparative study is carried out to evaluate their accuracy, robustness, and computational complexity.

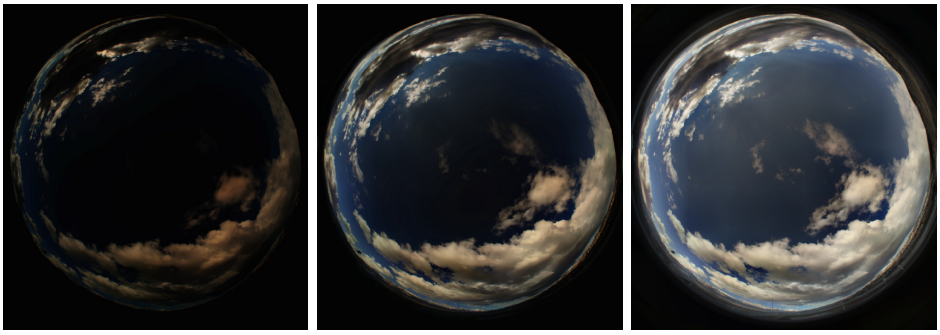

(a) GC = 0.2. (b) GC = 0.4. (c) GC = 0.8.

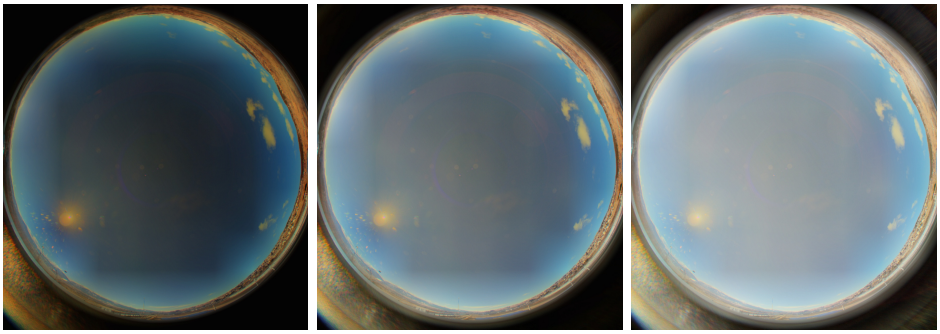

(d) GC = 0.2. (e) GC = 0.4. (f) GC = 0.8.

Figure 4.8: Influence of the gamma correction GC.

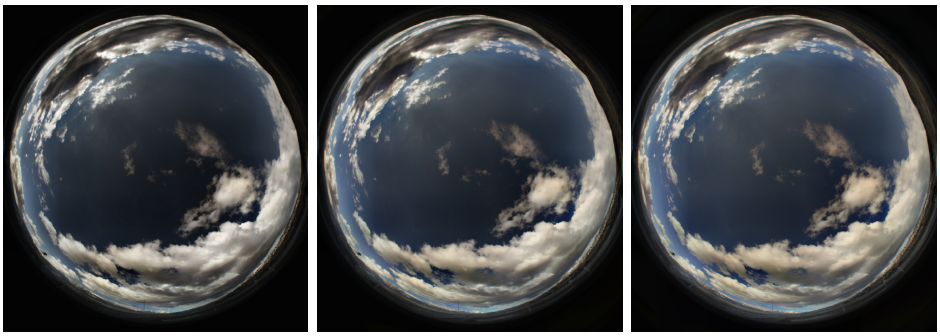

(a) LAF = 0.2. (b) LAF = 0.4. (c) LAF = 0.8.

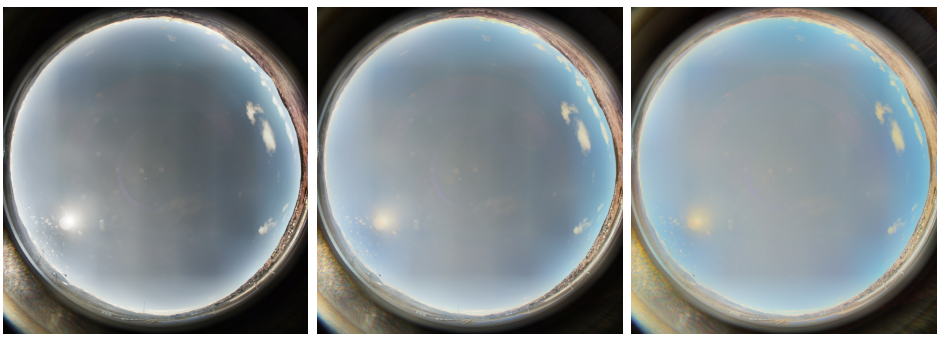

(d) LAF = 0.2. (e) LAF = 0.4. (f) LAF = 0.8.

Figure 4.9: Influence of the intensity adaptation factor LAF.

Existing works can be grouped in two main approaches.

- Threshold-based algorithms: these algorithms use thresholds (on various features) in order to perform cloud segmentation. However, cloud luminosity, thickness, and position in the sky, as well as the clear-sky radiance anisotropy complicate the cloud detection task. As a result, algorithms based on one fixed threshold perform poorly, and several improvements have been introduced. The hybrid thresholding algorithm (HYTA), consisting in an adaptive threshold on the red-to-blue channel, has been introduced in [128]. In [129, 96] the minimum cross entropy (MCE) algorithm found in the HYTA is enhanced by saturating the threshold, and then defining different regions of interest in the image, which permits to calculate a local threshold in each region. The difference between the blue and the red channels proved to be a good candidate to perform the segmentation [130]. More sophisticated methods are introduced in [131]: a fuzzy C-means clustering is applied on the normalized difference between the red-to-blue channels, in order to gather some seeds (labeled pixels that are used to initialize the segmentation model), and then the graph cut method [132, 133, 134] is applied to classify the pixels. Threshold calculation based on the Otsu method is used also to segment the cloud/sky pixels [135] (the gray scale is used). Finally, a method that uses two features simultaneously is proposed in [136]. The threshold is calculated as follows: the average of the two highest classes of the red-to-blue ratio histogram is averaged with the mean of the red-to-blue ratio values holding the highest local standard deviation of the grayscale image.

- Machine-learning-based algorithms: due to their threshold-free nature and the possibility of combining multiple features, these algorithms can solve problems related to Sun glare, and cloud variability and positioning. For example, in [137], a support vector machine (SVM) classifier is trained, combining different inputs: the RGB (red, green, and blue) channels; local standard deviation; and the Laplacian of Gaussian. In [138], a neural network with various inputs is used: hue, saturation, and brightness (HSV); the RGB channels; the red-to-blue ratio (RBR); the red-blue difference (RBD); pixels' estimated movement; pixels' distance from the Sun; Sun azimuth and Sun zenith angles. Different combinations of inputs can be used [139]: the normalized RBR; the normalized saturation-value ratio; the RBR; gray-scale values; and the RGB channels. Furthermore, [140] proposed an ANN that uses the variance of the red channel; the mean of the red channel; and the mean of the blue channel on a given neighbor. A pre-processing step can be added before the implementation of the ANN [141] to help the model learn: first, the image is grouped to one of three clusters based on its characteristic, and then a group-specific ANN is used to identify clouds.

The threshold-based approaches perform accurately in simple cases, where clouds' intensity is uniform, but when different types of clouds (cirrostratus, cirrocumulus, cirrus, altostratus, etc.) are to be identified, the threshold-based methods pose the problem of over- or under-identification depending on the aggressivity of the threshold and the tolerance on details. Also, these methods lose accuracy on the boundaries of the image (note that they are generally applied on images from a camera having a fisheye lens, where boundaries contain important information). Finally, the Sun glare affects these methods drastically. The machine-learning-based models can overcome these problems during the learning process. Thus, the goal is to overcome the Sun glare problem, preserve as much information as possible, and present a model without predefined parameters that can process HDR images.

To achieve the required performance, two supervised machine learning models are developed and detailed in the following sections. The first method is a deep neural network with multiple layers and the second method is a k-nearest neighbors model (k-NN) trained with several features. The proposed models are then compared, visually and numerically, with the following state-of-the-art approaches.

- The updated MCE algorithm. For the sake of this comparative study, the enhanced version of this algorithm is used [96].

- The graph cut method [131]. It is an advanced approach to segment images, where seeding is done with the help of fuzzy C-means clustering. The feature used is the normalized difference of the red-to-blue channels.

- The Otsu method, using the grayscale feature [135].

- The Huo and Lu method [136], in which the threshold is calculated by averaging the highest two classes in the red-to-blue ratio histogram, and then averaging this value with the average of the 20 red-to-blue ratio holding the highest standard deviation values. This method is proposed for mixed cases only, since its performance degrades drastically for overcast and clear-sky (no clouds) cases.

4.4.3.1 Artificial neural network model

A neural network model can be expressed as follows:

$$Y = F(X) \tag{4.14}$$

where X is a vector of features of each pixel and Y is the pixel class (label) decision, and F is a black-box holding the weights and biases of each node in the network. The mapping is performed by applying these trained parameters on the normalized input vector X.

As presented in Figure 4.10, a deep neural network consists of multiple connected hidden layers. The output of a neuron can be written as follows:

$$y(x, w) = f\left(\sum_{i=1}^{d} w_i x_i + b\right) \tag{4.15}$$

where f is the activation function, w and x are the vectors of the weights and inputs from the d neurons of the previous layer, and b is the bias. These parameters are estimated during the training phase. Neural networks use a variety of learning techniques and optimizers, but the most popular is the back-propagation algorithm [142].

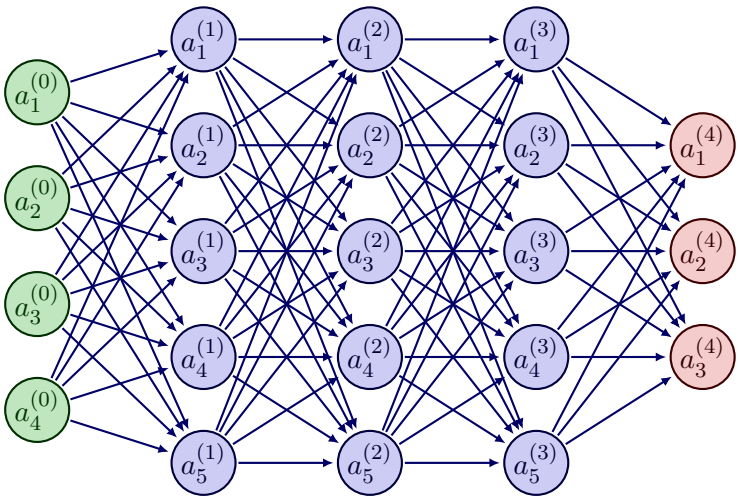

Figure 4.10: A fully-connected deep artificial neural network characterized by its input layer with 4 neurons (in green), its hidden layers with 5 neurons each (in blue), and its output layer with 3 neurons (in pink).

As discussed in Section 3.1, artificial neural networks are a powerful artificial intelligence tool. However, to achieve high accuracy, the predictors have to be picked wisely: as in any machine learning model, specific features that will help match the input to the output are required. As seen in the related work, the most used features are:

- the RGB channels;
- the red-to-blue ratio:

$$\mathrm{RBR} = \frac{\mathrm{R}}{\mathrm{B}} \tag{4.16}$$

- the normalized red-to-blue ratio:

$$\mathrm{NRBR} = \frac{\mathrm{R} - \mathrm{B}}{\mathrm{R} + \mathrm{B}} \tag{4.17}$$

- the local standard deviation on a specified neighborhood;
- the Laplacian of Gaussian;
- the gray scale.

These features are illustrated in Figure 4.11. As can be seen, they improve the visual contrast between sky and clouds, which help to discriminate between cloud and sky pixels. It should be mentioned that the RBR and the NRBR can be combined, as using several combinations of red and blue channels results in increased performance [131]. The local standard deviation on a specified neighborhood helps learning patterns concerning the relation of the pixel with its neighborhood [137]: it alerts the network to variations in the intensity, which can indicate an edge or variations in cloud thickness; thus, with the help of the other features, the network can classify easier. The Laplacian of Gaussian provides binary information concerning clouds' edge. Finally, the gray scale helps identifying clouds based on pixels' intensity. These features can be visualized in Figure 4.11. Based on this analysis, these features are used as ANN inputs, so that it can learn patterns concerning cloud edges, intensities, and relation between pixels and their neighborhood. The training and validation dataset consists of 15 days:

- first, four images with different sky situations (clear-sky, overcast, and mixed situations) have been carefully labeled manually using the *Image Segmenter Matlab Toolbox*; after eliminating the physical mask (building and trees around the camera), the dataset consists of 4 425 990 observations;
- then, to help performing this tedious task and enrich the database, an ANN has been trained using these four images; with its help, 11 additional (crude) cloud masks have been obtained, before being refined manually;
- in the end, the database consists in 15 images (4 clear-sky images, 5 overcast images, and 6 mixed images), representing 12 193 471 observations. This dataset is split into 70% used for training and 30% for validation.

After training different architectures, the best performing network scored 97% of validation accuracy and 11% of validation loss (the accuracy is given by dividing the number of correctly-labelled pixels by the total number of pixels involved, and the loss is calculated by the binary cross-entropy method [143]). The network consists of 8 hidden layers with 64, 128, 256, 512, 512, 256, 128, and 64 neurons, respectively. As for activation functions: the Rectified Linear Unit (ReLU), which proved to be fast in the learning phase, is used in the intermediate layers, and the sigmoid function, which is used for probabilistic problems where the output is between zero and one, is used in output layer (see Figure 4.12). The network is then trained for three

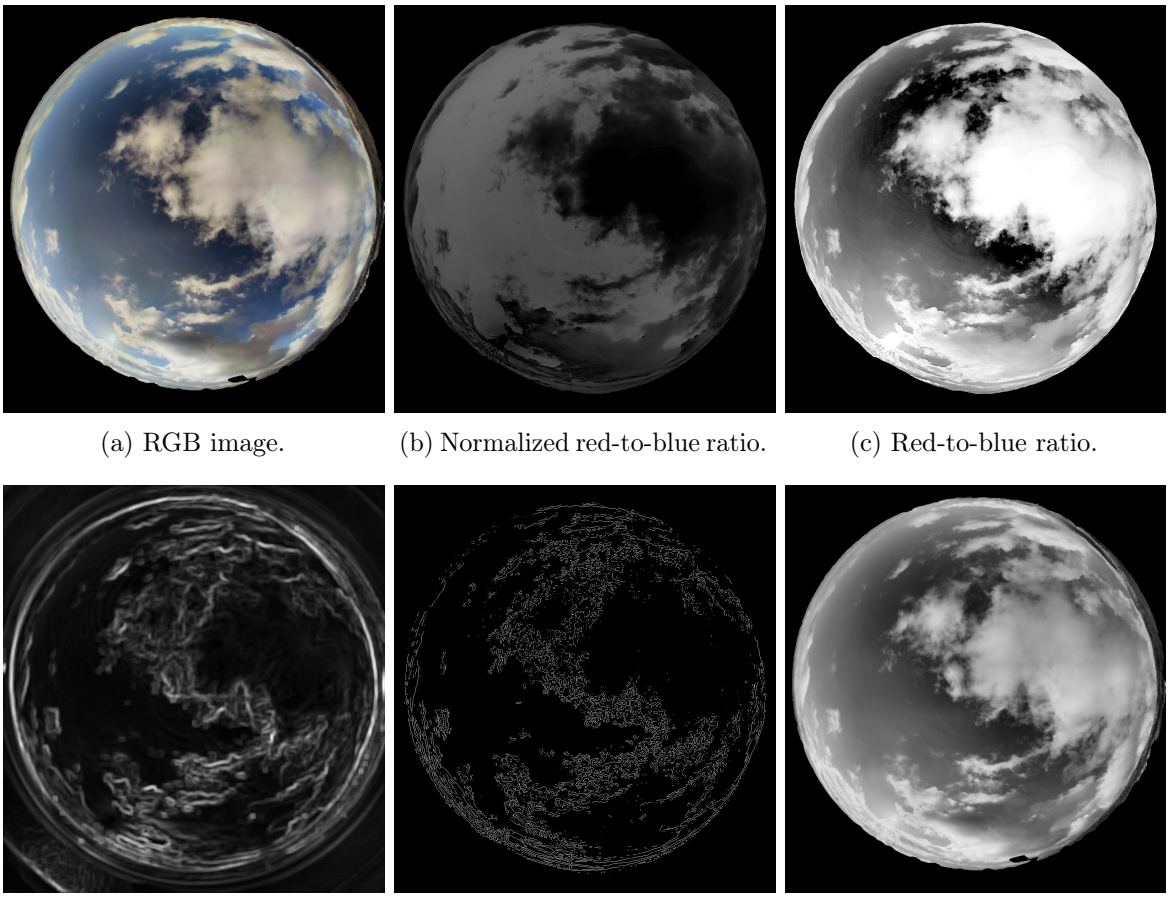

(a) RGB image. (b) Normalized red-to-blue ratio. (c) Red-to-blue ratio.

(d) Local standard deviation. (e) Laplacian of Gaussian. (f) Gray scale.

Figure 4.11: Visualization of the different features used for cloud/sky segmentation.

epochs using the TensorFlow - Keras GPU aided version [144]. Each epoch lasted 30 min to 40 min using ADAM optimizer on a machine having Intel I7-4510U CPU @ 2.00-2.60 GHz as the CPU and Nvidia Geforce 840M as the GPU[2]. Once trained, the model provides a probabilistic segmentation mask of the image (1300×1216 pixels) in 40 s to 50 s. The pixels' value of this mask corresponds to the probability of the current pixel to be a cloud, ranging from zero to one.

A fixed threshold is applied on the circumsolar region to overcome the Sun glare problem [121]. This region is defined by applying the model on 15 clear-sky images, then defining the region affected by Sun glare, and finally a fixed region is defined. Tests showed that 0.83 is a good threshold value. This approach is impossible to apply on a binary mask, which is another advantage of having a probabilistic mask.

4.4.3.2 k-NN model

A k-NN is a non-parametric model frequently used for classification and regression. It classifies data using a similarity measure, based on a distance metric. There are several k-NN variants, characterized by specific parameters such as:

- the distance metric, such as the city block, the Chebychev distance, the Euclidean distance, etc. [145];

[2]Please note that this is a different computer than the one used for all other developments, which is described in Section 2.2.5.

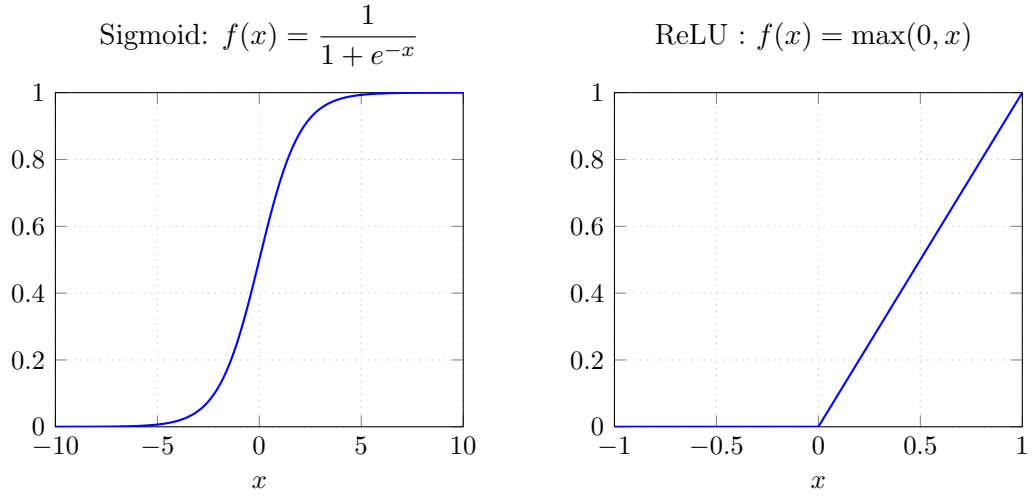

Figure 4.12: Sigmoid and ReLU activation functions.

- the number of nearest neighbors, which generally ranges from 1 to 100;
- the nearest neighbor search method, such as the k-d tree method [146].

Each combination of these parameters affects the model's execution time, learning speed, flexibility, interpretability, implementation behavior, etc.

After multiple trials, the model with the highest accuracy takes as input: the RGB channels, the local standard deviation (using 11×11 neighbors) and the normalized red-to-blue ratio. The model's distance metric is the Euclidean metric (as it is a good choice for properly scaled learning datasets [145]), the number of neighbors is set to 100, and the model uses the k-d tree searching method. The *Matlab Classification Learner* is used to perform the learning, which took 40 minutes and achieved a validation accuracy of 97 %, where the accuracy metric is the binary accuracy calculated by dividing the number of correct clouds/sky predictions over the total number of pixels involved in the dataset.

4.4.3.3 Comparative study of cloud detection algorithms

In this section, the machine learning models are compared with the state-of-the-art methods presented in Section 4.4.3. Here, the test dataset consists of 27 images, not involved in the training or validation of the models: Test 1 with two images with manually-labelled ground truths to provide a quantitative analysis (see the two case studies presented in Figure 4.13), Test 2 with twenty images to evaluate the execution time of the compared models, and Test 3 with five images that helped perform a visual assessment.

Table 4.2: RMSE obtained on the two test images (Test 1).

Method	Otsu	MCE	Hou et Lu	k-NN	NN Model
Case 1	0.55	0.47	0.26	0.21	0.15
Case 2	0.13	0.11	0.27	0.13	0.10

Test 1 is presented in Figure 4.13; note that this is the only test where manually-labelled ground truth has been produced. The sky image is a whole image with apparent Sun, clear-sky and some shattered clouds; the aim is to test the robustness of the algorithms to Sun glare. The second sky image is a specific part of a cloudy image, used to evaluate the performance of the proposed approaches in regions where threshold-based algorithms usually perform well.

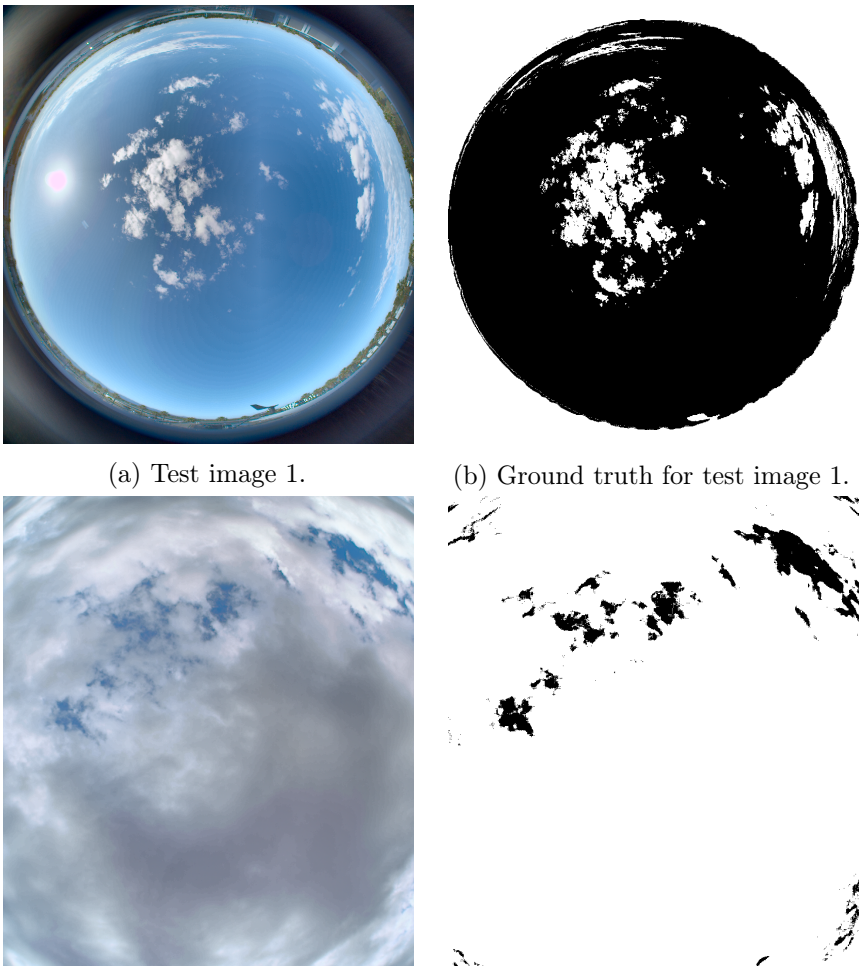

(a) Test image 1.

(b) Ground truth for test image 1.

(c) Test image 2.

(d) Ground truth for test image 2.

Figure 4.13: The two case studies, along with the associated ground truths.

The RMSE obtained by each cloud detection algorithm is presented in Table 4.2. The ANN and k-NN models outperform the state-of-the-art methods in the two cases, which proves that the proposed models are robust to Sun glare (sky image 1) and accurate enough locally (sky image 2). The average execution time of each model, calculated on 20 images in the test dataset, is given for Test 2 (Table 4.3). As can be seen, the ANN high accuracy comes at the cost of a long execution time, while the other models have similar execution times.

Table 4.3: Average execution time on 20 test images (Test 2).

Method	Otsu	MCE	Huo et Lu	k-NN	NN Model
Time [s]	0.22	0.55	0.74	0.43	52.63

Test 3 presents five images selected from the test database as shown in Table 4.4: two local images and three whole images (two sunny images and one fully clouded image). These images have been selected to provide a qualitative study, showing that the proposed approaches can overcome the problems generally faced by cloud detection algorithms: Sun glare (columns 3 and 4), thin and thick clouds (columns 1, 2, and 5), and clear-sky radiance anisotropy (columns 3 and 4). Indeed, it is advised to perform local thresholding to overcome the problem posed by the fisheye lens distortion, especially on images' boundaries, where false detection

is common in threshold-based algorithms. In learning-based algorithms, this problem is not usually encountered and there is no need to separate images into regions of interest.

As can be seen in Table 4.4, the state-of-the-art methods suffer from over- or under-identification[3] due to the way the threshold is calculated (it can be sensitive to thin clouds but miss-classifies Sun glare as clouds, or not sensitive enough that it miss-classifies cloud pixels as sky), while for learning-based algorithms, the probabilistic nature of the approach is sufficient to confront the problem, as shown in the first two columns. In addition, the threshold-based algorithms need some additional support and special treatment in case of dark clouds (such as in the last column of Table 4.4); for example, in the fixed threshold approaches, the threshold might be too high for some situations, which implies that some additional post-processing step should be proposed to solve this problem, as in e.g. [97]. Meanwhile, the proposed models learned to distinguish this type of clouds without additional post-processing, which serves the purpose of finding a robust algorithm.

Another observation to be mentioned is that the learning-based approaches are sensitive to details but robust to Sun glare (columns 3 and 4); the updated MCE algorithm is sensitive to details, but it drastically fails on the neighborhood of the Sun, since the threshold will not treat the glare specially; this results in false detection as seen in columns 3 and 4 of Table 4.4. The other methods are more robust to Sun glare, but fail to detect small details and thin clouds like, e.g., the Hou and Lu method. This leads to the second strong point of the proposed approaches, that mix high sensitivity and robustness to Sun glare. We can see that the graph cut method based on the fuzzy C-means clustering failed on the whole image, and even on the local image the results were not as satisfying and detailed as intended. This might be explained by the fact that this method is based on seeds: the accuracy is highly dependent on the quality of the chosen seeds. Otsu is the best-performing threshold-based method, but the proposed approaches are slightly better or equivalent in terms of detection. Needless to say, the Otsu algorithm yields a binary mask while the proposed ANN model yield a probabilistic mask. As for the Huo and Lu method, it does not provide great details as shown in the first two columns of Table 4.4. And the Sun glare poses a clear problem for this approach as shown in the third columns of Table 4.4. Furthermore, when the sky is completely covered by clouds (last column of Table 4.4), we can see that most of the methods lose their accuracy on the boundaries, while the proposed algorithms do not face any problem. In terms of accuracy, even though both the proposed models performed well compared to the other models, the performance of the ANN model is generally better than that of the k-NN model. Furthermore, the ANN model provides probabilistic map and performs better than the k-NN around the Sun. However, the ANN's computation time is noticeably high, while the k-NN model provides an accurate binary cloud mask and is much faster.

To conclude, the ANN provides high accuracy and multiple advantages such as probabilistic map, accuracy on circumsolar region, accuracy on boundaries, etc. The k-NN model performs well in the testing step as shown in Tables 4.2 and 4.4 , where it provides the advantage of high accuracy and short execution time. In addition, the proposed models are able to deal with the problems posed by the threshold-based algorithms, such as the effect of the lens distortion, Sun glare, over- and under-identification. Based on the good performance of the k-NN model and the long execution time of the ANN model, the k-NN model is chosen as the segmentation approach for the rest of the study.

4.4.4 Cloud motion estimation

In this section, the algorithm responsible for cloud motion estimation is presented. After a short review of state-of-the-art approaches, the chosen algorithm is detailed. Its implementation is then discussed, before studying its robustness to intensity and shape variations.

[3]Over-identification is when a high number of false positives for clouds label is obtained, and under-identification is when a high number of false negatives for clouds label is obtained.

Table 4.4: Comparison between the tested approaches on five images selected from the test database (Test 3).

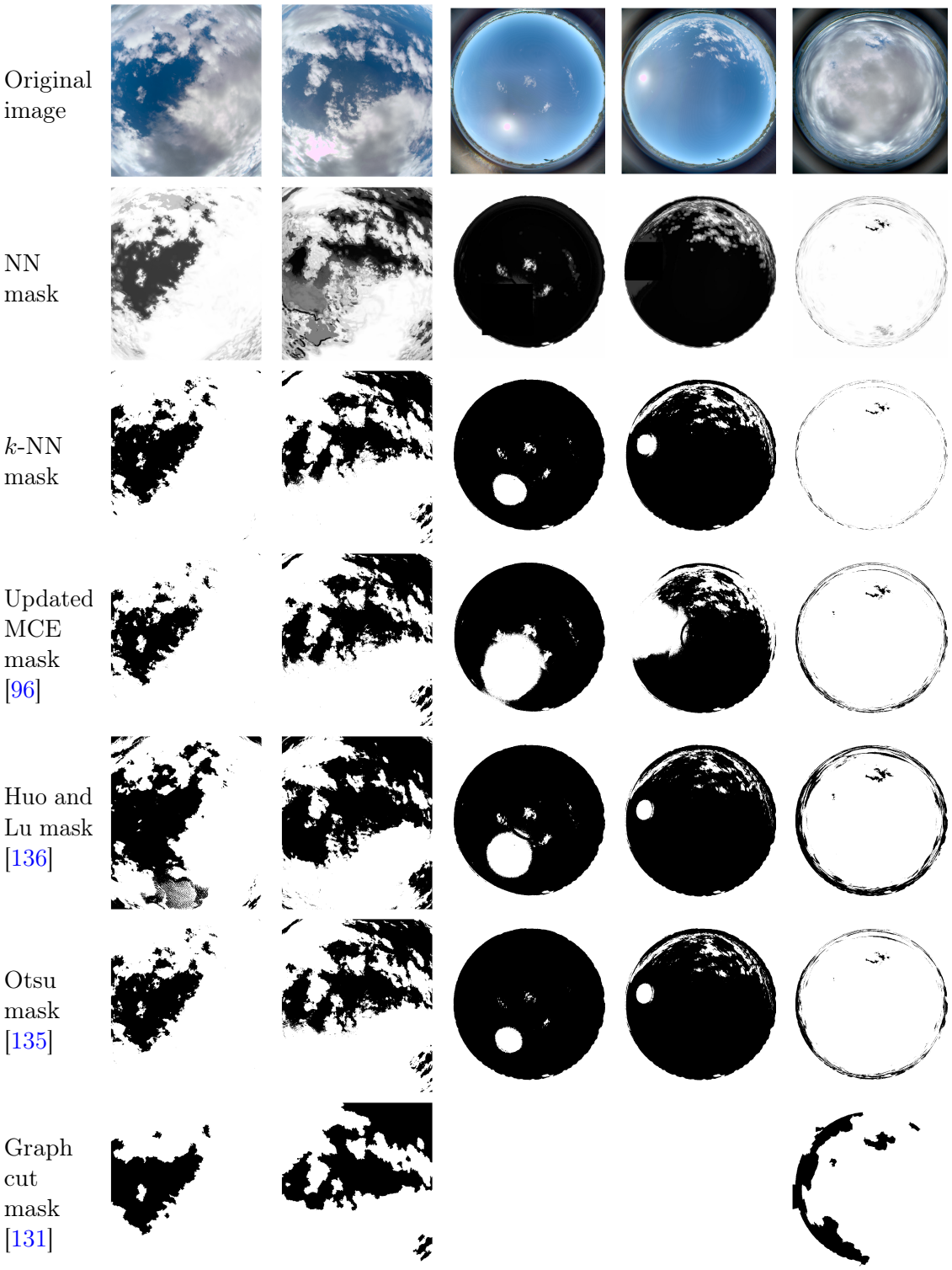

4.4.4.1 Method presentation

Multiple approaches have been implemented to estimate cloud motion. The cross-correlation method (CCM), proposed in [147], is applied on two successive sky images to calculate motion vectors, and then filtered through a 5-minute moving average filter [97]. Cloud tracking techniques can be employed as well: the cloud mask is distributed into an angular/radial grid and clouds' general motion is estimated using the CCM between every cell in the grid [86]. Particle image velocimetry (PIV) [148] has been used as well in order to determine cloud motion [95]. This estimation can be improved by applying k-means clustering on the calculated motion vectors [96], in order to estimate the dominant cloud motion. Finally, optical flow algorithms can be used. The model proposed in [94] uses a dense optical flow algorithm that provides motion estimation for every pixel [149]. In [138], cloud motion is estimated based on the Farnebäck optical flow algorithm, showing robust and accurate motion estimation. The accurate estimation of cloud motion [94, 138] is due to the two main assumptions of optical flow algorithms: the persistence of pixels' intensity, and that the adjacent pixels move similarly. In most cases, cloud motion meets these assumptions (a robustness study is carried out in Section 4.4.4.2 to ensure the validity of this approach). In addition, the optical flow algorithm is specialized in motion estimation with small magnitudes [150], which can be the case for clouds. For this reason, the optical flow algorithm is employed in this work to estimate cloud motion. This method takes two successive 8-bit[4] frames in order to estimate the displacement. Now, since the optical flow algorithm is based on the persistence of the object's intensity I, the two successive images can be written as:

$$I(x, y, t) = I(x + \Delta x, y + \Delta y, t + \Delta t) \tag{4.18}$$

then, Taylor series approximation is applied on the right-hand side of Equation (4.18) to give:

$$I(x + \Delta x, y + \Delta y, t + \Delta t) = I(x, y, t) + \frac{\partial I}{\partial x}\Delta x + \frac{\partial I}{\partial y}\Delta y + \frac{\partial I}{\partial t}\Delta t + \dots \tag{4.19}$$

Combining Equation (4.18) and Equation (4.19), and keeping the first-order terms only gives:

$$\frac{\partial I}{\partial x}\Delta x + \frac{\partial I}{\partial y}\Delta y + \frac{\partial I}{\partial t}\Delta t = 0 \tag{4.20}$$

Finally, dividing by Δt we get:

$$I_x u' + I_y v' + I_t = 0 \tag{4.21}$$

where u' and v' are the pixel's displacement:

$$u' = \frac{\Delta x}{\Delta t} \qquad\qquad v' = \frac{\Delta y}{\Delta t} \tag{4.22}$$

and I_x, I_y, and I_t are the spatial and temporal gradients of the object's intensity I:

$$I_x = \frac{\partial I}{\partial x} \qquad I_y = \frac{\partial I}{\partial y} \qquad I_t = \frac{\partial I}{\partial t} \tag{4.23}$$

Now, in order to determine u' and v', the ill-posed Equation (4.21) should be solved: to do so, additional constraints must be formulated, leading to different approaches (see [151]). The most popular optical flow algorithms are the sparse and dense optical flow algorithms [152]. The sparse optical flow algorithms compute the motion vector of a predefined set of pixels, thus requiring some pre-processing in order to determine the objects to track. The

[4] Using 8-bit images is a requisite for the OpenCV implemention of the algorithm [121], which is used in this work.

dense optical flow algorithms estimate the motion of every pixel. They can be carried out using the dense pyramid Lucas-Kanade algorithm [153], the Farnebäck algorithm [154, 155], among others. In this work, the Farnebäck algorithm, which proved its success in previous works [94, 138], is used to calculate the motion vectors. The main idea behind this algorithm is to approximate the neighbors of a specific pixel in the first image by a quadratic equation. The detailed mathematical solution of the ill-posed Equation (4.21) can be found in [155]. Finally, it should be noted that each motion vector is expressed in polar coordinates, in order to facilitate the estimation of dominant direction and magnitude, as explained in the following.

4.4.4.2 Implementation of the cloud motion estimation algorithm

In this section, the implementation of this algorithm using the openCV library [121] is presented, then the robustness of the approach to different types of motions is examined on artificially generated test cases. Finally, the algorithm is tested on real test cases.

Several parameters have to be fixed to implement this algorithm. For example, the Farnebäck algorithm divides the images into smaller averaging windows (to fight against noise), whose dimension has to be fixed. Increasing the dimension of the window will result in a robust and better motion estimation, however it risks to increase its blurriness due to the averaging nature of the window. Then, pyramid layers (akin to convolutional layers) are constructed for every window in the image. This is done to account for fast motion in the image. The number of layers and the resolution change in the convolution process are to be defined. After the layers are formed, the optical flow is applied on the highest layer and up-sampled to the original image. After several tests, the average window size is fixed to 15 by 15 pixels (which corresponds to the smallest window size possible that did not result motion blurriness), and the number of pyramid layers is fixed to 10 layers (determined by the visual assessment of the motion estimation layers).

This method is applied on a first test case, shown in Figures 4.14a and 4.14b, where a cloud is manually shifted (by translating the pixels' value) by 20 pixels to the bottom, which corresponds to an angle of 90° in the image coordinate system, while its intensity and shape are preserved. The resulting motion, presented in Figures 4.14c and 4.14d, shows that the Farnebäck algorithm is able to accurately estimate the magnitude and the direction of the artificial motion in this case. A second test case examines the robustness of this method against intensity and texture variations. In addition to the same shifting than in the first test case, the cloud's intensity is uniformly fixed to 15% of the clouds' maximal intensity value to induced texture variation, as shown in Figures 4.15a and 4.15b. The results shown in Figures 4.15c and 4.15d highlight the effects of object's intensity change: the algorithm is able to accurately detect the motion direction and magnitude even though the intensity and the texture is changed.

The robustness of the algorithm to deformation is now tested in the third test case. The cloud is shrunk by 10% towards the center of the box highlighted in red in Figures 4.16a and 4.16b. The resulting estimated motion is shown in Figures 4.16c and 4.16d. The shift between the applied motion magnitude and the peak of the histogram in Figure 4.16d is explained by the fact that the motion applied to the center of the shape is different than the motion applied to boundaries since the shape shrunk: the algorithm detects motion on the boundaries (where gradients exist) and since the intensity of the center is uniform for the two frames, no motion can be detected (no gradient can be calculated). This fact indicates that the dominant magnitude should not be determined directly from the histogram peak (which does not correspond to the true cloud motion magnitude), but rather that a smarter approach, robust to non-rigid motion types, should be considered.

Finally, let us study two real cases. The first example, given in Figure 4.17, consists in the classical case of a single layer of clouds subject to a translation-like motion. The corresponding histograms of the motion vectors are given in Figures 4.17c and 4.17d. However the resulting

(a) Original image.

(b) Image with manually-shifted cloud and estimated spatial gradient (in red).

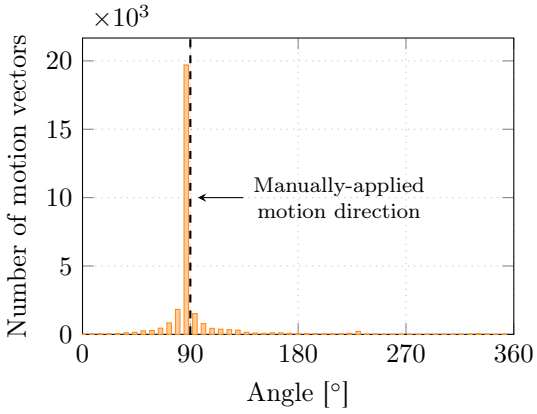

(c) Distribution of motion vectors' direction.

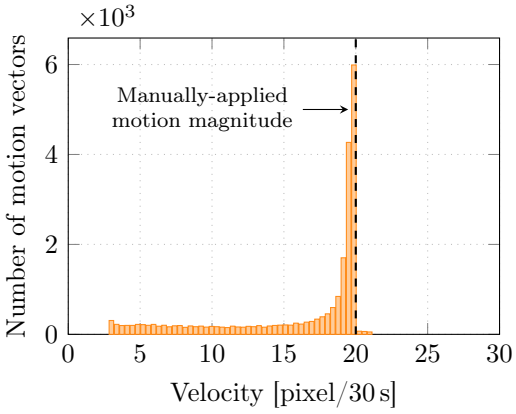

(d) Distribution of motion vectors' magnitude.

Figure 4.14: Cloud motion estimation: test case 1.

histograms can not be compared to the ground truth values, but the visual analysis of this example asserted that the peak direction corresponds to the clouds motion direction. In the second example, the more complex case of two cloud layers with distinct motions is considered. As can be seen in Figure 4.18, the estimated cloud motion shows two different directions expressed by the two peaks[5] appearing in Figure 4.18c. It should be mentioned that even though only one motion direction is considered in the sequel (see Section 4.4.5), this examples shows that the optical flow algorithm allows to consider the complex situations of cloud layers with different motions, which may lead to improved results in such cases.

4.4.5 Localization of the region of interest

The proposed hybrid algorithm uses a so-called region of interest (ROI), determined using the estimated dominant direction and dominant magnitude of the cloud cover. These values are determined using the k-means clustering algorithm [156], which is used in [95, 86, 96]. A two-class k-means clustering is applied on the directions of all non-zero motion vectors; the dominant center is then selected as the dominant direction of clouds. The decision of choosing two-class k-means clustering is based on the ability of the model to handle two

[5]The correctness of these two estimated directions has been confirmed visually by examining a sequence of images.

(a) Original image.

(b) Image with manually-shifted cloud, and changed intensity and texture (in gray).

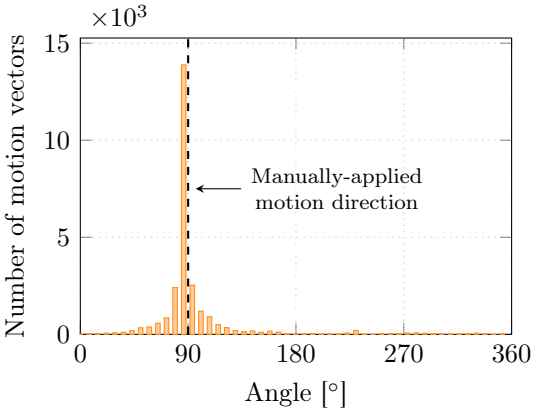

(c) Distribution of motion vectors' direction.

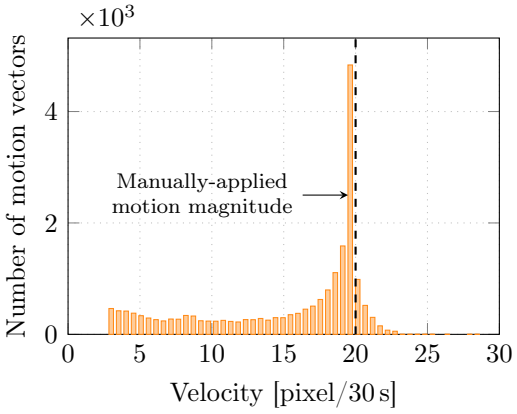

(d) Distribution of motion vectors' magnitude.

Figure 4.15: Cloud motion estimation: test case 2.

different clouds motion direction and the extreme rarity of the three-direction cloud motion situation. Finally, the dominant magnitude of motion vectors is obtained as the center of a one-class k-means clustering of all non-zero motion vectors having the dominant direction $\pm 5°$. Generally speaking, only one peak can be found for motion vectors having the dominant direction. This approach has been applied to the example presented in Figure 4.17: the histogram of each motion vector's direction, along with the estimated dominant direction is presented in Figure 4.19a; the histogram of each motion vector in the dominant direction, along with the estimated dominant magnitude is shown in Figure 4.19b. It should be noted that for situations with multiple cloud directions as in Figure 4.18, the dominant direction is chosen to be the one with the higher occurrence; in that example, the chosen dominant direction would be 125°, which corresponds to the second peak.

Now, with the help of the estimated direction σ_d and magnitude σ_s of the dominant cloud motion, the polar coordinates of the center of the ROI, in a local coordinate system centered on the Sun, are obtained as:

$$\phi = \sigma_d + \pi \tag{4.24}$$

$$\ell = \sigma_s H \tag{4.25}$$

where H is the forecast horizon.

(a) Original image.

(b) Image with shrunk and manually-shifted cloud (the shrunk area is highlighted in red).

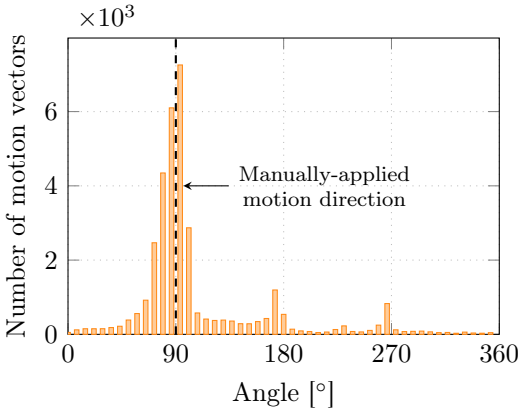

(c) Distribution of motion vectors' direction.

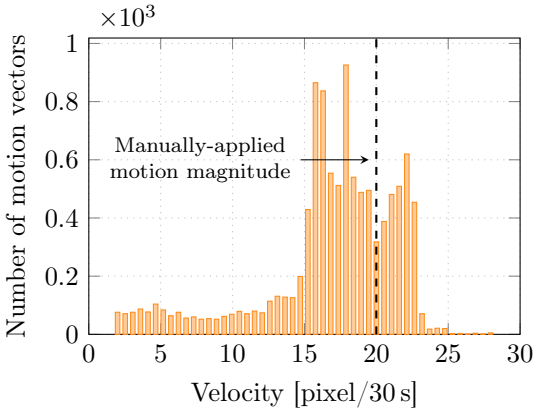

(d) Distribution of motion vectors' magnitude.

Figure 4.16: Cloud motion estimation: test case 3.

The ROI corresponding to the images presented in Figure 4.17 is given in Figure 4.20b. It should be noted that the ROI is chosen to be larger than the Sun's apparent size to compensate for the uncertainties in the calculation of the dominant motion (inaccuracies in its estimation, non-rigid transformations of clouds, etc.). Also, instead of a circle, the shape of the ROI is an ellipse with its semi-minor axis parallel to the dominant direction, because there are more uncertainties on the dominant direction than on the dominant magnitude. As a result, the ROI has a surface of around 29 times the Sun's (56548 pixels, whereas the Sun has an apparent size of around 1963 pixels); this value has been fixed after multiple tries to find an optimal trade of between having a too small ROI (in which case it would not contain enough information[6]) and a too large one (in which case it may contain irrelevant information, such as clouds that will not interact with the Sun). Finally, note that a square circumscribing the ellipse-shaped ROI is extracted from the RBG image, to be later introduced as an input to the DNI forecast model (noted as $\mathrm{ROI}_H^{\mathrm{RGB}}$ in Figure 4.5).

Using a ROI localized using dominant direction and magnitude ensures that the information extracted corresponds to the required DNI forecast, by analyzing the cloud motion (magnitude and direction) with respect to the Sun, which are the main cause of DNI ramps, as shown in Figure 4.1. It should however be noted that this approach also limits the validity of the

[6]See Section 4.7.2.2 for an illustration of what could happen if the chosen ROI is too small.

(a) Sky image taken at instant $t - 30$ seconds.

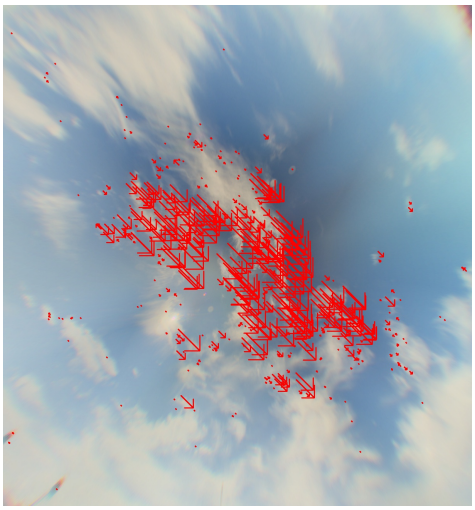

(b) Motion estimation map on the sky image taken at instant t; estimated speed is proportional to the arrows' length (for clarity's sake, the motion of some pixels only is displayed).

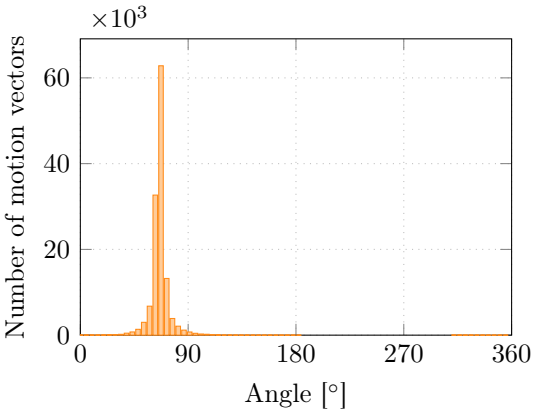

(c) Distribution of motion vectors' direction.

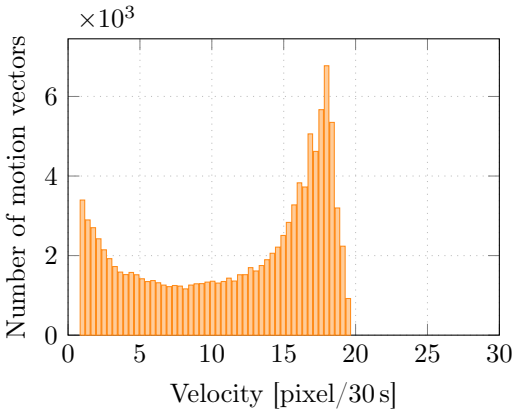

(d) Distribution of motion vectors' magnitude.

Figure 4.17: Cloud motion estimation: real case 1.

proposed model: since the value ℓ is determined by the cloud motion magnitude and the forecast horizon, the ROI can be localized outside the image frame when long forecast horizons are considered or when cloud speed is high. As a consequence, the ROI localization algorithm is tested on seven days from different seasons (with different solar heights, different cloud speeds and directions), and the percentage of the ROI localized outside the image frame, for each forecast horizon H between 5 min and 30 min, is recorded. This test shows that:

- for $H = 5$ min and $H = 10$ min, 0% of ROIs are outside the image frame;
- for $H = 15$ min, 10% of ROIs are outside the image frame;
- for $H = 20$ min, 50% of ROIs are outside the image frame;
- for $H = 25$ min, 79% of ROIs are outside the image frame;
- for $H = 30$ min, 95% of ROIs are outside the image frame;

As a result, this algorithm will not face problems for forecast horizons: 5, 10, and 15 minutes, however, for longer forecast horizons, the proposed hybrid model should be coupled with other

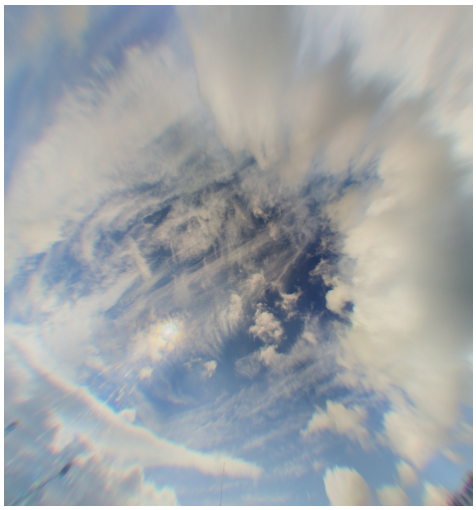

(a) Sky image taken at instant $t - 30$ seconds.

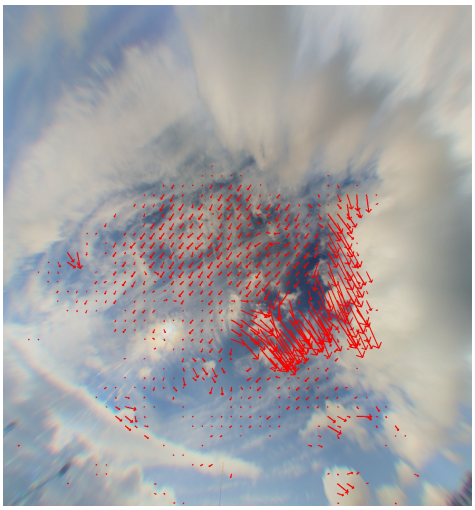

(b) Motion estimation map shown on the sky image captured at instant t.

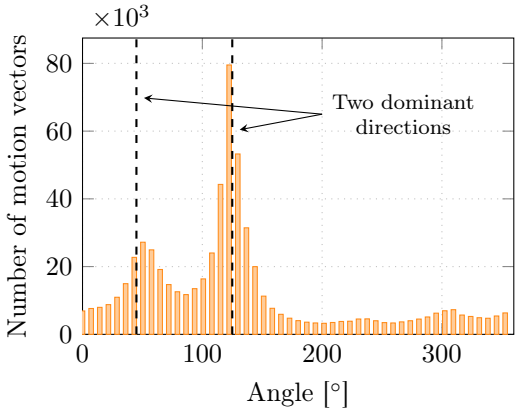

(c) Distribution of motion vectors' direction.

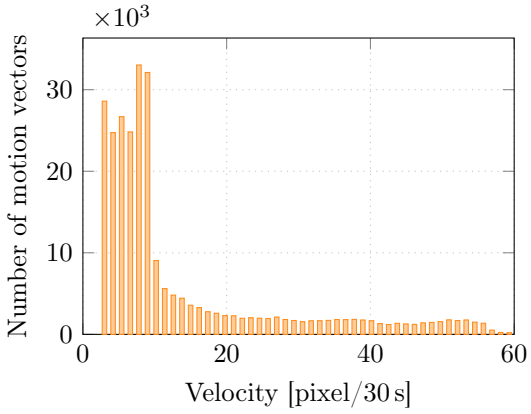

(d) Distribution of motion vectors' magnitude.

Figure 4.18: Cloud motion estimation: real case 2.

forecast model, in case the ROI localized is outside the image frame. Thus, the forecast horizon is limited to 15 min, and for the 10% of ROIs are outside the image frame[7] (for $H = 15$ min), the model will use a shifted ROI, so that it is entirely within the image bounds (the dominant direction is thus respected, while the dominant speed is adapted).

4.4.6 Determination of the cloud fraction in the ROI

Provided that the ROI is accurately localized, the mean value of its cloud mask at time k, referred to as the cloud fraction in the ROI ($\mathrm{CF}_{\mathrm{ROI}_H}(k)$), will strongly influence the DNI value at time $k + h$. This feature can thus be very informative in the learning process of the DNI forecast model. However, since the cloud fraction in the ROI is calculated using a binary cloud mask (obtained using the k-NN approach described in Section 4.4.3), it can lead to an inaccurate forecast of the DNI amplitude, since no distinction is made between thin and thick clouds. To compensate for this effect, in case of thin clouds, $\mathrm{CF}_{\mathrm{ROI}_H}$ is replaced by a value $\mathrm{CF}'_{\mathrm{ROI}_H}$. This case is detected if the Sun is blocked by clouds (as detected by the k-NN model), but still apparent (as detected using a function, built-in in the camera, that provide information about the visibility of the Sun). The new value $\mathrm{CF}'_{\mathrm{ROI}_H}$ is then obtained as a

[7] These cases essentially happen at the end of the day, when the SZA is low.

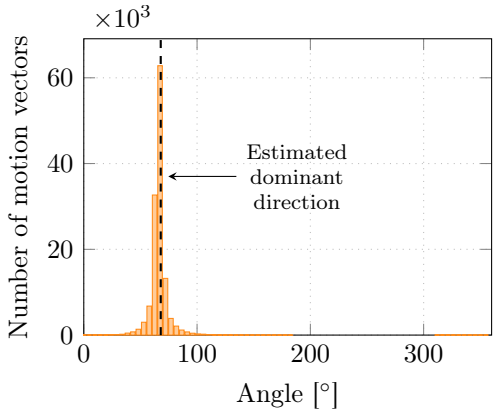

(a) Distribution of the motion vectors' direction of every pixel in the image; the dominant direction of clouds' displacement is then determined using the k-means clustering method.

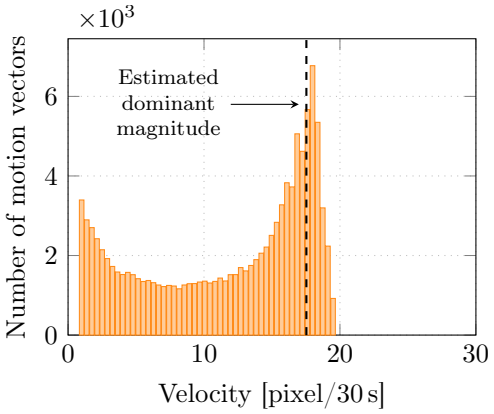

(b) Distribution of the motion vectors' magnitude having the dominant direction previously estimated; the dominant magnitude of the motion vectors in the dominant direction is then determined using the k-means clustering method.

Figure 4.19: Histograms showing the distribution of (a) the motion vectors' direction and (b) the motion vectors' magnitude in the dominant direction (results based on the images presented in Figure 4.17).

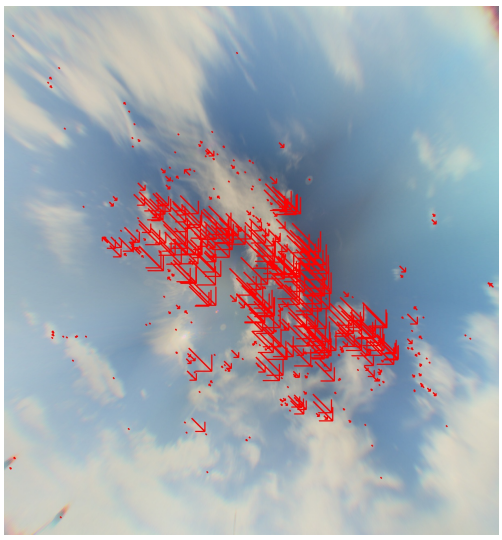

(a) Flow estimation map (estimated speed is proportional to the red segments' length). For clarity's sake, the motion of some pixels only is displayed.

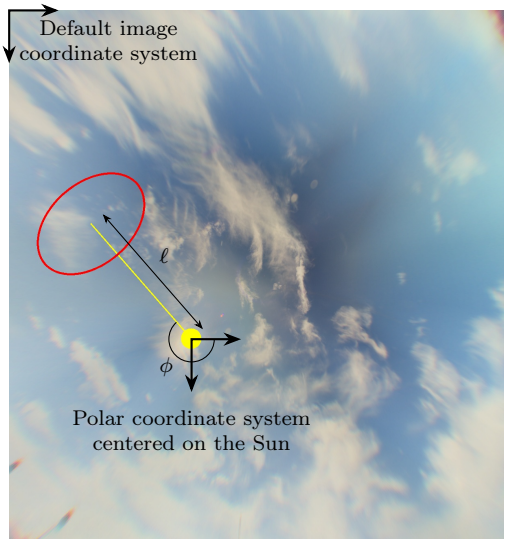

(b) Resulting dominant direction (yellow line) and region of interest for $H = 15$ min (red ellipse).

Figure 4.20: Determination of the region of interest: (a) Estimated motion using the Farnebäck optical flow algorithm on two successive images, and (b) obtained region of interest using the k-means clustering method.

weighted average of $\mathrm{CF}_{\mathrm{ROI}_H}$ and k_c:

$$\mathrm{CF}'_{\mathrm{ROI}_H}(k) = \begin{cases} \beta(k)\mathrm{CF}_{\mathrm{ROI}_H}(k) + (1-\beta(k))k_c(k), & \alpha(k) > \beta(k) \\ (1-\alpha(k))\mathrm{CF}_{\mathrm{ROI}_H}(k) + \alpha(k)k_c(k), & \alpha(k) \leqslant \beta(k) \end{cases} \tag{4.26}$$

where $\alpha(k)$ is the prediction error at time $k-h$ of a simple model based on the estimated cloud fraction in the ROI:

$$\alpha(k) = \mathrm{DNI}(k) - \mathrm{DNI}_{\mathrm{CS}}(k)\mathrm{CF}_{\mathrm{ROI}_H}(k-h) \tag{4.27}$$

and $\beta(k)$ is the prediction error at time $k-h$ of a simple model based on a persistence of k_c:

$$\beta(k) = \mathrm{DNI}(k) - \mathrm{DNI}_{\mathrm{CS}}(k)k_c(k-h) \tag{4.28}$$

The idea is simple: when, during the previous forecast with these simple models, a persistence on k_c gave better results, use a weighted average with more weight to k_c; if not, give more weight to $\mathrm{CF}_{\mathrm{ROI}_H}$.

4.5 Hybrid DNI forecast model

As illustrated in Figure 4.21, the DNI forecast model can be divided into three main parts that are detailed in the following sections. The first part, responsible for image feature extraction, is a convolutional neural network (CNN). The second part is a multi-layer perceptron (MLP) with the cloud fraction ($\mathrm{CF}_{\mathrm{ROI}_H}$) and the clear-sky DNI forecast as inputs. The outputs of the CNN and the MLP networks are then fed to a 'Regression MLP', used to merge extracted features and provide the DNI forecast.

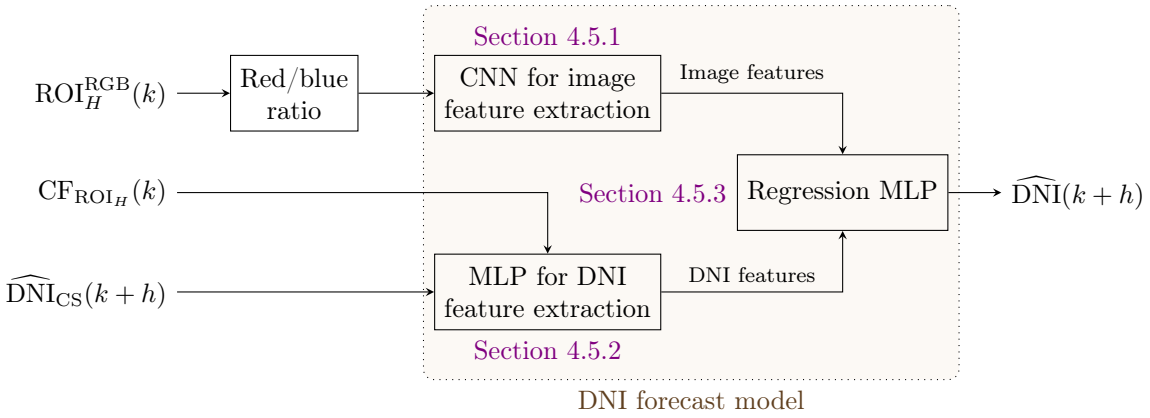

Figure 4.21: DNI forecast model that takes the RGB image of the region of interest ($\mathrm{ROI}_H^{\mathrm{RGB}}$), the cloud fraction in the region of interest ($\mathrm{CF}_{\mathrm{ROI}_H}$), and the clear-sky DNI forecast ($\widehat{\mathrm{DNI}}_{\mathrm{CS}}$) as inputs, and outputs the DNI forecast ($\widehat{\mathrm{DNI}}$). This process is done through three NNs: a CNN to extract image features from the red-to-blue ratio of the $\mathrm{ROI}_H^{\mathrm{RGB}}$, a MLP to extract DNI features from $\mathrm{CF}_{\mathrm{ROI}_H}$ and $\widehat{\mathrm{DNI}}_{\mathrm{CS}}$, and a MLP responsible for combining theses features and forecast DNI.

4.5.1 CNN for image feature extraction

To help highlighting clouds, the red-to-blue (R/B) ratio of the ROI determined in Section 4.4.5 is now introduced to a CNN. By definition, a CNN consists of an input layer, a convolutional part, fully connected layers, and an output layer. The convolutional part of the CNN may consist of the following layers.

- A convolutional layer performs a dot product of the convolution kernel. As this kernel slides along the input matrix, the convolution operation generates a feature map, which becomes the input of the next layer.
- A pooling layer is responsible for the spatial size reduction, is applied on the features map extracted from the convolutional layer, and reduces its dimension by combining the output of some neuron clusters.

The fully connected network is a dense neural network with different number of layers and neurons per layer. The goal of this network is to learn the relation between DNI and clouds' optical depth. To achieve this goal, and prevent overfitting while learning, the architecture should be carefully chosen by optimizing the following:

- the number of convolutional and pooling layers;
- the number of filters in each convolutional layer (a filter is a mathematical operation that extracts features from the input);
- the filter dimension;
- the pooling window and type, responsible for the input image's downsampling;
- the position and rate of dropout layers (acting as regularization layers);
- the number of fully-connected layers;
- the number of neurons per fully-connected layer;
- the activation functions.

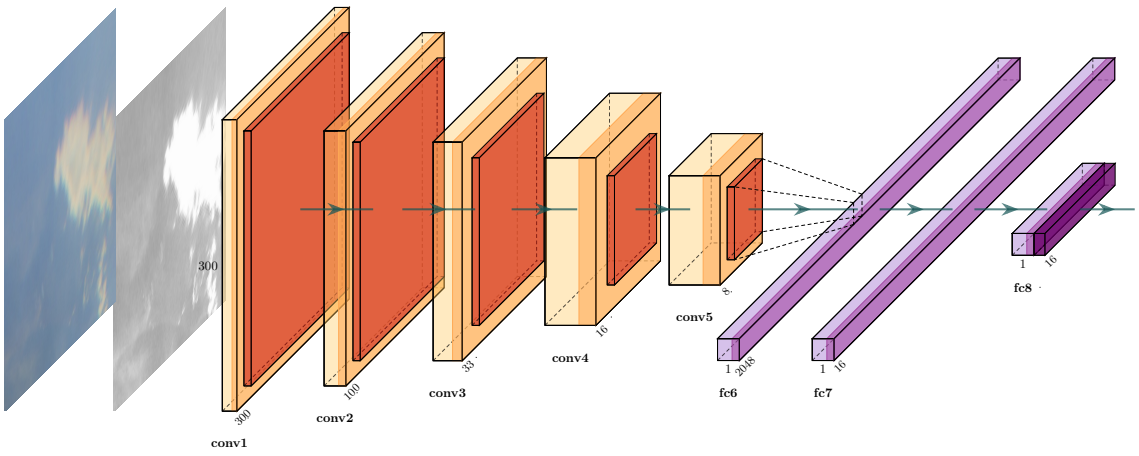

Figure 4.22: A CNN network characterized by its convolutional layers (in light yellow), its pooling layers (in orange), and its fully-connected layers (in purple); it takes the red-to-blue ratio of the ROI RGB image as input, and provides image features as output.

The CNN input is the red-to-blue ratio of the 300×300 RGB image of the ROI. The RGB image is bigger than the ellipse ROI to give the CNN more spatial information about the current ROI. After many tests, based on trial and error, during which multiple networks have been trained, the best performing network, in terms of validation results, has been obtained. It is a network with five convolutional layers network having an increasing number of filters from

16 in the first layer, to 32, 128, and 255 for the intermediate layers; This number then decreases to 128 on the last convolutional layer, before the fully-connected part of the architecture. The filter dimension is chosen to be 30×30 for the first layer, then 3×3, and finally 2×2 for the three remaining layers. Maxpooling has been used, with a 3×3 window for the first two layers and a 2×2 for the last three. The fully-connected part consists of three layers: a flatten layer, a 16-neuron layer, and a 16-neuron output layer. It should be noted that a dropout regularization with a rate of 50% is performed for each layer, and that the activation function used for all the neurons in the fully-connected layers is the sigmoid function.

4.5.2 MLP for DNI feature extraction

A MLP network (a dense network consisting of multiple fully-connected hidden layers) is responsible for learning the correlation between $\mathrm{CF}_{\mathrm{ROI}_H}$ and $\mathrm{DNI}_{\mathrm{CS}}$. It is characterized by:

- the number of hidden layers;
- the number of neurons per layer;
- the activation function used;
- the position and rate of dropout layers.

Again, based on various tests, the following topology has been determined: 2 hidden layers with 8 and 16 neurons, respectively, and a 16-neuron output layer. A dropout regularization with a rate of 50% has been performed after each layer, and the activation function used is the sigmoid function.

4.5.3 Regression MLP

This MLP is merely responsible for combining the outputs of the two previous networks. Its topology, determined by trial and error, is the following: two 8-neuron layers, and a 1-neuron output layer providing the DNI forecast. A dropout regularization with a rate of 50% has been performed after each layer, and the activation function used is the sigmoid function.

4.5.4 DNI forecast model training and evaluation

As explained in Section 3.3.1, the database consists of 40 days, each with 1200 observations (sky images and DNI measurements) starting from 7:00 AM till 5:00 PM, with a sampling time of 30 seconds. This database is split into 22 days for training and cross-validation (representing 26400 observations), 16 days for testing (representing 19200 observations), and two days for cases studies (representing 2400 observations). The DNI forecast model is trained and validated using a cross-validation technique: the dataset is randomly but equally divided into five groups of samples called folds; in each fold 70% of data is used for training and 30% for validation. Adaptive moments (Adam), a computationally efficient stochastic gradient descent optimization method based on an adaptive estimation of the momentum [116], is used. To prevent overfitting, dropout regularization is performed for each layer in the network with a rate of 50%. After testing, the loss function is chosen to be the mean squared error over the mean average error. Finally, the models are trained using 20 epochs for each fold in order to assure convergence.

The DNI variability analysis for the 34 days in the training and validation dataset, and the test dataset, performed in Section 3.3.1, is recalled in Table 4.5. It presents the mean and standard deviation of DNI variations and the normalized ramp count. The high mean and standard deviation of DNI variations obtained shows the high variability of the mixed situations appearing in Odeillo, especially for long forecast horizons. These characteristics

explain why state-of-the-art models usually struggle with these complex situations, and why persistence models fail to provide acceptable results.

Table 4.5: Variability analysis for the 34 mixed situations in the training and validation dataset, and in the test dataset. $\mu_{\Delta\text{DNI}}$ and $\sigma_{\Delta\text{DNI}}$ are the mean and standard deviation of DNI variations, respectively, and nRC is the normalized ramp count.

Dataset	Metric	Forecast horizon H [min]		
		5	10	15
Training and validation	$\mu_{\Delta\text{DNI}}$ [W m^{-2}]	86.00	116.41	135.28
	$\sigma_{\Delta\text{DNI}}$ [W m^{-2}]	179.72	215.79	234.63
	nRC	0.20	0.24	0.27
Test	$\mu_{\Delta\text{DNI}}$ [W m^{-2}]	101.30	132.84	154.48
	$\sigma_{\Delta\text{DNI}}$ [W m^{-2}]	189.86	221.44	239.07
	nRC	0.25	0.32	0.35

4.6 Results

In this section, the hybrid model performance is evaluated based on some performance metrics. First, these performance metrics are presented, then the hybrid model's training and testing (on clear-sky, overcast, and mixed situations) is analyzed to highlight it pros and cons.

4.6.1 Performance metrics

Three performance metrics are used here to evaluate the models:

1. the normalized root mean squared error (nRMSE);
2. the skill factor (SF);
3. the ramp detection index (RDI).

The reader is referred to Section 2.2.5 for a detailed description of these metrics.

4.6.2 Analytical discussion

In this section, the effect of using HDR sky images in the forecasting process is analyzed by testing the hybrid model. The topology of the various neural networks appearing in this model has already been detailed in Section 4.5.

First, the results obtained on mixed situations only are analyzed: it represents 22 days in the training and cross-validation dataset, and 10 days in the test dataset. The values of nRMSE and SF are given in Figure 4.23. As can be seen, the hybrid model consistently outperforms the persistence model for each forecast horizon, with a SF ranging between 10% and 26%. The nRMSE values show that the model is able to accurately predict DNI on days not included in the model's training data, confirming the model's generalization ability. Note that higher SF values are observed in the test results (compared to cross-validation), because the performance of the forecast model is highly influenced by the image processing step, and some of the training days contain complex cloud patterns with highly variable DNI, leading to poor performance of the smart persistence model. The relation between nRMSE and DNI variability is studied in Section 4.7.2.

To showcase the performance of the proposed model under simpler sky situations, where the persistence model generally scores very low nRMSE values, the hybrid model is now applied

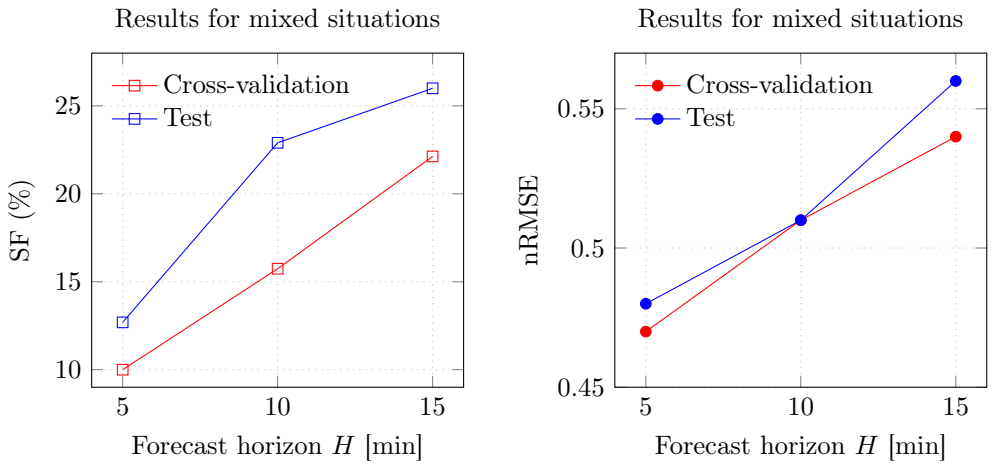

Figure 4.23: Hybrid model results for mixed situations: values of the normalized root mean squared error (nRMSE) and the skill factor (SF) as a function of the forecast horizon H.

on the 6 days in the test dataset that are not classified as mixed situations: 3 clear-sky days and 3 overcast days from different seasons, representing a total of 7200 observations. The results are found in Figure 4.24. As can be seen, the hybrid model once again consistently outperforms the persistence model for each forecast horizon, but – as expected – with a lower SF, ranging between 6% and 9.5%. The low nRMSE values and the positive SF scored by the hybrid model confirm that the model learned to distinguish clear-sky and overcast situations, which is another proof of the model's generalization ability. In addition, the model is able to compensate for seasonal variations of the maximal clear-sky DNI value thanks to the adaptive clear-sky model used in this study.

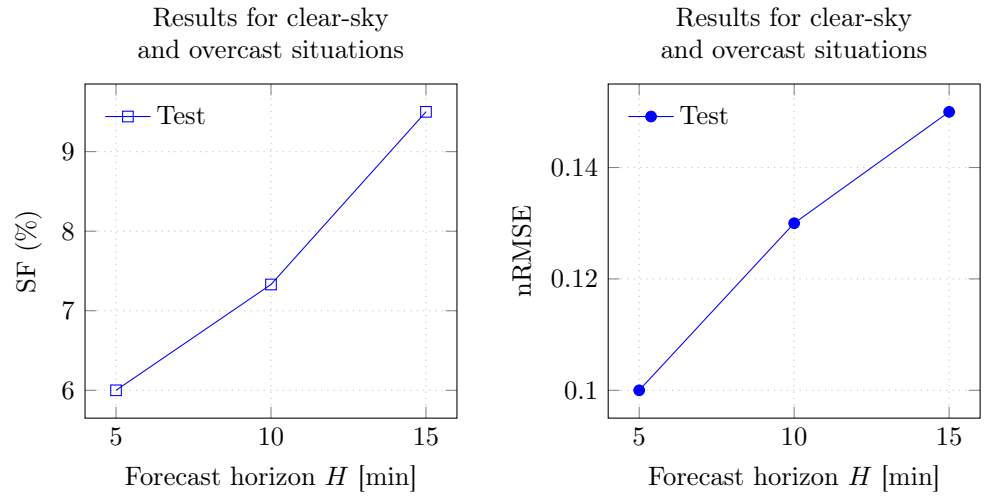

Figure 4.24: Hybrid model results on clear-sky and completely overcast situations: values of the normalized root mean squared error (nRMSE) and the skill factor (SF) as a function of the forecast horizon H.

4.7 Comparative study: hybrid model vs. RNN models

In this section, the hybrid model is pit against the observation-based RNN models (Section 3.3.3). First, the models performances on clear-sky, overcast, and mixed situations are compared by presenting the nRMSE, SF, and RDI on different datasets. Then, two cases with

different DNI variability are studied to gain more insight on the accuracy and performance of the hybrid model versus the RNN models.

4.7.1 Analytical discussion

In this section, the performance of the hybrid, LSTM, and CNN-LSTM models (determined in Section 3.3.3) are first compared on mixed situations in the test dataset (10 days), which are characterized by high DNI variability and hard-to-handle profiles. The results can be found in Figure 4.25: the hybrid model scores the lowest nRMSE values and the highest SF and RDI for each forecast horizon. LSTM and CNN-LSTM models, which are based on past DNI observations only, do not forecast DNI ramps as well as the hybrid model: cloud motion is indeed critical to better anticipate DNI variations. This superior performance justifies the integration and processing of HDR sky images, that translates into better ramp detection and accurate DNI forecasts compared to the models based on DNI measurements only. Finally, as already seen in Chapter 3, the CNN-LSTM slightly outperforms the LSTM model thanks to its additional convolutional layer.

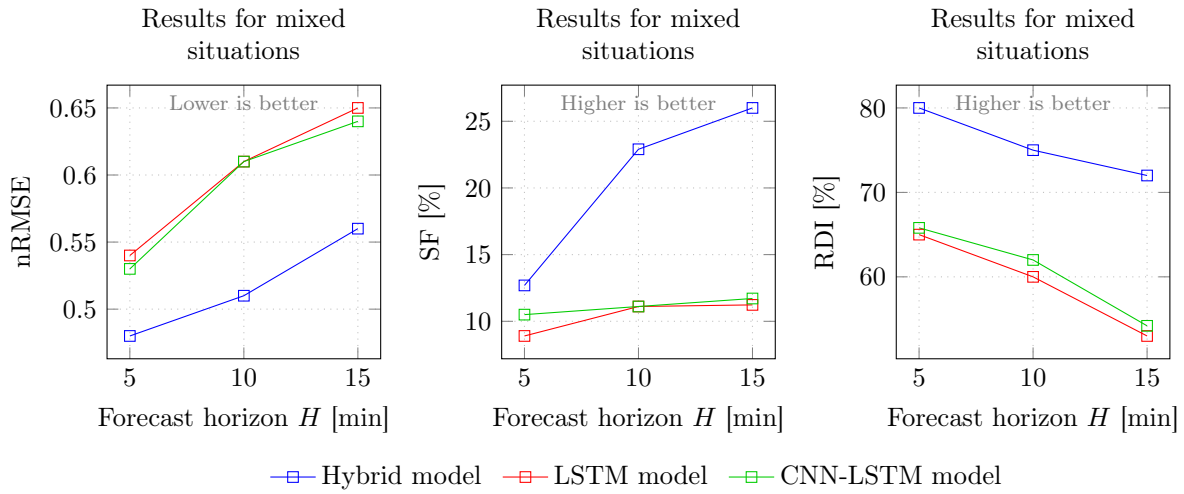

Figure 4.25: Comparison between LSTM, CNN-LSTM, and hybrid models on mixed situations in the test dataset. Left: normalized root mean squared error (nRMSE), center: skill factor (SF), right: ramp detection index (RDI).

The LSTM model, the CNN-LSTM model and the hybrid model are now compared on 6 days in the test dataset that are not classified as mixed situations: 3 clear-sky days and 3 overcast days from different seasons, representing 7200 observations. The smart persistence model generally scores very low nRMSE values on such cases. The results are given in Figure 4.26. As already seen in Section 4.6.2, the hybrid model consistently outperforms the smart persistence model for each forecast horizon, with a SF ranging between 6% and 9.5%. The low nRMSE values and the positive SF scored by the hybrid model confirm that the model learned to distinguish clear-sky and completely overcast situations. However, on such low-variability situations, the results obtained by the LSTM and CNN-LSTM models are considerably inferior to the results obtained by the smart persistence model. Contrary to the hybrid model, they are not able to correctly handle these situations, that were not included in the training database: although the nRMSE they obtain is low (around 0.16%), the smart persistence model is so performant in these cases that the RNN models score negative SF values (around -120% for $H = 5\,\text{min}$, -50% for $H = 10\,\text{min}$ and -25% for $H = 15\,\text{min}$). This demonstrates the benefits of including sky images: even though it has been trained with the same DNI measurements, the hybrid model is able to generalize to these situations.

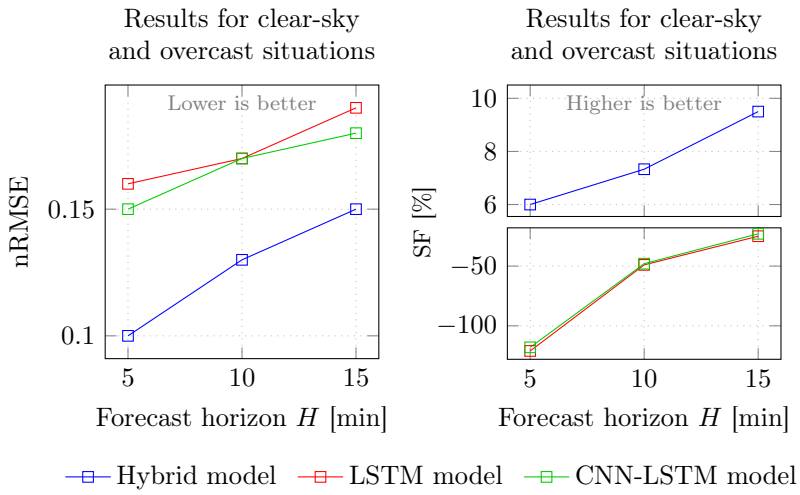

Figure 4.26: Comparison between LSTM, CNN-LSTM, and hybrid models on clear-sky and overcast days in the test dataset. Left: normalized root mean squared error (nRMSE), right: skill factor (SF). Note that the RDI is not represented, because there are very few ramps during these low-variability cases.

4.7.2 Case studies

In this section, to gain further insight into the performance of the LSTM, the CNN-LSTM, and the hybrid models, we focus here on the 15 min forecasts they provide during two additional mixed situations in the test database: one day with a high variability, and one day with a low variability.

4.7.2.1 Low-variability case

A low-variability case is presented in Figure 4.27: most of the day features a clear-sky situation, with thin clouds in the morning and the evening. The smart persistence model typically provides great results on such days: here, it outperforms both the LSTM and CNN-LSTM models ($\mathrm{nRMSE}_{\mathrm{PE}} = 0.13$, while $\mathrm{nRMSE}_{\mathrm{CNN-LSTM}} = 0.18$ and $\mathrm{nRMSE}_{\mathrm{LSTM}} = 0.19$), but the hybrid model still manages to come up with better results ($\mathrm{nRMSE}_{\mathrm{HM}} = 0.08$).

Thin clouds pose some serious problems for ordinary methods based on the cloud fraction, since they usually do not take into consideration clouds' thickness, leading to overestimation of the cloud fraction. As shown in Figure 4.27 before 10:00 and after 16:00, the use of the $\mathrm{CF}_{\mathrm{ROI}_H}$ correction ($\mathrm{CF}'_{\mathrm{ROI}_H}$) (see Section 4.4.6) and the red-to-blue ratio (Section 4.5.1) helps the hybrid model to compensate for these problems: without these corrections, the forecast DNI values would have been close to zero.

Let us focus now on a specific instant during the day: in Figure 4.27, the sky image taken at 15:30 is presented – precisely 15 min before a drop in DNI. The forecast given by the hybrid model shows a decrease in DNI because of the presence of clouds in the ROI, and, as predicted, a negative ramp takes place 15 min later.

4.7.2.2 High-variability case

A high-variability day is now presented in Figure 4.28. After a few hours of clear-sky (until 10:00), sudden high-frequency variations are observed. This case is challenging due to these fast and hard-to-predict DNI variations. Here, the smart persistence model performs very poorly, scoring $\mathrm{nRMSE}_{\mathrm{PE}} = 0.56$, while the LSTM and CNN-LTM models give $\mathrm{nRMSE}_{\mathrm{CNN-LSTM}} = 0.5$ and $\mathrm{nRMSE}_{\mathrm{LSTM}} = 0.52$; again, the hybrid model performs significantly better with $\mathrm{nRMSE}_{\mathrm{HM}} = 0.35$.

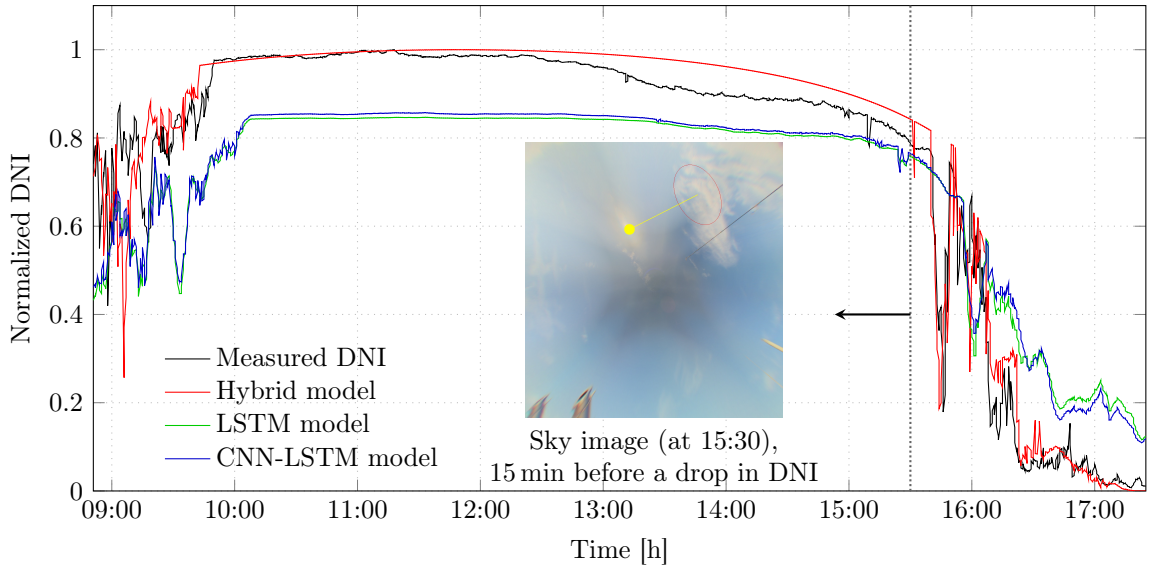

Figure 4.27: Low-variability DNI forecast at horizon $H = 15$ min. Associated nRMSE values are: $\text{nRMSE}_{\text{PE}} = 0.13$ for the smart persistence model, $\text{nRMSE}_{\text{CNN-LSTM}} = 0.18$ for the CNN-LSTM model, $\text{nRMSE}_{\text{LSTM}} = 0.19$ for the LSTM model, and $\text{nRMSE}_{\text{HM}} = 0.08$ for the hybrid model.

This high-variability day is a good example of the HDR sky images' contribution in the forecasting process: the LSTM and CNN-LSTM models are not able to predict DNI ramps, while the hybrid model is able to anticipate them due to the cloud motion analysis. In particular, the hybrid model is able to predict sudden DNI variations in the period between 11:00 and 13:00. The LSTM and CNN-LSTM models, however, fail to predict most of the ramps and perform poorly. Let us focus now on two specific instants during the day.

- Sky image 1, taken at 10:52, shows a situation with clouds in the ROI, leading to the correct forecast of a negative ramp 15 min later. Note also that the clouds are not in the center of the ROI: had a ROI of the same size as the Sun been chosen, that negative ramp would not have been correctly forecast.

- Sky images 2 and 3, taken at 15:25 and 15:40, respectively, feature a complicated sky situation, with thin clouds around the Sun and thick clouds approaching. In this situation, methods without special treatment for thin clouds would perform poorly. The proposed hybrid model proves to be robust and manages to detect the ramp provoked by the thick clouds that are in the ROI in sky image 2 and are starting to block the Sun 15 min later.

Table 4.6: Average execution time for the hybrid model, the LSTM model and the CNN-LSTM model (the computer used is described in Section 2.2.5).

Model	Execution time [s]						
Hybrid model	Distortion correction 0.12	Cloud detection 0.43	Cloud motion 0.45	ROI localisation 0.35	CF calculation 0.24	DNI forecast model $\ll 1$	Total 1.6
LSTM and CNN-LSTM models	Data acquisition $\ll 1$				DNI forecast $\ll 1$		Total $\ll 1$

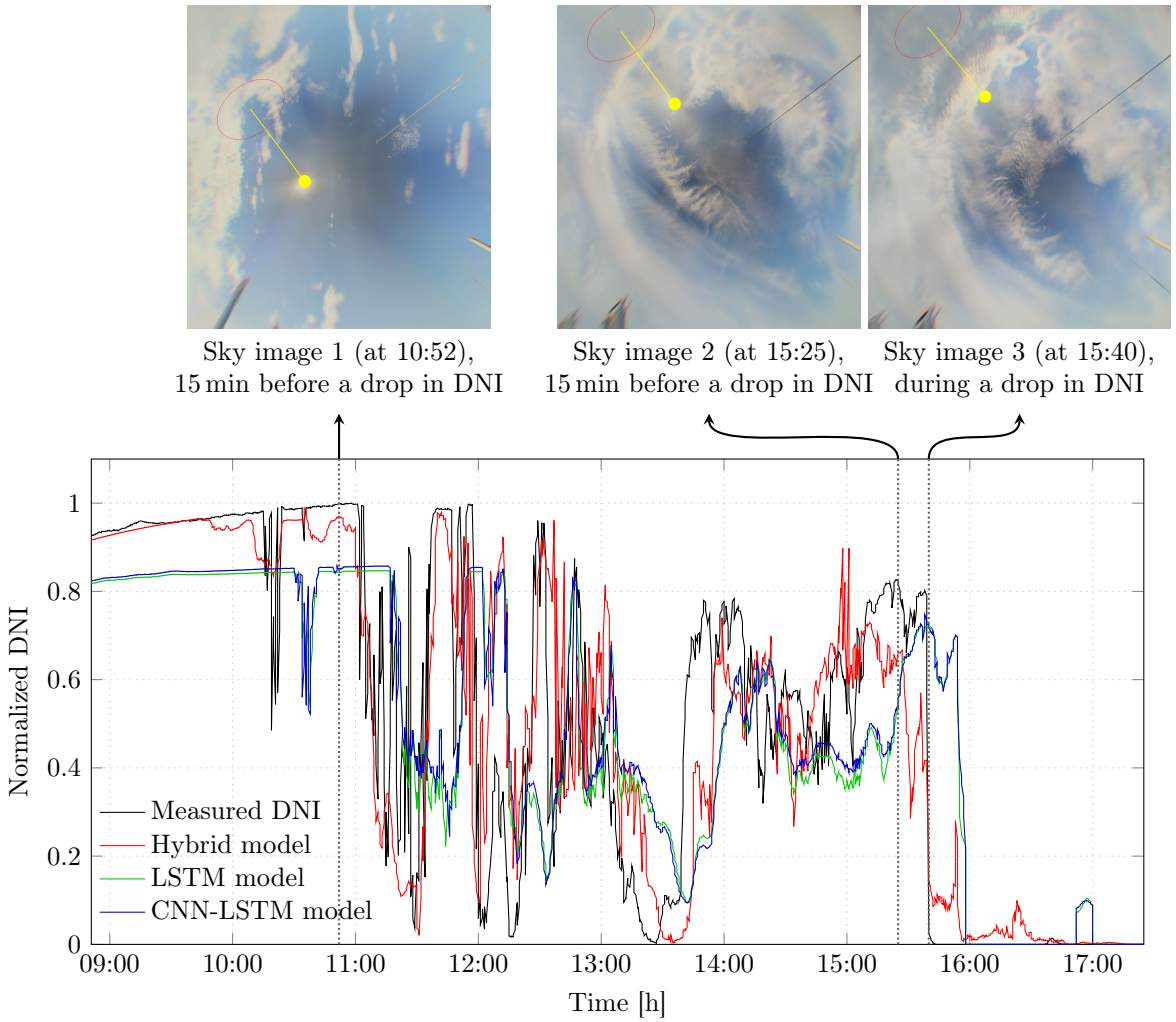

Figure 4.28: High-variability DNI forecast at horizon $H = 15$ min. Associated nRMSE values are: $\text{nRMSE}_{\text{PE}} = 0.56$ for the smart persistence model, $\text{nRMSE}_{\text{CNN-LSTM}} = 0.5$ for the CNN-LSTM model, $\text{nRMSE}_{\text{LSTM}} = 0.51$ for the LSTM model, and $\text{nRMSE}_{\text{HM}} = 0.35$ for the hybrid model.

4.7.3 Complexity study

The average execution time of all models, using the same computer as described in Section 4.5.4, is given in Table 4.6. The clear difference between the RNN models and the hybrid model, in terms of complexity, is due to their different functionalities. The hybrid model, based on image processing (cloud detection, dense motion estimation, etc.), is much more complex, whereas for statistical models like the RNN models, the data processing and forecasting steps are less time-consuming. Finally, it should be noted that all models provide forecasts within the sampling time (30 s) and can thus function in a real-time framework, such as model-based predictive control.

4.8 Online implementation of the hybrid model

The ultimate goal of the development of the hybrid model is to provide accurate DNI forecasts in real time. Thus, This model has been implemented on a server with Intel(R) Xeon(R) CPU E3-1230 v5 @3.40 GHz with 4 GB Ram. The HDR sky images are transferred every 30 seconds to a hard drive mounted on the described machine. The algorithm is able to read the HDR sky images stream and perform all the image processing tasks in real time to provide DNI forecasts. For every time step and after the code execution, the code registers in a Json file including the DNI forecasts, a description of the sky situation (clear-sky, overcast, or mixed) derived from the cloud segmentation model, and the cloud motion estimation (magnitude and direction). Finally, a sky image with the ROI is saved to help understand the provided forecasts. This information is provided to CSP infrastructure users via a graphical user interface (GUI), as shown in Figure 4.29.

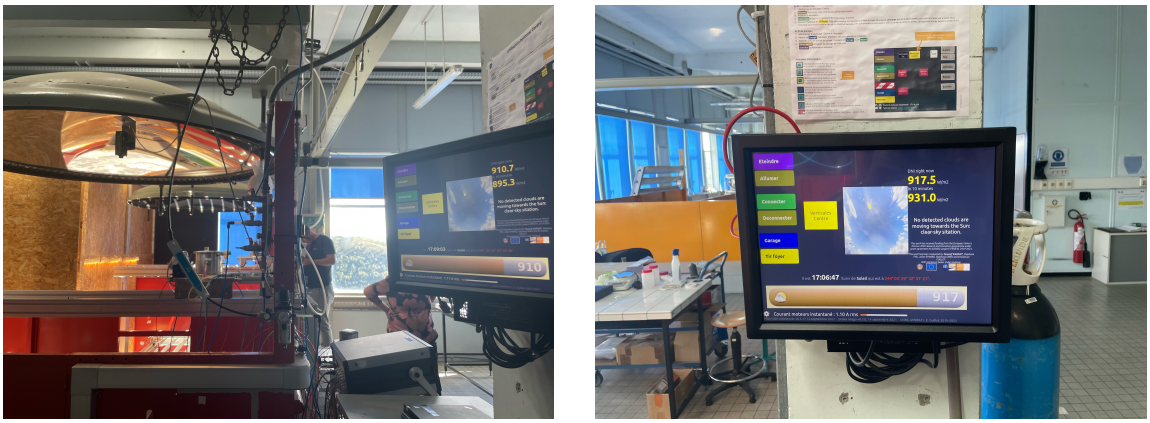

Figure 4.29: The GUI providing DNI forecasts to CSP infrastructure users (Odeillo, France).

4.9 Conclusion

This chapter deals with the development of a hybrid intrahour forecast model, combining knowledge-based and machine-learning approaches and taking DNI measurements and HDR sky images as inputs. This hybrid model is compared to LSTM and CNN-LSTM models that take solely past DNI observations as input, in order to assess the benefits of integrating HDR sky images in the forecasting process. The smart persistence model is also used as reference for the comparison.

Various image processing steps are performed in the proposed hybrid model. Cloud segmentation is carried out by a k-NN model, robust to the problems faced by threshold-based algorithms. A cloud motion estimation map, provided by a dense optical flow algorithm, allows

to determine an adaptive region of interest, with the help of the k-means clustering method. The forecasting step is performed using a combination of two neural networks: a CNN, which processes the ROI; and a MLP that takes the cloud fraction in the ROI and a forecast of the clear-sky DNI as inputs to finally forecast DNI at horizons between 5 min and 15 min.

The models are trained and cross-validated over 22 days (mixed situations) from different seasons, exhibiting various sky situations and clouds' types. Another dataset of 18 days is used for testing the developed models: 10 mixed situation test dataset, 2 mixed situation case studies, and 6 clear-sky and overcast situations. For mixed situations, results show that the tested models are capable of outperforming the smart persistence model: for the hybrid model, skill factor values range from 12% to 26% as the forecast horizon increases from 5 min to 15 min, whereas the LSTM and CNN-LSTM models score around 10% for all horizons, which means that the hybrid model is able to consistently outperform the LSTM and CNN-LSTM models. The ramp detection index shows that the tested models are capable of predicting DNI ramps: the hybrid model is able to forecast 72% to 80% of the ramps, whereas the LSTM and CNN-LSTM models are less efficient and detected between 53% and 66% of the ramps. This difference is due to the fact that LSTM and CNN-LSTM models are purely statistical and rely solely on past DNI observations to perform forecasts, without taking into account the sky situation: efficient cloud detection and accurate cloud motion estimation translates into better ramp detection and accurate DNI forecasts. For clear-sky and overcast situations, the smart persistence model produces very good results, and the results obtained by the LSTM and CNN-LSTM models are considerably inferior. However, the hybrid model still manages to outperform the smart persistence model, with skill factor values ranging from 6% to 9.5%. Thanks to the inclusion of HDR sky images, it successfully manages clear-sky, overcast, and mixed situations. As for the complexity of the models, the analysis shows that, while the hybrid model is more complex, time-consuming, and demands more computational resources, it is still able to provide forecasts within 7% of the 30 s sampling time.

In the framework of the H2020 project SFERA III, the proposed model has been implemented in situ to provide real-time DNI forecasts to CSP infrastructure users.

Part II

Model-based predictive control of a solar reactor dedicated to syngas production

Chapter 5

Modeling of the solar reactor

5.1 Introduction

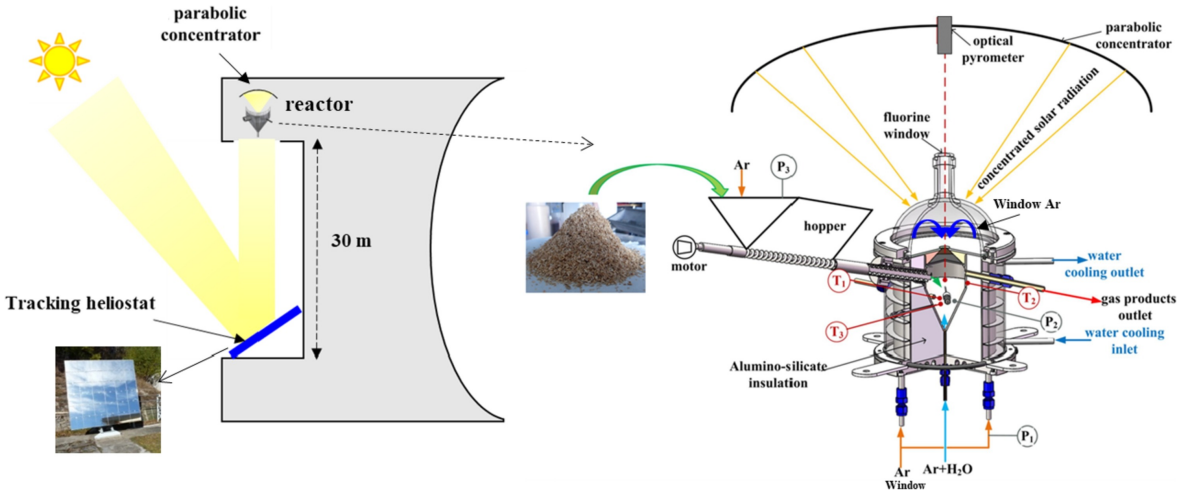

Figure 5.1: Solar reactor design [157].

The present chapter explores the modeling and dynamic control of a solar thermochemical reactor dedicated to the high-temperature steam-gasification of biomass (see Figure 5.1). Solar gasifiers have been experimentally studied since the early 80s, with the works of Gregg et al. [158] and Taylor et al. [159] about packed-bed and fluidized-bed technologies. Interest in solar thermochemistry has grown with climate-change considerations [160], especially since the mid 2000, leading to major innovative design investigations, as reviewed in Puig-Arnavat et al. [161]. More recent works have been proposed about double-loop fluidized beds, to separate oxidation and reduction zones for thermodynamic-cycle-based operation [162], or to separate gasification and combustion zones for a solar-autothermal hybrid operation [163]. A solar spouted-bed gasifier was conceived by Bellouard et al. [164], and its hybrid solar-autothermal operation was investigated successively by Boujjat et al. [157] and Curcio et al. [165] (see Figure 5.1). Other recent experimental works have demonstrated the feasibility of such hybrid operation [166, 167], but the question of its dynamic control is still open. It should be mentioned that the laboratory PROMES possesses a solar reactor prototype (see Figure 5.2), designed with the help of the CEA-LITEN, in order to contribute to the WP8 of the SFERA project which aims to:

- develop high-performance diagnostic and dynamic control tools for solar thermochemical fuel production system using concentrated solar energy;

- benchmarking the various technologies available for solar fuel production via CST technologies;
- developing techniques for testing of components, subsystems, and materials performance and reliability;
- developing dedicated software and algorithms for dynamic control and optimized operation of each subsystem and of the entire integrated fuel production system.

Thus in this part, a dynamic controller is developed, using image-based DNI forecasts inspired from the first part of this thesis, to maintain the performance and stability of the solar reactor. To be able to achieve this task, a reactor model is required. This model is provided following the collaboration between PROMES-CNRS and CEA-LITEN [157, 50].

Due to unavoidable variations of the direct normal irradiance (DNI), the design of solar systems had to come with the development of control strategies. A great variety of control algorithms has been investigated in the years 1980 to 2000, essentially for the thermal regulation of solar collectors. This application implies controlling the heat-transfer fluid mass flow rate, in order to regulate the fluid's temperature at the collector's outlet. For instance, back in 1981, Maffezzoni and Parigi [168] showed the advantage of dynamic compensators-based systems over proportional–integral–derivative (PID) controllers for the operation of a solar steam generator. Later advances are those of Camacho et al. [169], who monitored an oil-heating distributed collector through a self-tuning PID controller, and those of Rubio et al. [170], who implemented fuzzy logics-based control to the same plant. Non-linear control has then been explored in the late 90s, on the basis of simplified non-linear physical models [171] or black-box neural networks models [172]. Reviews of those early developments are found in [173] and [174], pointing the importance of non-linear, high-order, model-based control methods over linearized PI or PID-based methods, when applicable.

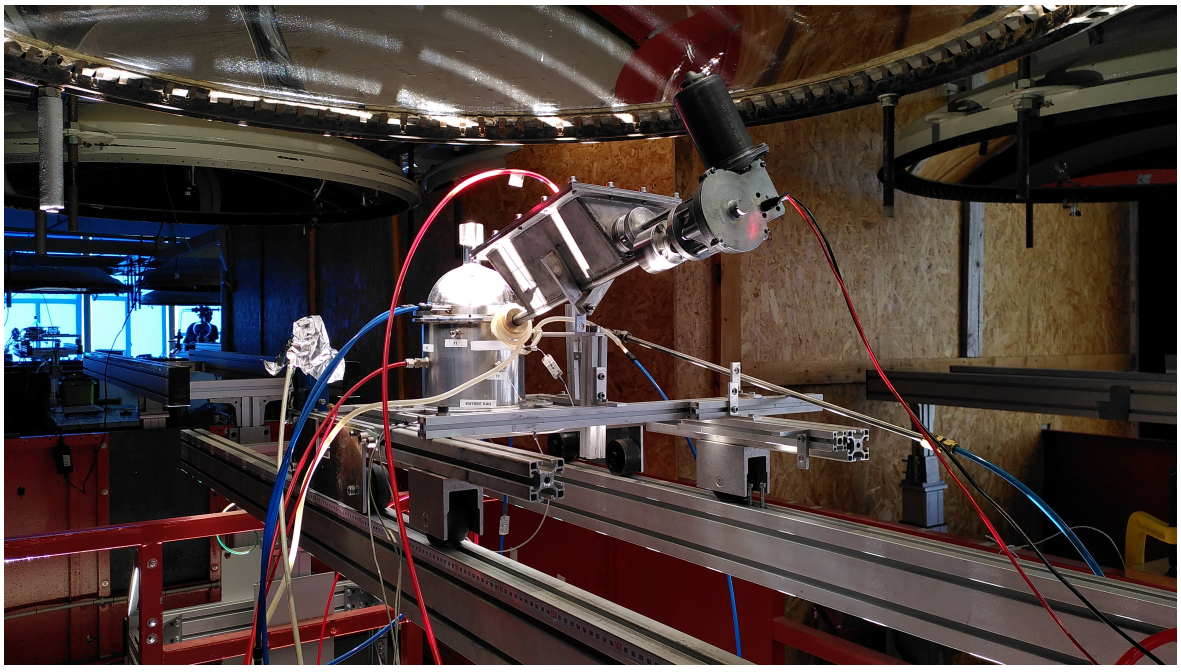

Figure 5.2: PROMES's solar reactor prototype (Odeillo, France).

The research field of solar thermochemical reactors, much less studied, brings an additional complexity by the consideration of complex chemical mechanisms. Multiple outcomes can be of interest, such as the reactor's temperature, the energy conversion efficiency, and the syngas production rates and yields. The work in Petrasch et al. [175] firstly led to optimized energy

efficiency and product quality through the day, thanks to a feedforward-feedback controller applied to a model linearized around a nominal operating point. Later on, Saade et al. [176] regulated the quality of the syngas produced thanks to a multi-input, multi-output, constrained control system; the proposed model-based predictive controller proved more efficient in rejecting DNI disturbances than a multi-loop approach. In the same time, Muroyama et al. [177] proposed a dynamic regulation of the reactor's temperature through the injection of oxygen and additional feedstock, aiming at triggering in-situ combustion under low DNI. A PI-based system was implemented, using a linearized model of the gasifier. Such dynamic control was also considered in Boujjat et al. [50], with the dynamic modeling of an extrapolated spouted-bed gasifier, continuously kept at 1200 °C through day and night operation. Aa MPC implementation was investigated by Saade et al. [176], where the persistence forecast model was used to provide DNI forecasts (an attempt to provide image-based forecasts, using sky images, was recorded in this work, however, the proposed model was not able to outperform the persistence model); the MPC goal was to maintain nominal operating values for the syngas gas fraction and the CO/CO_2 ratio.

The present work aims at conciliating the solar-autothermal hybrid control strategy of a gasifier with the efficient implementation of an MPC algorithm. Several strategies can be developed, such as the maximizing syngas production, maintaining reactor's stability, etc. However, in this work and based on the developed reactor model, the goal is to maintain reactor's stability to ensure optimal conditions for the chemical reactions taking place in the reactor. This, to ensure the reactor's stability, the aim is to maintain the reactor's temperature at its nominal value, despite a varying DNI, while injecting a minimal flow rate of oxygen during operation time. The original model of a solar spouted-bed gasifier is considered [50], including global thermal balances and a chemical model at thermodynamic equilibrium. For the first time, DNI forecasts are integrated into the dynamic control, in order to achieve better smoothing of the disturbances through the day, thus taking full advantage of the model-based predictive approach. The MPC controller acts on the oxygen flow and the mirrors' defocusing factor, in order to maintain the nominal temperature of the reactor, ensuring its stability. At this level, two MPC strategies are proposed: first strategy aims to maintain the reactor's temperature at any cost; the second strategy aims to maintain the reactor's temperature while minimizing the oxygen consumption in the process. This controller is then compared to an optimized adaptive PID controller to highlight the amelioration brought by MPC. Furthermore, MPC controller is implemented with different forecasts: perfect forecasts, smart persistence forecasts, and forecasts provided by a sky-imaging-based model. Also, a study is carried out to discuss the effect of forecast errors on the MPC performance. Finally, a model simplification is proposed to solve the long computation time needed by the MPC controller when using the original reactor model. The controller robustness to this simplification is examined as well.

5.2 Modeling of the solar reactor

The model is inspired by the work of Boujjat et al. [50], who computed the production of a solar biomass gasifier over one year to assess its allothermal-autothermal hybridization. The gasifier is designed to be heated by both concentrated solar power (allothermal heating) and in-situ combustion (autothermal heating) [164, 157], enabling a continuous conversion of biomass around the clock. For a biomass flow rate maintained constant at $1.465\,\mathrm{t\,h^{-1}}$, the reactor parameters are set so that the nominal temperature of 1473 K (1199.85 °C) is reached for a DNI equal to $800\,\mathrm{W\,m^{-2}}$, which corresponds to around 80% of the maximum DNI obtained during a year. At thermodynamic equilibrium, the chemical reactions taking place in the solar reactor are modeled as follows (a schematic is given in Figure 5.3).

- When DNI is higher than $800\,\mathrm{W\,m^{-2}}$ and the reactor's temperature is at its nominal value, only the endothermic reaction of gasification occurs, as described by the following

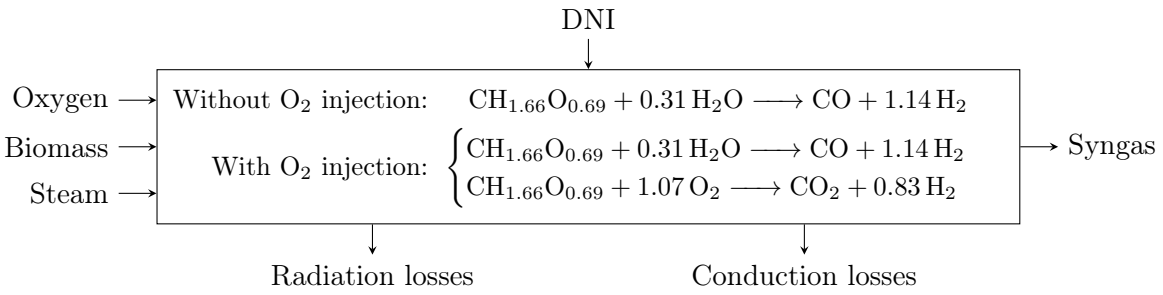

Figure 5.3: Chemical reactions taking place in the solar reactor.

equation:

$$CH_{1.66}O_{0.69} + 0.31\,H_2O \longrightarrow CO + 1.14\,H_2 \tag{5.1}$$

with an enthalpy change $\Delta H_r^o = 143\,\mathrm{kJ\,mol^{-1}}$ (endothermic reaction). A flow rate of H_2O with a steam-to-biomass mole ratio 1.22 times higher than the one at stoichiometry is injected, to ensure that all the biomass is converted.

- When DNI is lower than $800\,\mathrm{W\,m^{-2}}$ and the reactor's temperature is lower than its nominal value, the injection of oxygen is necessary to maintain the reactor's temperature at its steady state level. The impact of oxygen injection can be described by, as a first approximation[1], the oxy-combustion of wood:

$$CH_{1.66}O_{0.69} + 1.07\,O_2 \longrightarrow CO_2 + 0.83\,H_2 \tag{5.2}$$

with an enthalpy change $\Delta H_r^o = -452\,\mathrm{kJ\,mol^{-1}}$ (exothermic reaction).

The model also includes the thermal balance of the reactor walls, and a thermodynamic calculation coded with the open-source library CANTERA [178] (see Table 5.1 for the meaning of the parameters and variables appearing in the model):

$$\begin{cases} Q_{Sun} = D \cdot C \cdot \eta_{optical} \cdot A_{aperture} \cdot \mathrm{DNI} & \text{(5.3a)} \\ Q_{radiationloss} = \sigma \cdot A_{aperture} \cdot (T^4 - T_{amb}^4) & \text{(5.3b)} \\ Q_{conductionloss} = (T - T_{amb})/R & \text{(5.3c)} \\ Q_{reaction} = \sum_{i=1}^{n_{rea}} f_i^{in} h_i(T_{amb}) - \sum_{i=1}^{n_{prod}} f_i^{out} h_i(T) & \text{(5.3d)} \end{cases}$$

The solar power input is proportional to DNI (Equation (5.3a)): it depends on the defocusing factor D, the concentration factor C, the optical efficiency $\eta_{optical}$, and the cavity aperture area $A_{aperture}$. This aperture is minimized so that the radiation losses (Equation (5.3b)) are as low as possible. A global conduction loss is modeled as well (Equation (5.3c)) to account for heat transfer through the insulation. Finally, the $Q_{reaction}$ term (Equation (5.3d)) represents the power required to convert the cold reactants into a syngas at reactor's temperature. It is computed via a heterogeneous thermodynamic equilibrium between a pure solid carbon phase and a gaseous phase. The solid phase is modeled as graphite carbon, and is supposed to be fully consumed at over-stoichiometric H_2O injection rates. However, it should be mentioned that incomplete conversion may still occur at temperatures lower than 800 °C, whatever the quantity of injected steam [179]. The gas phase is modeled as a mixture of H_2, CO, CO_2, CH_4,

[1]Thermodynamic equilibrium calculations are more accurate to model the coupled impact of H_2O and O_2 injection over the products distribution.

Table 5.1: Parameters and variables appearing in the model.

Notation	Definition	Value or unit
DNI	Direct normal irradiance	$\mathrm{W\,m^{-2}}$
T	Reactor's temperature	K
h_i	Enthalpy of reactants and products	kJ
f_i^{in}	Inflow of reactants	$\mathrm{kg\,s^{-1}}$
f_i^{out}	Outflow of products	$\mathrm{kg\,s^{-1}}$
n_{rea}, n_{prod}	Number of reactants and products	–
D	Defocusing factor	$D \in [0, 1]$
$Q_{reaction}$	Power gained from the chem. reaction	W
Q_{Sun}	Power obtained from the Sun	W
$Q_{radiationloss}$	Power lost by radiation	W
$Q_{conductionloss}$	Power lost by conduction	W
m	Mass of the reactor walls	kg
$C_{p,w}$	Specific heat of the reactor walls	$\mathrm{J\,kg^{-1}\,K^{-1}}$
C	Concentration factor	3000
$\eta_{optical}$	Optical efficiency	0.6
$A_{aperture}$	Aperture's area	$3.15\,\mathrm{m^2}$ (0 if DNI $< 150\,\mathrm{W\,m^{-2}}$)
σ	Stefan–Boltzmann constant	$5.67 \times 10^{-8}\,\mathrm{W\,m^{-2}\,K^{-4}}$
T_{amb}	Ambient temperature	298 K
R	Conduction thermal resistance	$2.25 \times 10^{-1}\,\mathrm{K\,W^{-1}}$

H_2O, O_2 and Ar, whose properties are given by the NASA GRI-MECH 3.0 database [180]. The elemental chemical composition of the mixture is determined by the wood input flow rate, its moisture fraction (8.9% in weight), and its molecular composition ($CH_{1.66}O_{0.69}$, on a dry basis). The high heating value (HHV) of the reference wood sample, measured by calorimetry, is also provided to compute the corresponding standard enthalpy of formation, enabling the calculation of the inlet flow enthalpy. The outlet flow enthalpy at reactor's temperature is given directly by CANTERA. All these heat transfers are applied to the reactor walls, of mass m and heat capacity $C_{p,w}$, and determine the impact of both DNI variations and chemical inputs on the reactor's temperature. Thus, the reactor's temperature can be modeled through the following first-order non linear ordinary differential equation:

$$\begin{cases} m \cdot C_{p,w} \cdot \dfrac{\mathrm{d}T}{\mathrm{d}t} = Q_{reaction}(f_{steam}^{in}, f_{biomass}^{in}, f_{oxygen}^{in}, T) + Q_{net} & \text{(5.4a)} \\ Q_{net} = Q_{Sun} - Q_{radiationloss} - Q_{conductionloss} & \text{(5.4b)} \end{cases}$$

where Equation (5.4a) represents the heat balance equation of the reactor, determined by the designed parameters (m and $C_{p,w}$), the gasification reaction ($Q_{reaction}$), and the net power Q_{net} resulting from the solar power gained and the power lost due to the radiation and conduction losses (Equation (5.4b)).

So, when the nominal temperature of 1473 K is reached and DNI $= 800\,\mathrm{W\,m^{-2}}$, $1.465\,\mathrm{t\,h^{-1}}$ of biomass are converted into syngas (mainly H_2, CO, CO_2 and H_2O) thanks to the over-stoichiometric stream of water. Above a DNI value of $800\,\mathrm{W\,m^{-2}}$, a reduction of the input solar power is necessary to maintain the reactor's temperature at 1473 K. As a consequence, a defocusing factor D is introduced (Equation (5.3a)). Below this DNI value, oxygen is added to heat the reactor thanks to in-situ combustion, which directly alters the syngas composition by shifting the thermodynamic equilibrium. Finally, when DNI is lower than $150\,\mathrm{W\,m^{-2}}$, the reactor's aperture is closed to limit the radiation loss.

5.3 Model simulation

As showed in the previous section, the reactor's temperature is modeled by a non-linear ordinary differential equation. DNI and the reactants' flow (biomass, oxygen, and steam) are the model's inputs (see Figure 5.3). In this section, the model is simulated by solving this differential equation in different scenarios, with varying DNI profiles and reactants' flow.

5.3.1 Without oxygen injection

First, with a constant biomass flow rate of $1.465\,\mathrm{t\,h^{-1}}$ and starting from an initial reactor's temperature equal to 1073 K, the model's response to DNI steps of three different amplitudes is simulated (from 0 to $700\,\mathrm{W\,m^{-2}}$, $800\,\mathrm{W\,m^{-2}}$ and $900\,\mathrm{W\,m^{-2}}$, respectively). Results can be found in Figure 5.4. As expected, when DNI $= 800\,\mathrm{W\,m^{-2}}$, the steady-state temperature is equal to 1473 K, the nominal temperature. For DNI $= 700\,\mathrm{W\,m^{-2}}$, the nominal temperature is not reached: oxygen should then be injected to compensate for the lack of power. On the contrary, when DNI $= 900\,\mathrm{W\,m^{-2}}$, the temperature exceeds the nominal temperature: in this case, the mirrors should be defocussed to decrease the reactor's temperature.

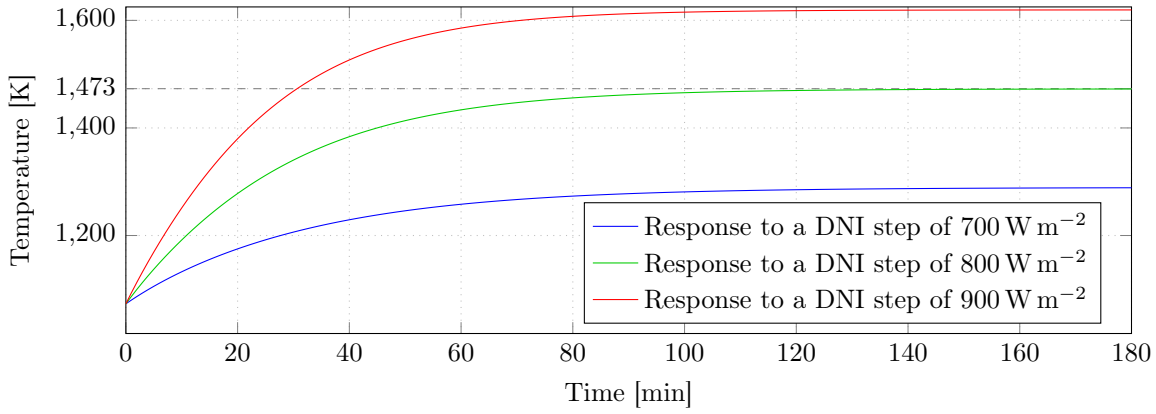

Figure 5.4: Evolution of the reactor's temperature in response to various DNI steps (the biomass flow rate is $f^{in}_{biomass} = 1.465\,\mathrm{t\,h^{-1}}$ and the initial temperature is 1073 K).

As can be seen in Figure 5.4, the static gain, the time constant τ (the time needed to reach 63% of the steady-state value), and the rise time T_r (the time needed to rise from 10% to 90% of the total variation) all depend on the amplitude of the DNI step. The estimated value of these three parameters can be found in Table 5.2: with higher input the gain increases while τ and T_r decreases, rendering the system faster. This means that, not only does the reactor reach higher temperatures with higher DNI values, but it also does so faster. This change in system dynamics must be taken into consideration for an accurate temperature control.

Table 5.2: Parameters of a first-order dynamic model corresponding to the curves of Figure 5.4.

DNI [$\mathrm{W\,m^{-2}}$]	Gain	τ [min]	T_r [min]
700	0.3	31.5	69.3
800	0.5	26.3	58
900	0.6	23	50.6

The power balance corresponding to the steady state of the three DNI steps of Figure 5.4 is given in Figure 5.5. When DNI increases, the conduction loss remains approximatively the same, while the radiation loss increases and the power gained from the chemical reaction decreases.

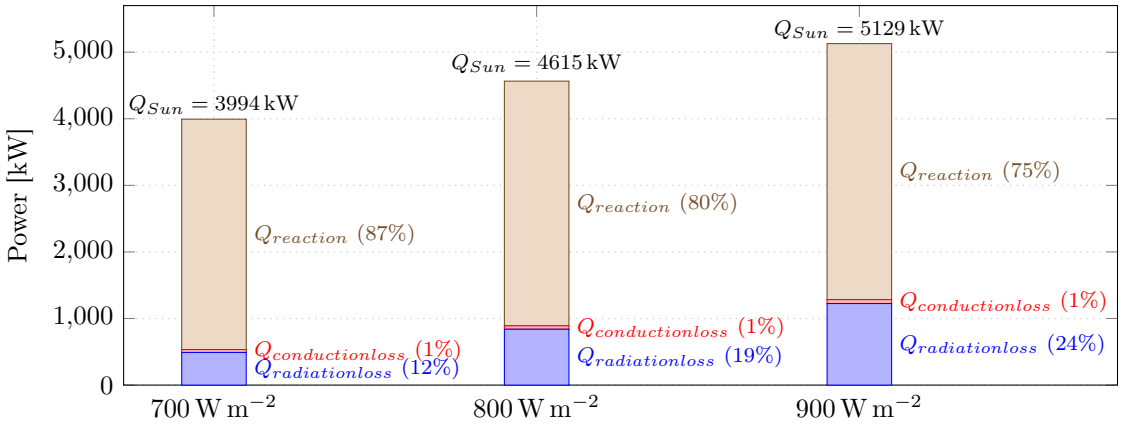

Figure 5.5: Power balance corresponding to the steady state of the DNI steps in Figure 5.4.

To show the effect of DNI variations on the reactor's temperature, while functioning at the nominal design values ($T = 1473\,\text{K}$, $\text{DNI} = 800\,\text{W m}^{-2}$ and $f^{in}_{biomass} = 1.465\,\text{t h}^{-1}$), its response to sudden DNI variations is given in Figure 5.6. The first change, a DNI drop of $200\,\text{W m}^{-2}$, caused the reactor's temperature to drop by 13.13 K; the nominal temperature is reached again after approximatively 90 min. The second change, a DNI rise of $200\,\text{W m}^{-2}$, increased the reactor's temperature by 13.43 K. This simulation shows that sudden DNI variations have a strong effect on the reactor's temperature, that could be compensated if DNI forecasts are provided to the controller. In addition, the long duration before the reactor reaches its nominal temperature after the DNI pulses can be minimized by injecting oxygen, which can help to increase the reactor's temperature faster, as will be shown in the next section.

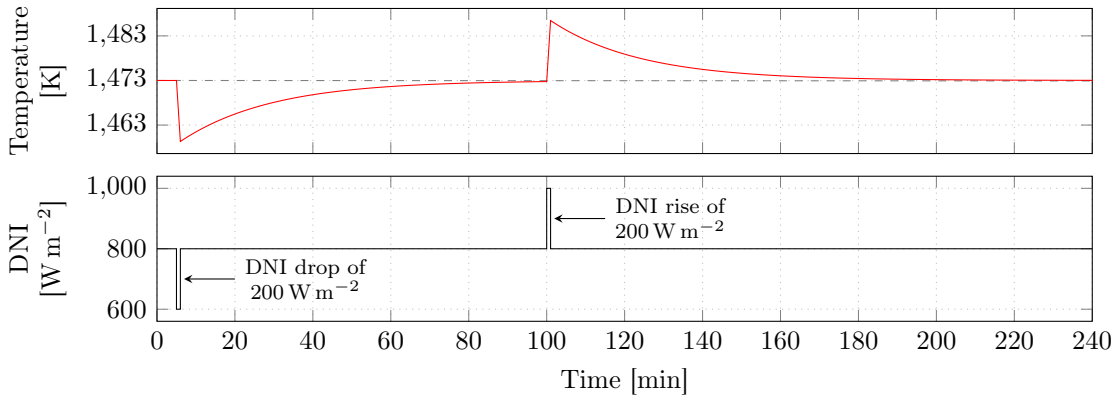

Figure 5.6: Reactor's response to sudden DNI variations, while functioning at its nominal design values ($T = 1473\,\text{K}$, $\text{DNI} = 800\,\text{W m}^{-2}$ and $f^{in}_{biomass} = 1.465\,\text{t h}^{-1}$).

Finally, the evolution of the reactor's temperature against different biomass flow rates is studied in Figure 5.7. Here, DNI is fixed at $900\,\text{W m}^{-2}$. It can be observed that, as the biomass flow rate increases, the temperature decreases and more syngas is produced. However, it should mentioned that the biomass flow rate cannot be a control input, since the model considered in this study does not take the inertia of the gasification reaction into consideration.

5.3.2 With oxygen injection

The reactor's temperature can be decreased by either increasing the biomass flow rate or by varying the energy received from the Sun, using the defocusing factor D. However, in case of

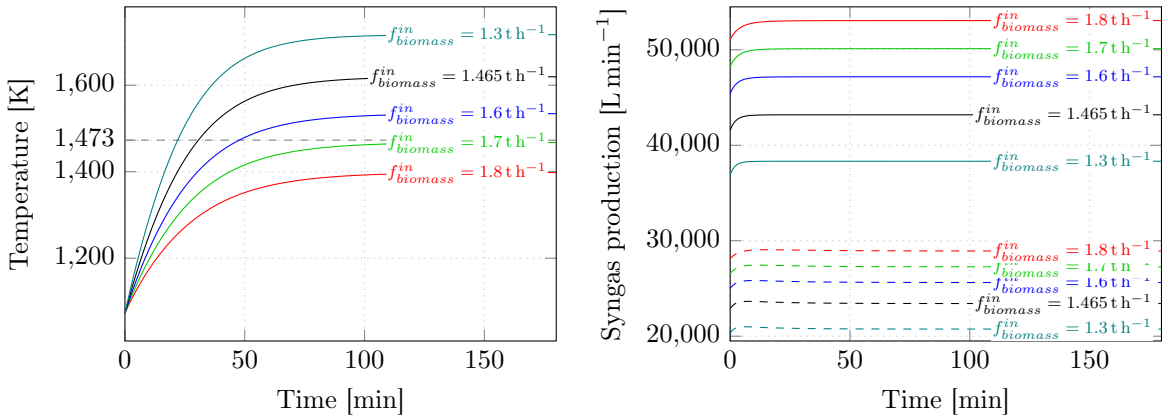

Figure 5.7: Evolution of the reactor's temperature for various biomass flow rates when DNI = 900 W m^{-2}, and corresponding syngas production (dashed line: H_2, solid line: CO+H_2).

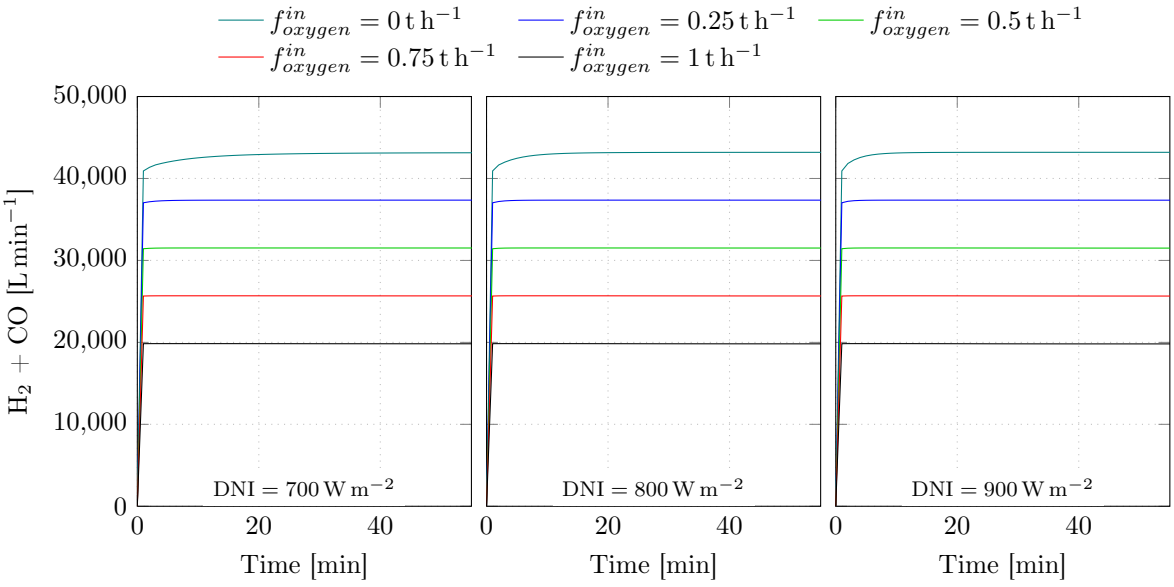

Figure 5.8: Syngas (H_2+CO) production for various oxygen flow rates and DNI levels.

DNI deficit (less than $800\,\mathrm{W\,m^{-2}}$), to increase the temperature without decreasing the biomass flow, oxygen has to be injected to burn the biomass. Since the burnt biomass is not used in the gasification process, less syngas is produced, as shown in Figure 5.8. The simulations presented in Figure 5.9 show that the oxygen injection can increase the reactor's temperature rapidly. For DNI $= 800\,\mathrm{W\,m^{-2}}$, the reactor crossed the 1473 K level after 4 minutes only with $f^{in}_{oxygen} = 2\,\mathrm{t\,h^{-1}}$. This input can correct the reactor's temperature rapidly in case of sudden DNI deficit, as shown in Figure 5.6. When DNI $< 150\,\mathrm{W\,m^{-2}}$, the reactor's aperture is closed, and its temperature can be maintained by injecting $0.88\,\mathrm{t\,h^{-1}}$ of oxygen, as shown in Figure 5.10.

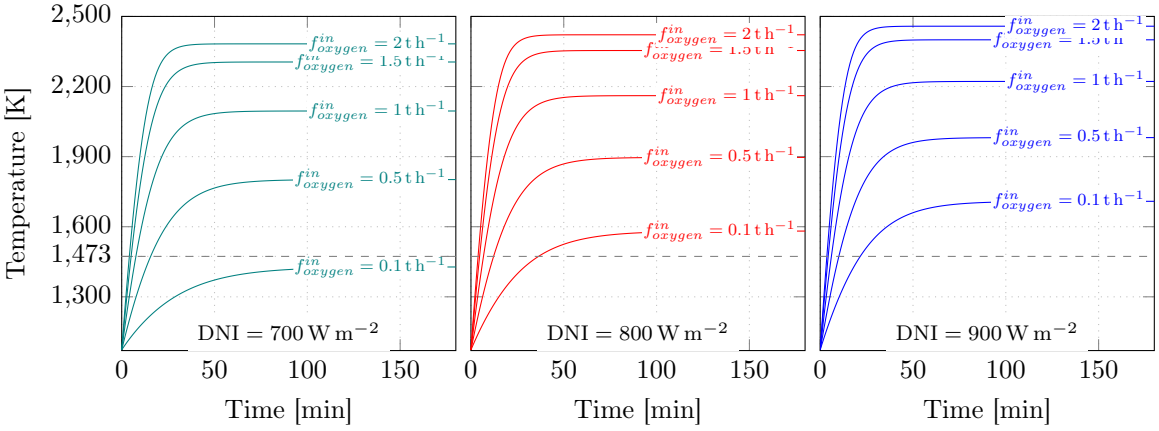

Figure 5.9: Evolution of the reactor's temperature for various oxygen flow rates and DNI levels ($f^{in}_{biomass} = 1.465\,\mathrm{t\,h^{-1}}$ and initial temperature of 1073 K).

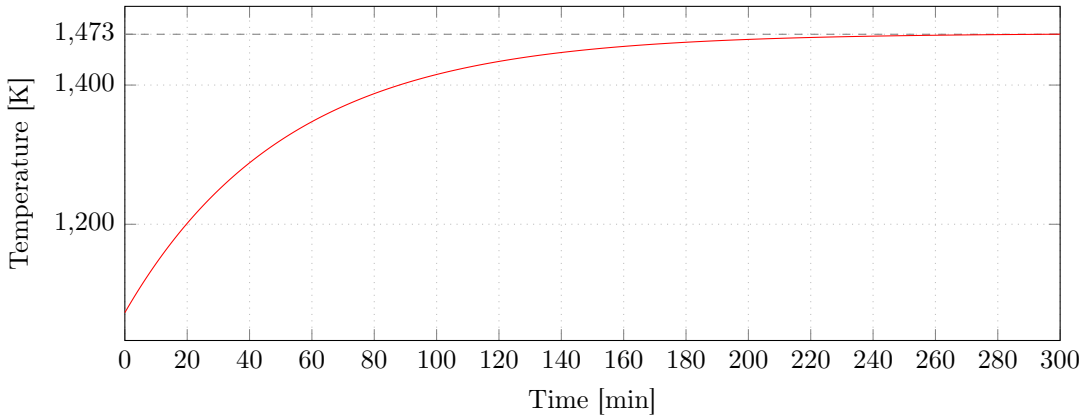

Figure 5.10: Evolution of the reactor's temperature in case of a closed aperture and an oxygen flow rate of $f^{in}_{oxygen} = 0.88\,\mathrm{t\,h^{-1}}$ ($f^{in}_{biomass} = 1.465\,\mathrm{t\,h^{-1}}$ and initial temperature of 1073 K).

5.4 Conclusion

In this chapter, a model of the solar reactor is developed and implemented. The model is based on the thermochemical equilibrium and the heat balance. The reactor's temperature variation is thus calculated by considering the reactor design parameters, the concentrated solar power, the power losses due to conduction and radiation, and the power needed by the gasification reaction at equilibrium. After simulation the model, it can be shown that: in case of DNI deficit (DNI $< 800\,\mathrm{W\,m^{-2}}$), oxygen should be injected to maintain the reactor's temperature at its nominal value; in case of DNI surplus (DNI $> 800\,\mathrm{W\,m^{-2}}$) the reactor's mirrors should

be defocused to eliminate the DNI power surplus; and finally, the reactor's temperature is highly influenced by DNI variations. These main observations will be the backbones of the control strategies presented in the next chapter.

Chapter 6

Dynamic control of the solar reactor

6.1 Development of control strategies for the solar reactor

This section starts with the development of the reference controller, which is a combination of a rule-based controller and an optimized adaptive PID controller. Then, the proposed MPC strategies are presented by explaining the different objective functions, the corresponding constraints, and the developed DNI forecast model. These controllers are then evaluated in the following sections. The discretized reactor model $\mathcal{M}$ is represented as follows:

$$T(k+1) = \mathcal{M}(D(k), f^{in}_{oxygen}(k), T(k)) \tag{6.1}$$

It should be noted that the time step Δt is equal to the data sampling time, namely 30 s ($t = k \cdot \Delta t$, with $\Delta t = 30\,\text{s}$). In the sequel, the biomass flow rate $f^{in}_{biomass}$ and the steam flow rate f^{in}_{steam} are fixed to their nominal design values of $1.465\,\text{t}\,\text{h}^{-1}$ and $0.26\,\text{t}\,\text{h}^{-1}$, respectively.

6.1.1 Reference controller

The goal of this controller is to maintain the temperature inside the reactor at its nominal value (1473 K) to ensure its stability. This controller is developed in order to have a reference to which the MPC controller can be compared. The control variables are:

- the oxygen flow rate (f^{in}_{oxygen}): in case of a DNI deficit (DNI $\leqslant 800\,\text{W}\,\text{m}^{-2}$), oxygen can be injected to increase the reactor's temperature by burning biomass;
- the defocusing factor (D): in case of an excess of DNI (DNI $> 800\,\text{W}\,\text{m}^{-2}$), the mirrors can be defocussed to compensate for the surplus.

This controller is thus composed of two controllers (see Figure 6.1): the oxygen flow rate is controlled by an optimized adaptive PID controller, as detailed in Section 6.1.1.1, and the defocusing factor is determined by a rule-based controller, as explained in Section 6.1.1.2.

6.1.1.1 Adaptive PID controller for the oxygen flow rate

An optimized adaptive PID controller is implemented to perform a closed loop control of the oxygen injection (see Figure 6.1). It can be described as follows:

$$f^{in}_{oxygen}(k) = K_p \cdot e(k) + K_i \cdot \sum_{i=1}^{k} e(i) + K_d \cdot \frac{e(k) - e(k-1)}{\Delta t} \text{ with } e(k) = S_p - T(k) \tag{6.2}$$

where S_p is the temperature setpoint, T is the reactor's temperature, and [181]:

- K_p is the proportional gain, helping the controller reach the setpoint faster, with the risk of overshooting; a small value will result in an important steady-state error;

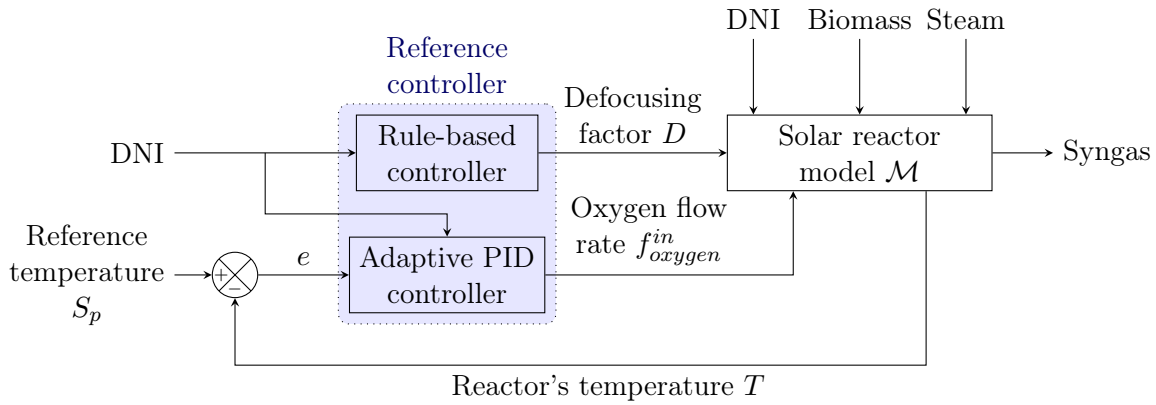

Figure 6.1: The reference controller, defined as a combination of a rule-based controller and an adaptive PID controller.

- K_i is the integral gain, helping to eliminate the steady-state error; a large value can result in a longer settling time and higher oscillations;
- K_d is the derivative gain, generating a fast response and a stabilizing effect in dynamic regime.

An adaptive PID controller, where gains change with the measured DNI, is implemented. This choice has been considered because the reactor's mode of functioning depends on DNI as follows:

- DNI $< 150\,\mathrm{W\,m^{-2}}$: in this case, the reactor's aperture is closed ($A_{aperture} = 0$), changing the thermal equilibrium; the PID controls the system by injecting a minimum of $0.88\,\mathrm{t\,h^{-1}}$ (see Section 5.3.2);
- $150\,\mathrm{W\,m^{-2}} \leqslant$ DNI $\leqslant 800\,\mathrm{W\,m^{-2}}$: the aperture is not closed and the amount of DNI received is not sufficient to maintain the reactor's temperature without oxygen injection; the PID controller determines the oxygen flow rate to minimize the error between the setpoint and the measured temperature.
- DNI $> 800\,\mathrm{W\,m^{-2}}$: the DNI surplus forces the PID to recommend a minimal oxygen flow rate to allow the reactor to cool down.

For each of the three intervals of DNI values, the optimized PID gains have been obtained by minimizing the following objective function:

$$(K_p, K_i, K_d) = \operatorname{argmin} \sum_{k=1}^{n} (S_p - T(k))^2 \tag{6.3}$$

where K_p, K_i and K_d are the PID gains, S_p is the temperature setpoint, T is the reactor's temperature, and n is the number of time steps.

This tuning strategy, targeting a certain performance described by the objective function, is considered the optimal approach to design a PID controller [182]. The optimized PID gains are given in Table 6.1. Note that the gains are significantly lower when DNI $> 800\,\mathrm{W\,m^{-2}}$, which is explained by the necessity to inject less oxygen in this case, to allow the reactor to cool down. Also, in all cases, K_i is significantly lower than the other gains except for the case DNI $> 800\,\mathrm{W\,m^{-2}}$, where the PID gains should be low to inject the minimal oxygen flow rate, which permits the reactor to cool down if needed. This means that the optimizer found that the optimal performance, based on the provided objective function, does not need the integral effect.

Table 6.1: Optimized gains of the adaptive PID controller.

	$\mathrm{DNI} < 150\,\mathrm{W\,m^{-2}}$	$150\,\mathrm{W\,m^{-2}} \leqslant \mathrm{DNI} \leqslant 800\,\mathrm{W\,m^{-2}}$	$\mathrm{DNI} > 800\,\mathrm{W\,m^{-2}}$
K_p	1.6×10^{-2}	3.4×10^{-2}	1.5×10^{-3}
K_i	0	9.0×10^{-4}	1.5×10^{-4}
K_d	1.2×10^{-2}	2.5×10^{-2}	1.0×10^{-5}

6.1.1.2 Rule-based controller for the defocusing factor

The mirrors' defocusing factor is controlled as follows:

$$D(k) = \begin{cases} 1, & \text{if } \mathrm{DNI}(k) \leqslant 800\,\mathrm{W\,m^{-2}} \text{ and } T(k) < 1473\,\mathrm{K} \\ \dfrac{800}{\mathrm{DNI}(k)}, & \text{if } \mathrm{DNI}(k) > 800\,\mathrm{W\,m^{-2}} \text{ and } T(k) > 1473\,\mathrm{K} \end{cases} \tag{6.4}$$

In the first case, the exploitation of the solar power is maximized, while in the second case there is an excess of DNI and, provided the reactor is at its nominal temperature, the defocusing factor is used to supply a power equivalent to the one obtained when $\mathrm{DNI} = 800\,\mathrm{W\,m^{-2}}$.

6.1.2 Model-based predictive control of the solar reactor

In this section, the two MPC strategies are detailed: a schematic is given in Figure 6.2, the two optimization problems considered are described in Section 6.1.2.1, and the developed approach to forecast DNI is explained in Section 6.1.2.2. These two presented strategies are: (1) MPC strategy 1 aiming to maintain the reactor's temperature without considering oxygen consumption and (2) MPC strategy 2 aiming to maintain the reactor's temperature while exploiting the available solar energy and minimizing oxygen consumption. As for the PID controller, the two control inputs are the mirrors' defocusing factor D and the oxygen flow rate f_{oxygen}^{in}. The objective is still to maintain the reactor's temperature at 1473 K, in order to preserve the reactor's stability. One of the major advantages of MPC over PID control is its predictive nature. The MPC controller can find the optimal sequence of inputs, based on the forecasts provided and the model of the system. This is a huge advantage for the problem at hand, since as seen before, the reactor is very sensitive to DNI variations. In addition, based on the required performance and constraints, the MPC controller can find the optimal combination of multiple inputs simultaneously.

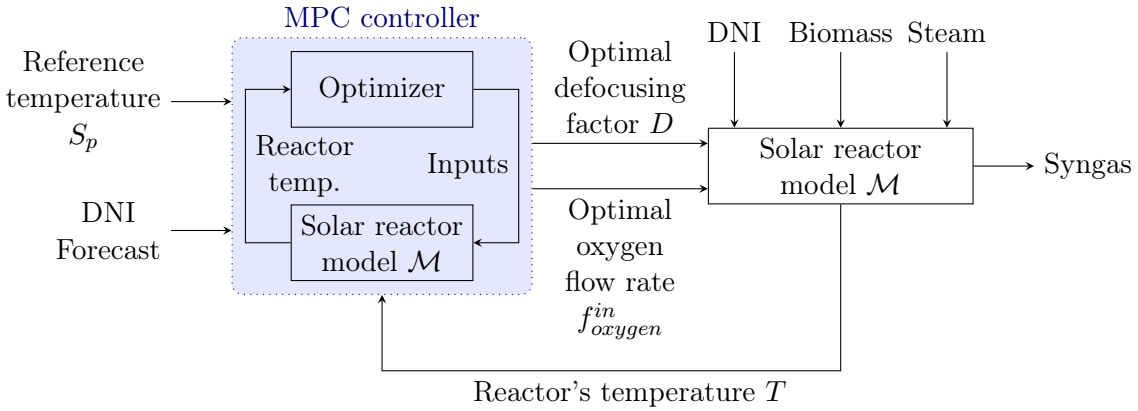

Figure 6.2: The MPC controller.

6.1.2.1 Optimization problem

Let n be the number of time steps in the prediction horizon of the controller. At each of those n time steps, an optimization problem is solved to find optimal inputs $\boldsymbol{D} \in \mathbb{R}^n$ and $\boldsymbol{f}^{in}_{oxygen} \in \mathbb{R}^n$ [183], for a given objective function, a set of constrains, and bounds. This optimization problem thus defines the control strategy. In this chapter, two strategies are presented (see Table 6.2 for a list of the variables appearing in the optimization problems). The first proposed strategy (MPC strategy 1) is about solving the following optimization problem to find $D^\star$ and $f^{in\,\star}_{oxygen}$:

$$\begin{aligned}(D^\star, f^{in\,\star}_{oxygen}) = \text{argmin} \quad & \sum_{i=1}^{n} \big(S_p - T(k+i)\big)^2 \\ \text{where} \quad & T(k+1) = \mathcal{M}\big(T(k), D(k), f^{in}_{oxygen}(k)\big) \\ \text{subject to} \quad & 0 \leqslant D(k+i) \leqslant 1 \text{ and } 0 \leqslant f^{in}_{oxygen}(k+i) \leqslant 2\end{aligned} \tag{6.5}$$

It focuses on minimizing the squared difference between the temperature setpoint and the simulated temperature over the considered prediction horizon, without constraints on the oxygen consumption or the usage of solar energy. The second proposed strategy (MPC strategy 2) is about solving the following optimization problem to find $D^\star$ and $f^{in\,\star}_{oxygen}$:

$$\begin{aligned}(D^\star, f^{in\,\star}_{oxygen}) = \text{argmin} \quad & \sum_{i=1}^{n} \alpha\big(S_p - T(k+i)\big)^2 + \beta\big(f^{in}_{oxygen}(k+i)\big)^2 - \gamma\big(D(k+i)\big)^2 \\ \text{where} \quad & T(k+1) = \mathcal{M}\big(T(k), D(k), f^{in}_{oxygen}(k)\big) \\ \text{subject to} \quad & 0 \leqslant D(k+i) \leqslant 1 \text{ and } 0 \leqslant f^{in}_{oxygen}(k+i) \leqslant 2\end{aligned} \tag{6.6}$$

As can be seen, the goal is here to make a trade-off between following the temperature setpoint, minimizing the oxygen consumption, and maximizing the use of solar energy. This trade-off is determined by the weights α, β, and γ. It should be noted that DNI forecasts are needed to solve these optimization problems. How these forecasts are obtained is the subject of the following section.

Table 6.2: Variables appearing in the optimization problems.

Variable	Definition
α	Control weight on the reference error
β	Control weight on the oxygen flow rate
γ	Control weight on the defocusing factor
S_p	Temperature setpoint
D	Defocusing factor
f^{in}_{oxygen}	Oxygen flow rate
P	Prediction horizon of the MPC controller
$\mathcal{M}$	Reactor model in discrete time
T	Reactor's temperature

6.1.2.2 DNI forecast unit

The predictive aspect of the MPC controller is the reason behind its implementation. It compensates for DNI variations, while minimizing the objective function. To do so, DNI forecasts must be provided to the MPC controller for every prediction step. Depending on the required forecast horizon H (here $H = h \cdot T_s$, with $T_s = 30\,\text{s}$), several approaches can

be considered: statistical models, that are trained on a dataset of past DNI observations to learn patterns concerning DNI variations; image-based models, where sky images are processed to extract information related to the sky situation that will affect DNI. As presented in Section 6.2.1, the optimal prediction horizon of the MPC controller is less than 2.5 minutes: for such short forecast horizons, persistence models score very low forecast errors; however, they fail to predict DNI ramps, which are very influential, as shown in Figure 5.6. Thus, the goal is to develop a forecasting model that not only scores low forecast errors, but predict most DNI ramps. This eliminates models based on past DNI observations only, and justifies the integration of ground-based sky images (for very short forecast horizon, satellite-based imagery does not provide the required accuracy in time or space). Therefore, in this work, a hybridization between statistical and image-based approaches is presented to harness the advantages of both, and to provide forecasts for very short forecast horizons. Thus, a model inspired from the approach described in Chapter 4 is adapted so that it can be hybridized with the smart persistence model.

The proposed model relies on an hybridization between the smart persistence model and a recurrent neural network (RNN) model, based on past DNI observations, used to forecast DNI by estimating DNI ramps. This model, presented in Figure 6.3, can be described as follows:

- first, a high dynamic range (HDR) image is processed to detect clouds and estimate their motion, in order to localize the part of the sky image that will interact with the Sun at time $k+h$; this part is called region of interest (ROI) in the sequel;
- then, the cloud fraction (CF) in the ROI, $\mathrm{CF}_{\mathrm{ROI}_H}(k)$, is determined by dividing the number of pixels representing clouds by the number of pixels in the ROI, where the clouds are detected using a segmentation model;
- then, using the variation of $\mathrm{CF}_{\mathrm{ROI}_H}(k)$ over time, the model determines if a ramp will occur and forecasts its magnitude using a RNN model;
- finally, the DNI forecast is obtained by either a persistence (if there is no ramp), or a persistence to which the ramp magnitude is added (if there is a ramp). The DNI forecast at time $k+h$ is thus obtained as:

$$\widehat{\mathrm{DNI}}(k+h) = \mathrm{DNI}(k) + \delta(k)\widehat{\mathrm{RM}}(k) \tag{6.7}$$

where DNI is the measured DNI, $\widehat{\mathrm{RM}}$ is the forecast ramp magnitude and δ is given by:

$$\delta(k) = \begin{cases} 1, & \text{if a positive ramp is expected} \\ -1, & \text{if a negative ramp is expected} \\ 0, & \text{if no ramp is expected} \end{cases} \tag{6.8}$$

6.1.2.2.1 Sky images and DNI measurements database The sky images are provided by the sky imager described in Section 4.2. The fact that it provides HDR images is key for accurate short-term DNI forecasting: the lower the forecast horizon, the closer to the Sun the region of interest is. The circumsolar area, where pixel values are usually saturated, thus contain very important information for very short-term DNI forecasting. The sky imager registers an image every 30 seconds, which corresponds to the shortest sampling time that is not a problem for the cloud motion estimation algorithm if cloud motion is slow (estimating the motion slow-moving clouds can be hard to do if the motion magnitude and the sampling time are both low). The database used in this study is the same database used in Section 4.2: it consists of 373 days (images and DNI measurements) without missing data with 128 clear-sky days (34.4%), 49 overcast days (13.1%) and 196 days with mixed situations (52.5%).

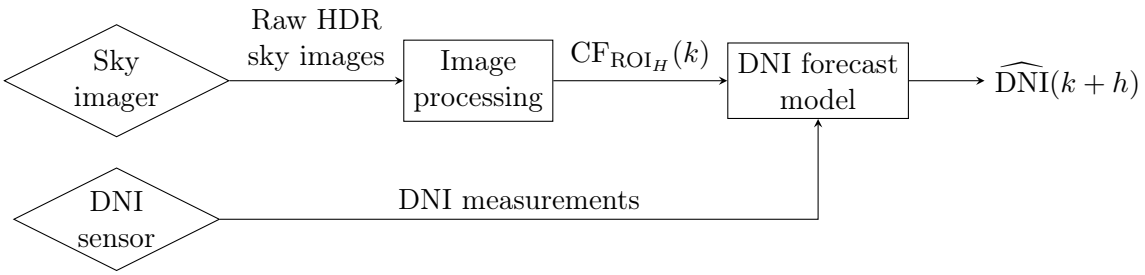

Figure 6.3: Global architecture of the proposed forecast model, showing two main steps: image processing and DNI forecast model. CF_{ROI_H} is the cloud fraction in the region of interest (ROI).

6.1.2.2.2 Image processing In this step, features are extracted from the acquired images (Figure 6.4). The HDR images are processed to correct the fisheye lens distortion, detect the clouds using a k-NN model [184], and estimate their motion using the Farnebäck optical flow algorithm [155]. A region of interest (ROI) is then localized, based on the estimated cloud motion, with the aid of the k-means clustering method. Finally, the cloud fraction in the ROI is calculated (CF_{ROI_H}) and fed to the DNI forecast model to determine if a ramp is expected. The steps in this section are identical to the image processing section discussed in Section 4.4; however, only $CF_{ROI_H}(k)$ is computed as the RGB image of the ROI is not needed here.

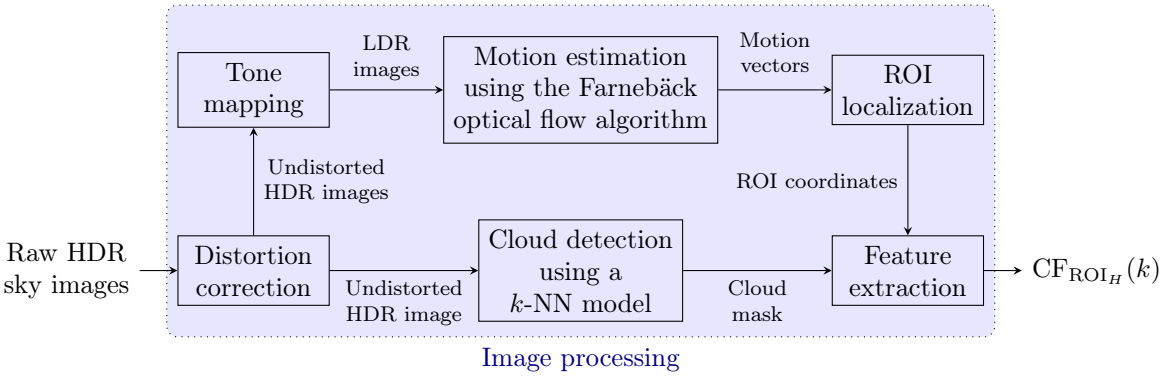

Figure 6.4: Image processing steps leading to the feature extraction. It starts with the distortion correction of the HDR image, followed by cloud motion estimation and cloud detection. Based on that, the region of interest (ROI) is located and the cloud fraction in the ROI is calculated (CF_{ROI_H}).

6.1.2.2.3 DNI forecast model After the image processing step, the forecast model determines if a ramp is expected by analyzing variations of the cloud fraction in the ROI between two time steps. The cloud fraction is equal to the number of cloud pixels divided by the number of clear-sky pixels: it ranges from 0 (if there are no clouds in the ROI) to 255 (if the ROI contains only clouds)[1]. If this variation is greater that 3% of its maximum value[2], then a ramp is expected. This approach also determines the ramp's direction, since an increase in CF_{ROI_H} indicates a possible decrease in DNI, and vice versa. Thus, the value of δ can be

[1]For each pixel, the output of the segmentation model is either 0 (corresponding to a clear-sky pixel) or 255 (corresponding to a cloud pixel).

[2]This value is set to 3% to avoid ramp detection due to noise in the CF_{ROI_H} signal.

calculated as follows:

$$\delta(k) = \begin{cases} 1, & \text{if } \Delta \mathrm{CF}_{\mathrm{ROI}_H}(k) < -7.65 \\ -1, & \text{if } \Delta \mathrm{CF}_{\mathrm{ROI}_H}(k) > 7.65 \\ 0, & \text{else} \end{cases} \tag{6.9}$$

where:

$$\Delta \mathrm{CF}_{\mathrm{ROI}_H}(k) = \mathrm{CF}_{\mathrm{ROI}_H}(k) - \mathrm{CF}_{\mathrm{ROI}_H}(k-1) \tag{6.10}$$

Once the value of δ is determined, the ramp magnitude $\widehat{\mathrm{RM}}$ is estimated in order to forecast DNI (see Equation (6.7)). To do so, a long short-term memory (LSTM) model is trained to forecast the absolute value of the ramp magnitude for every required forecast horizon. The optimal LSTM architecture for each forecast horizon H, determined using an optimization framework [118], is presented in Table 6.3.

Table 6.3: Optimal LSTM architecture for each forecast horizon H.

H [min]	Time support (obs.)	LSTM layers (units)				Fully connected layers (units)		
		1st	2nd	3rd	4th	1st	2nd	3rd
0.5	8	179	229	204	104	20	5	5
1	8	254	204	219	229	20	5	∅
1.5	8	229	54	204	179	5	20	20
2	8	254	104	79	229	5	20	20
2.5	8	154	179	104	4	5	5	∅

Four performance metrics are used here to evaluate the models. The reader is referred to Section 2.2.5 for a detailed description of these metrics.

1. the root mean squared error (RMSE).
2. the mean average error (MAE).
3. the skill factor (SF).
4. the ramp detection index (RDI).

The LSTM models are trained and validated on 17 days (representing 20400 observation) of mixed situations, with various DNI profiles, where 70% of this dataset is used for training and 30% is used for validation. The loss function is chosen to be the mean average error (MAE), which performed better than other possible loss functions for this application. The training and validation results are shown in Figure 6.5. The models performed well on the learning and validation dataset, which means that they did not overfit. As expected, the MAE increases as the forecast horizon increases, since forecasting becomes more and more difficult.

Finally, this approach is tested on seven days, plotted in Figure 6.6, that are not included in the training dataset, nor in the validation dataset. These days are characterized by important DNI variations in the three predefined DNI levels ($\mathrm{DNI} < 150\,\mathrm{W\,m^{-2}}$, $150\,\mathrm{W\,m^{-2}} \leqslant \mathrm{DNI} \leqslant 800\,\mathrm{W\,m^{-2}}$ and $\mathrm{DNI} > 800\,\mathrm{W\,m^{-2}}$). It should be mentioned that cases with important DNI variations are more challenging in terms of forecasting or controlling the reactor's temperature. The resulting forecast performance on the test dataset is shown in Figure 6.7. As can be seen, the proposed approach outperforms the smart persistence model on all days in the test dataset, for each forecast horizon. It can be noticed that the SF increases with the forecast horizon, which can be explained by the degrading results of the smart persistence model. The ramp detection ability of the approach ranges between 55% and 64% as the horizons varies. In addition, the RDI does not vary much for the different forecast horizons, since the temporal difference between the horizons is small (30 seconds).

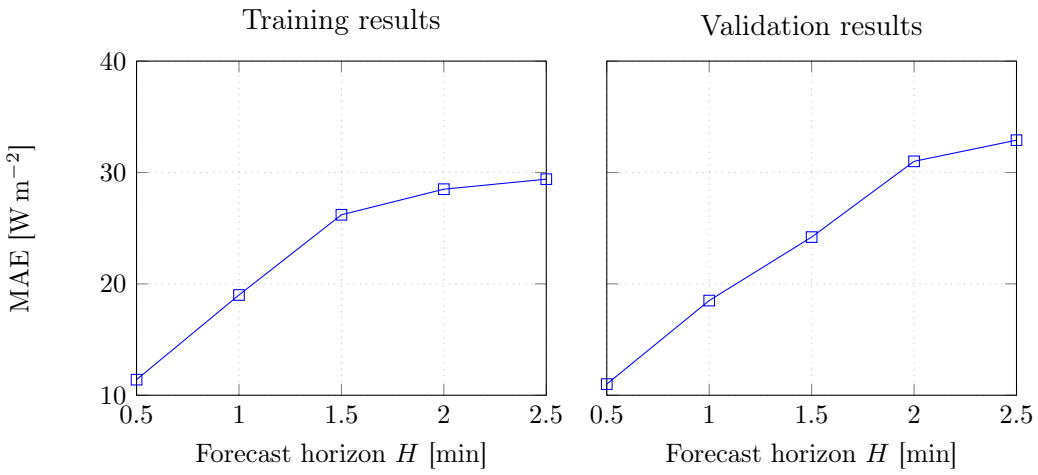

Figure 6.5: LSTM model results (training and validation): values of MAE as a function of the forecast horizon H.

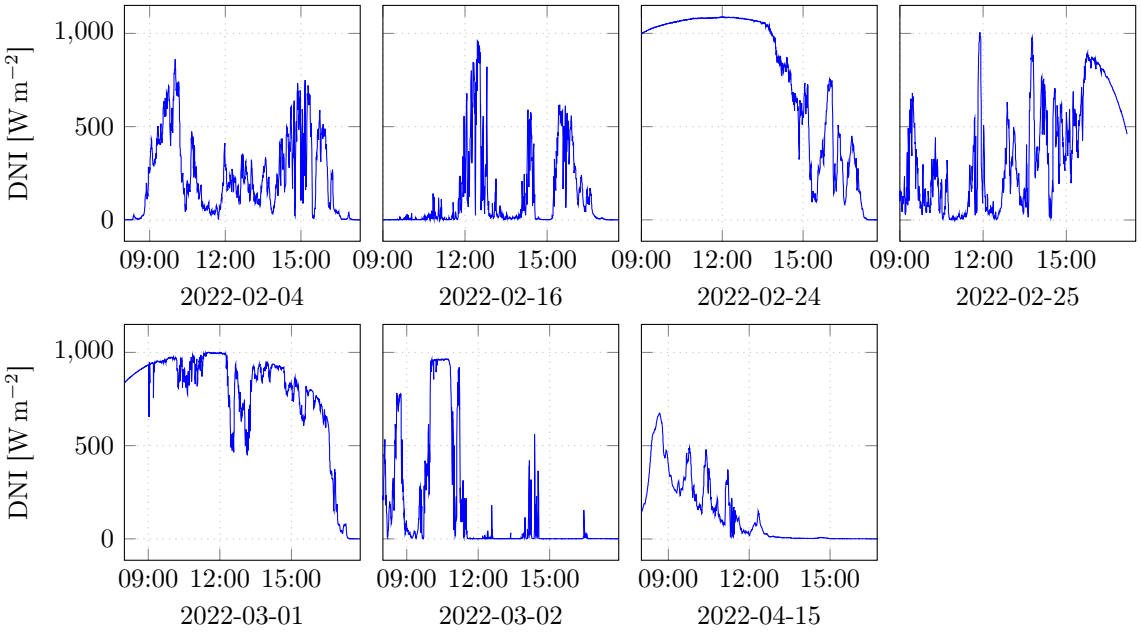

Figure 6.6: The seven days included in the test dataset (also used for the comparative study presented in Section 6.2).

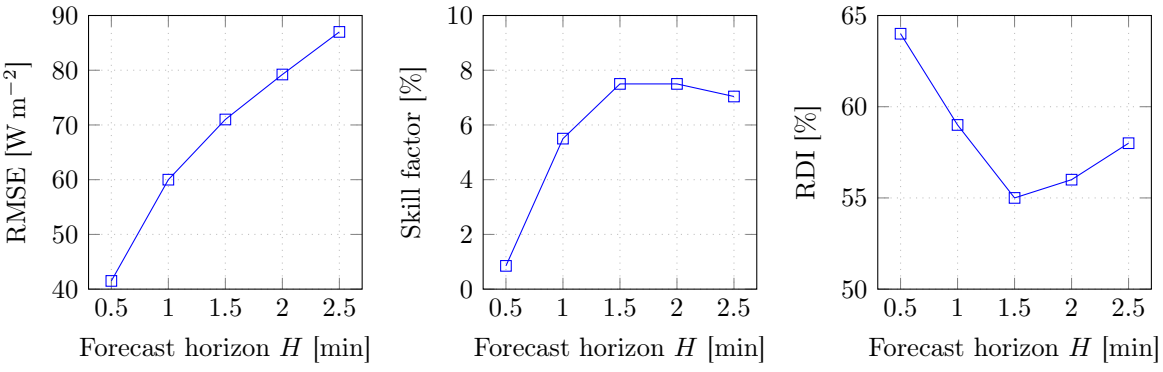

Figure 6.7: Forecast performance (RMSE, SF and RDI) of the proposed approach on the test dataset.

6.2 Evaluation of the control strategies

The controllers' performance is evaluated by calculating the root mean squared error (RMSE), the amount of oxygen used in the simulation (m_{O_2}), and the average temperature variation (ATV), which estimates the magnitude of temperature variation inside the reactor (except for DNI $< 150\,\mathrm{W\,m^{-2}}$, since in this case the reactor is closed and there is no power loss; the temperature can thus be easily maintained by injecting $0.88\,\mathrm{t\,h^{-1}}$:

$$\mathrm{RMSE} = \sqrt{\frac{1}{n}\sum_{k=1}^{n}\left(S_p - T(k)\right)^2} \tag{6.11}$$

$$m_{O_2} = \sum_{k=1}^{n} f_{oxygen}^{in}(k) \cdot \Delta t \tag{6.12}$$

$$\mathrm{ATV} = \frac{1}{n}\sum_{k=1}^{n}|T(k) - T(k-1)| \tag{6.13}$$

where n is the number of time steps. Since the reactor's stability requires minimal temperature variations, lower ATV is recommended. Based on this simulation, a comparative study is carried out to highlight the superior performance of the MPC controller and its robustness versus forecast error. Then, a case study is presented to show the different behaviors of the developed controllers. The computer used to perform the simulation is described in Section 2.2.5.

6.2.1 Comparative study: reference strategy vs. MPC strategies, and the influence of DNI forecasts

The comparative study presented here has the following objectives:

- compare the results of the reference controller and the two MPC controllers;
- shed light on the differences between the two MPC strategies introduced in Section 6.1.2.1;
- see how the DNI forecast errors impact the MPC controller performance, by testing three different cases: perfect forecasts, smart persistence forecasts and the proposed image-based forecasts.

This study is made over the 7-day test dataset plotted in Figure 6.6. It should be mentioned that night-time periods are not included, since they are identical to the case with DNI $< 150\,\mathrm{W\,m^{-2}}$ where injecting $0.88\,\mathrm{t\,h^{-1}}$ is sufficient to maintain the reactor's temperature perfectly. The control inputs, for both objective functions, are initialized as follows:

- $D(k+i) = 1\ \forall i \in [\![1; n]\!]$. This initialization is chosen so that the optimal input found is near 1, which means solar energy is used at its best;
- $f_{oxygen}^{in}(k+i) = 0.5\ \forall i \in [\![1; n]\!]$. This initialization is chosen so that the optimizer converges fast to the optimal solution, which is around $0.5\,\mathrm{t\,h^{-1}}$. Other initialization values resulted in an increase in computation time and some performance degradation.

In this work, the trust-region constrained algorithm [185] is used for its ability to solve non-linear optimization problems and its high robustness and its ability to handle various objective functions.

6.2.1.1 MPC strategy 1

The results obtained with the reference strategy and MPC strategy 1 (see Equation (6.5)) are given in Table 6.4. It should be noted that this strategy penalizes the tracking error only by minimizing the summation of the squared tracking error over the prediction horizon: as a consequence, it suffices to compare the RMSE values to evaluate the performance. Starting with the perfect forecasts, the RMSE for all horizons is less than 1×10^{-2} K, however the oxygen consumption ranges between 44 558.27 kg to 45 151.26 kg. The MPC controller based on the smart persistence model scored a RMSE between 1.45 K to 1.60 K with the lowest error value of 1.45 K for a prediction horizon $P = 2$ min. The oxygen consumption increases as the forecast horizon increases (except for $P = 2.5$ min). Implementing the image-based forecast model shows amelioration over the smart persistence model on every aspect for every prediction horizon: lower RMSE values (around 9.8%); lower oxygen consumption (saving up to 1000 kg of oxygen). The optimal prediction horizon is chosen to be 2 min, since it scores the lowest RMSE for MPC controllers with the smart persistence and image-based forecasts (RMSE amelioration is minimal for perfect forecasts since RMSE scored is less than 0.01 for all prediction horizon). The MPC controller outperforms the reference controller by scoring lower RMSE and ATV value at the cost of an increase of less than 5% in oxygen consumption. This increase in oxygen consumption is due to the fact that the reference controller uses less oxygen but allows high temperatures variations. Comparing the MPC performance based on the different forecasting models, one can note that: the image-based forecast model helped the MPC to score lower RMSE for every horizon (up to 9.8%), and lower oxygen consumption for all horizons except the first and the last one.

Table 6.4: Performance results for MPC strategy 1 (test dataset).

Controller	Performance criterion	Prediction horizon of the MPC controller P [min]				
		0.5	1	1.5	2	2.5
MPC controller with perfect forecasts	RMSE [K]	$\ll$0.01	$\ll$0.01	$\ll$0.01	$\ll$0.01	$\ll$0.01
	m_{O_2} [kg]	45 151.26	44 676.80	44 558.27	41 920.60	41 920.60
	ATV [K]	$\ll$0.01	$\ll$0.01	$\ll$0.01	$\ll$0.01	$\ll$0.01
MPC controller with smart pers. forecasts	RMSE [K]	1.60	1.54	1.53	1.45	1.50
	m_{O_2} [kg]	34 505.13	35 576.43	36 415.00	38 509.25	35 246.56
	ATV [K]	1.49	1.44	1.42	1.32	1.42
MPC controller with image-based forecasts	RMSE [K]	1.54	1.45	1.38	1.34	1.34
	m_{O_2} [kg]	34 554.20	35 079.86	35 924.70	36 365.80	36 813.61
	ATV [K]	1.48	1.42	1.35	1.32	1.30
Reference controller	RMSE [K]			4.88		
	m_{O_2} [kg]			31 933.00		
	ATV [K]			2.27		

The mean optimization time per time step is presented in Table 6.5. This table shows that the time needed to perform the optimization process is less than the sampling time (30 s), but the time needed is still very long, especially for high prediction horizons. It should be mentioned that as the quality of forecasts increase the mean optimization time slightly increases.

6.2.1.2 MPC strategy 2

In Table 6.6, a comparative study is presented to shed light on the performance of MPC strategy 2 (see Equation (6.6)) on the same week than in the first comparative study. This strategy tolerates more reference tracking error for less oxygen consumption. So in order to

Table 6.5: Mean optimization time per time step for MPC strategy 1.

Controller	Prediction horizon of the MPC controller P [min]				
	0.5	1	1.5	2	2.5
MPC controller with perfect forecasts	1.5 s	4.7 s	9.7 s	15.0 s	30.0 s
MPC controller with smart persistence forecasts	0.9 s	4.1 s	9.1 s	14.0 s	28.0 s
MPC controller with image-based forecasts	1.0 s	4.3 s	9.3 s	14.3 s	29.6 s

evaluate this performance and to choose the optimal prediction horizon per forecast model, the objective function (f_{obj}) used in the optimization problem (Equation (6.6)) is calculated for every prediction horizon, as shown in Equation (6.14):

$$f_{obj} = \sum_{i=1}^{n} \alpha\big(S_p - T(k+i)\big)^2 + \beta\big(f^{in}_{oxygen}(k+i)\big)^2 - \gamma\big(D(k+i)\big)^2 \tag{6.14}$$

where $\alpha = 5$, $\beta = 5$, and $\gamma = 10$. The higher weight on the defocusing factor ensures that the reactor receives the highest possible solar power, while using the minimal possible oxygen input. This performance comes at the cost of an higher tracking error.

Table 6.6: Performance results for MPC strategy 2 (test dataset).

Controller	Performance criterion	Prediction horizon of the MPC controller P [min]				
		0.5	1	1.5	2	2.5
MPC controller with perfect forecasts	RMSE [K]	0.45	0.07	0.08	0.08	0.08
	m_{O_2} [kg]	31 945.55	31 968.33	31 964.17	31 988.02	31 959.63
	ATV [K]	0.02	0.03	0.03	0.03	0.04
	f_{obj}	−42 139.13	−48 657.01	−48 653.24	−48 549.71	−48 559.12
MPC controller with smart pers. forecasts	RMSE [K]	1.92	1.79	1.71	1.72	1.71
	m_{O_2} [kg]	32 080.55	32 074.03	32 089.23	32 075.46	32 090.00
	ATV [K]	1.50	1.47	1.54	1.58	1.47
	f_{obj}	74 260.74	56 858.36	48 620.45	49 702.90	48 638.47
MPC controller with image-based forecasts	RMSE [K]	1.88	1.72	1.64	1.60	1.61
	m_{O_2} [kg]	32 142.00	32 058.87	32 063.25	32 091.25	32 143.56
	ATV [K]	3.00	1.45	1.46	1.54	1.47
	f_{obj}	68 903.00	49 334.44	40 786.92	36 446.05	37 996.54
Reference controller	RMSE [K]			4.88		
	m_{O_2} [kg]			31 933.00		
	ATV [K]			2.27		
	f_{obj}			762 262.65		

Starting with the perfect forecasts, the RMSE value for all horizons is less than 0.5 K however the oxygen consumption ranges between 31 945.55 kg to 31 988.02 kg. The optimal prediction horizon is 1 min which scored the lowest $f_{obj} = -48657.01$. The MPC with smart persistence forecasts scores a RMSE ranging between 1.67 K to 1.92 K with the lowest RMSE of 1.77 K and $f_{obj} = 48620.45$ for $P = 1.5$ min. The oxygen consumption increases as the forecast horizon increases. The image-based forecast model shows amelioration over the smart persistence model for all prediction horizons: lower RMSE values (around 4%) for an increase

of less than 0.1% in oxygen consumption in some cases. The optimal prediction horizon is chosen to be $P = 1.5\,\text{min}$ for the MPC controller with smart persistence forecasts and $P = 2\,\text{min}$ for the MPC controller with image-based forecasts. This strategy has proven to be better than the reference startegy as well, scoring lower RMSE and ATV values at the cost of an increase of less than 0.5% in oxygen consumption. The mean optimization time per time step for MPC strategy 2 is presented in Table 6.7. As seen for MPC strategy 1, the time needed to solve the optimization problem is less than the sampling time (30 s), but the time needed is still very long, especially for high prediction horizons.

Table 6.7: Mean optimization time per time step for MPC strategy 2.

Controller	Prediction horizon of the MPC controller P [min]				
	0.5	1	1.5	2	2.5
MPC controller with perfect forecasts	1.5 s	5.0 s	10.0 s	15.0 s	30.0 s
MPC controller with smart persistence forecasts	1.0 s	4.6 s	9.7 s	14.5 s	29.0 s
MPC controller with image-based forecasts	1.5 s	5.0 s	10.0 s	15.0 s	30.0 s

6.2.1.3 Comparison between the two proposed MPC strategies

The two proposed MPC strategies have their advantages and disadvantages. Table 6.8 presents the MPC controllers' performance, for the optimal prediction horizons. When perfect forecast are provided, MPC strategy 2 is considered a better approach since the reference tracking error increase is minimal compared to the amount of saved oxygen (around 28%). However, when forecasts are provided by the smart persistence model or the proposed image-based model, MPC strategy 1 is better if low RMSE and ATV values are required, since MPC strategy 1 scores around 16% lower RMSE than MPC strategy 2 (MPC controller with image-based forecasts). The second approach can be adopted if the oxygen injected should be absolutely minimized, since it can save around 11% of oxygen consumption (MPC controller with image-based forecasts).

Table 6.8: Comparison between the two proposed MPC strategies with optimal prediction horizons. For MPC strategy 1, the optimal prediction horizon of the MPC controller is 2 min for all forecasting models. For MPC strategy 2, the optimal prediction horizons of the MPC controller are 1 min (perfect forecasts), 1.5 min (smart persistence forecasts) and 2 min (image-based forecasts).

Strategy	Performance criterion	Perfect forecasts	Image-based forecasts	Smart persistence forecasts
MPC strategy 1	RMSE [K]	$\ll 0.01$	1.34	1.45
	m_{O_2} [kg]	41 920.00	36 365.80	38 509.00
	ATV [K]	$\ll 0.01$	1.32	1.32
MPC strategy 2	RMSE [K]	0.07	1.60	1.71
	m_{O_2} [kg]	31 968.33	32 091.00	32 089.23
	ATV [K]	0.03	1.54	1.54

6.2.2 Case study

6.2.2.1 Reference controller

To gain some insight into the reference controller's behavior, detailed results obtained for three days in the test dataset are given in Figure 6.8. These days have been chosen because DNI was highly variable, with clear-sky, overcast, and mixed situations. Night-time periods are not included, since they are identical to the case where DNI $< 150\,\mathrm{W\,m^{-2}}$: injecting $0.88\,\mathrm{t\,h^{-1}}$ is sufficient to perfectly maintain the reactor's temperature. Figure 6.8 displays several plots against time; from top to bottom: the reactor's temperature T, the defocusing factor D, the oxygen flow rate f^{in}_{oxygen}, and the measured DNI. As can be seen, the reference controller is able to maintain the reactor's temperature, but it is very sensitive to DNI variations. It is able to operate for the three main DNI levels, thanks to its adaptive nature. When the reactor is closed, the temperature is maintained perfectly, as shown from 100 min to 150 min. When the reactor receives a surplus of solar power, from 150 min to 200 min for example, the mirror's controller adjusts the defocusing factor D to maintain the reactor's temperature by eliminating the solar power surplus. Needless to say, during this case, the oxygen injections are minimal. Finally, the adaptive PID controller provided acceptable results when DNI varies between 150 and $800\,\mathrm{W\,m^{-2}}$. It should be mentioned that although the PID controller is able to correctly manage the system, the temperature variations are important.

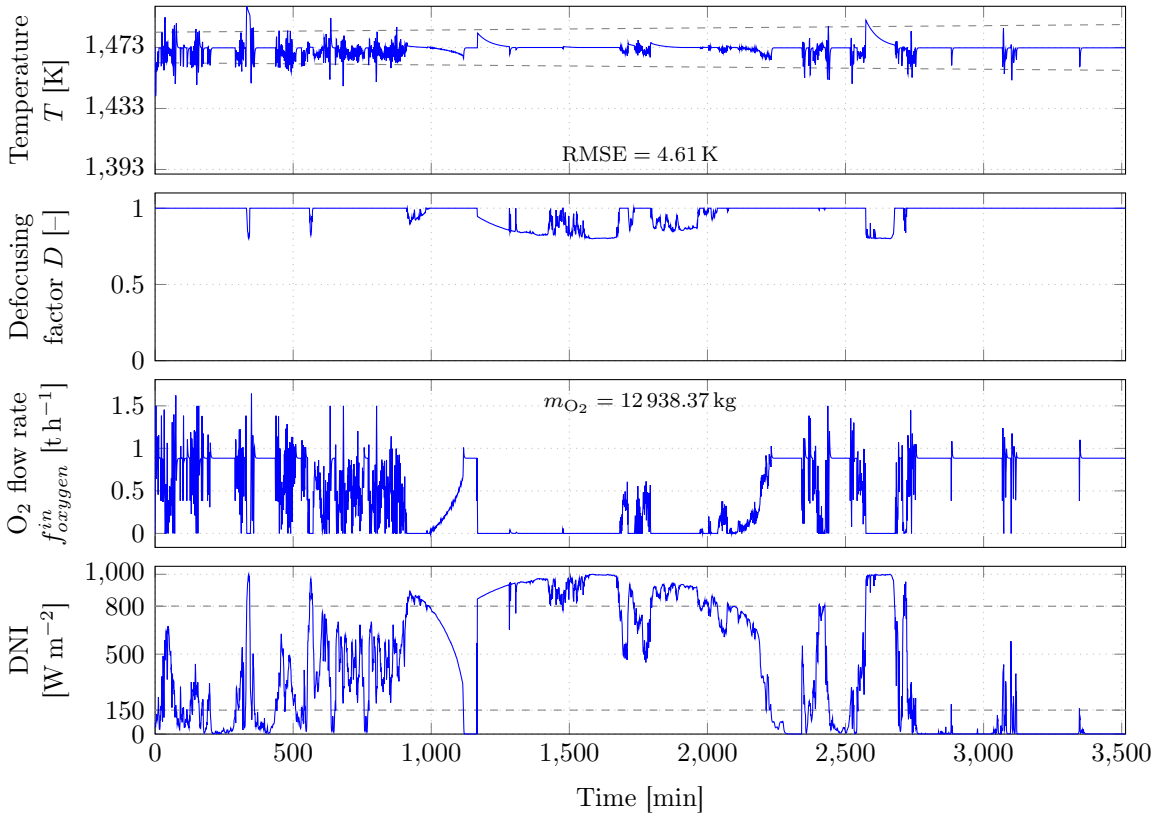

Figure 6.8: Case study: results of the reference controller.

6.2.2.2 MPC controllers

The MPC controllers results are presented for the three forecast models (perfect forecasts, smart persistence forecasts, and image-based forecasts). The chosen prediction horizons, based on the study presented in Section 6.2.1, are recalled in Table 6.9.

Table 6.9: Optimal prediction horizons for the two proposed MPC controllers.

Strategy	Optimal prediction horizon of the MPC controller [min]		
	Perfect forecasts	Smart persistence forecasts	Image-based forecasts
MPC strategy 1	2	2	2
MPC strategy 2	1	1.5	2

6.2.2.2.1 MPC implementation with perfect forecasts Perfect DNI forecasts are provided to showcase the MPC optimal performance. Analyzing Figure 6.9a, the MPC controller is able to perfectly maintain the reactor's temperature (scoring a RMSE of 0.007 K) despite the important DNI variations. The controller is able to operate properly in the closed-reactor case (DNI $< 150\,\mathrm{W\,m^{-2}}$), by injecting the right amount of oxygen ($0.88\,\mathrm{t\,h^{-1}}$). The DNI surplus is compensated by defocusing the mirrors. MPC strategy 2 is able to maintain the temperature, scoring RMSE of 0.073 K, while injecting 12 920.11 kg (−36.2% oxygen consumption compared to MPC strategy 1). Comparing Figure 6.9a and Figure 6.9b, MPC strategy 2 tends to tilt the mirrors only in case of a DNI surplus, which aims to maximize the Sun power received by the reactor (thus using less oxygen), while MPC strategy 1 searches for the input combination for the lowest possible error. For the MPC controller with perfect forecasts, MPC strategy 1 is not interesting, since the tracking error for both strategies is less than 0.1 K, and MPC strategy 2 allows a 36.2% reduction of oxygen consumption.

6.2.2.2.2 MPC implementation with smart persistence forecasts In this section, the DNI forecasts are provided by the smart persistence model. Analyzing Figure 6.10, one can observe that the MPC controller is able to maintain the reactor's temperature (scoring a RMSE of 1.44 K), however some fluctuation can be observed due to inaccurate DNI forecasts. The controller is able to function properly in the closed-reactor scenario and around it (DNI $< 150\,\mathrm{W\,m^{-2}}$) by injecting the right amount of oxygen ($0.88\,\mathrm{t\,h^{-1}}$). The DNI surplus is compensated by defocusing the concentration mirrors. The controller tends to defocalizes the mirrors to compensate for the strong DNI variations as well, thus wasting solar power to maintain the reactor's temperature accurately. Moreover, MPC strategy 2 produces some degradation of the reference tracking performance, scoring a RMSE of 1.66 K (higher by 13.2% compared to MPC strategy 1), but consuming 24.6% less oxygen than MPC strategy 1.

6.2.2.2.3 MPC implementation with image-based forecasts In this section, the DNI forecasts are provided by the image-based model discussed in Section 6.1.2.2. Analyzing Figure 6.11a, one can note that the MPC controller is able to maintain the reactor's temperature (scoring a RMSE of 1.29 K), however some fluctuation can be observed due to DNI ramps not detected using the sky images. The controller is able to function properly in the closed-reactor scenario (DNI $< 150\,\mathrm{W\,m^{-2}}$) by injecting the right amount of oxygen ($0.88\,\mathrm{t\,h^{-1}}$). The DNI surplus is compensated by defocusing the concentration mirrors. As seen before, MPC strategy 2 economizes the oxygen consumption at the cost of a higher tracking error. In this case, the tracking error is increased by 15.1%, which results in reduction of 15.4% in oxygen consumption.

6.3 Solar reactor control with simplified reactor model

The long optimization time is due to the Cantera function, which takes on average 0.05 s to calculate $Q_{reaction}$ for one time step. To solve this problem, $Q_{reaction}$ should be calculated faster. That's why in this section, a replacement for the Cantera function is proposed, then

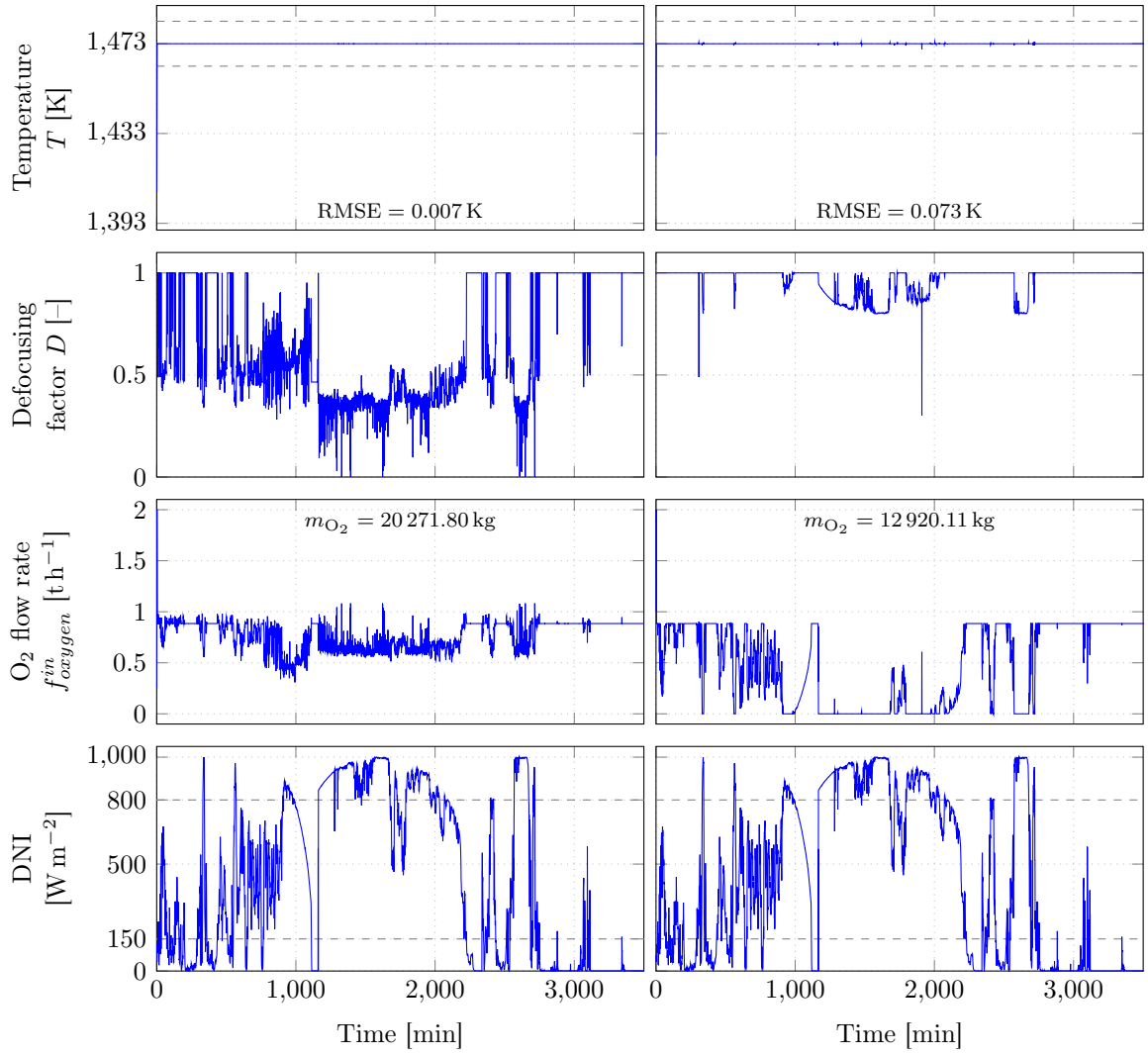

(a) MPC strategy 1 ($P = 2$ min). (b) MPC strategy 2 ($P = 1$ min).

Figure 6.9: Case study: results of the two MPC strategies with perfect forecasts.

the robustness of the MPC controller to the model simplification is examined.

6.3.1 Model simplification

The reaction power $Q_{reaction}$ is calculated for a given temperature and reactant (biomass, steam, and oxygen) flow rates using the Cantera function. Since the biomass and steam flow rates are fixed to their nominal values, the Cantera function could be replaced with a function that takes the current reactor's temperature and the oxygen flow rate as inputs, and computes $Q_{reaction}$. After analyzing the influence of the reactor's temperature and the oxygen flow rate on $Q_{reaction}$ (Figure 6.12), it can be observed that :

- for a given reactor's temperature, $Q_{reaction}$ is mainly a linear function of the oxygen flow rate ($0\,\mathrm{t\,h^{-1}} \leqslant f^{in}_{oxygen} \leqslant 1.8\,\mathrm{t\,h^{-1}}$);
- for a given oxygen flow rate, $Q_{reaction}$ is a linear function of the reactor's temperature ($1453\,\mathrm{K} \leqslant T \leqslant 1493\,\mathrm{K}$).

The chosen neighborhood is around the nominal performance ($1453\,\mathrm{K} \leqslant T \leqslant 1493\,\mathrm{K}$), while respecting the oxygen flow rate constraint ($0\,\mathrm{t\,h^{-1}} \leqslant f^{in}_{oxygen} \leqslant 1.8\,\mathrm{t\,h^{-1}}$).

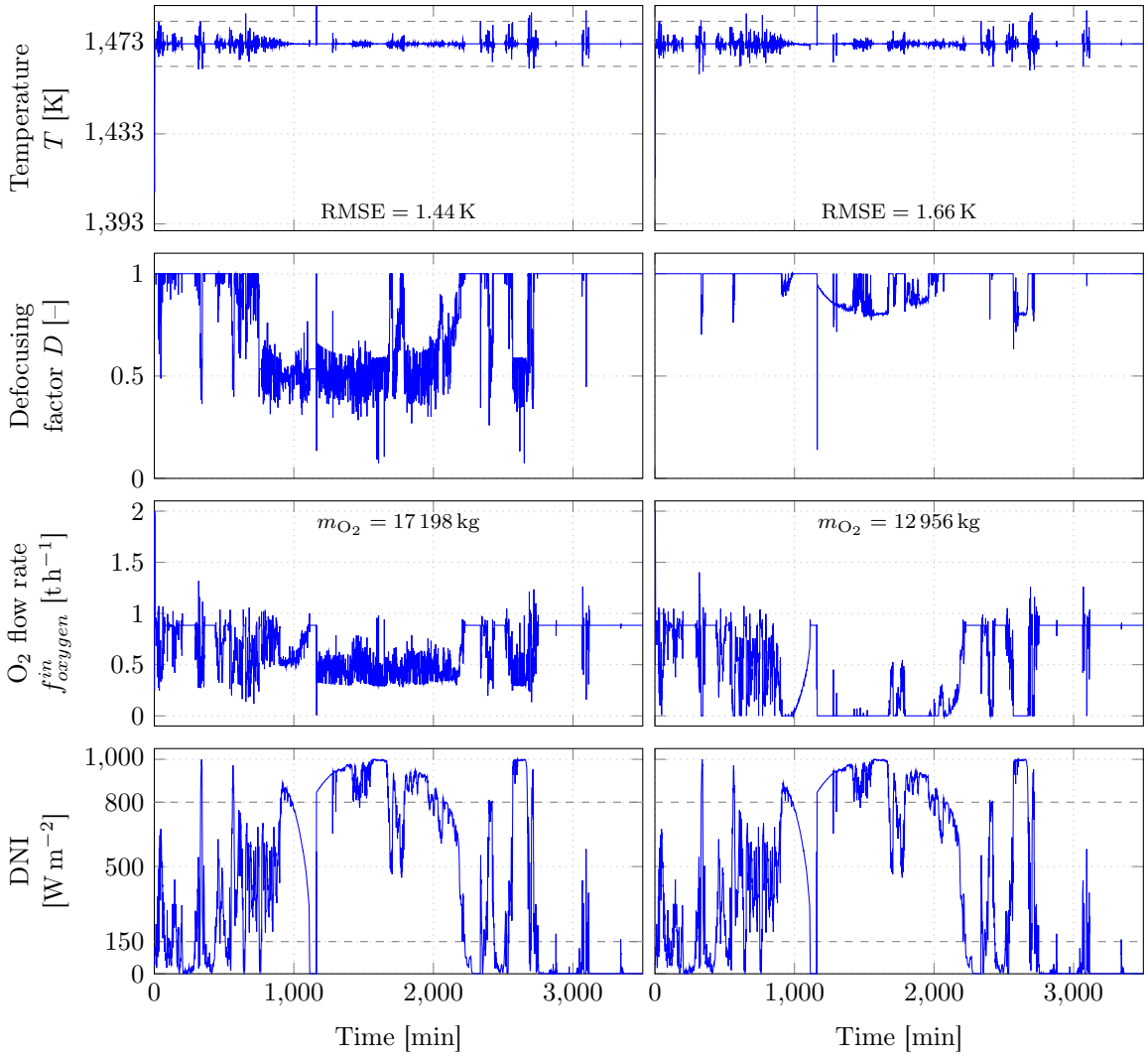

(a) MPC strategy 1 ($P = 2$ min). (b) MPC strategy 2 ($P = 1.5$ min).

Figure 6.10: Case study: results of the two MPC strategies with smart persistence forecasts.

Thus the proposed solution is to replace the Cantera function with a 2D interpolation function, where the various input combinations used to compute $Q_{reaction}$ are saved and used to estimate $Q_{reaction}$ for new combinations. The combinations used to generate the 2D interpolation function are the resulting points in a mesh grid determined by the two discretized input vectors: oxygen flow rate f^{in}_{oxygen}, where the discretization step is equal to 0.05; the reactor's temperature T, where the discretization step is equal to 0.05. It should be noted that the 2D interpolation function needs 0.5 s to treat one day, versus 70 s for the Cantera function.

This approach is tested on 545232 different combinations (not included in the interpolation database), and the resulting mean absolute error between the output of the interpolation function and the Cantera function is 2.14 kW, which induces an error of 0.01 K on temperature variations. This low mean absolute error and this fast execution time justify the replacement of the Cantera function with a 2D interpolation function.

6.3.2 MPC evaluation using the simplified reactor model

In this section, the MPC controllers are implemented using the simplified model for the optimization step and the original model to perform the simulation and test the robustness of the approach to errors induced by model simplification.

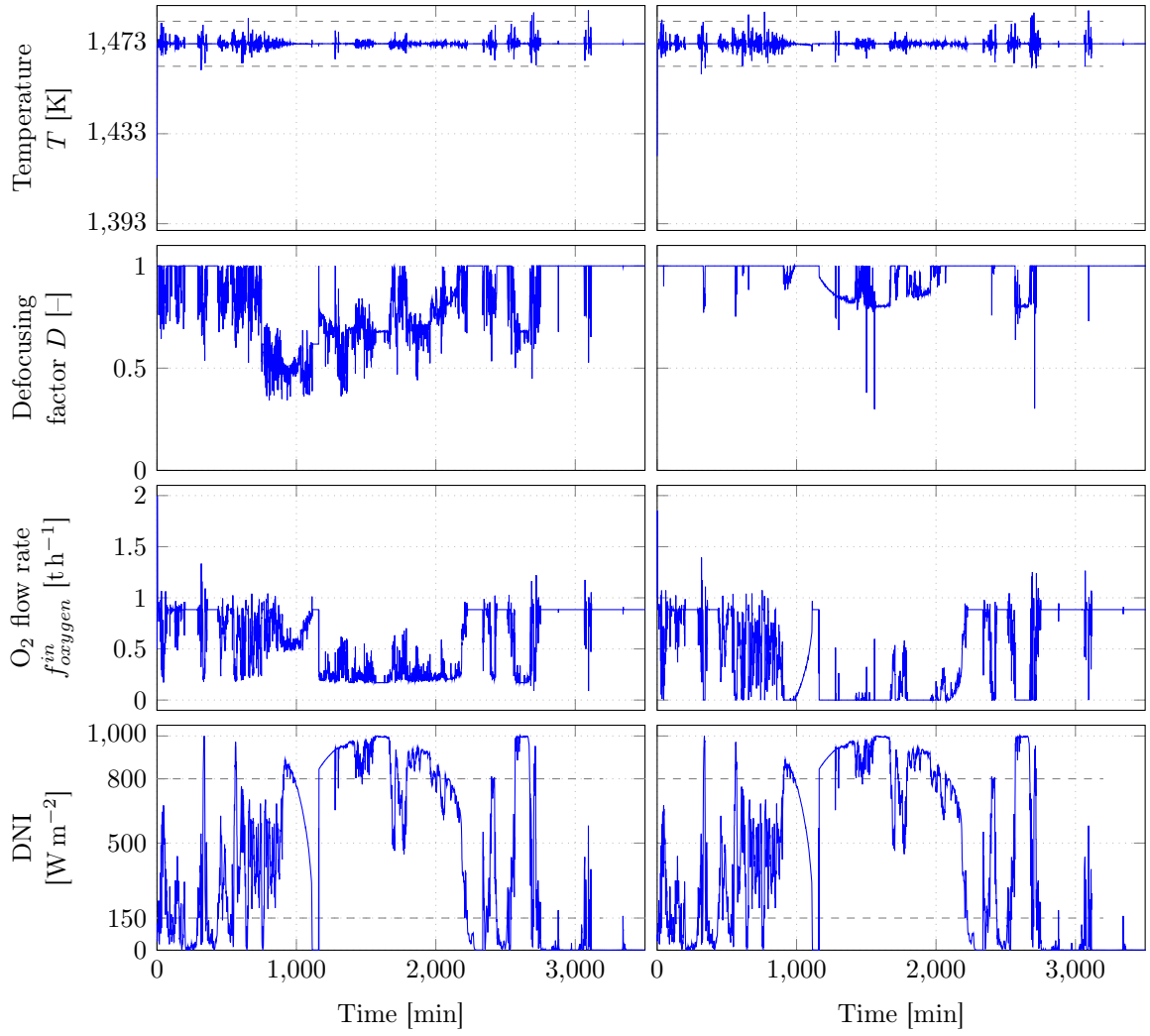

(a) MPC strategy 1 ($P = 2$ min). (b) MPC strategy 2 ($P = 2$ min).

Figure 6.11: Case study: results of the two MPC strategies with image-based forecasts.

6.3.2.1 MPC strategy 1

Table 6.10 presents a comparison between the MPC controller with original reactor model versus the MPC controller with simplified reactor model (MPC strategy 1). This table shows that the MPC controller is robust to the errors caused by model simplification, however, the RMSE increases for all horizons and all forecast models. The MPC controller with image-based forecasts still manages to score lower RMSE values than the MPC controller with smart persistence forecasts, which highlights the importance of accurate DNI forecast, even when the simplified model is used. In terms of computational complexity, using the simplified model reduces drastically the optimization time (up to 58 times for $P = 2.5$ min), as shown in Table 6.10.

6.3.2.2 MPC strategy 2

Table 6.11 presents a comparison between the MPC controller with original reactor model versus the MPC controller with simplified reactor model (MPC strategy 2). This table shows that the MPC controller, with the simplified model, is robust to errors resulting from model simplification: the controller is able to maintain the reactor's temperature, while minimizing the oxygen consumption in the process. The MPC controller with image-based forecasts

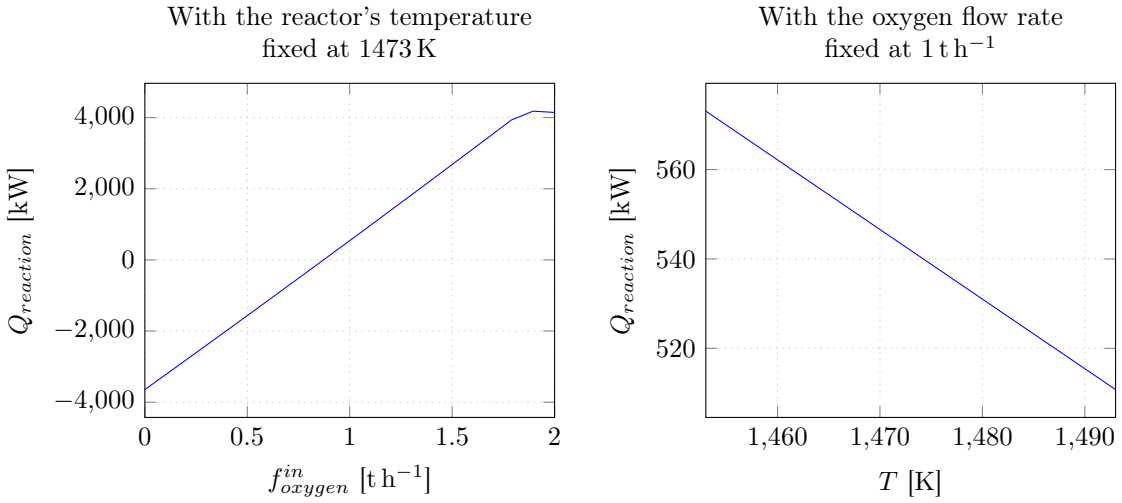

Figure 6.12: Power resulting from the gasification reaction as a function of oxygen flow rate variations (left) and reactor's temperature variations (right).

Table 6.10: MPC strategy 1: simplified reactor model vs. original reactor model.

Controller	Performance criterion	Prediction horizon of the MPC controller P [min]				
		0.5	1	1.5	2	2.5
MPC controller with perfect forecasts and simplified model	RMSE [K]	0.02	0.01	0.02	0.02	0.02
	m_{O_2} [kg]	36 642.00	36 767.00	36 870.00	37 004.00	37 006.00
	ATV [K]	0.01	0.01	0.01	0.01	0.01
	Compu. time [s]	0.10	0.20	0.30	0.40	0.50
MPC controller with perfects forecast and original model	RMSE [K]	$\ll$0.01	$\ll$0.01	$\ll$0.01	$\ll$0.01	$\ll$0.01
	m_{O_2} [kg]	45 151.26	44 676.80	44 558.27	41 920.60	41 920.60
	ATV [K]	$\ll$0.01	$\ll$0.01	$\ll$0.01	$\ll$0.01	$\ll$0.01
	Compu. time [s]	1.54	4.70	9.70	15.00	30.00
MPC controller with smart pers. forecasts and simplified model	RMSE [K]	1.70	1.56	1.55	1.55	1.55
	m_{O_2} [kg]	34 453.00	35 595.00	35 963.00	36 222.00	36 010.00
	ATV [K]	1.49	1.44	1.43	1.41	1.41
	Compu. time [s]	0.10	0.20	0.30	0.40	0.50
MPC controller with smart pers. forecasts and original model	RMSE [K]	1.60	1.54	1.53	1.45	1.50
	m_{O_2} [kg]	34 505.13	35 576.43	36 415.00	38 509.25	35 246.56
	ATV [K]	1.49	1.44	1.42	1.32	1.42
	Compu. time [s]	0.90	4.10	9.10	14.00	28.00
MPC controller with image-based forecasts and simplified model	RMSE [K]	1.63	1.52	1.50	1.47	1.47
	m_{O_2} [kg]	34 557.00	35 178.00	35 579.00	36 052.00	36 448.00
	ATV [K]	1.50	1.46	1.45	1.42	1.42
	Compu. time [s]	0.10	0.20	0.30	0.40	0.50
MPC controller with image-based forecasts and original model	RMSE [K]	1.54	1.45	1.38	1.34	1.34
	m_{O_2} [kg]	34 554.20	35 079.86	35 924.70	36 365.80	36 813.61
	ATV [K]	1.48	1.42	1.35	1.32	1.30
	Compu. time [s]	1.00	4.30	9.30	14.30	29.60

still manages to score lower RMSE and use less oxygen than the MPC controller with smart persistence forecasts, which highlights the importance of accurate DNI forecasts, even when the simplified model is used. In terms of computational complexity, using the simplified reactor model reduces the optimization time drastically (up to 58 times for $P = 2.5\,\text{min}$).

Table 6.11: MPC strategy 2: simplified reactor model vs. original reactor model.

Controller	Performance criterion	Prediction horizon of the MPC controller P [min]				
		0.5	1	1.5	2	2.5
MPC controller with perfect forecasts and simplified model	RMSE [K]	0.49	0.10	0.10	0.11	0.11
	m_{O_2} [kg]	31 956.00	31 961.00	31 965.00	31 972.00	31 979.00
	ATV [K]	0.04	0.05	0.05	0.05	0.05
	f_{obj}	−40 831.19	−48 508.93	−48 500.45	−48 493.56	−48 487.42
	Comp. time [s]	0.10	0.20	0.30	0.40	0.50
MPC controller with perfects forecast and original model	RMSE [K]	0.45	0.07	0.08	0.08	0.08
	m_{O_2} [kg]	31 945.55	31 968.33	31 964.17	31 988.02	31 959.63
	ATV [K]	0.02	0.03	0.03	0.03	0.04
	f_{obj}	−42 139.13	−48 657.01	−48 653.24	−48 549.71	−48 559.12
	Comp. time [s]	1.50	5.00	10.00	15.00	30.00
MPC controller with smart pers. forecasts and simplified model	RMSE [K]	2.01	1.97	1.74	1.73	1.74
	m_{O_2} [kg]	32 043.00	32 093.00	32 137.00	32 152.00	32 106.00
	ATV [K]	1.60	1.50	1.50	1.49	1.50
	f_{obj}	85 065.71	80 101.00	51 807.00	51 350.00	51 652.50
	Comp. time [s]	0.10	0.20	0.30	0.40	0.50
MPC controller with smart pers. forecasts and original model	RMSE [K]	1.92	1.79	1.71	1.72	1.71
	m_{O_2} [kg]	32 080.55	32 074.03	32 089.23	32 075.46	32 090.00
	ATV [K]	1.50	1.47	1.54	1.58	1.47
	f_{obj}	74 260.74	56 858.36	48 620.45	49 702.90	48 638.47
	Comp. time [s]	1.00	4.60	9.70	14.50	29.00
MPC controller with image-based forecasts and simplified model	RMSE [K]	1.97	1.89	1.64	1.62	1.63
	m_{O_2} [kg]	32 102.00	32 081.00	32 114.00	32 126.00	32 146.00
	ATV [K]	3.10	1.47	1.47	1.47	1.47
	f_{obj}	80 943.00	69 440.00	41 032.92	38 072.00	40 028.00
	Comp. time [s]	0.10	0.20	0.30	0.40	0.50
MPC controller with image-based forecasts and original model	RMSE [K]	1.88	1.72	1.64	1.60	1.61
	m_{O_2} [kg]	32 142.00	32 058.87	32 063.25	32 091.25	32 143.56
	ATV [K]	3.00	1.45	1.46	1.47	1.47
	f_{obj}	68 903.00	49 334.44	40 786.92	36 446.05	37 996.54
	Comp. time [s]	1.50	5.00	10.00	15.00	30.00

6.3.2.3 MPC controllers vs. reference controller

The MPC controllers (using the simplified reactor model), with optimal prediction horizons, are compared with the reference controller in Table 6.12. This table shows that, even when the simplified reactor model is used, the MPC controllers still manage to outperform the reference controller by scoring lower RMSE and ATV values at a cost of an increase of less than 0.01% in oxygen consumption for MPC strategy 2 and around 0.1% for MPC strategy 1.

6.4 Conclusion

This chapter deals with the control of a solar reactor that takes advantage of concentrated solar energy to produce syngas. Two MPC controllers are proposed and compared to a reference

Table 6.12: Comparison between the two proposed MPC strategies (with optimal prediction horizon per forecasting model) and the reference strategy. For MPC strategy 1, the optimal prediction horizons are 1 min (perfect forecasts), 2 min (smart persistence forecasts) and 2 min (image-based forecasts). For MPC strategy 2, the optimal prediction horizons are 1 min (perfect forecasts), 2 min (smart persistence forecasts) and 2 min (image-based forecasts).

Strategy	Performance criterion	Perfect forecasts	Image-based forecasts	Smart pers. forecasts
MPC strategy 1	RMSE [K]	0.01	1.47	1.55
	m_{O_2} [kg]	36 767.00	36 052.00	36 222.00
	ATV [K]	0.01	1.42	1.41
MPC strategy 2	RMSE [K]	0.10	1.62	1.73
	m_{O_2} [kg]	31 961.00	32 126.00	32 152.00
	ATV [K]	0.05	1.47	1.49
Reference strategy	RMSE [K]		4.88	
	m_{O_2} [kg]		31 933.00	
	ATV [K]		2.27	

controller which consists of a rule-based controller and an optimized adaptive PID controller. These two strategies target different performances: MPC strategy 1 focuses on maintaining the reactor's temperature at any cost whereas MPC strategy 2 aim at finding a trade-off between maintaining the reactor's temperature and minimizing the oxygen consumption. The ultimate goal of these strategies is to ensure the reactor's stability by maintaining the reactor's temperature at its nominal value despite DNI variations. This study can then be extended to more complicated strategies like maximizing the syngas production, however, this would necessitate a model adapted to this goal. Different DNI forecasts are provided to the MPC controllers: perfect forecasts, which produce optimal performance, smart persistence forecasts, which produce reference performance, and image-based forecasts, where the proposed model processes HDR sky images to forecast possible DNI ramps. This study is carried out to showcase the robustness of the MPC controllers to forecast errors. Finally, due to the long optimization time needed when using the original reactor model (based on the Cantera function), a model simplification is proposed, and the MPC controllers' performance with this simplified model is discussed.

The MPC implementation results over one week show that the MPC controller is able to maintain the reactor's temperature (MPC strategy 1) and to exploit the solar power by minimizing oxygen consumption (MPC strategy 2). Furthermore, the integration of image-based forecasts results in better performance for both strategies: the MPC controller with image-based forecasts scores lower RMSE values (around 9.8%) and lower oxygen consumption (saving up to 1000 kg of oxygen) (MPC strategy 1) and scores lower RMSE values (around 4%) for an increase in oxygen consumption of less than 0.1% (MPC strategy 2). In addition, the MPC controller, with all forecast models, manages to outperform the reference controller by scoring lower RMSE and ATV values at the cost of an increase in oxygen consumption of less than 5% (MPC strategy 1) and less than 0.5% (MPC strategy 2). This analysis ensures the robustness of the MPC controllers to forecasts errors and proves the feasibility of the approach.

Finally, a simplified reactor model is developed by replacing the Canetra function with a 2D interpolation function, which allows to reduce computation time (the simplified model is up to 58 times faster than the original model) at the cost of a slight performance degradation.

General conclusion and outlook

The detrimental repercussions on the environment of human activity, due in part to the large-scale use of fossil fuels, are becoming undeniable. Thus, a global consensus is forming around the urgency of finding sustainable energy sources to meet the growing power demand, and the development of renewable-energy-based power generation is seeing increasing interest. Among these renewable-energy-based solutions are concentrated solar power (CSP) systems, that can be used for power generation or hydrogen production. However, these systems pose several technological and scientific bottlenecks that limit their true potential. The work presented in this thesis contributes to two work packages of the European project SFERA III, in order to tackle some of these challenges: WP10, which aims to solve problems related to solar irradiance intermittence and variability by providing a intrahour direct normal irradiance (DNI) forecasting model, based on DNI observations and sky images from a ground-based camera; and WP8, which aims to propose a dynamic controller, taking advantage of DNI forecasts, to maintain stability of a solar reactor designed to produce syngas.

The review of the state-of-the-art DNI forecasting models showed that while some models handle rather well the clear-sky and overcast situations, they all struggle when dealing with the other cases, coined "mixed situations" in this work. Thus, the interest is shifted toward developing a model that can mainly handle such situations, while still providing accurate forecasts for less complicated situations. That's why a hybrid intrahour forecast model, combining knowledge-based and machine-learning-based approaches, is developed. To assess the benefits of integrating sky images in the forecasting process, this hybrid model is compared to the smart persistence model, and two RNN-based models, i.e., a LSTM model and a CNN-LSTM model, that take solely past DNI observations as input. After optimizing the RNN networks' architectures, the models are compared on a test dataset of DNI with mixed situations. The results show that RNNs can forecast DNI, scoring a positive skill factor (SF) up to 12.5% for the CNN-LSTM model and 11.66% for the LSTM model. However, these statistical models have poor ramp detection capabilities. This is explained by their nature as pure statistical models, with no input concerning the clouds' motion and interaction with the Sun (which is the main cause for a DNI ramp). The low ramp detection index (RDI) values, scored by both RNN models, prove that these models can not be trusted for ramp detection. This analysis explains the motivation behind the integration of sky images and the corresponding image processing steps.

Various image processing steps are performed in the proposed hybrid model. Cloud segmentation is carried out by a k-nearest neighbor model, robust to the problems faced by threshold-based algorithms. A cloud motion estimation map, provided by a dense optical flow algorithm, allows to determine an adaptive region of interest (ROI), with the help of the k-means clustering method. The DNI forecasting step is performed using a combination of two neural networks: a CNN, which processes the ROI, and a MLP that takes the cloud fraction in the ROI and the clear-sky DNI forecast as inputs, to finally forecast DNI at horizons between 5 min and 15 min.

The models are trained and cross-validated over 22 days (mixed situations) from different seasons, exhibiting various sky situations and atmospheric conditions. Another dataset of 18 days (12 days with mixed situations and 6 days with clear-sky and overcast situations) is used

for testing the developed models. For mixed situations, results show that the tested models are capable of outperforming the smart persistence model: for the hybrid model, skill factor values range from 12% to 26% as the forecast horizon increases from 5 min to 15 min, whereas the LSTM and CNN-LSTM models score around 10% for all horizons, which means that the hybrid model is able to consistently outperform the LSTM and CNN-LSTM models. The ramp detection index shows that the tested models are capable of predicting DNI ramps: the hybrid model is able to forecast 72% to 80% of the ramps, whereas the LSTM and CNN-LSTM models are less efficient and detected between 53% and 66% of the ramps. This difference is due to the fact that LSTM and CNN-LSTM models are purely statistical and rely solely on past DNI observations to perform forecasts, without taking into account the sky situation: efficient cloud detection and accurate cloud motion estimation translate into better ramp detection and precise DNI forecasts. For clear-sky and overcast situations, the smart persistence model produces very good results, and the results obtained by the LSTM and CNN-LSTM models are considerably inferior. However, the hybrid model still manages to outperform the smart persistence model, with skill factor values ranging from 6% to 9%. Thanks to the inclusion of HDR sky images, it successfully manages clear-sky, overcast, and mixed situations. As for the complexity of the models, the analysis shows that, while the hybrid model is more complex and demands more computational resources, it is still able to provide forecasts within 7% of the 30 s sampling time.

It is unquestionable that the proposed hybrid model can benefit from extra improvements and ameliorations. To name a few examples: the proposed model could be improved by integrating an accurate and fast probabilistic cloud segmentation model, that could fight against problems posed by thin clouds. Also, in the ROI localization step, one could develop an improved algorithm to handle situations where there are two (or more) cloud layers with different motions. Finally, the hybrid model could be adjusted to handle longer forecast horizons (more than 15 minutes), by hybridizing it with a RNN model, for example, that can handle situations where the localized ROI is outside the image bounds.

The second part of the thesis deals with the modeling and control of a solar reactor designed to produce syngas using concentrated solar power. A model based on the thermodynamic equilibrium is first developed, and then, two model-based predictive control (MPC) strategies are proposed and compared to a reference strategy. The reference controller is a combination of a rule-based controller and an optimized adaptive PID controller. The rule-based controller acts on the defocusing factor to eliminate the DNI surplus if the reactor's temperature is higher than its nominal value and if DNI is higher than $800\,\mathrm{W\,m^{-2}}$, the optimized adaptive PID controller manages the oxygen flow rate to heat up the reactor, if needed, for the different DNI levels ($\mathrm{DNI} < 150\,\mathrm{W\,m^{-2}}$, $150\,\mathrm{W\,m^{-2}} < \mathrm{DNI} < 800\,\mathrm{W\,m^{-2}}$, and $\mathrm{DNI} > 800\,\mathrm{W\,m^{-2}}$). The two MPC strategies were proposed to target different performances: MPC strategy 1 aims to maintain the reactor's temperature at any cost and MPC strategy 2 aims to maintain the reactor's temperature, while minimizing the oxygen consumption, thus maximizing the use of solar energy. The robustness of the controller to forecast errors is studied by testing different types of DNI forecasts: perfect forecasts, which provide optimal performance; smart persistence forecasts, which provide reference performance; and image-based forecasts, obtained by processing HDR sky images.

The results over one week show that the MPC controller is able to maintain the reactor's temperature (MPC strategy 1) and to exploit the solar power by minimizing the oxygen consumption (MPC strategy 2). Furthermore, the integration of image-based forecasts results in better performance for both strategies compared with results obtained using other forecasting models. The MPC controller with image-based forecasts scores lower root mean square error (around 9.8%) and lower oxygen consumption (saving up to 1000 kg of oxygen) for MPC strategy 1. This controller scored lower root mean square error (around 4%), with comparable levels of oxygen consumption for MPC strategy 2. In addition, the MPC controller, with all

forecasting models, manages to outperform the reference controller by scoring lower root mean square error and average temperature variation at the cost of less than a 5% increase in oxygen consumption for MPC strategy 1, and less than a 0.5% increase for MPC strategy 2.

Finally, due to the long optimization time needed when using the reactor model, a model simplification is proposed, and the MPC controller's performance with this simplified model is discussed. The simplified reactor model is developed by replacing the Cantera function with a 2D interpolation function, which allows to drastically reduce the computation time (the simplified model is up to 58 times faster than the original model), at the cost of a slight performance degradation: the root mean square error is increased by around 0.15 K for MPC strategy 1, and around 0.2 K with less than 0.5% increase in oxygen consumption for MPC strategy 2.

The study conducted in this second part of the thesis is a solid base for the development of more sophisticated control strategies. For example, one can imagine developing a strategy that focuses on the maximization of syngas production, while ensuring reactor's stability. However, this strategy requires a model specific to this goal, that can provide accurate production estimation, while considering the kinetics of the chemical reactions. In addition, different control inputs can be utilized in the control strategy, for example, the biomass flow rate can be considered as a controlled input that can compensate for DNI surplus or deficit. For this strategy, the model should account for the kinetics of the biomass gasification reaction as well.

Bibliography

[1] M. Bergquist, A. Nilsson, and P. W. Schultz. "Experiencing a Severe Weather Event Increases Concern About Climate Change". In: *Frontiers in Psychology* 10 (Feb. 2019). DOI: 10.3389/fpsyg.2019.00220.

[2] Z. W. Kundzewicz. "Extreme Weather Events and their Consequences". In: *Papers on Global Change IGBP* 23.1 (Jan. 2016), pp. 59–69. DOI: 10.1515/igbp-2016-0005.

[3] N. Wunderling, M. Willeit, J. F. Donges, and R. Winkelmann. "Global warming due to loss of large ice masses and Arctic summer sea ice". In: *Nature Communications* 11.1 (Oct. 2020). DOI: 10.1038/s41467-020-18934-3.

[4] S. A. Kulp and B. H. Strauss. "New elevation data triple estimates of global vulnerability to sea-level rise and coastal flooding". In: *Nature Communications* 10.1 (Oct. 2019). DOI: 10.1038/s41467-019-12808-z.

[5] IPCC. *Climate Change 2014: Synthesis Report*. Tech. rep. Geneva, Switzerland, 2014.

[6] W. F. Lamb, T. Wiedmann, J. Pongratz, R. Andrew, M. Crippa, J. G. J. Olivier, D. Wiedenhofer, G. Mattioli, A. A. Khourdajie, J. House, S. Pachauri, M. Figueroa, Y. Saheb, R. Slade, K. Hubacek, L. Sun, S. K. Ribeiro, S. Khennas, S. de la Rue du Can, L. Chapungu, S. J. Davis, I. Bashmakov, H. Dai, S. Dhakal, X. Tan, Y. Geng, B. Gu, and J. Minx. "A review of trends and drivers of greenhouse gas emissions by sector from 1990 to 2018". In: *Environmental Research Letters* 16.7 (June 2021), p. 073005. DOI: 10.1088/1748-9326/abee4e.

[7] S. Solomon, G.-K. Plattner, R. Knutti, and P. Friedlingstein. "Irreversible climate change due to carbon dioxide emissions". In: *Proceedings of the National Academy of Sciences* 106.6 (Feb. 2009), pp. 1704–1709. DOI: 10.1073/pnas.0812721106. eprint: https://www.pnas.org/doi/pdf/10.1073/pnas.0812721106.

[8] *IEA, Global Energy Review, Paris*. https://www.iea.org/reports/global-energy-review-2021. 2021.

[9] *Statistical Review of World Energy, 2019*. https://www.bp.com/en/global/corporate/energy-economics/statistical-review-of-world-energy.html.

[10] *The International Energy Outlook (IEO)*. Tech. rep. U.S. Energy Information Administration's (EIA), 2021.

[11] World Energy Council. *World energy resources 2016*. Tech. rep. 2016.

[12] European Network of Transmission System Operators for Electricity. "Electricity in Europe 2017".

[13] D. Fantazzini, M. Höök, and A. Angelantoni. "Global oil risks in the early 21st century". In: *Energy Policy* 39.12 (Dec. 2011), pp. 7865–7873. DOI: 10.1016/j.enpol.2011.09.035.

[14] R. Bentley. "Global oil & gas depletion: an overview". In: *Energy Policy* 30.3 (Feb. 2002), pp. 189–205. ISSN: 0301-4215. DOI: https://doi.org/10.1016/S0301-4215(01)00144-6.

[15] S. Sorrell, J. Speirs, R. Bentley, A. Brandt, and R. Miller. "Global oil depletion: A review of the evidence". In: *Energy Policy* 38.9 (Sept. 2010), pp. 5290–5295. DOI: 10.1016/j.enpol.2010.04.046.

[16] International Energy Agency. *World energy outlook 2010*. Tech. rep. 2010.

[17] N. K. M. A. Alrikabi. "Renewable Energy Types". In: *Journal of Clean Energy Technologies* (2014), pp. 61–64. DOI: 10.7763/jocet.2014.v2.92.

[18] European Commission. *2030 climate and energy framework*. 2014.

[19] *National low-carbon strategy for climate*. https://www.gouvernement.fr/en/adoption-of-the-national-low-carbon-strategy-for-climate. 2015.

[20] *Multiannual energy plan*. https://www.ecologie.gouv.fr/programmations-pluriannuelles-lenergie-ppe. 2017.

[21] M. Nachmany, S. Fanhauser, J. Setzer, and A. Averchenkova. *Global trends in climate change legislation and litigation*. Tech. rep. European Commission, 2017.

[22] International Energy Agency. *Electricity information 2018*. Tech. rep. 2018.

[23] *Renewables 2020 : Analysis and forecast to 2025*. Tech. rep. U.S. Energy Information Administration, 2020.

[24] J. Buonocore. "Climate policy not so costly". In: *Nature Climate Change* 4.10 (Sept. 2014), pp. 861–862. DOI: 10.1038/nclimate2391.

[25] H. Zhang, J. Baeyens, J. Degrève, and G. Cacères. "Concentrated solar power plants: Review and design methodology". In: *Renewable and Sustainable Energy Reviews* 22 (June 2013), pp. 466–481. DOI: 10.1016/j.rser.2013.01.032.

[26] A. Panesar. "Organic Rankine cycle – review and research directions in engine applications". In: *E3S Web of Conferences* 22 (2017). Ed. by B. Kaźmierczak, M. Kutyłowska, K. Piekarska, H. Jouhara, and J. Danielewicz, p. 00132. DOI: 10.1051/e3sconf/20172200132.

[27] R. Chauvin. "Evaluation de la ressource solaire pour la gestion optimisée de centrales CSP". PhD thesis. University of Perpignan Via Domitia, 2016.

[28] N. E. Gharbi, H. Derbal, S. Bouaichaoui, and N. Said. "A comparative study between parabolic trough collector and linear Fresnel reflector technologies". In: *Energy Procedia* 6 (2011), pp. 565–572. ISSN: 1876-6102. DOI: 10.1016/j.egypro.2011.05.065.

[29] IRENA. *Renewable Power Generation Costs in 2014*. International Renewable Energy Agency. 2015.

[30] International Energy Agency. *Technology Roadmap : Solar Photovoltaic Energy – 2014 edition*. 2014.

[31] S. D. Fraia, R. D. Figaj, M. Filipowiczh, and L. Vanoli. "Solar-based systems". In: *Polygeneration Systems*. Elsevier, 2022, pp. 193–237. DOI: 10.1016/b978-0-12-820625-6.00005-0.

[32] S. Qazi. "Solar Thermal Electricity and Solar Insolation". In: *Standalone Photovoltaic (PV) Systems for Disaster Relief and Remote Areas*. Elsevier, 2017, pp. 203–237. DOI: 10.1016/b978-0-12-803022-6.00007-1.

[33] E. Zarza, E. Simonot, A. Martínez, T. Winkler, C.-D. Pérez-Segarra, L. Crespo, M. Sanchez, and R. Pitz-Paal. *Future renewable energy costs: solar-thermal electricity*. Tech. rep. KIC InnoEnergy, 2015.

[34] A. Giostri, M. Binotti, P. Silva, E. Macchi, and G. Manzolini. "Comparison of Two Linear Collectors in Solar Thermal Plants: Parabolic Trough Versus Fresnel". In: *Journal of Solar Energy Engineering* 135.1 (June 2012). DOI: 10.1115/1.4006792.

[35] S. Balaji, K. Reddy, and T. Sundararajan. "Optical modelling and performance analysis of a solar LFR receiver system with parabolic and involute secondary reflectors". In: *Applied Energy* 179 (Oct. 2016), pp. 1138–1151. DOI: 10.1016/j.apenergy.2016.07.082.

[36] G. Morin, J. Dersch, W. Platzer, M. Eck, and A. Häberle. "Comparison of Linear Fresnel and Parabolic Trough Collector power plants". In: *Solar Energy* 86.1 (Jan. 2012), pp. 1–12. DOI: 10.1016/j.solener.2011.06.020.

[37] P. Breeze. "Solar Towers". In: *Solar Power Generation*. Elsevier, 2016, pp. 35–40. DOI: 10.1016/b978-0-12-804004-1.00005-1.

[38] Z. Wang. "Introduction". In: *Design of Solar Thermal Power Plants*. Elsevier, 2019, pp. 1–46. DOI: 10.1016/b978-0-12-815613-1.00001-8.

[39] H. Jin and H. Hong. "Hybridization of concentrating solar power (CSP) with fossil fuel power plants". In: *Concentrating Solar Power Technology*. Elsevier, 2012, pp. 395–420. DOI: 10.1533/9780857096173.2.395.

[40] A. Ferrière. "Centrales solaires thermodynamiques". In: *Ressources énergétiques et stockage* (Apr. 2008). DOI: 10.51257/a-v1-be8903.

[41] A. Buscemi, V. L. Brano, C. Chiaruzzi, G. Ciulla, and C. Kalogeri. "A validated energy model of a solar dish-Stirling system considering the cleanliness of mirrors". In: *Applied Energy* 260 (Feb. 2020), p. 114378. DOI: 10.1016/j.apenergy.2019.114378.

[42] R. Gil, C. Monné, N. Bernal, M. Muñoz, and F. Moreno. "Thermal Model of a Dish Stirling Cavity-Receiver". In: *Energies* 8.2 (Jan. 2015), pp. 1042–1057. DOI: 10.3390/en8021042.

[43] F. Nepveu, A. Ferriere, and F. Bataille. "Thermal model of a dish/Stirling systems". In: *Solar Energy* 83.1 (Jan. 2009), pp. 81–89. DOI: 10.1016/j.solener.2008.07.008.

[44] J.-P. Säck, M. Roeb, C. Sattler, R. Pitz-Paal, and A. Heinzel. "Development of a system model for a hydrogen production process on a solar tower". In: *Solar Energy* 86.1 (Jan. 2012), pp. 99–111. DOI: 10.1016/j.solener.2011.09.010.

[45] R. Boudries and R. Dizene. "Potentialities of hydrogen production in Algeria". In: *International Journal of Hydrogen Energy* 33.17 (Sept. 2008), pp. 4476–4487. DOI: 10.1016/j.ijhydene.2008.06.050.

[46] A. Kudo and Y. Miseki. "Heterogeneous photocatalyst materials for water splitting". In: *Chem. Soc. Rev.* 38.1 (2009), pp. 253–278. DOI: 10.1039/b800489g.

[47] S. Abanades and G. Flamant. "Thermochemical hydrogen production from a two-step solar-driven water-splitting cycle based on cerium oxides". In: *Solar Energy* 80.12 (Dec. 2006), pp. 1611–1623. DOI: 10.1016/j.solener.2005.12.005.

[48] R. Bhattacharyya, A. Misra, and K. Sandeep. "Photovoltaic solar energy conversion for hydrogen production by alkaline water electrolysis: Conceptual design and analysis". In: *Energy Conversion and Management* 133 (Feb. 2017), pp. 1–13. DOI: 10.1016/j.enconman.2016.11.057.

[49] R. Boudries. "Techno-economic study of hydrogen production using CSP technology". In: *International Journal of Hydrogen Energy* 43.6 (Feb. 2018), pp. 3406–3417. DOI: 10.1016/j.ijhydene.2017.05.157.

[50] H. Boujjat, G. M. Y. Junior, S. Rodat, and S. Abanades. "Dynamic simulation and control of solar biomass gasification for hydrogen-rich syngas production during allothermal and hybrid solar/autothermal operation". In: *International Journal of Hydrogen Energy* 45.48 (Sept. 2020), pp. 25827–25837. DOI: 10.1016/j.ijhydene.2020.01.072.

[51] International Energy Agency. *Global Energy Review*. https://www.iea.org/reports/global-energy-review-2020. 2020.

[52] International Energy Agency. *Annual renewable electricity capacity additions, main and accelerated cases, 2014-2026*. IEA, Paris. https://www.iea.org/data-and-statistics/charts/annual-renewable-electricity-capacity-additions-main-and-accelerated-cases-2014-2026.

[53] M. Mehos, C. Turchi, J. Vidal, M. Wagner, Z. Ma, C. Ho, W. Kolb, C. Andraka, and A. Kruizenga. *Concentrating Solar Power Gen3 Demonstration Roadmap*. Tech. rep. Jan. 2017. DOI: 10.2172/1338899.

[54] P. Viebahn, Y. Lechon, and F. Trieb. "The potential role of concentrated solar power CSP in Africa and Europe—A dynamic assessment of technology development, cost development and life cycle inventories until 2050". In: *Energy Policy* 39.8 (2011), pp. 4420–4430.

[55] G. Manzolini, A. Giostri, C. Saccilotto, P. Silva, and E. Macchi. "Development of an innovative code for the design of thermodynamic solar power plants part B: Performance assessment of commercial and innovative technologies". In: *Renewable Energy* 36.9 (Sept. 2011), pp. 2465–2473. DOI: 10.1016/j.renene.2011.02.003.

[56] S. Kuravi, J. Trahan, D. Y. Goswami, M. M. Rahman, and E. K. Stefanakos. "Thermal energy storage technologies and systems for concentrating solar power plants". In: *Progress in Energy and Combustion Science* 39.4 (Aug. 2013), pp. 285–319. DOI: 10.1016/j.pecs.2013.02.001.

[57] X. Py, N. Sadiki, R. Olives, V. Goetz, and Q. Falcoz. "Thermal energy storage for CSP (Concentrating Solar Power)". In: *EPJ Web of Conferences* 148 (2017). Ed. by D. Cahen, L. Cifarelli, D. Ginley, A. Slaoui, A. Terrasi, and F. Wagner, p. 00014. DOI: 10.1051/epjconf/201714800014.

[58] G. Alva, L. Liu, X. Huang, and G. Fang. "Thermal energy storage materials and systems for solar energy applications". In: *Renewable and Sustainable Energy Reviews* 68 (Feb. 2017), pp. 693–706. DOI: 10.1016/j.rser.2016.10.021.

[59] C. Parrado, A. Girard, F. Simon, and E. Fuentealba. "2050 LCOE (Levelized Cost of Energy) projection for a hybrid PV (photovoltaic)-CSP (concentrated solar power) plant in the Atacama Desert, Chile". In: *Energy* 94 (Jan. 2016), pp. 422–430. DOI: 10.1016/j.energy.2015.11.015.

[60] *European project SFERA III*. https://sfera3.sollab.eu/.

[61] M. Schroedter-Homscheidt, A. Benedetti, and N. Killius. "Verification of ECMWF and ECMWF/MACC's global and direct irradiance forecasts with respect to solar electricity production forecasts". In: *Meteorologische Zeitschrift* 26.1 (Feb. 2017), pp. 1–19. DOI: 10.1127/metz/2016/0676.

[62] M. Collares-Pereira and A. Rabl. "Simple procedure for predicting long term average performance of nonconcentrating and of concentrating solar collectors". In: *Solar Energy* 23.3 (1979), pp. 235–253. DOI: 10.1016/0038-092x(79)90163-4.

[63] E. W. Law, A. A. Prasad, M. Kay, and R. A. Taylor. "Direct normal irradiance forecasting and its application to concentrated solar thermal output forecasting–A review". In: *Solar Energy* 108 (2014), pp. 287–307. DOI: 10.1016/j.solener.2014.07.008.

[64] *CNRS images*. https://images.cnrs.fr/reportage-photo/rep000641.

[65] M. Beckers, B. Weise, S. Kalapis, T. Gries, G. Seide, and C.-A. Bunge. "Basics of light guidance". In: *Polymer Optical Fibres*. Elsevier, 2017, pp. 9–46. DOI: 10.1016/b978-0-08-100039-7.00002-6.

[66] P. Ineichen and R. Perez. "A new airmass independent formulation for the Linke turbidity coefficient". In: *Solar Energy* 73.3 (Sept. 2002), pp. 151–157. DOI: 10.1016/s0038-092x(02)00045-2.

[67] G. Kopp. "An assessment of the solar irradiance record for climate studies". In: *Journal of Space Weather and Space Climate* 4 (2014), A14. DOI: 10.1051/swsc/2014012.

[68] H. Li, Y. Lian, X. Wang, W. Ma, and L. Zhao. "Solar constant values for estimating solar radiation". In: *Energy* 36.3 (Mar. 2011), pp. 1785–1789. DOI: 10.1016/j.energy.2010.12.050.

[69] G. Kopp and J. L. Lean. "A new, lower value of total solar irradiance: Evidence and climate significance". In: *Geophysical Research Letters* 38.1 (Jan. 2011). DOI: 10.1029/2010gl045777.

[70] C. A. Gueymard. "A reevaluation of the solar constant based on a 42-year total solar irradiance time series and a reconciliation of spaceborne observations". In: *Solar Energy* 168 (July 2018), pp. 2–9. DOI: 10.1016/j.solener.2018.04.001.

[71] P. Blanc and L. Wald. "The SG2 algorithm for a fast and accurate computation of the position of the Sun for multi-decadal time period". In: *Solar Energy* 86.10 (Oct. 2012), pp. 3072–3083. DOI: 10.1016/j.solener.2012.07.018.

[72] Í. Rapp-Arrarás and J. M. Domingo-Santos. "Functional forms for approximating the relative optical air mass". In: *Journal of Geophysical Research: Atmospheres* 116.D24 (Dec. 2011), n/a–n/a. DOI: 10.1029/2011jd016706.

[73] F. Kasten and A. T. Young. "Revised optical air mass tables and approximation formula". In: *Applied Optics* 28.22 (Nov. 1989), p. 4735. DOI: 10.1364/ao.28.004735.

[74] P. Blanc, B. Espinar, N. Geuder, C. Gueymard, R. Meyer, R. Pitz-Paal, B. Reinhardt, D. Renné, M. Sengupta, L. Wald, and S. Wilbert. "Direct normal irradiance related definitions and applications: The circumsolar issue". In: *Solar Energy* 110 (Dec. 2014), pp. 561–577. DOI: 10.1016/j.solener.2014.10.001.

[75] P. Blanc, B. Espinar, N. Geuder, C. Gueymard, R. Meyer, R. Pitz-Paal, B. Reinhardt, D. Renné, M. Sengupta, L. Wald, and S. Wilbert. "Direct normal irradiance related definitions and applications: The circumsolar issue". In: *Solar Energy* 110 (Dec. 2014), pp. 561–577. DOI: 10.1016/j.solener.2014.10.001.

[76] D. Buie and A. Monger. "The effect of circumsolar radiation on a solar concentrating system". In: *Solar Energy* 76.1-3 (Jan. 2004), pp. 181–185. DOI: 10.1016/j.solener.2003.07.032.

[77] A. Rabl and P. Bendt. "Effect of Circumsolar Radiation on Performance of Focusing Collectors". In: *Journal of Solar Energy Engineering* 104.3 (Aug. 1982), pp. 237–250. DOI: 10.1115/1.3266308.

[78] A. Rabl. "Comparison of solar concentrators". In: *Solar Energy* 18.2 (1976), pp. 93–111. DOI: 10.1016/0038-092x(76)90043-8.

[79] World Meteorological Organization. *Guide to Instruments and Methods of Observation (WMO-No. 8)*. 2018.

[80] Kipp and Zonen. *CH1 Pyrheliometer*. 2001.

[81] N. Geuder and V. Quaschning. "Soiling of irradiation sensors and methods for soiling correction". In: *Solar Energy* 80.11 (Nov. 2006), pp. 1402–1409. DOI: 10.1016/j.solener.2006.06.001.

[82] B. Pape, J. Batlles, N. Geuder, Rayco Zurita Piñero, F. Adan, and B. Pulvermueller. "Soiling impact and correction formulas in solar measurements for CSP projects". In: *SolarPACES 2009: International Conference on Concentrating Solar Power and Chemical Energy Systems*. Berlin, Germany, Sept. 2009.

[83] N. Geuder, R. Affolter, B. Kraas, and S. Wilbert. "Long-term Behavior, Accuracy and Drift of LI-200 Pyranometers as Radiation Sensors in Rotating Shadowband Irradiometers (RSI)". In: *Energy Procedia* 49 (2014), pp. 2330–2339. DOI: 10.1016/j.egypro.2014.03.247.

[84] R. Chauvin, J. Nou, S. Thil, and S. Grieu. "System for measuring components of solar radiation". WO2019053232. 2019.

[85] F. Antonanzas-Torres, R. Urraca, J. Polo, O. Perpiñán-Lamigueiro, and R. Escobar. "Clear sky solar irradiance models: A review of seventy models". In: *Renewable and Sustainable Energy Reviews* 107 (June 2019), pp. 374–387. DOI: 10.1016/j.rser.2019.02.032.

[86] S. Quesada-Ruiz, Y. Chu, J. Tovar-Pescador, H. T. C. Pedro, and C. F. M. Coimbra. "Cloud-tracking methodology for intra-hour DNI forecasting". In: *Solar Energy* 102 (Apr. 2014), pp. 267–275. DOI: 10.1016/j.solener.2014.01.030.

[87] M. Iqbal. *An Introduction to Solar Radiation*. Elsevier, 1983. DOI: 10.1016/b978-0-12-373750-2.x5001-0.

[88] J. Nou, R. Chauvin, S. Thil, and S. Grieu. "A new approach to the real-time assessment of the clear-sky direct normal irradiance". In: *Applied Mathematical Modelling* 40.15 (Aug. 2016), pp. 7245–7264. ISSN: 0307-904X. DOI: https://doi.org/10.1016/j.apm.2016.03.022.

[89] L. Ramírez and J. M. Vindel. "Forecasting and nowcasting of DNI for concentrating solar thermal systems". In: *Advances in Concentrating Solar Thermal Research and Technology*. Ed. by M. J. Blanco and L. R. Santigosa. Woodhead Publishing, 2017.

[90] L. Martín, L. F. Zarzalejo, J. Polo, A. Navarro, R. Marchante, and M. Cony. "Prediction of global solar irradiance based on time series analysis: Application to solar thermal power plants energy production planning". In: *Solar Energy* 84.10 (2010), pp. 1772–1781.

[91] S. Mishra and P. Palanisamy. "Multi-time-horizon solar forecasting using recurrent neural network". In: *2018 IEEE Energy Conversion Congress and Exposition (ECCE)*. IEEE. 2018, pp. 18–24. DOI: 10.1109/ECCE.2018.8558187.

[92] S. Malakar, S. Goswami, B. Ganguli, A. Chakrabarti, S. S. Roy, K. Boopathi, and A. G. Rangaraj. "Designing a long short-term network for short-term forecasting of global horizontal irradiance". In: *SN Applied Sciences* 3.477 (Mar. 2021). DOI: 10.1007/s42452-021-04421-x.

[93] B. Brahma and R. Wadhvani. "Solar Irradiance Forecasting Based on Deep Learning Methodologies and Multi-Site Data". In: *Symmetry* 12.11 (Nov. 2020), p. 1830. ISSN: 2073-8994. DOI: 10.3390/sym12111830.

[94] J. Du, Q. Min, P. Zhang, J. Guo, J. Yang, and B. Yin. "Short-Term Solar Irradiance Forecasts Using Sky Images and Radiative Transfer Model". In: *Energies* 11.5 (May 2018), p. 1107. ISSN: 1996-1073. DOI: 10.3390/en11051107.

[95] Y. Chu, H. T. C. Pedro, and C. F. M. Coimbra. "Hybrid intra-hour DNI forecasts with sky image processing enhanced by stochastic learning". In: *Solar Energy* 98 (Dec. 2013), pp. 592–603. ISSN: 0038-092X. DOI: 10.1016/j.solener.2013.10.020.

[96] R. Marquez and C. F. M. Coimbra. "Intra-hour DNI forecasting based on cloud tracking image analysis". In: *Solar Energy* 91 (May 2013), pp. 327–336. DOI: 10.1016/j.solener.2012.09.018.

[97] M. Caldas and R. Alonso-Suárez. "Very short-term solar irradiance forecast using all-sky imaging and real-time irradiance measurements". In: *Renewable Energy* 143 (Dec. 2019), pp. 1643–1658. DOI: 10.1016/j.renene.2019.05.069.

[98] A. Moncada, W. Richardson, and R. Vega-Avila. "Deep Learning to Forecast Solar Irradiance Using a Six-Month UTSA SkyImager Dataset". In: *Energies* 11.8 (July 2018), p. 1988. DOI: 10.3390/en11081988.

[99] H. T. C. Pedro and C. F. M. Coimbra. "Nearest-neighbor methodology for prediction of intra-hour global horizontal and direct normal irradiances". In: *Renewable Energy* 80 (Aug. 2015), pp. 770–782. ISSN: 0960-1481. DOI: 10.1016/j.renene.2015.02.061.

[100] J. O. Kamadinata, T. L. Ken, and T. Suwa. "Sky image-based solar irradiance prediction methodologies using artificial neural networks". In: *Renewable Energy* 134 (2019), pp. 837–845. ISSN: 0960-1481.

[101] J. Nou, R. Chauvin, J. Eynard, S. Thil, and S. Grieu. "Towards the intrahour forecasting of direct normal irradiance using sky-imaging data". In: *Heliyon* 4.4 (2018), e00598.

[102] Y. Chu, H. T. C. Pedro, M. Li, and C. F. M. Coimbra. "Real-time forecasting of solar irradiance ramps with smart image processing". In: *Solar Energy* 114 (Apr. 2015), pp. 91–104. ISSN: 0038-092X. DOI: 10.1016/j.solener.2015.01.024.

[103] M. Gardner and S. Dorling. "Artificial neural networks (the multilayer perceptron)—a review of applications in the atmospheric sciences". In: *Atmospheric Environment* 32.14-15 (Aug. 1998), pp. 2627–2636. DOI: 10.1016/s1352-2310(97)00447-0.

[104] L. Alzubaidi, J. Zhang, A. J. Humaidi, A. Al-Dujaili, Y. Duan, O. Al-Shamma, J. Santamaría, M. A. Fadhel, M. Al-Amidie, and L. Farhan. "Review of deep learning: concepts, CNN architectures, challenges, applications, future directions". In: *Journal of Big Data* 8.1 (Mar. 2021). DOI: 10.1186/s40537-021-00444-8.

[105] Y. Yu, X. Si, C. Hu, and J. Zhang. "A Review of Recurrent Neural Networks: LSTM Cells and Network Architectures". In: *Neural Computation* 31.7 (July 2019), pp. 1235–1270. DOI: 10.1162/neco_a_01199.

[106] A. Nanduri and L. Sherry. "Anomaly detection in aircraft data using Recurrent Neural Networks (RNN)". In: *Integrated Communications Navigation and Surveillance (ICNS)*. IEEE, Apr. 2016. DOI: 10.1109/icnsurv.2016.7486356.

[107] H. Nguyen, K. Tran, S. Thomassey, and M. Hamad. "Forecasting and Anomaly Detection approaches using LSTM and LSTM Autoencoder techniques with the applications in supply chain management". In: *International Journal of Information Management* 57 (Apr. 2021), p. 102282. DOI: 10.1016/j.ijinfomgt.2020.102282.

[108] D. Debajit, E. D. Preetha, M. Dhruv, and J. Anukriti. "Neural Machine Translation using Recurrent Neural Network". In: *International Journal of Engineering and Advanced Technology* 9.4 (Apr. 2020), pp. 1395–1400. DOI: 10.35940/ijeat.d7637.049420.

[109] K. Lilis and S. Arif. "Sentiment Analysis using Recurrent Neural Network". In: *Journal of Physics: Conference Series* 1471.1 (Feb. 2020), p. 012018. DOI: 10.1088/1742-6596/1471/1/012018.

[110] S. M. Tony and S. Sasikumar. "Music Generation Using Supervised Learning and LSTM". In: *Lecture Notes in Electrical Engineering*. Springer Singapore, July 2021, pp. 477–485.

[111] S. Pal, S. Ghosh, and A. Nag. "Sentiment Analysis in the Light of LSTM Recurrent Neural Networks". In: *International Journal of Synthetic Emotions* 9.1 (Jan. 2018), pp. 33–39. DOI: 10.4018/ijse.2018010103.

[112] L. Jian, H. Xiang, and G. Le. "LSTM-Based Attentional Embedding for English Machine Translation". In: *Scientific Programming* 2022 (Mar. 2022). Ed. by B. Ding, pp. 1–8. DOI: 10.1155/2022/3909726.

[113] T. Mealey and T. M. Taha. "Accelerating Inference In Long Short-Term Memory Neural Networks". In: *NAECON 2018 - IEEE National Aerospace and Electronics Conference*. IEEE, July 2018. DOI: 10.1109/naecon.2018.8556674.

[114] A. Sherstinsky. "Fundamentals of Recurrent Neural Network (RNN) and Long Short-Term Memory (LSTM) Network". In: *CoRR* abs/1808.03314 (2018). arXiv: 1808.03314.

[115] C. Zhang, Z. Yan, C. Ma, and X. Xu. "Prediction of Direct Normal Irradiation Based on CNN-LSTM Model". In: *Proceedings of the 5th International Conference on Multimedia Systems and Signal Processing*. ICMSSP 2020. Chengdu, China: Association for Computing Machinery, May 2020, pp. 74–80. ISBN: 9781450377485. DOI: 10.1145/3404716.3404719.

[116] D. P. Kingma and J. Ba. "Adam: A Method for Stochastic Optimization". In: *3rd International Conference on Learning Representations, ICLR 2015*. San Diego, CA, USA, May 2015.

[117] N. Srivastava, G. Hinton, A. Krizhevsky, and R. Sutskever Ilyaand Salakhutdinov. "Dropout: A Simple Way to Prevent Neural Networks from Overfitting". In: *Journal of Machine Learning Research* 15 (June 2014), pp. 1929–1958.

[118] T. Akiba, S. Sano, T. Yanase, T. Ohta, and M. Koyama. "Optuna: A Next-generation Hyperparameter Optimization Framework". In: *Proceedings of the 25th ACM SIGKDD International Conference on Knowledge Discovery & Data Mining*. July 2019. DOI: 10.1145/3292500.3330701.

[119] D. Scaramuzza, A. Martinelli, and R. Siegwart. "A Toolbox for Easily Calibrating Omnidirectional Cameras". In: *2006 IEEE/RSJ International Conference on Intelligent Robots and Systems*. Oct. 2006, pp. 5695–5701.

[120] R. Chauvin, J. Nou, S. Thil, and S. Grieu. "Modelling the clear-sky intensity distribution using a sky imager". In: *Solar Energy* 119 (2015), pp. 1–17.

[121] G. Bradski. "The OpenCV Library". In: *Dr. Dobb's Journal of Software Tools* (2000).

[122] F. Drago, K. Myszkowski, T. Annen, and N. Chiba. "Adaptive Logarithmic Mapping For Displaying High Contrast Scenes". In: *Computer Graphics Forum* 22.3 (Sept. 2003), pp. 419–426. DOI: 10.1111/1467-8659.00689.

[123] F. Durand and J. Dorsey. "Fast bilateral filtering for the display of high-dynamic-range images". In: *ACM Transactions on Graphics* 21.3 (July 2002), pp. 257–266. DOI: 10.1145/566654.566574.

[124] R. Mantiuk, K. Myszkowski, and H.-P. Seidel. "A perceptual framework for contrast processing of high dynamic range images". In: *ACM Transactions on Applied Perception* 3.3 (July 2006), pp. 286–308. DOI: 10.1145/1166087.1166095.

[125] E. Reinhard and K. Devlin. "Dynamic Range Reduction Inspired by Photoreceptor Physiology". In: *IEEE Transactions on Visualization and Computer Graphics* 11.01 (Jan. 2005), pp. 13–24. DOI: 10.1109/tvcg.2005.9.

[126] S. Rahman, M. M. Rahman, M. Abdullah-Al-Wadud, G. D. Al-Quaderi, and M. Shoyaib. "An adaptive gamma correction for image enhancement". In: *EURASIP Journal on Image and Video Processing* 2016.1 (Oct. 2016). DOI: 10.1186/s13640-016-0138-1.

[127] M. Bertalmío. "Adaptation and efficient coding". In: *Vision Models for High Dynamic Range and Wide Colour Gamut Imaging*. Elsevier, 2020, pp. 65–93. DOI: 10.1016/b978-0-12-813894-6.00009-0.

[128] C. N. Long, J. M. Sabburg, J. Calbó, and D. Pagès. "Retrieving Cloud Characteristics from Ground-Based Daytime Color All-Sky Images". In: *Journal of Atmospheric and Oceanic Technology* 23.5 (May 2006), pp. 633–652. DOI: 10.1175/jtech1875.1.

[129] Q. Li, W. Lu, and J. Yang. "A Hybrid Thresholding Algorithm for Cloud Detection on Ground-Based Color Images". In: *Journal of Atmospheric and Oceanic Technology* 28.10 (Oct. 2011), pp. 1286–1296. DOI: 10.1175/jtech-d-11-00009.1.

[130] S. Liu, L. Zhang, Z. Zhang, C. Wang, and B. Xiao. "Automatic Cloud Detection for All-Sky Images Using Superpixel Segmentation". In: *IEEE Geoscience and Remote Sensing Letters* 12.2 (Feb. 2015), pp. 354–358. DOI: 10.1109/lgrs.2014.2341291.

[131] S. Dev, Y. H. Lee, and S. Winkler. "Color-based segmentation of sky/cloud images from ground-based cameras". In: *IEEE Journal of Selected Topics in Applied Earth Observations and Remote Sensing* 10.1 (Jan. 2017), pp. 231–242. DOI: 10.1109/JSTARS.2016.2558474.

[132] Y. Boykov, O. Veksler, and R. Zabih. "Fast approximate energy minimization via graph cuts". In: *IEEE Transactions on Pattern Analysis and Machine Intelligence* 23.11 (2001), pp. 1222–1239. DOI: 10.1109/34.969114.

[133] V. Kolmogorov and R. Zabih. "What energy functions can be minimized via graph cuts?" In: *IEEE Transactions on Pattern Analysis and Machine Intelligence* 26.2 (Feb. 2004), pp. 147–159. DOI: 10.1109/tpami.2004.1262177.

[134] Y. Boykov and V. Kolmogorov. "An experimental comparison of min-cut/max- flow algorithms for energy minimization in vision". In: *IEEE Transactions on Pattern Analysis and Machine Intelligence* 26.9 (Sept. 2004), pp. 1124–1137. DOI: 10.1109/tpami.2004.60.

[135] N. Otsu. "A Threshold Selection Method from Gray-Level Histograms". In: *IEEE Transactions on Systems, Man, and Cybernetics* 9.1 (Jan. 1979), pp. 62–66. DOI: 10.1109/TSMC.1979.4310076.

[136] J. Huo and D. Lu. "Cloud Determination of All-Sky Images under Low-Visibility Conditions". In: *Journal of Atmospheric and Oceanic Technology* 26.10 (Oct. 2009), pp. 2172–2181. DOI: 10.1175/2009jtecha1324.1.

[137] Z. Peng, D. Yu, D. Huang, J. Heiser, and P. Kalb. "A hybrid approach to estimate the complex motions of clouds in sky images". In: *Solar Energy* 138 (Nov. 2016), pp. 10–25. ISSN: 0038-092X. DOI: 10.1016/j.solener.2016.09.002.

[138] S. R. West, D. Rowe, S. Sayeef, and A. Berry. "Short-term irradiance forecasting using skycams: Motivation and development". In: *Solar Energy* 110 (Dec. 2014), pp. 188–207. DOI: 10.1016/j.solener.2014.08.038.

[139] P. Tuominen and M. Tuononen. "Cloud detection and movement estimation based on sky camera images using neural networks and the Lucas-Kanade method". In: *AIP Conference Proceedings* 1850 (June 2017), p. 140020. DOI: 10.1063/1.4984528.

[140] A. Cazorla, F. Olmo, and L. Arboledas. "Development of a sky imager for cloud cover assessment". In: *Journal of the Optical Society of America. A - Optics, image science, and vision* 25 (Feb. 2008), pp. 29–39. DOI: 10.1364/JOSAA.25.000029.

[141] A. Linfoot and R. J. Alliss. "A cloud detection algorithm applied to a whole sky imager instrument using neural networks". In: *19th Conference on Probability and Statistics – 6th Conference on Artificial Intelligence Applications to Environmental Science*. 2008.

[142] D. E. Rumelhart, G. E. Hinton, and R. J. Williams. "Learning representations by back-propagating errors". In: *Nature* 323.6088 (Oct. 1986), pp. 533–536. DOI: 10.1038/323533a0.

[143] A. U. Ruby, P. Theerthagiri, I. J. Jacob3, and Y. Vamsidhar. "Binary cross entropy with deep learning technique for Image classification". In: *International Journal of Advanced Trends in Computer Science and Engineering* 9.4 (Aug. 2020), pp. 5393–5397. DOI: 10.30534/ijatcse/2020/175942020.

[144] F. Chollet et al. *Keras*. https://keras.io. 2015.

[145] H. A. A. Alfeilat, A. B. A. Hassanat, O. Lasassmeh, A. S. Tarawneh, M. B. Alhasanat, H. S. E. Salman, and V. B. S. Prasath. "Effects of Distance Measure Choice on K-Nearest Neighbor Classifier Performance: A Review". In: *Big Data* 7.4 (Dec. 2019), pp. 221–248. DOI: 10.1089/big.2018.0175.

[146] J. L. Bentley. "Multidimensional binary search trees used for associative searching". In: *Communications of the ACM* 18.9 (Sept. 1975), pp. 509–517. DOI: 10.1145/361002.361007.

[147] T. M. Hamill and T. Nehrkorn. "A Short-Term Cloud Forecast Scheme Using Cross Correlations". In: *Weather and Forecasting* 8.4 (Dec. 1993), pp. 401–411. DOI: 10.1175/1520-0434(1993)008<0401:ASTCFS>2.0.CO;2.

[148] N. Mori and K.-A. Chang. *Introduction to MPIV*. http://www.oceanwave.jp/softwares/mpiv. 2003.

[149] D. Sun, S. Roth, and M. J. Black. "A Quantitative Analysis of Current Practices in Optical Flow Estimation and the Principles Behind Them". In: *International Journal of Computer Vision* 106.2 (Sept. 2014), pp. 115–137. ISSN: 0920-5691. DOI: 10.1007/s11263-013-0644-x.

[150] J. Huang, W. Zou, Z. Zhu, and J. Zhu. "An Efficient Optical Flow Based Motion Detection Method for Non-stationary Scenes". In: *2019 Chinese Control And Decision Conference (CCDC)*. IEEE, June 2019. DOI: 10.1109/ccdc.2019.8833206.

[151] D. K. Sharma, R. Radhakrishnan, and V. Murthy. "A Review On Particle Image Velocimetry And Optical Flow Methods In Riverine Environment". In: *1st International Conference on Recent Trends in Engineering and Technology*. Feb. 2017.

[152] J. Wulff and M. J. Black. "Efficient sparse-to-dense optical flow estimation using a learned basis and layers". In: *2015 IEEE Conference on Computer Vision and Pattern Recognition (CVPR)*. IEEE, June 2015. DOI: 10.1109/cvpr.2015.7298607.

[153] J.-Y. Bouguet. "Pyramidal implementation of the Lucas Kanade feature tracker Description of the algorithm". In: *Intel Corporation, Microprocessor Research Labs* (1999).

[154] G. Farnebäck. "Polynomial Expansion for Orientation and Motion Estimation". Dissertation No 790, ISBN 91-7373-475-6. PhD thesis. SE-581 83 Linköping, Sweden: Linköping University, Sweden, 2002.

[155] G. Farnebäck. "Two-Frame Motion Estimation Based on Polynomial Expansion". In: *Image Analysis*. Ed. by J. Bigun and T. Gustavsson. Berlin, Heidelberg: Springer Berlin Heidelberg, 2003, pp. 363–370. ISBN: 978-3-540-45103-7.

[156] X. Jin and J. Han. "K-Means Clustering". In: *Encyclopedia of Machine Learning and Data Mining*. Springer US, 2017, pp. 695–697. DOI: 10.1007/978-1-4899-7687-1_431.

[157] H. Boujjat, S. Rodat, S. Chuayboon, and S. Abanades. "Experimental and numerical study of a directly irradiated hybrid solar/combustion spouted bed reactor for continuous steam gasification of biomass". In: *Energy* 189 (Dec. 2019), p. 116118. DOI: 10.1016/j.energy.2019.116118.

[158] D. Gregg, R. Taylor, J. Campbell, J. Taylor, and A. Cotton. "Solar gasification of coal, activated carbon, coke and coal and biomass mixtures". In: *Solar Energy* 25.4 (1980), pp. 353–364. DOI: 10.1016/0038-092x(80)90347-3.

[159] R. Taylor, R. Berjoan, and J. Coutures. "Solar gasification of carbonaceous materials". In: *Solar Energy* 30.6 (1983), pp. 513–525. DOI: 10.1016/0038-092x(83)90063-4.

[160] D. Yadav and R. Banerjee. "A review of solar thermochemical processes". In: *Renewable and Sustainable Energy Reviews* 54 (Feb. 2016), pp. 497–532. DOI: 10.1016/j.rser.2015.10.026.

[161] M. Puig-Arnavat, E. Tora, J. Bruno, and A. Coronas. "State of the art on reactor designs for solar gasification of carbonaceous feedstock". In: *Solar Energy* 97 (Nov. 2013), pp. 67–84. DOI: 10.1016/j.solener.2013.08.001.

[162] M. Milanese, G. Colangelo, F. Iacobazzi, and A. de Risi. "Modeling of double-loop fluidized bed solar reactor for efficient thermochemical fuel production". In: *Solar Energy Materials and Solar Cells* 160 (Feb. 2017), pp. 174–181. DOI: 10.1016/j.solmat.2016.10.028.

[163] A. Gómez-Barea, M. Suárez-Almeida, and A. Ghoniem. "Analysis of fluidized bed gasification of biomass assisted by solar-heated particles". In: *Biomass Conversion and Biorefinery* 11.1 (Sept. 2020), pp. 143–158. DOI: 10.1007/s13399-020-00865-0.

[164] Q. Bellouard, S. Abanades, and S. Rodat. "Biomass Gasification in an Innovative Spouted-Bed Solar Reactor: Experimental Proof of Concept and Parametric Study". In: *Energy Fuels* 31.10 (Sept. 2017), pp. 10933–10945. DOI: 10.1021/acs.energyfuels.7b01839.

[165] A. Curcio, S. Rodat, V. Vuillerme, and S. Abanades. "Experimental assessment of woody biomass gasification in a hybridized solar powered reactor featuring direct and indirect heating modes". In: *International Journal of Hydrogen Energy* 46.75 (Oct. 2021), pp. 37192–37207. DOI: 10.1016/j.ijhydene.2021.09.008.

[166] A. P. Muroyama, I. Guscetti, G. L. Schieber, S. Haussener, and P. G. Loutzenhiser. "Design and demonstration of a prototype 1.5 kWth hybrid solar/autothermal steam gasifier". In: *Fuel* 211 (Jan. 2018), pp. 331–340. DOI: 10.1016/j.fuel.2017.09.059.

[167] B. J. Hathaway and J. H. Davidson. "Autothermal hybridization and controlled production of hydrogen-rich syngas in a molten salt solar gasifier". In: *International Journal of Hydrogen Energy* 46.29 (Apr. 2021), pp. 15257–15267. DOI: 10.1016/j.ijhydene.2021.02.048.

[168] C. Maffezzoni and F. Parigi. "Dynamic analysis and control of a solar power plant—II. Control system design and simulation". In: *Solar Energy* 28.2 (1982), pp. 117–128. DOI: 10.1016/0038-092x(82)90290-0.

[169] E. Camacho, F. Rubio, and F. Hughes. "Self-tuning control of a solar power plant with a distributed collector field". In: *IEEE Control Systems* 12.2 (Apr. 1992), pp. 72–78. DOI: 10.1109/37.126858.

[170] F. Rubio, M. Berenguel, and E. Camacho. "Fuzzy logic control of a solar power plant". In: *IEEE Transactions on Fuzzy Systems* 3.4 (1995), pp. 459–468. DOI: 10.1109/91.481955.

[171] R. Pickhardt. "Nonlinear modelling and adaptive predictive control of a solar power plant". In: *Control Engineering Practice* 8.8 (Aug. 2000), pp. 937–947. DOI: 10.1016/s0967-0661(00)00009-5.

[172] M. Arahal, M. Berenguel, and E. Camacho. "Neural identification applied to predictive control of a solar plant". In: *Control Engineering Practice* 6.3 (Mar. 1998), pp. 333–344. DOI: 10.1016/s0967-0661(98)00025-2.

[173] E. Camacho, F. Rubio, M. Berenguel, and L. Valenzuela. "A survey on control schemes for distributed solar collector fields. Part I: Modeling and basic control approaches". In: *Solar Energy* 81.10 (Oct. 2007), pp. 1240–1251. DOI: 10.1016/j.solener.2007.01.002.

[174] E. Camacho, F. Rubio, M. Berenguel, and L. Valenzuela. "A survey on control schemes for distributed solar collector fields. Part II: Advanced control approaches". In: *Solar Energy* 81.10 (Oct. 2007), pp. 1252–1272. DOI: 10.1016/j.solener.2007.01.001.

[175] J. Petrasch, P. Osch, and A. Steinfeld. "Dynamics and control of solar thermochemical reactors". In: *Chemical Engineering Journal* 145.3 (Jan. 2009), pp. 362–370. DOI: 10.1016/j.cej.2008.07.051.

[176] E. Saade, D. E. Clough, and A. W. Weimer. "Model predictive control of a solar-thermal reactor". In: *Solar Energy* 102 (Apr. 2014), pp. 31–44. DOI: 10.1016/j.solener.2013.12.029.

[177] A. Muroyama, T. Shinn, R. Fales, and P. G. Loutzenhiser. "Modeling of a Dynamically-Controlled Hybrid Solar/Autothermal Steam Gasification Reactor". In: *Energy Fuels* 28.10 (Sept. 2014), pp. 6520–6530. DOI: 10.1021/ef501535r.

[178] D. G. Goodwin, R. L. Speth, H. K. Moffat, and B. W. Weber. *Cantera: An Object-oriented Software Toolkit for Chemical Kinetics, Thermodynamics, and Transport Processes*. 2021. DOI: 10.5281/ZENODO.4527812.

[179] C. Dupont, G. Boissonnet, J.-M. Seiler, P. Gauthier, and D. Schweich. "Study about the kinetic processes of biomass steam gasification". In: *Fuel* 86.1-2 (Jan. 2007), pp. 32–40. DOI: 10.1016/j.fuel.2006.06.011.

[180] G. P. Smith, D. M. Golden, M. Frenklach, N. W. Moriarty, B. Eiteneer, M. Goldenberg, C. T. Bowman, R. K. Hanson, S. Song, W. C. Gardiner, V. V. Lissianski, and Z. Qin. http://combustion.berkeley.edu/gri-mech/version30/text30.html.

[181] K. H. Ang, G. Chong, and Y. Li. "PID control system analysis, design, and technology". In: *IEEE Transactions on Control Systems Technology* 13.4 (July 2005), pp. 559–576. DOI: 10.1109/tcst.2005.847331.

[182] G. Liu and S. Daley. "Optimal-tuning PID control for industrial systems". In: *Control Engineering Practice* 9.11 (Nov. 2001), pp. 1185–1194. DOI: 10.1016/s0967-0661(01)00064-8.

[183] C. E. García, D. M. Prett, and M. Morari. "Model predictive control: Theory and practice—A survey". In: *Automatica* 25.3 (May 1989), pp. 335–348. DOI: 10.1016/0005-1098(89)90002-2.

[184] Y. Karout, S. Thil, J. Eynard, and S. Grieu. "Cloud/sky segmentation from ground camera based on supervised machine learning approach". In: *33rd Efficiency, cost, optimization, simulation and environmental impact of energy systems*. Osaka, Japan, 2020.

[185] A. R. Conn, N. I. M. Gould, and P. L. Toint. *Trust Region Methods*. Society for Industrial and Applied Mathematics, Jan. 2000. DOI: 10.1137/1.9780898719857.

Abstract

As a result of human activity in recent decades, the planet is facing existential threats that require swift action. SFERA III is one of several research projects aiming to fulfill the EU's green vision. Its goal is to provide adapted technical solutions for concentrated solar power systems. This thesis contributes to SFERA III in two ways: first, solve problems related to solar irradiance intermittence, by providing an intrahour direct normal irradiance (DNI) forecasting model; second, propose a model-based predictive controller, taking advantage of DNI forecasts, to maintain the stability of a solar reactor designed to produce syngas, while preserving performance.

The first part of this thesis exhibits a hybrid model for the intrahour forecasting of DNI. It combines a knowledge-based model, that is used for clear-sky DNI forecasting from DNI measurements, with a machine-learning-based model, that evaluates the impact of atmospheric disturbances on the solar resource, through the processing of high dynamic range sky images provided by a ground-based camera. The performance of the hybrid model is compared with that of two machine learning models based on past DNI observations only. The results highlight the pertinence of combining knowledge-based models with data-driven models, and of integrating sky-imaging data in the DNI forecasting process.

The second part of the thesis deals with the modeling and control of a solar reactor designed to produce syngas, by exploiting concentrated solar power. A reactor model based on the thermodynamic equilibrium is developed. Then, two model-based predictive control strategies are proposed: MPC strategy 1 aims to maintain the reactor's temperature at its nominal value; MPC strategy 2 aims to maintain the reactor's temperature at nominal value, while maximizing the use of solar energy. Finally, these controllers are compared to a reference controller, which is a combination of a rule-based controller and an optimized adaptive PID controller. The robustness of the controller to forecast errors is also studied by testing different DNI forecasting models.

Keywords: solar resource forecast; direct normal irradiance; sky-imaging data; knowledge-based model; machine learning; model-based predictive control; solar reactor; syngas production.

Résumé

En raison de l'activité humaine au cours de ces dernières décennies, la planète est confrontée à des menaces existentielles qui nécessitent une action rapide. SFERA III est l'un des nombreux projets de recherche visant à concrétiser la vision verte de l'UE. Son objectif est de fournir des solutions techniques adaptées aux systèmes basés sur l'énergie solaire concentrée. Cette thèse contribue à SFERA III de deux manières : un modèle de prévision infra-horaire de l'éclairement normal direct (DNI) a été développé pour résoudre les problèmes liés à l'intermittence de la ressource solaire ; un contrôleur prédictif, tirant profit de prévisions du DNI, a été développé pour garantir la stabilité d'un réacteur solaire déstiné à la production de gaz de synthèse, tout en préservant ses performances.

La première partie de cette thèse traite du dévelopement d'un modèle hybride pour la prévision infra-horaire du DNI. Il combine un modèle de connaissance, qui est utilisé pour la prévision du DNI par ciel clair à partir de mesures du DNI, avec un modèle fondé sur l'apprentissage automatique, qui évalue l'impact des perturbations atmosphériques sur la ressource solaire, par le traitement d'images du ciel à plage dynamique élevée. Les performances du modèle hybride sont comparées à celles de deux modèles statistiques basés sur des observations passées du DNI. Les résultats soulignent la pertinence du modèle hybride et de la prise en compte d'images du ciel dans le processus de prévision du DNI.

La deuxième partie de cette thèse porte sur la modélisation et le contrôle d'un réacteur solaire destiné à la production de gaz de synthèse. Un modèle basé sur l'équilibre thermodynamique a été développé. Ensuite, deux stratégies prédictives ont été proposées : la première stratégie vise à maintenir la température du réacteur à sa valeur nominale ; la deuxième stratégie vise à maintenir la température du réacteur à sa valeur nominale, tout en maximisant l'utilisation de l'énergie solaire concentrée. Enfin, ces contrôleurs ont été comparés à un contrôleur de référence qui associe un contrôleur basé sur des règles et un contrôleur PID adaptatif. Différents modèles de prévision du DNI ont été testés et la robustesse des contrôleurs aux erreurs de prévision a été évaluée.

Mots-clés : prévision de la ressource solaire; éclairement normal direct ; image du ciel ; modèle de connaissance ; apprentissage automatique ; contrôle prédictif ; réacteur solaire ; production de gaz de synthèse.